GWTC-3: Compact Binary Coalescences Observed by LIGO and Virgo during the Second Part of the Third Observing Run

R. Abbott *et al.*[*]
(LIGO Scientific Collaboration, Virgo Collaboration, and KAGRA Collaboration)

(Received 10 November 2021; accepted 5 June 2023; published 4 December 2023)

The third Gravitational-Wave Transient Catalog (GWTC-3) describes signals detected with Advanced LIGO and Advanced Virgo up to the end of their third observing run. Updating the previous GWTC-2.1, we present candidate gravitational waves from compact binary coalescences during the second half of the third observing run (O3b) between 1 November 2019, 15:00 Coordinated Universal Time (UTC) and 27 March 2020, 17:00 UTC. There are 35 compact binary coalescence candidates identified by at least one of our search algorithms with a probability of astrophysical origin $p_{\mathrm{astro}} > 0.5$. Of these, 18 were previously reported as low-latency public alerts, and 17 are reported here for the first time. Based upon estimates for the component masses, our O3b candidates with $p_{\mathrm{astro}} > 0.5$ are consistent with gravitational-wave signals from binary black holes or neutron-star–black-hole binaries, and we identify none from binary neutron stars. However, from the gravitational-wave data alone, we are not able to measure matter effects that distinguish whether the binary components are neutron stars or black holes. The range of inferred component masses is similar to that found with previous catalogs, but the O3b candidates include the first confident observations of neutron-star–black-hole binaries. Including the 35 candidates from O3b in addition to those from GWTC-2.1, GWTC-3 contains 90 candidates found by our analysis with $p_{\mathrm{astro}} > 0.5$ across the first three observing runs. These observations of compact binary coalescences present an unprecedented view of the properties of black holes and neutron stars.

DOI: 10.1103/PhysRevX.13.041039 Subject Areas: Astrophysics, Gravitation

I. INTRODUCTION

The Advanced Laser Interferometer Gravitational-Wave Observatory (LIGO) [1] and Advanced Virgo [2] detectors have revealed the Universe's abundance of gravitational-wave (GW) sources. Here, we present the third LIGO Scientific, Virgo, and KAGRA (LVK) Collaboration Gravitational-Wave Transient Catalog (GWTC-3), which records transient GW signals discovered up to the end of LIGO-Virgo's third observing run (O3). This updates the previous GWTC-2 [3] and GWTC-2.1 [4] by including signals found in the second part of O3 (O3b): This period comprises data taken between 1 November 2019, 15:00 Coordinated Universal Time (UTC) and 27 March 2020, 17:00 UTC. GWTC-3 adds 35 GW candidates from O3b that have an inferred probability of astrophysical compact binary coalescence (CBC) origin of $p_{\mathrm{astro}} > 0.5$ based upon the results of our search algorithms. Additionally, there are 1048 subthreshold O3b candidates that do not meet the CBC p_{astro} threshold but have a false alarm rate (FAR) $<2.0\ \mathrm{day}^{-1}$. With the inclusion of O3b candidates, GWTC-3 is the most comprehensive set of GW observations presented to date, and it will further advance our understanding of astrophysics [5], fundamental physics [6], and cosmology [7].

GWTC-3 contains candidate GWs from CBCs: merging binaries consisting of black holes (BHs) and neutron stars (NSs). We analyze in detail the properties of candidates with $p_{\mathrm{astro}} > 0.5$. Previously reported from O3b are the GW candidates GW200115_042309 and GW200105_162426, which are consistent with originating from neutron-star–black-hole binaries (NSBHs) [8]. The naming of these GW candidates follows the format GWYYMMDD_hhmmss, encoding the date and UTC of the signal. In the GWTC-3 analysis, GW200105_162426 is found to have $p_{\mathrm{astro}} < 0.5$; however, it remains a candidate of interest, and it is discussed in detail in later sections. In addition to GW200115_042309 and GW200105_162426, the O3b candidates include GW191219_163120 which is consistent with originating from a NSBH, and GW200210_092254 which could either be from a NSBH or from a binary black hole (BBH), as its less massive component has a mass ($m_2 = 2.83^{+0.47}_{-0.42} M_\odot$, quoting the median and symmetric 90% credible interval) that spans the range for possible NSs and BHs. All the other candidates are

[*]Full author list given at the end of the paper.

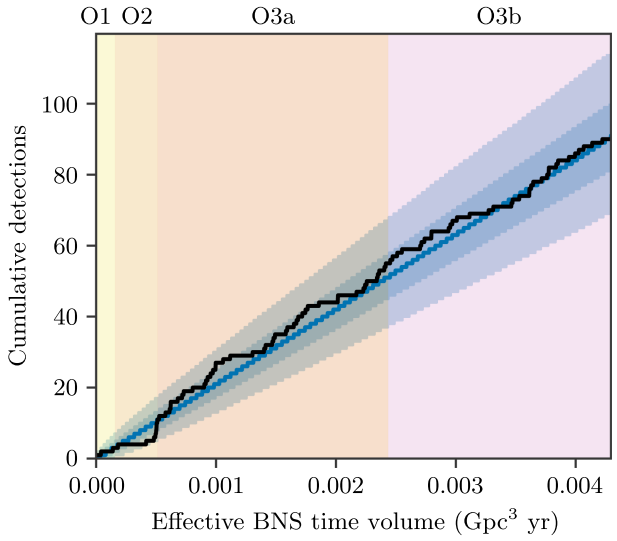

FIG. 1. The number of CBC detection candidates with a probability of astrophysical origin $p_{\text{astro}} > 0.5$ versus the detector network's effective surveyed time volume for BNS coalescences [3]. The colored bands indicate the different observing runs. The final datasets for O1, O2, O3a, and O3b consist of 49.4, 124.4, 149.8 (177.2), and 125.5 days (142.0 days) with at least two detectors (one detector) observing, respectively. The cumulative number of probable candidates is indicated by the solid black line, while the blue line, dark blue band, and light blue band are the median, 50% confidence interval, and 90% confidence interval for a Poisson distribution fit to the number of candidates at the end of O3b.

consistent with being GW signals from BBHs, as their inferred component masses are above the theoretical upper limit of the NS maximum mass [9,10]. Among the O3b candidates with $p_{\text{astro}} > 0.5$, we expect approximately 10%–15% of candidates to be false alarms caused by instrumental noise fluctuations; a smaller, higher-purity sample of candidates could be obtained by adopting a stricter threshold.

During O3, low-latency public alerts were issued through Gamma-ray Coordinate Network (GCN) Notices and Circulars for GW candidates found by initial searches of the data [3,11]. These public alerts enable the astronomy community to search for multimessenger counterparts to potential GW signals. There were 39 low-latency candidates reported during O3b. Of these, 18 (excluding GW200105_162426) survive our detailed analyses to be included as potential CBC signals in GWTC-3. Additionally, GWTC-3 includes 17 candidates with $p_{\text{astro}} > 0.5$ that have not been previously presented. No confident multimessenger counterparts have currently been reported from the O3b candidates (as we review in Appendix A).

The total number of GW candidates with $p_{\text{astro}} > 0.5$ in GWTC-3 is 90, compared with three candidates found by LVK analyses after the end of the first observing run (O1) [12,13], 11 in GWTC-1 after the end of the second observing run (O2) [14], and 55 in GWTC-2.1 after the end of the first part of O3 (O3a) [4]. Additional candidates have also been reported by other searches of public data [15–21]. The dramatic increase in the number of GW candidates during O3 was enabled by the improved sensitivity of the detector network. A conventional measure of sensitivity is the binary neutron star (BNS) inspiral range, which quantifies the average distance at which a fiducial $1.4M_\odot + 1.4M_\odot$ BNS could be detected with a signal-to-noise ratio (SNR) of 8 [22–24]. During O3b observations, the median BNS inspiral ranges for LIGO Livingston, LIGO Hanford, and Virgo were 133, 115, and 51 Mpc, respectively. In Fig. 1, we show the growth in the number of candidates in the LVK catalog across observing runs. Here, the search sensitivity is quantified by the BNS time volume, which should be approximately proportional to the search sensitivity to the overall astrophysical CBC population and hence to the number of detections [3]. The BNS time volume is defined as the observing time multiplied by the Euclidean sensitive volume for the detector network [24]. For O1 and O2, the observing time includes periods when at least two detectors were observing, and the Euclidean sensitive volume is the volume of a sphere with a radius equal to the BNS inspiral range of the second most sensitive detector in the network. For O3, to account for the potential of single-detector triggers, the observing time also includes periods when only one detector was observing, and the radius of the Euclidean sensitive volume is the greater of either (i) the BNS inspiral range of the second most sensitive detector, or (ii) the BNS inspiral range of the most sensitive detector divided by 1.5 (corresponding to a SNR threshold of 12) [3]. As the sensitivity of the detector network improves [25], the rate of discovery increases.

Further searches for GW transients in O3b data have been conducted focusing on intermediate-mass black-hole (IMBH) binaries (with a component $\gtrsim 65M_\odot$ and a final BH $\gtrsim 100M_\odot$) [26], subsolar-mass binaries [27], gravitationally lensed signals [28], signals coincident with gamma-ray bursts [29], cosmic strings [30], and both minimally modeled short-duration [$\lesssim \mathcal{O}(1)$ s, such as from supernova explosions] [31] and long-duration [$\gtrsim \mathcal{O}(1)$ s, such as from deformed magnetars or from accretion-disk instabilities] [32] signals. However, no high-significance candidates for types of signals other than the CBCs reported here have yet been found.

We begin with an overview of the status of the Advanced LIGO and Advanced Virgo detectors during O3b (Sec. II), and then we review the properties and quality of the data used in the analyses (Sec. III). We report the significance of the candidates identified by template-based and minimally modeled search analyses, and we compare this set of candidates to the low-latency public GW alerts issued during O3b (Sec. IV). We describe the inferred astrophysical parameters for the O3b candidates (Sec. V). Finally, we show the consistency of reconstructed

waveforms with those expected for CBCs (Sec. VI). In the Appendixes, we review public alerts and their multimessenger follow-up (Appendix A); we describe commissioning of the observatories for O3b (Appendix B); we detail the data-analysis methods used to assess data quality (Appendix C), search for signals (Appendix D), and infer source properties (Appendix E), and we discuss the difficulties in assuming a source type when performing a minimally modeled search analysis (Appendix F). A data release associated with this catalog is available from the Gravitational Wave Open Science Center (GWOSC) [33]; this includes calibrated strain time series around significant candidates, detection-pipeline results, parameter-estimation posterior samples, source localizations, and tables of inferred source parameters.

II. INSTRUMENTS

The Advanced LIGO [1] and Advanced Virgo [2] instruments are kilometer-scale laser interferometers [34–36]. The advanced generation of interferometers began operations in 2015, and observing periods have been alternated with commissioning periods [25]. After O1 [13,37] and O2 [14], the sensitivity of the interferometers has improved significantly [3,38]. The main improvements were the adjustment of in-vacuum squeezed-light sources, or squeezers, for the LIGO Hanford and LIGO Livingston interferometers and the increase of the laser power in the Virgo interferometer. The instrumental changes leading to improved sensitivities during O3b are discussed in Appendix B.

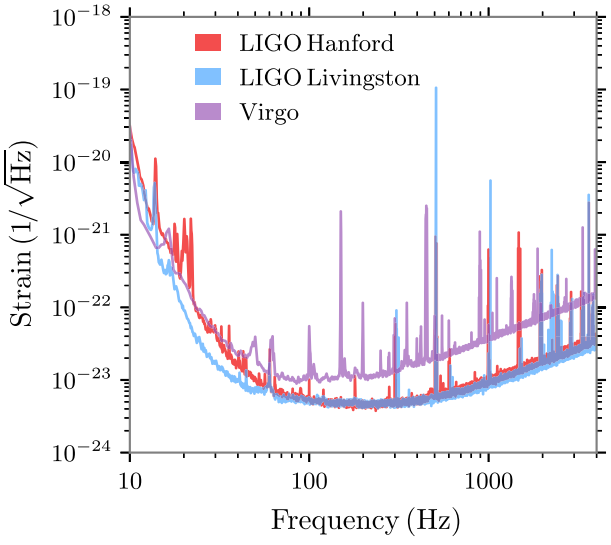

FIG. 2. Representative amplitude spectral density of the three interferometers' strain sensitivity: LIGO Livingston 4 January 2020 02:53:42 UTC, LIGO Hanford 4 January 2020 18:20:42 UTC, Virgo 9 February 2020 01:16:00 UTC. From the amplitude spectral densities we estimate BNS inspiral ranges [22–24] of 114, 133, and 59 Mpc for LIGO Hanford, LIGO Livingston and Virgo, respectively.

Figure 2 shows representative sensitivities during O3b for LIGO Hanford, LIGO Livingston, and Virgo, as characterized by the amplitude spectral density of the calibrated strain output. The sensitivity of the interferometers is primarily limited by the photon shot noise at high frequencies and by a superposition of several noise sources at lower frequencies [38]. The narrow-band features include vibrational modes of the suspension fibers, calibration lines, and 50- and 60-Hz electric power harmonics.

The left panel of Fig. 3 reports the evolution of the detectors' sensitivity over time, as measured by the BNS inspiral range [22–24]. Gaps in the range curve are due to maintenance intervals, instrumental failures, and earthquakes. The epochs marked on the graph correspond to improvements in LIGO Hanford (2 January 2020) and Virgo (28 January 2020) that are discussed in Appendix B. The median BNS inspiral range of Virgo over the whole of O3b was 51 Mpc, while the maximum value reached 60 Mpc. For comparison, the median range and the maximum range during O3a were 45 and 50 Mpc, respectively. The LIGO Hanford median BNS inspiral range improved from 108 Mpc in O3a to 115 Mpc in O3b, primarily due to the squeezed-light [39,40] source adjustments described in Appendix B. The LIGO Livingston median BNS inspiral range in O3b was 133 Mpc, consistent with the O3a value of 135 Mpc, with improvements due to squeezing counterbalanced by degradation primarily due to the reduced circulating power.

The duty cycles for the three interferometers, i.e., the fractions of the total O3b run duration in which the instruments were observing, were 79% (115.7 days) for LIGO Hanford, 79% (115.5 days) for LIGO Livingston, and 76% (111.3 days) for Virgo. As for previous observing runs, a subset of search analyses rejected additional data based on data-quality metrics, as described in Appendix C. The complete three-interferometer network was in observing mode for 51.0% of the time (75.0 days). Moreover, for 96.6% of the time (142.0 days) at least one interferometer was observing, while for 85.3% (125.5 days) at least two interferometers were observing. For comparison, during O3a the duty cycles were 71%, 76%, and 76% for LIGO Hanford, LIGO Livingston, and Virgo, respectively; at least one interferometer was observing 96.8% of the time, and at least two interferometers were observing 81.8% of the time. The duty cycles for both the Hanford and Livingston interferometers improved from O3a to O3b. This demonstrates a clear improvement in robustness as higher microseism and storm activity were observed during O3b compared to O3a. While the fraction of time with at least one detector observing in O3a and O3b was comparable, the fraction of time with two instruments in observing mode increased, improving the performance of the network for coincident observations.

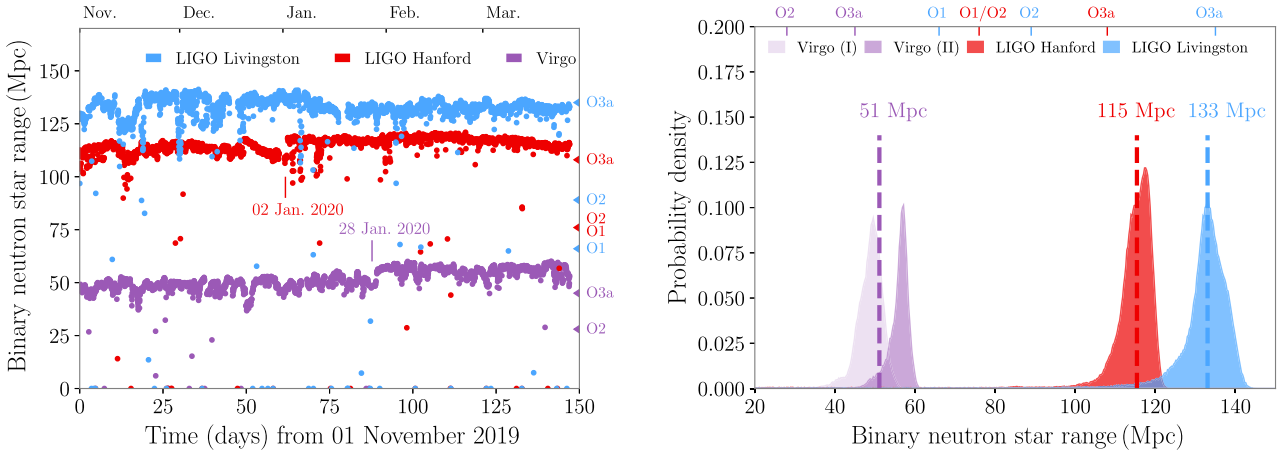

FIG. 3. The BNS inspiral range [22–24] of the LIGO and Virgo detectors. Left: the range evolution during O3b. Each data point corresponds to the median value of the range over a one-hour time segment. Right: distributions of the range and the median values for the entire duration of O3b; the data for Virgo are separately reported for the intervals before (I) and after (II) 28 January 2020 to illustrate changes in the range following detector improvements. An improvement in squeezer performance at LIGO Hanford is indicated at 2 January 2020.

III. DATA

Following the approach of previous analyses [3,4], we calibrate the data of each detector to GW strain and mitigate known instances of poor data quality before analyzing the LIGO and Virgo strain data for astrophysical sources. We include segments of data from each detector in our GW search analyses only when the detector was operating in a nominal state, and when there were no diagnostic measurements being made that might interfere with GW data collection.

Once data are recorded, they are calibrated in near-real time and in higher latency, as described in Sec. III A. We subtract noise from known long-duration, quasistationary instrumental sources [41–43]. We also exclude time periods containing identified and well-characterized noise likely to interfere with signal extraction from the astrophysical analyses, as described in Sec. III B. We thoroughly vet the data surrounding each GW candidate for evidence of transient noise, or glitches, or other anomalies that could impact accurate assessment of the candidate's significance or accurate source-parameter estimation. For GW candidates found near in time or overlapping with transient noise, we apply additional data-processing steps, including the modeling and subtraction of glitches and linear subtraction of glitches using a witness time series [44], as described in Appendix C.

A. Calibration and noise subtraction

The dimensionless strain time series measured by the LIGO and Virgo detectors are an input to the astrophysical analyses. They are reconstructed from different output signals from the detectors and detailed modeling of the response of the detector [42,45]. The reconstructed strain time series are timestamped following Global Positioning System (GPS) time, taking into account both the delays introduced in the synchronized distributed-clock timing system and data conditioning along the data-acquisition systems [46]. The detector responses are described as complex-valued frequency-dependent transfer functions [42,47]. Some control-system model parameters, such as the amount of light stored in the interferometer cavities and the gain of the actuators controlling the position of primary optics [1], vary slowly with time throughout operation of the interferometers. These parameters are monitored and, when possible, aspects of the calibration models are corrected in the strain reconstruction processing [42,45,48]. The analysis of the systematic error and uncertainty bounds for calibrated data throughout O3b is detailed in previous studies of LIGO [49,50] and Virgo data [51–53].

The three detectors use auxiliary lasers, known as photon calibrators [54–56], to induce fiducial displacement of test masses via photon radiation pressure. The fiducial displacements are known to better than 1% in LIGO and 1.8% in Virgo and are used to measure interferometer parameters' variation with time, develop accurate models, and establish estimates of systematic error and associated uncertainty.

Calibration models are estimated from a collection of measurements that characterize the full detector response and from other measurements of individual components [42,49,50], such as the various electronics and suspension systems, gathered while the detector is offline (roughly once per week). An initial version of calibrated strain data is produced in low latency throughout an observing period, and the final calibration models are assembled after the completion of an observing period where the detector configuration was stable [45,53]. As needed, the GW strain data stream is then regenerated offline from the optical

power variations and the control signals, and the systematic error estimate is updated based on the model used for the offline strain reconstruction.

The best available strain data for each detector are used for both detection of GW signals and estimation of the sources' astrophysical parameters. For LIGO, the offline recalibrated strain data are used [49,50]. Initial analysis of Virgo's collection of validation measurements during the run did not motivate offline improvement to the low-latency strain data. Hence, Virgo's low-latency strain data are used for all analyses [51–53].

After the completion of the run, we identified a narrow-band increased systematic error between 46 and 51 Hz in Virgo data, mainly related to a control loop designed to damp mechanical resonances of the suspensions at 49 Hz [52]. This damping loop was added between O3a and O3b and ultimately improved the Virgo detector's sensitivity around 49 Hz. However, since this damping loop was not included in the calibration models, it resulted in an increased systematic error in the calibrated strain data around 49 Hz during O3b. There was also a large increase in the systematic error between 49.5 and 50.5 Hz related to a control loop designed to reduce the electric power-grid line [53]. Overall, the Virgo calibration errors in the band 46–51 Hz increase from 5% in amplitude and 35 mrad in phase to up to 40% in amplitude and 600 mrad in phase [53]. This narrow-band increased systematic error is accounted for in source-parameter estimation by notching out these frequencies (as described in Appendix E).

Known noise sources are subtracted from both the LIGO and Virgo strain data. The sinusoidal excitations used for calibration, known as calibration lines, are subtracted from the LIGO strain data. The 60-Hz electric power-grid lines are subtracted in the LIGO strain data along with the corresponding harmonics up to and including 300 Hz [43]. Additionally, noise contributions due to nonstationary coupling of the power grid are subtracted from the LIGO strain data [41,57]. Numerous noise sources that limit the Virgo detector's sensitivity are measured and linearly subtracted from the Virgo low-latency strain data using witness auxiliary sensors that measure the source of the noise [42,53,58,59]. Calibration lines are also subtracted from the Virgo strain data.

All final source-parameter results, waveform reconstructions, and all but one search pipeline use strain data with all noise subtraction applied, as described above. The exception is the coherent WaveBurst (cWB) analysis [60], which searches for transient signals without assuming a model template. Following the GWTC-2 analysis [3], cWB uses LIGO strain data with the calibration lines and power-grid lines subtracted, but without the subtraction of the nonstationary coupling of the power grid. Comparison of analyses using different versions of noise subtraction indicates that the exact noise-subtraction procedure used does not significantly impact the cWB search results.

B. Data quality

The most limiting source of noise for identification and analysis of transient GW sources is frequent, short-duration glitches in GW detector data [61–64]. A summary of glitch rates for the three observatories over O3b is shown in Fig. 4. Each point corresponds to the average number of glitches per minute with SNR $\rho > 6.5$ and peak frequency between 20 and 2048 Hz, estimated every 2048 s, as measured with the Omicron algorithm [65]. Continuous solid lines indicate the daily median of the corresponding glitch rate. In all three detectors, we observe relatively high glitch rates dominated by glitches below approximately 50 Hz corresponding to seasonally bad weather between the beginning of O3b and January 2020; some peaks in the glitch rate are also visible in Virgo data during the second

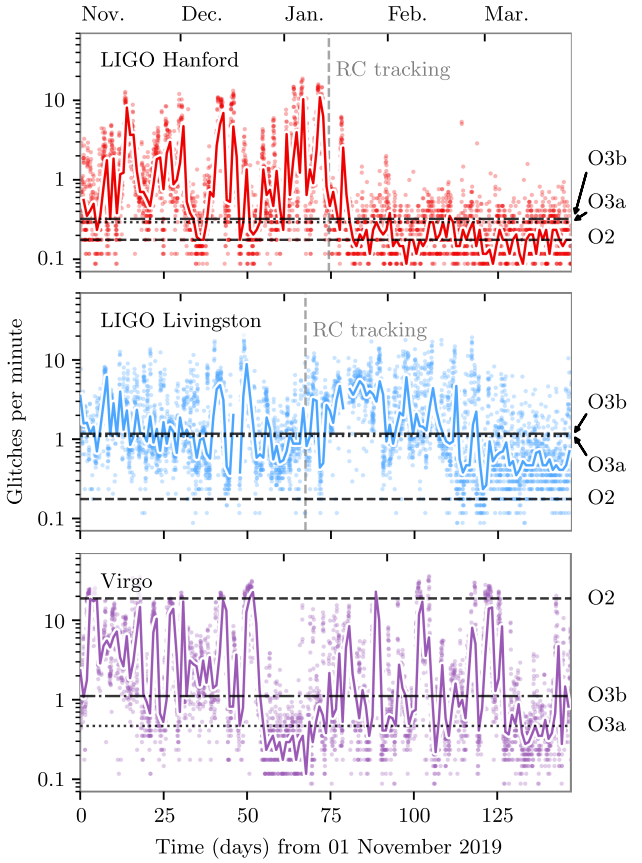

FIG. 4. The rate of single-interferometer glitches with SNR $\rho > 6.5$ and peak frequency between 20 and 2048 Hz identified by Omicron [65] in each detector during O3b. Each point represents the average rate per minute estimated over a 2048-s interval. Continuous curves represent the daily median of the rates. Black lines show the median rate over entire runs: dashed for O2, dotted for O3a, and dash-dotted for O3b. The vertical dashed lines indicate the implementation of reaction-chain (RC) tracking at the LIGO detectors, which reduces the rate of slow scattering glitches.

half of O3b corresponding to persistent unstable weather conditions [66].

The horizontal black lines in Fig. 4 indicate the median glitch rates during O2 (dashed), O3a (dotted), and O3b (dash-dotted). With respect to O3a, both LIGO detectors register a modest glitch rate increase in O3b, with the rate changing from 0.29 to 0.32 min^{-1} for Hanford and from 1.10 to 1.17 min^{-1} for Livingston; this variation is much more pronounced for Virgo, which increased its glitch rate from 0.47 to 1.11 min^{-1}. As discussed for GWTC-2 [3], the increase in glitch rate in the two LIGO detectors between O2 and O3a is largely due to scattered-light glitches, and the decrease in Virgo's glitch rate between O2 and O3 is due to mitigation of several noise sources.

A large fraction of the O3b glitches captured in Fig. 4 are due to light scattering, as described in Appendix B. When the relative displacement between a mirror and a nearby moving reflective surface is $\gtrsim 1$ μm (the main laser wavelength) in amplitude, low-frequency ground motion can be up-converted to scattered-light glitches in the sensitive band of GW detector data [67,68]. During O3, approximately 44% and 45% of all the transient noise with SNR $\rho > 10$ at LIGO Livingston and LIGO Hanford, respectively, was due to light scattering. A high rate of scattered-light glitches is partly a consequence of weather-related high microseismic ground motion at the detector sites during O3b [63,69,70].

Two separate populations of transient noise due to light scattering known as slow scattering and fast scattering polluted LIGO data quality in O3. As illustrated in the spectrograms of Fig. 5, slow scattering noise appears as longer-duration (approximately 2.0–2.5 s) arches in the time-frequency plane, while fast scattering noise appears as short-duration (approximately 0.2–0.3 s) arches [70].

Slow scattering tends to occur when ground motion is high in the earthquake (0.03–0.1 Hz) or microseism (0.1–0.5 Hz) frequency bands. For the LIGO detectors, we find the presence of the slow scattering arches to be strongly correlated with the relative motion between the end test-mass chain and the reaction-mass chain of the optic suspension system used to control the motion of the test masses. This led to implementing reaction-chain tracking [71,72] in January 2020 to reduce this relative motion, as discussed in Appendix B. The rate of glitches associated with slow scattering significantly decreases after the implementation of the reaction-chain tracking [69].

Figure 4 shows that the overall O3b glitch rate significantly decreases for LIGO Hanford after the implementation of the reaction-chain tracking, changing from 0.82 to 0.18 min^{-1}. Correlated with this drop in glitch rate, the noise background becomes more stable and the average fraction of O3b public alerts that are retracted drops from 0.55 to 0.21.

Fast scatteringis far more common at LIGO Livingston than at LIGO Hanford. During O3, it was the most frequent

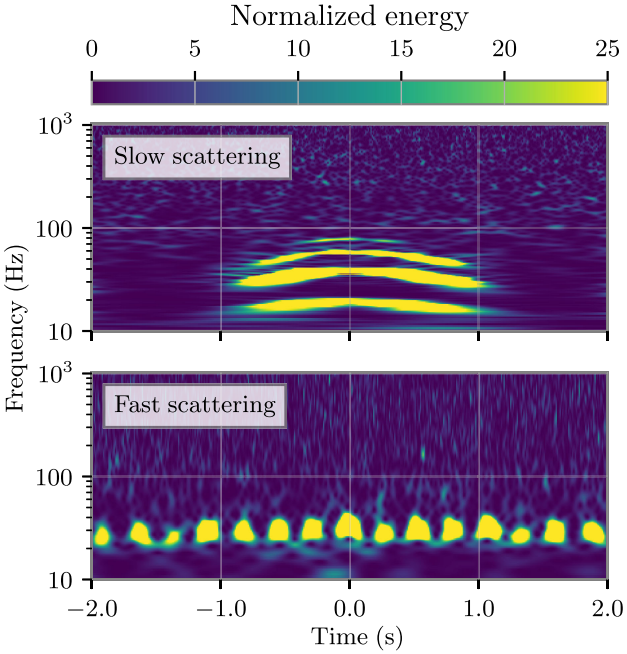

FIG. 5. Representative spectrograms [73] of glitches caused by light scattering. Top: slow scattering appears as long-duration arches in the time–frequency plane. The multiple arches are due to multiple reflections between the test-mass optics and the scattering surface. During O3, slow scattering was the most frequent and second most frequent source of transient noise at LIGO Hanford and LIGO Livingston respectively. Bottom: as compared to slow scattering, fast scattering transients appear as short-duration, rapidly repeating arches.

source of transient noise at Livingston. As shown in Fig. 5 and in Appendix C, fast scattering generally affects the GW data from 20 to 60 Hz, but occasionally manifests as high as 120 Hz. Increased ground motion in the anthropogenic (1–6 Hz) band, usually caused by bad weather conditions and human activity, especially with nearby heavy machinery such as logging trucks, increases the rate of fast scattering glitches. Physical environment and monitoring tests conducted at LIGO Livingston and LIGO Hanford found high-quality-factor mechanical resonances at frequencies close to 4 Hz [74,75] thought to be related to fast scattering. The fourth observing run (O4) upgrade plans include damping these resonances and studying the impact on the rate of fast scattering noise.

In Virgo, the initial high glitch rate and the subsequent peaks in Fig. 4 correspond predominantly to high numbers of glitches with central frequencies lower than 40 Hz. Across O3b, approximately 80% of glitches in Virgo with $\rho > 6.5$ have central frequencies lower than 40 Hz. These lower-frequency scattered-light glitches are largely the consequence of the activity of the sea, which is 15 km from the detector site [66,67].

All candidates reported in Tables I and II have undergone validation to check for plausible instrumental or environmental causes using the same methods as were applied to

TABLE I. Candidate GW signals. The time (UTC) of the signal is encoded in the name as GWYYMMDD_hhmmss (e.g., GW200112_155838 occurred on 2020-01-12 at 15:58:38). The names of candidates not previously reported are given in bold. The detectors observing at the merger time of the candidate are indicated using single-letter identifiers (e.g., H for LIGO Hanford); these are not necessarily the same detectors that contributed triggers associated with the candidate. Where a candidate is found with p_{astro} above the threshold value of 0.5 by at least one analysis but below the threshold by others, we include in italics the results from the other analyses, where available. Three center dots (⋯) indicate that a candidate was not found by an analysis. The two candidates labeled with a dagger (†) were found only above threshold in a single detector with the GstLAL analysis, and the FAR estimates were made using significant extrapolation of the background data, meaning that single-detector candidates have higher uncertainty than coincident candidates. A conservative estimate of the FAR for these single-detector candidates is one per live time of the analysis; this is approximately 3.16 yr^{-1} for both LIGO Hanford and LIGO Livingston.

		cWB			GstLAL			MBTA			PyCBC-broad			PyCBC-BBH		
Name	Inst.	FAR (yr^{-1})	SNR	p_{astro}	FAR (yr^{-1})	SNR	p_{astro}	FAR (yr^{-1})	SNR	p_{astro}	FAR (yr^{-1})	SNR	p_{astro}	FAR (yr^{-1})	SNR	p_{astro}
GW191103_012549	HL	⋯	⋯	⋯	⋯	⋯	⋯	*27*	*9.0*	*0.13*	4.8	9.3	0.77	0.46	9.3	0.94
GW191105_143521	HLV	⋯	⋯	⋯	*24*	*10.0*	*0.07*	0.14	10.7	>0.99	0.012	9.8	>0.99	0.036	9.8	>0.99
GW191109_010717	HL	<0.0011	15.6	>0.99	0.0010	15.8	>0.99	1.8×10^{-4}	15.2	>0.99	0.096	13.2	>0.99	0.047	14.4	>0.99
GW191113_071753	HLV	⋯	⋯	⋯	⋯	⋯	⋯	26	9.2	0.68	*1.1×10^{4}*	*8.3*	*<0.01*	*1.2×10^{3}*	*8.5*	*<0.01*
GW191126_115259	HL	⋯	⋯	⋯	*80*	*8.7*	*0.02*	*59*	*8.5*	*0.30*	*22*	*8.5*	*0.39*	3.2	8.5	0.70
GW191127_050227	HLV	⋯	⋯	⋯	*0.25*	*10.3*	*0.49*	1.2	9.8	0.73	*20*	*9.5*	*0.47*	4.1	8.7	0.74
GW191129_134029	HL	⋯	⋯	⋯	$<1.0 \times 10^{-5}$	13.3	>0.99	0.013	12.7	>0.99	$<2.6 \times 10^{-5}$	12.9	>0.99	$<2.4 \times 10^{-5}$	12.9	>0.99
GW191204_110529	HL	⋯	⋯	⋯	*21*	*9.0*	*0.07*	*$1.3{\times}10^{4}$*	*8.1*	*<0.01*	*980*	*8.9*	*<0.01*	3.3	8.9	0.74
GW191204_171526	HL	$<8.7 \times 10^{-4}$	17.1	>0.99	$<1.0 \times 10^{-5}$	15.6	>0.99	$<1.0 \times 10^{-5}$	17.1	>0.99	$<1.4 \times 10^{-5}$	16.9	>0.99	$<1.2 \times 10^{-5}$	16.9	>0.99
GW191215_223052	HLV	0.12	9.8	0.95	$<1.0 \times 10^{-5}$	10.9	>0.99	0.22	10.8	>0.99	0.0016	10.3	>0.99	0.28	10.2	>0.99
GW191216_213338	HV	⋯	⋯	⋯	$<1.0 \times 10^{-5}$	18.6	>0.99	9.3×10^{-4}	17.9	>0.99	0.0019	18.3	>0.99	7.6×10^{-4}	18.3	>0.99
GW191219_163120	HLV	⋯	⋯	⋯	⋯	⋯	⋯	⋯	⋯	⋯	4.0	8.9	0.82	⋯	⋯	⋯
GW191222_033537	HL	$<8.9 \times 10^{-4}$	11.1	>0.99	$<1.0 \times 10^{-5}$	12.0	>0.99	0.0099	10.8	>0.99	0.0021	11.5	>0.99	9.8×10^{-5}	11.5	>0.99
GW191230_180458	HLV	0.050	10.3	0.95	0.13	10.3	0.87	*8.1*	*9.8*	*0.40*	*52*	*9.6*	*0.29*	0.42	9.9	0.96
GW200112_155838	LV	⋯	⋯	⋯	$<1.0 \times 10^{-5\dagger}$	17.6	>0.99	⋯	⋯	⋯	⋯	⋯	⋯	⋯	⋯	⋯
GW200115_042309	HLV	⋯	⋯	⋯	$<1.0 \times 10^{-5}$	11.5	>0.99	0.0055	11.2	>0.99	$<1.2 \times 10^{-4}$	10.8	>0.99	⋯	⋯	⋯
GW200128_022011	HL	1.3	8.8	0.63	0.022	10.1	0.97	3.3	9.4	0.98	0.63	9.8	0.95	0.0043	9.9	>0.99
GW200129_065458	HLV	⋯	⋯	⋯	$<1.0 \times 10^{-5}$	26.5	>0.99	⋯	⋯	⋯	$<2.3 \times 10^{-5}$	16.3	>0.99	$<1.7 \times 10^{-5}$	16.2	>0.99
GW200202_154313	HLV	⋯	⋯	⋯	$<1.0 \times 10^{-5}$	11.3	>0.99	⋯	⋯	⋯	⋯	⋯	⋯	0.025	10.8	>0.99
GW200208_130117	HLV	⋯	⋯	⋯	0.0096	10.7	0.99	0.46	10.4	>0.99	0.18	9.6	0.98	3.1×10^{-4}	10.8	>0.99
GW200208 222617	HLV	⋯	⋯	⋯	*160*	*8.2*	*<0.01*	*420*	*8.9*	*0.02*	⋯	⋯	⋯	4.8	7.9	0.70
GW200209_085452	HLV	⋯	⋯	⋯	0.046	10.0	0.95	12	9.7	0.97	*550*	*9.2*	*0.04*	1.2	9.2	0.89
GW200210_092254	HLV	⋯	⋯	⋯	*1.2*	*9.5*	*0.42*	⋯	⋯	⋯	17	8.9	0.53	7.7	8.9	0.54
GW200216_220804	HLV	⋯	⋯	⋯	0.35	9.4	0.77	*2.4×10^{3}*	*8.8*	*0.02*	*970*	*9.0*	*<0.01*	7.8	8.7	0.54
GW200219_094415	HLV	0.77	9.7	0.85	9.9×10^{-4}	10.7	>0.99	0.18	10.6	>0.99	1.7	9.9	0.89	0.016	10.0	>0.99
GW200220_061928	HLV	⋯	⋯	⋯	⋯	⋯	⋯	⋯	⋯	⋯	⋯	⋯	⋯	6.8	7.5	0.62

(Table continued)

TABLE I. *(Continued)*

Name	Inst.	cWB FAR (yr^{-1})	cWB SNR	cWB p_{astro}	GstLAL FAR (yr^{-1})	GstLAL SNR	GstLAL p_{astro}	MBTA FAR (yr^{-1})	MBTA SNR	MBTA p_{astro}	PyCBC-broad FAR (yr^{-1})	PyCBC-broad SNR	PyCBC-broad p_{astro}	PyCBC-BBH FAR (yr^{-1})	PyCBC-BBH SNR	PyCBC-BBH p_{astro}
GW200220_124850	HL	···	···	···	*150*	*8.2*	*<0.01*	1.8×10^3	8.2	0.83	···	···	···	*30*	*7.8*	*0.20*
GW200224_222234	HLV	$<8.8 \times 10^{-4}$	18.8	>0.99	$<1.0 \times 10^{-5}$	18.9	>0.99	$<1.0 \times 10^{-5}$	19.0	>0.99	$<8.2 \times 10^{-5}$	19.2	>0.99	$<7.7 \times 10^{-5}$	18.6	>0.99
GW200225_060421	HL	$<8.8 \times 10^{-4}$	13.1	>0.99	0.079	12.9	0.93	0.0049	12.5	>0.99	$<1.1 \times 10^{-5}$	12.3	>0.99	4.1×10^{-5}	12.3	>0.99
GW200302_015811	HV	···	···	···	0.11†	10.6	0.91	···	···	···	···	···	···	···	···	···
GW200306_093714	HL	···	···	···	···	···	···	410	8.5	0.81	*3.4×10^3*	*7.8*	*<0.01*	*24*	*8.0*	*0.24*
GW200308_173609	HLV	···	···	···	*680*	*8.1*	*<0.01*	*6.9×10^4*	*8.3*	*0.24*	*770*	*7.9*	*<0.01*	2.4	8.0	0.86
GW200311_115853	HLV	$<8.2 \times 10^{-4}$	16.2	>0.99	$<1.0 \times 10^{-5}$	17.7	>0.99	$<1.0 \times 10^{-5}$	16.5	>0.99	$<6.9 \times 10^{-5}$	17.0	>0.99	$<7.7 \times 10^{-5}$	17.4	>0.99
GW200316_215756	HLV	···	···	···	$<1.0 \times 10^{-5}$	10.1	>0.99	*12*	*9.5*	*0.30*	0.20	9.3	0.98	0.58	9.3	0.98
GW200322_091133	HLV	···	···	···	···	···	···	450	9.0	0.62	*1.4×10^3*	*8.0*	*<0.01*	*140*	*7.7*	*0.08*

TABLE II. Marginal candidates found by the various analyses. The candidates in this table have a FAR below a threshold of 2.0 yr^{-1} in at least one analysis, but were not found with p_{astro} that meets our threshold for Table I ($p_{astro} > 0.5$ from a search analysis, with the additional requirement that cWB candidates have a counterpart from a matched-filter analysis). The probability of astrophysical origin p_{astro} quoted (i) assumes a CBC source, which may not always be applicable for candidates identified by the minimally modeled cWB analysis, and (ii) do not factor in data-quality information that was not used by the search algorithms. Further information on the cWB-only candidate 200214_224526 is available in Appendix F. Detector-identifying letters are the same as given in Table I. The instruments for each candidate are the ones which were operating at the time of the trigger, and are not necessarily the same as those which participated in the detection. The candidates are named according to the same convention as in Table I except that here we omit the GW prefix for the candidates found to be likely caused by instrumental artifacts, indicated with an asterisk (∗). Where a candidate was seen below the FAR threshold in at least one analysis but above threshold in others, we include in italics the information on that trigger from the other analyses as well where available. As in Table I, the dagger (†) indicates a candidate found by a single detector with the GstLAL analysis.

Name	Inst.	cWB FAR (yr^{-1})	cWB SNR	cWB p_{astro}	GstLAL FAR (yr^{-1})	GstLAL SNR	GstLAL p_{astro}	MBTA FAR (yr^{-1})	MBTA SNR	MBTA p_{astro}	PyCBC-broad FAR (yr^{-1})	PyCBC-broad SNR	PyCBC-broad p_{astro}
GW191118_212859	LV	···	···	···	···	···	···	*7.4×10^5*	*8.0*	*<0.01*	1.3	9.1	0.05
GW200105_162426	LV	···	···	···	0.20†	13.9	0.36	···	···	···	···	···	···
200121_031748*	HV	···	···	···	*58*	*9.1*	*0.02*	1.1	10.7	0.23	···	···	···
GW200201_203549	HLV	···	···	···	1.4	9.0	0.12	*850*	*8.9*	*<0.01*	*1.0×10^3*	*8.3*	*<0.01*
200214_224526*	HLV	0.13	13.1	0.91	···	···	···	···	···	···	···	···	···
200219_201407*	HLV	···	···	···	···	···	···	0.22	13.6	0.48	···	···	···
GW200311_103121	HL	···	···	···	*110*	*9.0*	*<0.01*	1.3	9.0	0.03	1.3	9.2	0.19

O3a candidates [3,63,64,76]. As discussed in Sec. IV D, none of the O3b candidates with CBC $p_{\rm astro} > 0.5$ have evidence of instrumental origin, but we identify three marginal candidates (which do not meet the $p_{\rm astro}$ threshold) as likely instrumental in origin. We also investigate non-Gaussian instrumental artifacts present in the data close to each candidate time that could bias measurements of the source parameters. In addition to the previously reported GW200105_162426 [8], we identify seven O3b candidates in Table I with nearby non-Gaussian artifacts that require mitigation before the data are further analyzed for source-parameter estimation. In order to mitigate instrument artifacts present near the time of these candidates, we follow a procedure similar to O3a [3]. Further details on data-quality mitigation techniques, including data-quality products publicly available via GWOSC, are given in Appendix C and in previous O3 analyses [3,63,77]. The specific mitigation methods applied for each of these candidates are described in Appendix E, with a summary for each candidate reported in Table XVI.

IV. CANDIDATE IDENTIFICATION

Identification of candidates and assessment of their significance relative to the background of detector noise is the first step in extracting catalog results. This is followed by detailed analyses to estimate source properties (Sec. V) and reconstruct waveforms (Sec. VI). We use multiple search algorithms to identify potential GW candidates in our data. Searches are performed at two different latencies: online searches are run in near-real time as data are collected, and offline searches are completed later, using the final calibrated and cleaned dataset. The online analyses allow for the rapid release of public alerts associated with candidates to enable the search for multimessenger counterparts, as described in Appendix A. The offline analyses benefit from improved background statistics, extensive data calibration, vetting, and conditioning as described in Sec. III, and the ability to perform more computationally expensive calculations to separate signals from background given the relaxation of latency requirements. Because of these factors, the offline analyses are more sensitive than the online analyses. The increased sensitivity of the offline analyses means that differences in the final candidate list compared to the online results are expected. While the lowest FAR candidates are expected to remain significant, candidates with a higher FAR (e.g., near the threshold for public low-latency alerts) are more likely to have changes in significance when reevaluated offline, causing them to move above or below the corresponding threshold for inclusion in this catalog. The differences between the online and offline search results are further discussed in Sec. IV D 1. In this catalog, we report on the results of offline analyses performed after the end of O3b.

Our search analyses use different approaches to find candidates, either filtering the data using CBC waveform templates to identify matches (described in Sec. IV A), or coherently searching data from the detector network for transient signals without assuming a waveform template (described in Sec. IV B). We use four pipelines to identify the candidates from O3b: three that search using CBC waveform templates, GstLAL [78–81], Multi-Band Template Analysis (MBTA) [82,83], and PyCBC [23,84–88], and one that searches for transient signals with minimal assumptions about sources, cWB [60,89,90]. The four pipelines used offline were also operated in online configurations, along with the waveform-based Summed Parallel Infinite Impulse Response (SPIIR) pipeline [91–93], to identify candidate GW signals in low latency. Of the four pipelines, cWB, GstLAL, and PyCBC are used for offline LVK analysis of O1 [13,94], O2 [14], and O3a [3,4] data, whereas MBTA was first used for offline analysis of O3a [4].

There are several technical and configuration differences across the pipelines used in the search analyses. While the CBC pipelines consider all possible (double or triple) detector combinations to form coincident triggers, cWB reports only analysis of pairs of detectors [31]. Another significant difference across pipelines is the data baseline used to assign FAR to candidates. The FAR is used as a measure of significance and defines how regularly we would expect to see a noise (nonastrophysical background) trigger with the same, or higher, ranking statistic as the candidate. GstLAL compares candidates to a global background from the full O3b time span, while cWB, MBTA, and PyCBC use local background from a typical time span of one to a few weeks. All pipelines estimate background distributions empirically from the O3b data. Further technical details of the search algorithms are given in Appendix D.

A. Modeled search analyses for transient sources

The dedicated CBC search algorithms use matched filtering [95,96], identifying candidates by correlating the data with templates. We use sets of templates, or banks, that provide a discrete sampling of the parameter space defined by the binary component masses m_1 and m_2 (the primary and secondary masses defining $m_1 \geq m_2$), and the corresponding dimensionless spins $\vec{\chi}_1$ and $\vec{\chi}_2$.

The signals expected from CBCs are well characterized by combinations of the binary component parameters. To leading order, the phase evolution during inspiral of a binary is determined by the chirp mass [97,98],

$$\mathcal{M} = \frac{(m_1 m_2)^{3/5}}{(m_1 + m_2)^{1/5}}. \tag{1}$$

We also use the total mass $M = m_1 + m_2$, and the mass ratio $q = m_2/m_1 \leq 1$ to describe a binary system. The dimensionless component spin $\vec{\chi}_i = c\vec{S}_i/(Gm_i^2)$, where $\vec{S}_i$ is the spin angular momentum and $i = \{1, 2\}$, can theoretically range in magnitude from 0 (nonspinning) to

1 (Kerr limit) for BHs. The two spins are combined to form the effective inspiral spin [99,100] defined as

$$\chi_{\rm eff} = \frac{(m_1\vec{\chi}_1 + m_2\vec{\chi}_2)\cdot\hat{L}_N}{M}, \tag{2}$$

where $\hat{L}_N$ is the unit vector in the direction of the Newtonian orbital angular momentum. In the modeled search analyses, the spins are assumed to be parallel to $\hat{L}_N$.

The banks cover systems with total masses, redshifted to the detector frame [101], ranging from a minimum value $2M_\odot$ for all pipelines to a maximum value of $200M_\odot$ (MBTA), $500M_\odot$ (PyCBC), or $758M_\odot$ (GstLAL). The minimum binary component mass is $1M_\odot$. Searches for binaries with component masses less than $1M_\odot$ have been completed in complementary analyses [27,102–106]. The PyCBC pipeline performs two search analyses. The first is an analysis encompassing a wide parameter space, allowing detection of many different types of CBC systems, which we refer to as the PyCBC-broad analysis. In addition to this broad analysis, PyCBC is also used in a different configuration, which we refer to as the PyCBC-BBH analysis: This analysis is restricted to BBH systems with total masses between $10M_\odot$ and $500M_\odot$, mass ratios in the range $1/3 \leq q \leq 1$, and component masses in the range $5M_\odot \leq m_1 \leq 350M_\odot$ and $m_2 \geq 5M_\odot$. This PyCBC-BBH analysis is designed to have higher sensitivity to BBH coalescences with component masses that are similar to those of the majority of previously detected systems. The range of templates is the same as used for the search of O3a [4].

For each template, the matched-filter correlation produces a time series of SNR values for each detector, and peaks in this time series form triggers. Only triggers with a matched-filter SNR exceeding a threshold are considered further in the analysis. This SNR threshold is $\rho > 4.0$ for PyCBC and GstLAL, and either 4.5 or 4.8, varying across the parameter space, for MBTA. MBTA and PyCBC assign a significance to triggers found with consistent binary parameters and times of arrival in at least two detectors, while GstLAL also does so for single-detector triggers. The SNR is combined with signal-consistency checks to rank triggers. Each pipeline uses a specific ranking statistic and background-estimation method to assess the significance and probability of astrophysical origin of these triggers and coincidences. Results from the various CBC search analyses are expected to differ due to differences in the waveform template banks and in algorithmic choices such as their ranking statistic and assumed signal distributions. Technical details of the GstLAL, MBTA, PyCBC, and (online-only) SPIIR analyses are given in Appendixes D 1, D 2, D 3, and D 4, respectively.

B. Minimally modeled search analyses for transient sources

The cWB pipeline searches for generic, short transient signals across a network of GW detectors [60,107–110]. It provides rapid detection of GW transient signals with its online instance, and signal reconstructions and estimates of their significance with the version that runs offline on the final dataset. Designed to operate without a specific waveform model, cWB identifies coherent excess power in multiresolution time-frequency representations of the detector strain data. The SNR for each detector is estimated from the reconstructed waveforms, and the network SNR is calculated by combining the SNRs from the individual detectors. The cWB search analyses and reconstructions reported in this catalog primarily target BBH sources and are limited to the (16–512)-Hz range [60] to boost computational efficiency given the expected frequency range of BBH signals. The analysis is further split into two configurations that target high-mass (central frequency $f_c < 80$ Hz) and low-mass ($f_c > 80$ Hz) BBH systems [111]. Technical details of the cWB analysis are given in Appendix D 5.

C. Probability of astrophysical origin

Our primary criterion for selecting candidates for further study is the probability of astrophysical origin $p_{\rm astro}$. In contrast to FAR, this measure of significance incorporates our knowledge of the astrophysical rate of signals for different classes of binary systems. For instance, given the strongly differing rates of detectable signals from BBH and BNS coalescences, at a given FAR the probability of being an astrophysical signal will naturally be different between candidates consistent with BBH versus BNS origin. The probability of astrophysical origin is well suited for selecting candidates from a catalog containing results from observing runs of differing sensitivities. As the true alarm rate increases with improved sensitivity, the FAR needed for a candidate to reach a given $p_{\rm astro}$ will change between observing runs.

In order to estimate $p_{\rm astro}$ and its complement, the probability of terrestrial origin $p_{\rm terr} = 1 - p_{\rm astro}$, for a candidate, we model foreground and background event rates using a Poisson mixture formalism [112], as in previous LVK results [3,4,13,113,114]. Technical details of the calculation of $p_{\rm astro}$ for each analysis pipeline are given in Appendix D 7.

For any candidate, $p_{\rm astro}$ depends on the trigger's ranking statistic and where the trigger lies in the parameter space, i.e., the template with which it was found in a matched-filter analysis, or whether it was found in the low- or high-mass configurations of the cWB analysis. To calculate $p_{\rm astro}$, we compare the expected number of astrophysical triggers and the expected number of background triggers for the given ranking statistic and measured parameters. The number of true astrophysical signals depends on merger

rates, which are jointly inferred as part of the $p_{\rm astro}$ estimation method [3,13,112,115], using assumptions about the populations of astrophysical sources, and the detectors' and analysis' sensitivity, which is calculated using simulated signals. The number of background triggers is derived from the same background distribution used to estimate FAR by the search analyses.

As we cannot provide full source-parameter estimates for all candidates with FAR $< 2.0\ \mathrm{day}^{-1}$, we instead estimate the probability to originate from different categories of binary source (BNS, NSBH, and BBH). These probabilities are estimated by each pipeline separately and rely primarily on the template masses with which triggers are recovered (see Appendix D 7 for more details). For calculating $p_{\rm astro}$, all triggers from the cWB analysis are assumed to be from BBH sources, as cWB has a reduced sensitivity to other population types. The source classes are defined in this calculation via an assumed boundary at $3M_\odot$: We consider any component with lower mass to be in the NS class and any component above as BH. These classes do not necessarily reflect the true division between NSs and BHs. The maximum mass of NSs is not currently known, but $3M_\odot$ should be a robust upper limit [9,10]. Therefore, the BBH category is intended to capture only BBHs, while the BNS and NSBH categories should capture all binaries with components that could be NSs in addition to possibly capturing some BBHs.

While the same approach is used by all analyses to assess $p_{\rm astro}$ for their candidates, the detailed implementation varies. Besides differences in their ranking statistic definition, analyses divide the parameter space in different ways to compute $p_{\rm astro}$, make slightly different assumptions about the astrophysical populations, have distinct responses to astrophysical sources, and have specific methods to evaluate their background. These differences will introduce a variation in results among pipelines. Each pipeline is subject to statistical and systematic uncertainties, such as how they respond to the observed noise fluctuations in ranking candidates, and the differences among pipelines mean that these uncertainties are not the same across pipelines. The details of these differences among pipelines are given in Appendix D. There is an extra uncertainty for single-detector candidates, where we can assume a conservative upper bound on FAR of 1 per observing time. However, we improve upon this estimate by extrapolating the noise background distribution. The $p_{\rm astro}$ values given in Sec. IV D represent our current best estimates of the origin of candidates using the information available from search pipelines and detector characterization.

After its calculation, we must set a threshold on $p_{\rm astro}$ for inclusion in the results presented here. As in previous publications [4,14], we choose the criterion $p_{\rm astro} > 0.5$, such that the selected candidates are all inferred to have a higher probability of astrophysical origin than terrestrial. Values of $p_{\rm astro}$ close to 1 are expected to be robust with respect to uncertainties in the astrophysical populations, whereas cases for which $p_{\rm astro}$ and $p_{\rm terr}$ are comparable are sensitive to such uncertainties. Uncertainties are greater for candidates that, if astrophysical, have properties that correspond to a small number of detections in the overall population. The mass distributions for BBH sources are now sufficiently well constrained [116] such that we expect related uncertainties on $p_{\rm astro}$ to be small for the bulk of this region; however, at particularly high masses these uncertainties are expected to be larger [4]. In contrast to the BBH population, the populations of BNS and NSBH sources remain poorly known [5]. Both the shape and the boundaries of the component mass distributions (especially for NSs) can have a significant impact on the value of $p_{\rm astro}$ inferred for a BNS or NSBH candidate, and this uncertainty can be greater than 0.1 for moderate $p_{\rm astro}$ values near the threshold of 0.5 [117]. We therefore expect that inferred values for $p_{\rm astro}$ may change for less significant candidates as our understanding of the population evolves with further observations [118–120].

D. Search results

There are many potential GW sources. Hence, in theory, GWTC-3 could contain a variety of source types. However, currently no high-significance (FAR $< 10^{-2}\ \mathrm{yr}^{-1}$) candidate transients have been reported for sources other than standard, quasicircular CBCs [26,29–32,121]. Therefore, we limit this GWTC-3 candidate list to the established source categories of BNSs, NSBHs, and BBHs.

Following GWTC-2.1 [4], we select candidates with a probability of an astrophysical CBC source $p_{\rm astro} > 0.5$ for detailed analysis. In applying this criterion, we follow the method used in GWTC-1 [14] and consider only cWB candidates that also have a BBH counterpart from one of the matched-filter analyses (i.e., a time-coincident candidate with $p_{\rm astro} > 0.1$). This is because cWB can potentially identify signals from a range of sources, but the calculation of $p_{\rm astro}$ assumes a CBC source, and so additional confirmation is needed to verify that the candidate signal is consistent with a CBC origin. However, all O3b cWB candidates with $p_{\rm astro} > 0.5$ also have $p_{\rm astro} > 0.5$ from a matched-filter analysis anyway, except for 200214_224526, which is identified as being of instrumental origin [26]. The requirement that cWB candidates have a matched-filter counterpart is discussed further in Appendix F.

We identify 35 CBC candidates in O3b passing our threshold; these include 17 new candidates that were not found in low latency and are reported here for the first time. Significance estimates for the CBC candidates with probability of astrophysical origin $p_{\rm astro} > 0.5$ are reported in Table I. We report the FAR, SNR, and $p_{\rm astro}$ for each search analysis that finds a trigger when at least one analysis finds the candidate above the threshold for inclusion. Additionally, the SNRs reported from each

detector are given in Table XI of Appendix D 6. By comparing the sum of $p_{\rm astro}$ values for candidates with $p_{\rm astro} > 0.5$ to the number of such candidates for each analysis, we estimate that the expected contamination from triggers of terrestrial origin is approximately 10%–15%, or approximately four to six candidates. A higher-purity selection of candidates could be obtained by adopting a stricter selection criterion; for example, adopting a threshold of $p_{\rm astro} > 0.9$ would result in a list of 22 O3b candidates. Probabilities for different source categories (BNS, NSBH, and BBH) are included in Table XIII in Appendix D 7. Updated values for $p_{\rm astro}$ for O3a candidates are given in Table XV in Appendix D 7; there is no change to the list of O3a candidates with $p_{\rm astro} > 0.5$ compared with GWTC-2.1 [4]. Results from O1 and O2 have not been recalculated [14]. The O3b candidates bring the total number of LVK-reported CBC candidates with $p_{\rm astro} > 0.5$ to 90.

Marginal candidates with $p_{\rm astro} < 0.5$ but FAR $< 2.0\ {\rm yr}^{-1}$ are discussed further in Sec. IV D 4. An extended list of candidates with FAR $< 2.0\ {\rm day}^{-1}$ is available from GWOSC [33] and discussed in Sec. IV D 5.

1. O3b online candidates

In O3b, there were 39 candidates reported in low latency (see Appendix A). All candidates identified by the online searches are assigned an internal identifier according to the date on which they occur, for example, S200105ae for GW200105_162426. These online analyses were carried out by the five pipelines: GstLAL, MBTAOnline, PyCBC Live, SPIIR, and cWB. The overall FAR threshold for a public alert was set to one per two months ($6\ {\rm yr}^{-1}$) for CBC sources, meaning that once a trials factor is applied, there was a public-alert threshold of $1.2\ {\rm yr}^{-1}$ for each online pipeline. Candidates found in low latency passing this threshold were disseminated to the public via GCN Notices and Circulars. This allowed for rapid follow-up searching for multimessenger counterparts. The online searches are necessarily limited in assessing the noise background as they can use only data collected up to the current time, and hence the FAR may be inaccurately calculated if there are sudden changes in the data quality. Among the 39 candidates reported in low latency, 16 were later retracted as they were likely due to detector noise.

None of the 16 retracted online candidates were found above our $p_{\rm astro}$ threshold in the offline analyses, and thus are not included in Table I. There were five public candidates that did not meet the threshold for inclusion in Table I that were not retracted:

(i) S191205ah was found in low latency by GstLAL as a low-SNR ($\rho < 10$) single-detector candidate in LIGO Livingston with a FAR of $0.39\ {\rm yr}^{-1}$. Such a FAR corresponds to modest significance, and thus, it is not surprising to find differences in the estimated significance by the initial online analysis and the end-of-run offline analyses. GstLAL did not recover an offline trigger at this time with FAR $< 2.0\ {\rm day}^{-1}$.

(ii) S191213g was found in low latency by GstLAL in both LIGO Hanford and LIGO Livingston, with low network SNR and a modest FAR of $1.1\ {\rm yr}^{-1}$. The offline trigger corresponding to this time was found with FAR $> 2.0\ {\rm day}^{-1}$, so it is not included in this catalog.

(iii) The NSBH candidate S200105ae (GW200105_162426 [8]) is reported as a marginal candidate (see Table II) and is further discussed below.

(iv) The cWB candidate S200114f was found online in the Hanford-Livingston-Virgo (HLV) three-detector network with FAR of $0.039\ {\rm yr}^{-1}$, meeting the significance threshold for a public alert. It was considered for inclusion in the O3 search for short-duration minimally modeled transients [31], but that analysis was uniformly carried out on the Hanford-Livingston (HL) network, where the trigger did not qualify because of its low coherence (cWB network correlation coefficient $c_c < 0.8$). This candidate was discussed at length in the context of the search for IMBH binaries, where a potential instrumental origin was examined [26]. The analysis for the IMBH search was carried out using both the HL and HLV networks, and this candidate came out as marginally significant in the HLV network. In the analysis done for this catalog, this candidate was reported only by the cWB pipeline (which performed a two-detector analysis). Since the cWB $p_{\rm astro}$ is low (<0.01), it does not meet the criteria for inclusion in Table I.

(v) S200213t was found in low latency by GstLAL as a low-SNR single-detector candidate in LIGO Hanford with a modest FAR of $0.56\ {\rm yr}^{-1}$. Similar to S191205ah and S191213g, there was no offline trigger corresponding to S200213t with a FAR $< 2.0\ {\rm day}^{-1}$, so it does not appear in this catalog. Single-detector candidates, such as S191205ah and S200213t, are particularly susceptible to changes in significance due to relatively minor changes in data processing.

The remaining 18 candidates reported in low latency also appear in Table I.

2. New O3b candidates

The 17 new candidates listed in this catalog, not previously shared via GCN, are indicated in bold in Table I. Almost all of these candidates are found with modest significance. They are all coincident triggers involving at least both of the LIGO Hanford and Livingston detectors. The inferred source properties for all the new candidates (discussed in Sec. V) are consistent with BBH masses, with the exceptions of GW191219_163120 and GW200210_092254 that may be from NSBHs.

The identification of these new candidates can be attributed to a combination of factors: (i) Offline searches benefit from data with better calibration, cleaning and data-quality information, as well as improved algorithms, resulting in better background rejection, and (ii) using a p_{astro} threshold allows us to highlight candidates in source-rich parts of the parameter space, including candidates with an (offline) FAR that would not meet the (online) threshold for public alerts.

3. Pipeline consistency

Not all candidates were found by all pipelines above the p_{astro} threshold of 0.5: Of the 35 candidates, ten candidates were found by cWB, 21 candidates were found by GstLAL (including the two candidates found in a single detector), 20 candidates were found by MBTA, and 29 candidates were found by one or both of the PyCBC-BBH and PyCBC-broad analyses. Among the O3b candidates, 21 were found by two or more analysis pipelines, 15 by three or more pipelines, and nine by all pipelines. We expect the analyses to find different sets of candidates, due to different search methods, tuning, and configuration choices. The impact of differences among search pipelines will be largest for candidates with low SNR; thus, it is expected that such candidates may be identified by only a subset of pipelines. As methods used by different pipelines will be more or less effective in suppressing specific types of noise artifacts, and the sensitivity of different pipelines will have different dependencies on binary signal parameters, combining information from multiple pipelines should lead to a greater understanding of the population of astrophysical sources [122–124].

Some candidates are unique to a pipeline and not found by other pipelines:

(i) The GstLAL analysis found two unique candidates (see Appendix D 6); these are both single-detector candidates which had also been reported in low latency. As only GstLAL is configured to identify single-detector signals, we expect a difference among pipelines here.

(ii) The MBTA analysis found four unique candidates, newly reported here, all of which are quiet signals inferred to be from BBHs. These candidates have $p_{\mathrm{astro}} > 0.5$ even though their FAR (integrated over a large parameter space) is high (see Appendix D 7 for further discussion), and their p_{terr} is also significant. GW191113_071753 may have an unusual mass ratio, and GW200322_091133 has significant uncertainties for its inferred source properties (see Sec. V), which may make these signals (if real GWs) outliers in the astrophysical population; therefore, the p_{astro} for these candidates is more uncertain than for more typical candidates [117].

(iii) The PyCBC analyses found eight unique candidates, all of which are newly reported in this catalog. Of these, two were found by both analyses, five were found in the PyCBC-BBH analysis, and one in the PyCBC-broad analysis. All the candidates found uniquely by PyCBC are relatively quiet. The lowest FAR, and therefore most significant, is that of GW191103_012549: 0.46 yr^{-1}.

The candidate found only by the PyCBC-broad analysis, GW191219_163120, was found as a potential NSBH candidate, with a mass ratio of 0.09. The relatively large asymmetry in the component masses and low mass of the secondary component as identified by the search, $1.84M_{\odot}$, meant that the template was not analyzed in the PyCBC-BBH analysis. GW191219_163120, with redshifted chirp mass $4.69M_{\odot}$, is included in the same mass bin as the population of significant BBH candidates for the estimation of event rates entering p_{astro} (see Appendix D 7). Such a simple binning scheme implies significant modeling uncertainty in p_{astro} for candidates with parameters outside known populations: For instance, with a minor change in bin boundaries that puts the candidate in a different bin from the BBH population, its p_{astro} would drop to 0.085. This example illustrates the sensitivity of p_{astro} calculations to the assumed astrophysical population. For candidates at the edges of (or outside of) the confidently detected populations, like GW191219_163120, there may be large, model-dependent systematic uncertainties in p_{astro}. Future observations will reduce the uncertainty in the rate of similar mergers, and thus enable us to better quantify the origin of GW191219_163120.

Despite its high SNR, GW200129_065458 was identified only by a subset of the search analyses due to a specific set of circumstances. A data-quality issue in Livingston was reported through active Burst and CBC category 2 flags (and required mitigation, as described in Appendix C). The category 2 flags mean that the Livingston data were ignored by the cWB, MBTA, and PyCBC analyses. Moreover, in the MBTA analysis the combination of signal and noise was loud enough to trigger gating in Hanford, but not loud enough in Virgo to create a Hanford-Virgo (HV) coincidence in the high-threshold analysis performed without gating (see Appendix D 2 for details about the internal gating procedure used to remove suspected artifacts in the data). The PyCBC analyses still identified a candidate using only the HV data, but the network SNR is lower than reported by GstLAL on account of not including the Livingston data. In the cWB analysis, the trigger was reconstructed in the HV network but was rejected by the postproduction cuts. The differences in data handling among analyses are expected to lead to such differences in uncommon cases like this.

GW191109_010717, GW200208_222617, and GW200220_061928 are candidates with high-mass sources that potentially make them also relevant in the context of the search for IMBH binaries [26]. GW191109_010717 is a

highly significant candidate that was also found in that IMBH binary search with a FAR as low as 10^{-3} yr^{-1}, but has a joint posterior distribution for the primary and remnant masses that does not match the strict criteria to be considered as an IMBH binary [26] (see Sec. V). GW200208_222617 and GW200220_061928 are low-SNR candidates, which were not identified as significant in the IMBH search; this difference is likely due to different choices of ranking statistic between the two searches as well as differences between their noise backgrounds arising from a different parameter space.

4. Marginal candidates and GW200105_162426

In Table II, we report the marginal candidates that are found by each analysis below a FAR threshold of 2.0 yr^{-1} but do not satisfy the p_{astro} threshold for inclusion in Table I. The naming of these marginal candidates follows the same YYMMDD_hhmmss format as that described for the candidates of Table I, except omitting the GW prefix for the two candidates found to be caused by instrumental artifacts; for the other marginal candidates, we cannot exclude the possibility that they are quiet GW signals.

The marginal candidates 200121_031748, 200214_224526, and 200219_201407 were found to be likely caused by instrument artifacts. At the time of 200121_031748, LIGO Hanford data contain excess power consistent with a blip glitch, a common glitch in LIGO detector data [63,125]. At the time of 200214_224526, LIGO Livingston data contained significant excess noise due to fast scattering, while LIGO Hanford data showed evidence for a weak scattering arch; this candidate was further examined in the search for IMBH binaries [26], and is discussed in Appendix F. At the time of 200219_201407, LIGO Hanford data are highly nonstationary, with multiple loud glitches visible within 1 s of the candidate time.

The marginal candidate GW200311_103121 is found by both MBTA and PyCBC-broad with a template consistent with a (redshifted) chirp mass of $1.17M_{\odot}$ in both pipelines, and hence, if it were an astrophysical signal, its source would correspond to a BNS. Its chirp mass is close to that of GW170817 [126] and is consistent with Galactic BNSs [127]. Future observations will better constrain the mass distribution of BNS mergers and thus enable a more accurate assessment of the origin of this candidate.

The NSBH candidate GW200105_162426 [8] was found as a single-detector trigger by GstLAL with a FAR of 0.20 yr^{-1}. This is comparable to the previously published value of 0.36 yr^{-1} [8], which used only data from the beginning of O3b until 22 January 2020. FARs are not assigned to single-detector triggers by the versions of the PyCBC and MBTA analyses used for these results (more recent developments do allow significance estimates for single-detector triggers in PyCBC searches [21,128]); however, GW200105_162426 was also seen by the PyCBC-broad and MBTA analyses as a Livingston trigger with SNRs of 13.1 and 13.2, respectively, which were well above the backgrounds for triggers from similar templates. Based on p_{astro}, GW200105_162426 is listed here as a marginal candidate, despite it being a clear outlier from the background noise [8]. The marginal status of this candidate can at least in part be explained from the underlying assumptions in the candidate's FAR estimation and p_{astro} computation.

The empirical background noise distribution available for evaluating the significance of single-detector candidates extends only as far as ranking statistics at which we see one noise trigger per observing time. In contrast, for multi-detector triggers, an extended background estimate can be obtained by constructing unphysical coincidences between triggers in different detectors. Consequently, for single-detector candidates like GW200105_162426 that lie outside the background noise distribution, the FAR estimation relies on an extrapolation. For triggers in the tail of the background distribution, this extrapolation comes with uncertainty that impacts the estimated FAR, and this uncertainty also propagates to the noise distribution used in the calculation of p_{astro} [3,8].

Additionally, the p_{astro} estimation for NSBH sources depends on the foreground distribution of ranking statistics as well as their merger rate. The former is subject to uncertainties coming from a lack of knowledge of the NSBH population, while the latter has large error bars due to a paucity of high-significance NSBH detections (order 1). Such uncertainties on p_{astro} have a significant impact on marginal candidates whose p_{astro} values hover around 0.5. As a consequence, the moderate p_{astro} value assigned at this time to GW200105_162426 does not allow us to draw a firm conclusion on its origin. Future observations will likely shed more light on the true provenance of this and similar candidates.

5. Subthreshold candidates

Following GWTC-2.1 [4], we provide an extended list of O3b candidates with FAR less than 2.0 day^{-1} as part of the data products available from GWOSC [33]. In addition to the 35 O3b candidates with $p_{\text{astro}} > 0.5$ listed in Table I, and the seven marginal candidates with FAR less than 2.0 yr^{-1} listed in Table II, there are 1041 further subthreshold O3b candidates in the extended list (giving a total of 1083 O3b candidates in the data release) [33]. The subthreshold candidates have not been scrutinized for possible instrumental origin, but the purity of the sample is expected to be low: $\lesssim 0.01$ when considering all subthreshold candidates, as estimated in Sec. IV E 2.

For each subthreshold candidate, we provide estimates of their p_{astro} (assuming a CBC source) and localization. Localization relies on the same tools that were used to provide low-latency localization for public GW alerts, namely, Bayestar [129,130] for GstLAL, MBTA, and PyCBC candidates, and cWB for its own candidates.

E. Search sensitivity

1. Sensitive hypervolume

To estimate the sensitivity of the search analyses, we calculate a sensitive time-volume hypervolume $\langle VT \rangle$ for each analysis during O3b. This hypervolume represents the sensitivity of each search analysis to a distribution of sources assumed to be uniformly distributed in comoving volume and source-frame time. The expected number of detections for a search analysis is

$$\hat{N} = \langle VT \rangle R, \tag{3}$$

where R is the rate of signals per unit volume and unit observing time. The different pipeline live times affect their calculated $\langle VT \rangle$. The pipeline live times are 94.9 days (cWB), 142.0 days (GstLAL), 124.5 days (MBTA), and 124.2 days (both PyCBC analyses). To estimate $\langle VT \rangle$ for each analysis, we add simulated signals (referred to as injections) into the data and test how many are recovered. The injections we use are designed to cover the detected population of BBHs, BNSs, and NSBHs, and are described further in Appendix D 7. We use the same sets of simulated signals for each analysis to consistently measure $\langle VT \rangle$, but since the PyCBC-BBH and cWB analyses are designed to search for BBH signals, we use only injections in the designated BBH regions for these searches. Rather than consider the total rate of signals, we consider signals corresponding to sources with specific masses to parametrize sensitivity to signals across parameter space.

In Table III, we report the O3b $\langle VT \rangle$ for simulated signals corresponding to sources with component masses close to the specified values. In Fig. 6, for each search, we show the variation in the O3b $\langle VT \rangle$ across the parameter space. The injections around the specified points are weighted so that they follow a log-normal distribution about the central mass with a width of 0.1. We also assume component spins are isotropically distributed with uniformly distributed magnitudes up to a maximum spin that depends on the source component mass; if $m_i < 2M_\odot$, we assume $\chi_{\max} = 0.4$ and otherwise assume $\chi_{\max} = 0.998$. We consider

(i) BHs at $35M_\odot$, which corresponds to a GW150914-like system [4,131], and is approximately where we infer a feature (potentially a bump or a break) in the BH mass spectrum [116];
(ii) BHs at $20M_\odot$, $10M_\odot$ and $5M_\odot$ to see how sensitivity varies across this range of previously detected BH masses;
(iii) NSs at $1.5M_\odot$, close to the canonical NS mass.

We use several combinations of masses in order to assess our sensitivity to BNS, NSBH, and (relatively equal-mass) BBH systems. From the masses considered, the search sensitivity is greatest for $35M_\odot + 35M_\odot$ binaries in all analyses, although our detectors generally survey larger volume for higher-mass populations up to source component masses of approximately $100M_\odot$ [132,133]. Equivalent

TABLE III. Sensitive hypervolume from O3b for the various search analyses with $p_{\text{astro}} > 0.5$ at the assessed points in the mass parameter space. The Any results come from calculating the sensitive hypervolume for injections found by at least one search analysis. For each set of binary masses, the given values are the central points of a log-normal distribution with width 0.1. For some regions and analyses, few injections are recovered such that the sensitive hypervolume cannot be accurately estimated; these cases are indicated by three center dots (⋯). As an example of this, the PyCBC-BBH and cWB analyses analyzed only injections in the designated BBH set, and so no injections were found in the BNS or NSBH regions. The injected population is described in Appendix D 7.

Binary masses ($M_\odot$)			Sensitive hypervolume (Gpc^3 yr)					
m_1	m_2	$\mathcal{M}$	cWB	GstLAL	MBTA	PyCBC-broad	PyCBC-BBH	Any
35.0	35.0	30.5	$2.6^{+0.1}_{-0.1}$	$4.1^{+0.1}_{-0.1}$	$3.3^{+0.2}_{-0.1}$	$3.3^{+0.1}_{-0.1}$	$4.3^{+0.2}_{-0.1}$	$5.3^{+0.1}_{-0.2}$
35.0	20.0	22.9	$1.35^{+0.09}_{-0.10}$	$2.3^{+0.2}_{-0.1}$	$1.8^{+0.1}_{-0.1}$	$1.9^{+0.1}_{-0.1}$	$2.5^{+0.1}_{-0.1}$	$3.1^{+0.1}_{-0.2}$
35.0	1.5	5.2	⋯	$1.8^{+0.2}_{-0.3} \times 10^{-2}$	$1.9^{+0.3}_{-0.3} \times 10^{-2}$	$3.1^{+0.3}_{-0.3} \times 10^{-2}$	⋯	$3.3^{+0.4}_{-0.3} \times 10^{-2}$
20.0	20.0	17.4	$0.56^{+0.04}_{-0.04}$	$1.34^{+0.06}_{-0.05}$	$1.10^{+0.05}_{-0.05}$	$1.14^{+0.05}_{-0.05}$	$1.42^{+0.06}_{-0.05}$	$1.71^{+0.06}_{-0.07}$
20.0	10.0	12.2	$0.24^{+0.03}_{-0.04}$	$0.60^{+0.05}_{-0.05}$	$0.51^{+0.05}_{-0.04}$	$0.56^{+0.05}_{-0.05}$	$0.65^{+0.05}_{-0.05}$	$0.77^{+0.06}_{-0.06}$
20.0	1.5	4.2	⋯	$1.9^{+0.2}_{-0.2} \times 10^{-2}$	$1.9^{+0.2}_{-0.2} \times 10^{-2}$	$2.7^{+0.2}_{-0.2} \times 10^{-2}$	⋯	$2.9^{+0.3}_{-0.2} \times 10^{-2}$
10.0	10.0	8.7	$6.8^{+0.8}_{-0.9} \times 10^{-2}$	$0.26^{+0.01}_{-0.02}$	$0.26^{+0.01}_{-0.02}$	$0.27^{+0.01}_{-0.02}$	$0.28^{+0.02}_{-0.02}$	$0.32^{+0.02}_{-0.01}$
10.0	5.0	6.1	$1.3^{+0.5}_{-0.4} \times 10^{-2}$	$0.10^{+0.02}_{-0.01}$	$0.10^{+0.02}_{-0.01}$	$0.12^{+0.01}_{-0.02}$	$0.11^{+0.02}_{-0.01}$	$0.13^{+0.02}_{-0.01}$
10.0	1.5	3.1	⋯	$1.6^{+0.1}_{-0.1} \times 10^{-2}$	$1.5^{+0.2}_{-0.1} \times 10^{-2}$	$1.8^{+0.1}_{-0.1} \times 10^{-2}$	⋯	$2.1^{+0.1}_{-0.1} \times 10^{-2}$
5.0	5.0	4.4	$5^{+1}_{-2} \times 10^{-3}$	$5.8^{+0.5}_{-0.4} \times 10^{-2}$	$4.5^{+0.4}_{-0.4} \times 10^{-2}$	$6.5^{+0.5}_{-0.4} \times 10^{-2}$	$5.0^{+0.5}_{-0.4} \times 10^{-2}$	$7.4^{+0.5}_{-0.5} \times 10^{-2}$
5.0	1.5	2.3	⋯	$1.12^{+0.05}_{-0.06} \times 10^{-2}$	$1.19^{+0.06}_{-0.05} \times 10^{-2}$	$1.21^{+0.06}_{-0.06} \times 10^{-2}$	⋯	$1.43^{+0.06}_{-0.06} \times 10^{-2}$
1.5	1.5	1.3	⋯	$2.7^{+0.1}_{-0.1} \times 10^{-3}$	$3.4^{+0.1}_{-0.1} \times 10^{-3}$	$3.5^{+0.1}_{-0.2} \times 10^{-3}$	⋯	$3.9^{+0.1}_{-0.2} \times 10^{-3}$

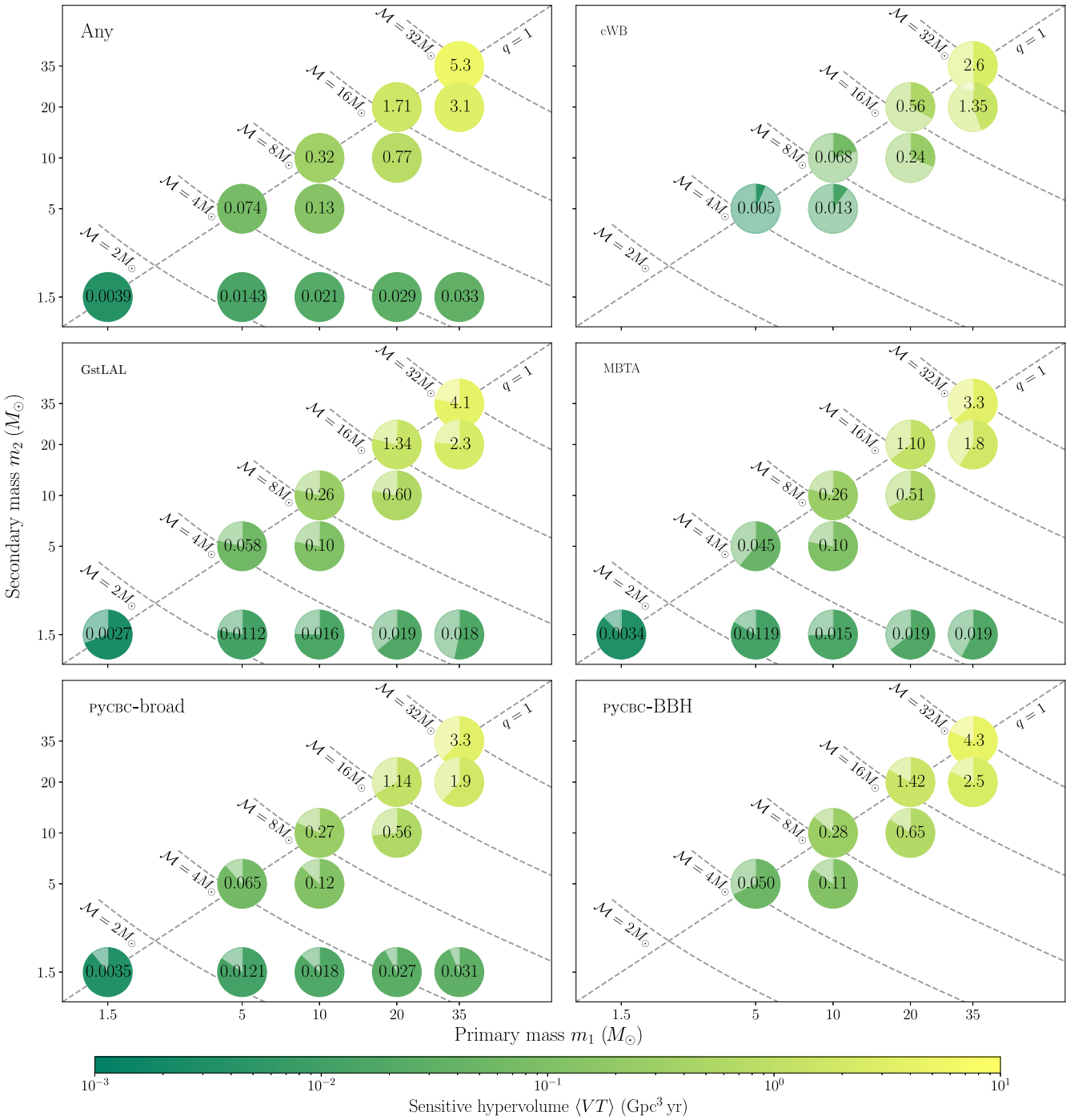

FIG. 6. Sensitive hypervolume $\langle VT \rangle$ from O3b for the various searches with $p_{\text{astro}} > 0.5$ at the assessed points in the mass parameter space. The Any results come from calculating the sensitive hypervolume for injections found by at least one search analysis. The plotted points correspond to the central points of the log-normal distributions (with widths 0.1) used for the calculation of $\langle VT \rangle$. Each point is marked by a pie chart, where the darker portion represents the fraction of the Any $\langle VT \rangle$ recovered. The color of the darker portion corresponds to the value of the sensitive $\langle VT \rangle$, as given by the scale bar. The values displayed are the same as those given in Table III.

results for the whole of O3 are given in Table XIV in Appendix D 7 a.

The sensitivity results presented in Table III are obtained considering a detection threshold of $p_{\text{astro}} > 0.5$ calculated as for our main results. The Any pipeline results come from taking the maximum p_{astro} for an injection from across the analyses and represent our overall sensitivity to CBCs in the specified region.

The cWB results are obtained using the standard $p_{\rm astro} > 0.5$ threshold; however, for candidates reported in Table I, we require that the cWB candidates must have an associated trigger from one of the matched-filter analyses, as the $p_{\rm astro}$ calculation performed by cWB assumes that the signal is from a CBC. Therefore, we also investigate the cWB $\langle VT \rangle$ using a cut of $p_{\rm astro} > 0.5$ from cWB together with the requirement that $p_{\rm astro} > 0.1$ from at least one matched-filter analysis to match the main results. We find these values to be comparable; for example, the $\langle VT \rangle$ for the $5M_\odot + 5M_\odot$ bin is unchanged, at $5^{+1}_{-2} \times 10^{-3}$ Gpc^3 yr, and the $10M_\odot + 10M_\odot$ bin changes from $6.8^{+0.8}_{-0.9} \times 10^{-2}$ to $6.7^{+0.9}_{-0.8} \times 10^{-2}$ Gpc^3 yr. The largest change is in the highest-mass $35M_\odot + 35M_\odot$ bin, where the $\langle VT \rangle$ changes from $2.6^{+0.1}_{-0.1}$ to $2.5^{+0.1}_{-0.1}$ Gpc^3 yr. Overall, adding the requirement that there be a CBC counterpart to cWB candidates makes little difference to the search sensitivity calculated from our CBC injections.

2. Subthreshold signal count via search sensitivities

The search sensitivities may also be calculated at the threshold of FAR < 2.0 day^{-1} corresponding to the subthreshold candidate set, enabling us to self-consistently estimate the number of astrophysical signals among these 1048 candidates. For an individual search pipeline, if the source population assumed in the $p_{\rm astro}$ calculation is sufficiently close to the (unknown) true population, then the sum of $p_{\rm astro}$ values over a candidate set gives the expectation of the number of true signals in the set [134]. This count of signals is itself a realization of a Poisson process with a mean proportional to the pipeline's $\langle VT \rangle$ for the true signal population. Hence, if the true population were known, we could scale the sum of $p_{\rm astro}$ values for each pipeline by its $\langle VT \rangle$ to obtain an estimate of the signal count at a given threshold for the combined Any pipeline analysis.

In lieu of the true population, we take as reference the $\langle VT \rangle$ values for the $35M_\odot + 35M_\odot$ point, as representing the largest proportion of detected signals. The resulting estimated signal counts for Any pipeline are consistent across pipelines within statistical uncertainties. Consistent and similar counts are also obtained for the modeled pipelines if the $20M_\odot + 20M_\odot$ or $10M_\odot + 10M_\odot$ points are taken as a reference, indicating that the result is not strongly sensitive to an assumed BBH mass distribution; the counts for cWB do vary, but the cWB contribution to the Any pipeline sensitivity varies significantly across the parameter space and is subdominant to the modeled pipelines for the lower-mass BBH points. The number of subthreshold signals is then the difference between signal counts (excluding the marginal candidates found to be likely caused by instrumental artifacts) for the thresholds FAR < 2.0 day^{-1} and $p_{\rm astro} > 0.5$, which averaged over pipelines yields approximately 7, with an expected uncertainty of approximately $\sqrt{7}$. This estimate is consistent with the ratio of $\langle VT \rangle$ values for Any pipeline between the two thresholds, which is 1.2–1.3 for the BBH mass points.

V. SOURCE PROPERTIES

Having identified candidate signals, we perform a coherent analysis of the data from the GW detector network to infer the properties of each source. Information about the source parameters is encoded within the amplitude and phase of the GW signal recorded by each detector in the network. To extract this information, we match model waveform templates to the observed data to calculate the posterior probability of a given set of parameters [135], assuming that the noise is Gaussian, stationary, and uncorrelated between detectors [96]. We use the waveform models `IMRPhenomXPHM` [136] and `SEOBNRv4PHM` [137] to describe BBH systems, and `IMRPhenomNSBH` [138] and `SEOBNRv4_ROM_NRTidalv2_NSBH` [139] to describe matter effects in NSBH systems. All templates assume quasicircular binaries, with the BBH models including the effects of spin precession and higher-order multipole moments [136,137,140,141]. As the higher-order multipole moments and spin precession effects incorporated into the BBH waveform templates are more important in describing the signal than the NSBH matter effects, we preferentially quote results using the BBH waveforms [8]. We use an equal combination of `IMRPhenomXPHM` and `SEOBNRv4PHM` samples [142,143]. Potential systematic uncertainties from differences in waveform modeling are discussed in Sec. V E. Analyses using the `IMRPhenomXPHM` or NSBH waveforms are performed with the Bilby family of codes [144–146] and analyses using the `SEOBNRv4PHM` waveforms are performed with RIFT [147–149]. The analysis closely follows the practices from previous studies [4,131], and further details are presented in Appendix E.

A summary of key results for O3b candidates is given in Table IV and shown in Figs. 7–9. We show results for the O3b candidates with $p_{\rm astro} > 0.5$ plus GW200105_162426, which, despite being a marginal candidate, is a clear outlier from the noise background [8]. On account of its low $p_{\rm astro}$, we highlight GW200105_162426 in figures and tables. We similarly highlight GW191219_163120 because, as discussed in Sec. IV D 3, the calculated $p_{\rm astro}$ is especially sensitive to the adopted population model, and, as discussed below, there is significant posterior support for mass ratios outside the range of calibration for the waveform models. Following previous analyses [3,4], results are calculated using default priors that are intended to not make strong assumptions about the underlying astrophysical population (e.g., uniform priors are used for redshifted component masses, an isotropic distribution is used for spin orientations, and it is assumed that sources are uniformly distributed in comoving volume and time).

TABLE IV. Median and 90% symmetric credible intervals for selected source parameters, and the 90% credible area for the sky localization for O3b candidates with $p_{\rm astro} > 0.5$ plus GW200105_162426. We highlight with italics GW200105_162426 as it has $p_{\rm astro} < 0.5$, as well as GW191219_163120 because of significant uncertainty in its $p_{\rm astro}$ and because it has significant posterior support outside of mass ratios where the waveform models are calibrated. An asterisk (∗) is used to indicate candidates for which the posterior distributions are dominated by potentially unphysical, low-likelihood modes at large distances and high masses, and are particularly prior sensitive. The columns show source total mass M, chirp mass $\mathcal{M}$, component masses m_i, effective inspiral spin $\chi_{\rm eff}$, luminosity distance D_L, redshift z, final mass M_f, final spin χ_f, sky localization $\Delta\Omega$, and the network matched-filter SNR. All quoted results are calculated using BBH waveform models; values come from averaging `IMRPhenomXPHM` and `SEOBNRv4PHM` results, except for the SNR (which is given for `IMRPhenomXPHM` because the RIFT analysis used for `SEOBNRv4PHM` does not output this quantity).

Candidate	$M(M_\odot)$	$\mathcal{M}(M_\odot)$	$m_1(M_\odot)$	$m_2(M_\odot)$	$\chi_{\rm eff}$	D_L(Gpc)	z	$M_f(M_\odot)$	χ_f	$\Delta\Omega(\mathrm{deg}^2)$	SNR
GW191103_012549	$20.0^{+3.7}_{-1.8}$	$8.34^{+0.66}_{-0.57}$	$11.8^{+6.2}_{-2.2}$	$7.9^{+1.7}_{-2.4}$	$0.21^{+0.16}_{-0.10}$	$0.99^{+0.50}_{-0.47}$	$0.20^{+0.09}_{-0.09}$	$19.0^{+3.8}_{-1.7}$	$0.75^{+0.06}_{-0.05}$	2500	$8.9^{+0.3}_{-0.5}$
GW191105_143521	$18.5^{+2.1}_{-1.3}$	$7.82^{+0.61}_{-0.45}$	$10.7^{+3.7}_{-1.6}$	$7.7^{+1.4}_{-1.9}$	$-0.02^{+0.13}_{-0.09}$	$1.15^{+0.43}_{-0.48}$	$0.23^{+0.07}_{-0.09}$	$17.6^{+2.1}_{-1.2}$	$0.67^{+0.04}_{-0.05}$	640	$9.7^{+0.3}_{-0.5}$
GW191109_010717	112^{+20}_{-16}	$47.5^{+9.6}_{-7.5}$	65^{+11}_{-11}	47^{+15}_{-13}	$-0.29^{+0.42}_{-0.31}$	$1.29^{+1.13}_{-0.65}$	$0.25^{+0.18}_{-0.12}$	107^{+18}_{-15}	$0.61^{+0.18}_{-0.19}$	1600	$17.3^{+0.5}_{-0.5}$
GW191113_071753	$34.5^{+10.5}_{-9.8}$	$10.7^{+1.1}_{-1.0}$	29^{+12}_{-14}	$5.9^{+4.4}_{-1.3}$	$0.00^{+0.37}_{-0.29}$	$1.37^{+1.15}_{-0.62}$	$0.26^{+0.18}_{-0.11}$	34^{+11}_{-10}	$0.45^{+0.33}_{-0.11}$	3600	$7.9^{+0.5}_{-1.1}$
GW191126_115259	$20.7^{+3.4}_{-2.0}$	$8.65^{+0.95}_{-0.71}$	$12.1^{+5.5}_{-2.2}$	$8.3^{+1.9}_{-2.4}$	$0.21^{+0.15}_{-0.11}$	$1.62^{+0.74}_{-0.74}$	$0.30^{+0.12}_{-0.13}$	$19.6^{+3.5}_{-2.0}$	$0.75^{+0.06}_{-0.05}$	1400	$8.3^{+0.2}_{-0.5}$
GW191127_050227	80^{+39}_{-22}	$29.9^{+11.7}_{-9.1}$	53^{+47}_{-20}	24^{+17}_{-14}	$0.18^{+0.34}_{-0.36}$	$3.4^{+3.1}_{-1.9}$	$0.57^{+0.40}_{-0.29}$	76^{+39}_{-21}	$0.75^{+0.13}_{-0.29}$	980	$9.2^{+0.7}_{-0.6}$
GW191129_134029	$17.5^{+2.4}_{-1.2}$	$7.31^{+0.43}_{-0.28}$	$10.7^{+4.1}_{-2.1}$	$6.7^{+1.5}_{-1.7}$	$0.06^{+0.16}_{-0.08}$	$0.79^{+0.26}_{-0.33}$	$0.16^{+0.05}_{-0.06}$	$16.8^{+2.5}_{-1.2}$	$0.69^{+0.03}_{-0.05}$	850	$13.1^{+0.2}_{-0.3}$
GW191204_110529	$47.1^{+9.1}_{-7.8}$	$19.8^{+3.6}_{-3.2}$	$27.3^{+10.8}_{-5.9}$	$19.2^{+5.5}_{-6.0}$	$0.05^{+0.25}_{-0.26}$	$1.9^{+1.7}_{-1.1}$	$0.34^{+0.25}_{-0.18}$	$45.0^{+8.7}_{-7.5}$	$0.71^{+0.11}_{-0.11}$	3400	$8.9^{+0.4}_{-0.6}$
GW191204_171526	$20.19^{+1.64}_{-0.95}$	$8.56^{+0.41}_{-0.28}$	$11.7^{+3.3}_{-1.7}$	$8.4^{+1.3}_{-1.7}$	$0.16^{+0.08}_{-0.05}$	$0.64^{+0.20}_{-0.26}$	$0.13^{+0.04}_{-0.05}$	$19.18^{+1.71}_{-0.93}$	$0.73^{+0.04}_{-0.03}$	310	$17.4^{+0.2}_{-0.3}$
GW191215_223052	$43.3^{+5.3}_{-4.3}$	$18.4^{+2.2}_{-1.7}$	$24.9^{+7.1}_{-4.1}$	$18.1^{+3.8}_{-4.1}$	$-0.04^{+0.17}_{-0.21}$	$1.93^{+0.89}_{-0.86}$	$0.35^{+0.13}_{-0.14}$	$41.4^{+5.1}_{-4.1}$	$0.68^{+0.07}_{-0.07}$	530	$11.2^{+0.3}_{-0.4}$
GW191216_213338	$19.80^{+2.70}_{-0.93}$	$8.33^{+0.22}_{-0.19}$	$12.1^{+4.6}_{-2.2}$	$7.7^{+1.6}_{-1.9}$	$0.11^{+0.13}_{-0.06}$	$0.34^{+0.12}_{-0.13}$	$0.07^{+0.02}_{-0.03}$	$18.87^{+2.81}_{-0.93}$	$0.70^{+0.03}_{-0.04}$	910	$18.6^{+0.2}_{-0.2}$
GW191219_163120	$32.3^{+2.2}_{-2.7}$	$4.31^{+0.12}_{-0.17}$	$31.1^{+2.2}_{-2.8}$	$1.17^{+0.07}_{-0.06}$	$0.00^{+0.07}_{-0.09}$	$0.55^{+0.24}_{-0.16}$	$0.11^{+0.05}_{-0.03}$	$32.2^{+2.2}_{-2.7}$	$0.14^{+0.06}_{-0.06}$	1500	$9.1^{+0.5}_{-0.8}$
GW191222_033537	79^{+16}_{-11}	$33.8^{+7.1}_{-5.0}$	$45.1^{+10.9}_{-8.0}$	$34.7^{+9.3}_{-10.5}$	$-0.04^{+0.20}_{-0.25}$	$3.0^{+1.7}_{-1.7}$	$0.51^{+0.23}_{-0.26}$	$75.5^{+15.3}_{-9.9}$	$0.67^{+0.08}_{-0.11}$	2000	$12.5^{+0.2}_{-0.3}$
GW191230_180458	86^{+19}_{-12}	$36.5^{+8.2}_{-5.6}$	$49.4^{+14.0}_{-9.6}$	37^{+11}_{-12}	$-0.05^{+0.26}_{-0.31}$	$4.3^{+2.1}_{-1.9}$	$0.69^{+0.26}_{-0.27}$	82^{+17}_{-11}	$0.68^{+0.11}_{-0.13}$	1100	$10.4^{+0.3}_{-0.4}$
GW200105_162426	$11.0^{+1.5}_{-1.4}$	$3.42^{+0.08}_{-0.08}$	$9.1^{+1.7}_{-1.7}$	$1.91^{+0.33}_{-0.24}$	$0.00^{+0.13}_{-0.18}$	$0.27^{+0.12}_{-0.11}$	$0.06^{+0.02}_{-0.02}$	$10.8^{+1.5}_{-1.4}$	$0.43^{+0.05}_{-0.02}$	9600	$13.7^{+0.2}_{-0.4}$
GW200112_155838	$63.9^{+5.7}_{-4.6}$	$27.4^{+2.6}_{-2.1}$	$35.6^{+6.7}_{-4.5}$	$28.3^{+4.4}_{-5.9}$	$0.06^{+0.15}_{-0.15}$	$1.25^{+0.43}_{-0.46}$	$0.24^{+0.07}_{-0.08}$	$60.8^{+5.3}_{-4.3}$	$0.71^{+0.06}_{-0.06}$	4300	$19.8^{+0.1}_{-0.2}$
GW200115_042309	$7.4^{+1.7}_{-1.7}$	$2.43^{+0.05}_{-0.07}$	$5.9^{+2.0}_{-2.5}$	$1.44^{+0.85}_{-0.28}$	$-0.15^{+0.23}_{-0.42}$	$0.29^{+0.15}_{-0.10}$	$0.06^{+0.03}_{-0.02}$	$7.2^{+1.8}_{-1.7}$	$0.42^{+0.09}_{-0.04}$	720	$11.3^{+0.3}_{-0.5}$
GW200128_022011	75^{+17}_{-12}	$32.0^{+7.5}_{-5.5}$	$42.2^{+11.6}_{-8.1}$	$32.6^{+9.5}_{-9.2}$	$0.12^{+0.24}_{-0.25}$	$3.4^{+2.1}_{-1.8}$	$0.56^{+0.28}_{-0.28}$	71^{+16}_{-11}	$0.74^{+0.10}_{-0.10}$	2600	$10.6^{+0.3}_{-0.4}$
GW200129_065458	$63.3^{+4.5}_{-3.4}$	$27.2^{+2.1}_{-2.3}$	$34.5^{+9.9}_{-3.1}$	$29.0^{+3.3}_{-9.3}$	$0.11^{+0.11}_{-0.16}$	$0.89^{+0.26}_{-0.37}$	$0.18^{+0.05}_{-0.07}$	$60.2^{+4.1}_{-3.2}$	$0.73^{+0.06}_{-0.05}$	54	$26.8^{+0.2}_{-0.2}$
GW200202_154313	$17.58^{+1.78}_{-0.67}$	$7.49^{+0.24}_{-0.20}$	$10.1^{+3.5}_{-1.4}$	$7.3^{+1.1}_{-1.7}$	$0.04^{+0.13}_{-0.06}$	$0.41^{+0.15}_{-0.16}$	$0.09^{+0.03}_{-0.03}$	$16.76^{+1.87}_{-0.66}$	$0.69^{+0.03}_{-0.04}$	160	$10.8^{+0.2}_{-0.4}$
GW200208_130117	$65.3^{+8.1}_{-6.8}$	$27.7^{+3.7}_{-3.1}$	$37.7^{+9.3}_{-6.2}$	$27.4^{+6.3}_{-7.3}$	$-0.07^{+0.21}_{-0.27}$	$2.23^{+1.02}_{-0.85}$	$0.40^{+0.15}_{-0.14}$	$62.5^{+7.5}_{-6.4}$	$0.66^{+0.09}_{-0.12}$	48	$10.8^{+0.3}_{-0.4}$
GW200208_222617	63^{+100}_{-26}	$19.8^{+10.5}_{-5.2}$	51^{+103}_{-30}	$12.3^{+9.2}_{-5.5}$	$0.45^{+0.42}_{-0.46}$	$4.1^{+4.4}_{-2.0}$	$0.66^{+0.53}_{-0.29}$	61^{+99}_{-26}	$0.83^{+0.14}_{-0.26}$	1900	$7.4^{+1.4}_{-1.2}$
GW200209_085452	$62.6^{+13.9}_{-9.4}$	$26.7^{+6.0}_{-4.2}$	$35.6^{+10.5}_{-6.8}$	$27.1^{+7.8}_{-7.8}$	$-0.12^{+0.24}_{-0.30}$	$3.4^{+1.9}_{-1.8}$	$0.57^{+0.25}_{-0.26}$	$59.9^{+13.1}_{-8.9}$	$0.66^{+0.10}_{-0.12}$	730	$9.6^{+0.4}_{-0.5}$
GW200210_092254	$27.0^{+7.1}_{-4.3}$	$6.56^{+0.38}_{-0.40}$	$24.1^{+7.5}_{-4.6}$	$2.83^{+0.47}_{-0.42}$	$0.02^{+0.22}_{-0.21}$	$0.94^{+0.43}_{-0.34}$	$0.19^{+0.08}_{-0.06}$	$26.7^{+7.2}_{-4.3}$	$0.34^{+0.13}_{-0.08}$	1800	$8.4^{+0.5}_{-0.7}$
GW200216_220804	81^{+20}_{-14}	$32.9^{+9.3}_{-8.5}$	51^{+22}_{-13}	30^{+14}_{-16}	$0.10^{+0.34}_{-0.36}$	$3.8^{+3.0}_{-2.0}$	$0.63^{+0.37}_{-0.29}$	78^{+19}_{-13}	$0.70^{+0.14}_{-0.24}$	2900	$8.1^{+0.4}_{-0.5}$
GW200219_094415	$65.0^{+12.6}_{-8.2}$	$27.6^{+5.6}_{-3.8}$	$37.5^{+10.1}_{-6.9}$	$27.9^{+7.4}_{-8.4}$	$-0.08^{+0.23}_{-0.29}$	$3.4^{+1.7}_{-1.5}$	$0.57^{+0.22}_{-0.22}$	$62.2^{+11.7}_{-7.8}$	$0.66^{+0.10}_{-0.13}$	700	$10.7^{+0.3}_{-0.5}$
GW200220_061928	148^{+55}_{-33}	62^{+23}_{-15}	87^{+40}_{-23}	61^{+26}_{-25}	$0.06^{+0.40}_{-0.38}$	$6.0^{+4.8}_{-3.1}$	$0.90^{+0.55}_{-0.40}$	141^{+51}_{-31}	$0.71^{+0.15}_{-0.17}$	3000	$7.2^{+0.4}_{-0.7}$
GW200220_124850	67^{+17}_{-12}	$28.2^{+7.3}_{-5.1}$	$38.9^{+14.1}_{-8.6}$	$27.9^{+9.2}_{-9.0}$	$-0.07^{+0.27}_{-0.33}$	$4.0^{+2.8}_{-2.2}$	$0.66^{+0.36}_{-0.31}$	64^{+16}_{-11}	$0.67^{+0.11}_{-0.14}$	3200	$8.5^{+0.3}_{-0.5}$
GW200224_222234	$72.3^{+7.2}_{-5.3}$	$31.1^{+3.3}_{-2.7}$	$40.0^{+6.7}_{-4.5}$	$32.7^{+4.8}_{-7.2}$	$0.10^{+0.15}_{-0.16}$	$1.71^{+0.50}_{-0.65}$	$0.32^{+0.08}_{-0.11}$	$68.7^{+6.7}_{-4.8}$	$0.73^{+0.06}_{-0.07}$	51	$20.0^{+0.2}_{-0.2}$
GW200225_060421	$33.5^{+3.6}_{-3.0}$	$14.2^{+1.5}_{-1.4}$	$19.3^{+5.0}_{-3.0}$	$14.0^{+2.8}_{-3.5}$	$-0.12^{+0.17}_{-0.28}$	$1.15^{+0.51}_{-0.53}$	$0.22^{+0.09}_{-0.10}$	$32.1^{+3.5}_{-2.8}$	$0.66^{+0.07}_{-0.13}$	370	$12.5^{+0.3}_{-0.4}$
GW200302_015811	$57.8^{+9.6}_{-6.9}$	$23.4^{+4.7}_{-3.0}$	$37.8^{+8.7}_{-8.5}$	$20.0^{+8.1}_{-5.7}$	$0.01^{+0.25}_{-0.26}$	$1.48^{+1.02}_{-0.70}$	$0.28^{+0.16}_{-0.12}$	$55.5^{+8.9}_{-6.6}$	$0.66^{+0.13}_{-0.15}$	6000	$10.8^{+0.3}_{-0.4}$
GW200306_093714	$43.9^{+11.8}_{-7.5}$	$17.5^{+3.5}_{-3.0}$	$28.3^{+17.1}_{-7.7}$	$14.8^{+6.5}_{-6.4}$	$0.32^{+0.28}_{-0.46}$	$2.1^{+1.7}_{-1.1}$	$0.38^{+0.24}_{-0.18}$	$41.7^{+12.3}_{-6.9}$	$0.78^{+0.11}_{-0.26}$	4600	$7.8^{+0.4}_{-0.6}$
GW200308_173609*	92^{+169}_{-48}	34^{+44}_{-18}	60^{+166}_{-29}	24^{+36}_{-13}	$0.16^{+0.58}_{-0.49}$	$7.1^{+13.9}_{-4.4}$	$1.04^{+1.47}_{-0.57}$	88^{+169}_{-47}	$0.72^{+0.22}_{-0.35}$	12 000	$4.7^{+2.5}_{-2.9}$
GW200311_115853	$61.9^{+5.3}_{-4.2}$	$26.6^{+2.4}_{-2.0}$	$34.2^{+6.4}_{-3.8}$	$27.7^{+4.1}_{-5.9}$	$-0.02^{+0.16}_{-0.20}$	$1.17^{+0.28}_{-0.40}$	$0.23^{+0.05}_{-0.07}$	$59.0^{+4.8}_{-3.9}$	$0.69^{+0.07}_{-0.08}$	35	$17.8^{+0.2}_{-0.2}$
GW200316_215756	$21.2^{+7.2}_{-2.0}$	$8.75^{+0.62}_{-0.55}$	$13.1^{+10.2}_{-2.9}$	$7.8^{+2.0}_{-2.9}$	$0.13^{+0.27}_{-0.10}$	$1.12^{+0.48}_{-0.44}$	$0.22^{+0.08}_{-0.08}$	$20.2^{+7.4}_{-1.9}$	$0.70^{+0.04}_{-0.04}$	190	$10.3^{+0.4}_{-0.7}$
GW200322_091133*	50^{+132}_{-22}	$15.0^{+29.5}_{-4.0}$	38^{+130}_{-22}	$11.3^{+24.3}_{-6.0}$	$0.27^{+0.54}_{-0.58}$	$3.5^{+12.5}_{-2.2}$	$0.59^{+1.43}_{-0.32}$	48^{+132}_{-22}	$0.77^{+0.19}_{-0.39}$	18 000	$4.5^{+2.7}_{-3.0}$

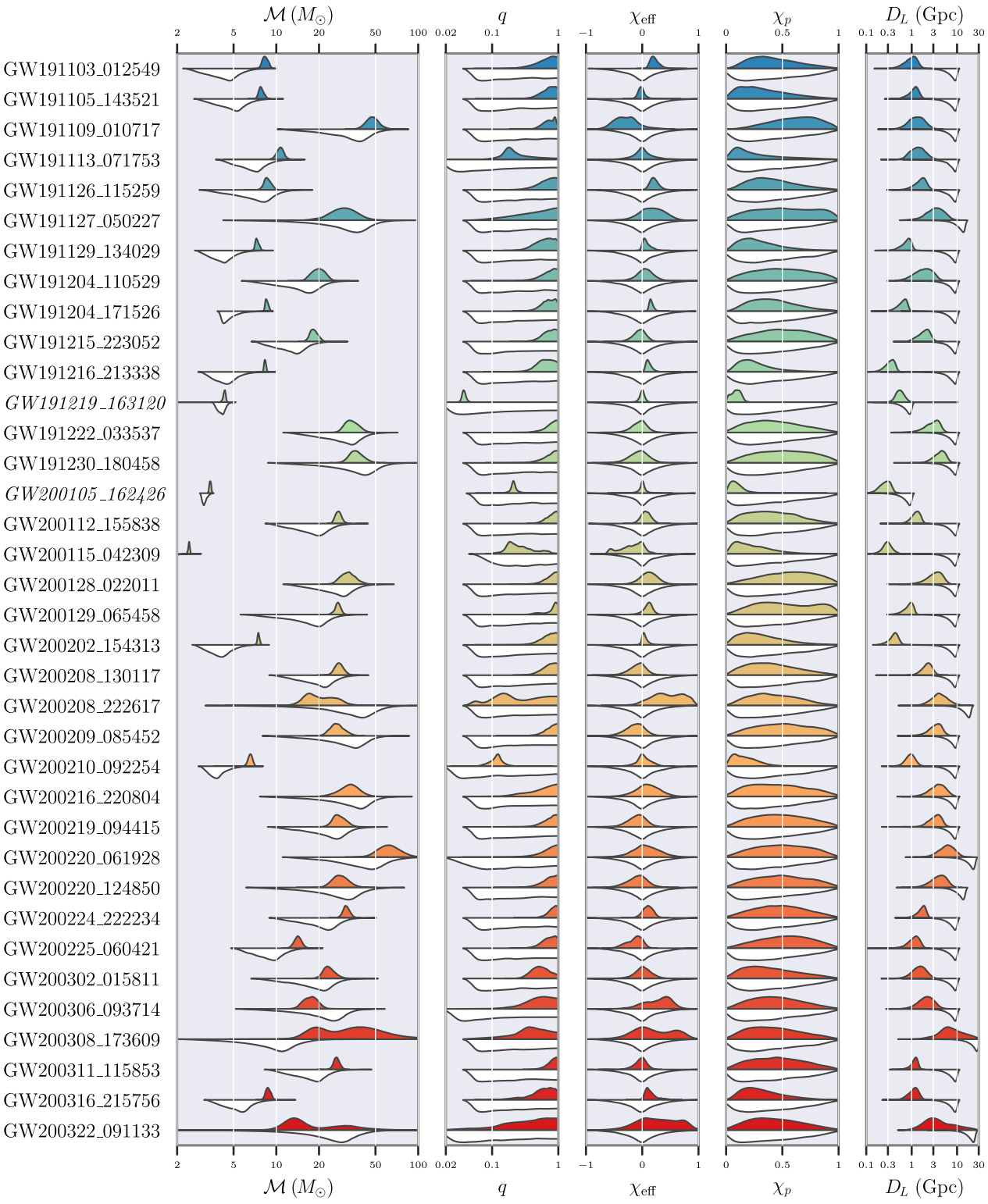

FIG. 7. Marginal probability distributions for the source chirp mass $\mathcal{M}$, mass ratio q, effective inspiral spin $\chi_{\rm eff}$, effective precession spin χ_p, and luminosity distance D_L for O3b candidates with $p_{\rm astro} > 0.5$ plus GW200105_162426. The colored upper half of the plot shows the marginal posterior distributions, and the white lower half of the plot shows the marginal prior distributions. The vertical extent of each colored region is proportional to one-dimensional marginal probability distribution at a given parameter value for the corresponding candidate. We highlight with italics GW200105_162426 as it has $p_{\rm astro} < 0.5$, as well as GW191219_163120 because of significant uncertainty in its $p_{\rm astro}$ and because it has significant posterior support outside of mass ratios where the waveform models have been calibrated. Results for GW200308_173609 and GW200322_091133 include a low-likelihood mode at large distances and high masses. Colors correspond to the date of observation.

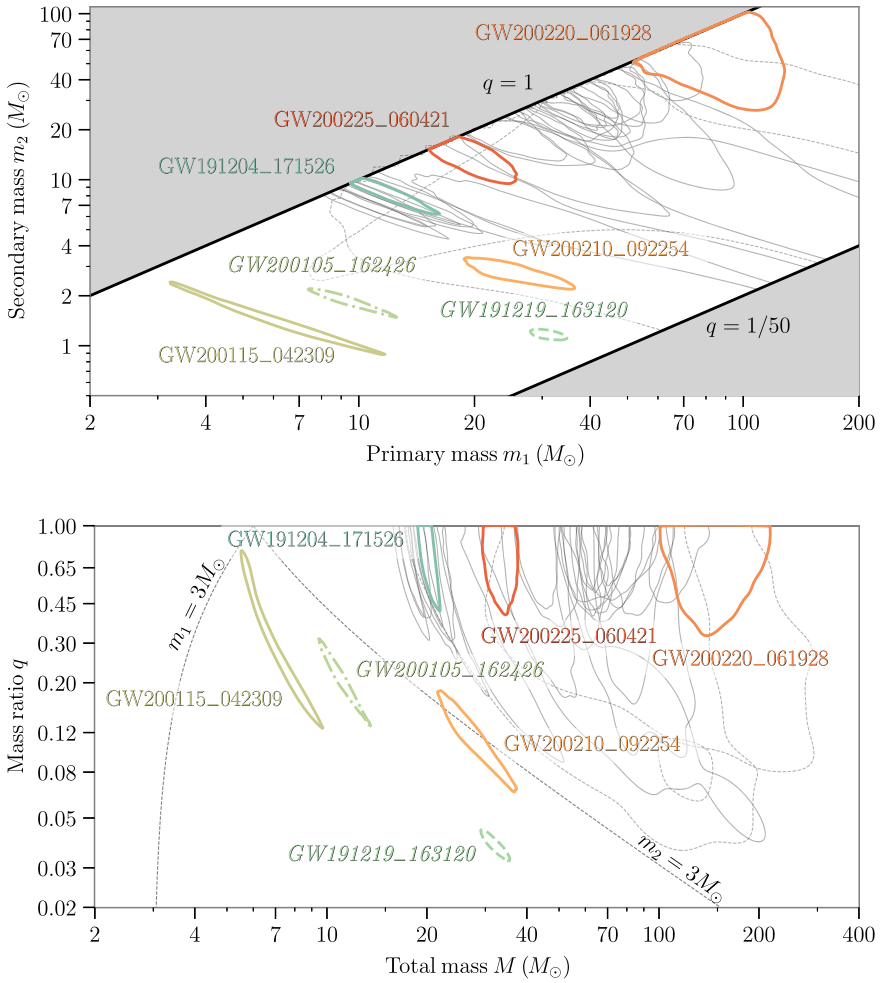

FIG. 8. Credible-region contours for the inferred masses of the O3b candidates with $p_{\text{astro}} > 0.5$ plus GW200105_162426. Top: results for the primary and secondary component masses m_1 and m_2. The shaded areas indicate regions excluded by the convention $m_1 \geq m_2$, and by the most extreme mass ratio considered in our analyses (detailed in Appendix E 3). Bottom: results for total mass M and mass ratio q. Each contour represents the 90% credible region for a different candidate. Highlighted contours are for the NSBH candidates GW191219_163120, GW200105_162426, and GW200115_042309; the NSBH or low-mass BBH candidate GW200210_092254; GW191204_171526, which has inferred $\chi_{\text{eff}} > 0$; GW200225_060421, which has 85% probability that $\chi_{\text{eff}} < 0$, and GW200220_061928, which probably has the most massive source of the O3b candidates. We highlight with italics GW200105_162426 as it has $p_{\text{astro}} < 0.5$, as well as GW191219_163120 because of significant uncertainty in its p_{astro} and because it has significant posterior support outside of mass ratios where the waveform models have been calibrated. Results for GW200308_173609 and GW200322_091133 are indicated with dashed lines to highlight that these include a low-likelihood mode at large distances and high masses, and are particularly prior sensitive. The dotted lines delineate regions where the primary and secondary can have a mass below $3M_\odot$. For the region above the $m_2 = 3M_\odot$ line, both objects in the binary have masses above $3M_\odot$.

Posterior samples are available from GWOSC [33], and the simple form of the prior probability distributions enables the samples to be conveniently reweighted to use alternative prior distributions [150,151]. Inferences about the underlying population of merging compact binaries are presented in a companion paper [5].

The O3b candidates show a diversity in their source properties. Many are similar to previous observations, but some do show unusual features. While the mass posterior probability distributions are typically unimodal, some results show multimodal behavior. For example, GW200129_065458 shows a bimodality in mass ratio that translates to a bimodality in m_2. GW200225_060421 and GW200306_093714 both show bimodality in their redshifted chirp-mass distributions, although their source-mass distributions (shown in Fig. 7) are unimodal, as the additional uncertainty from the inferred redshift is sufficient to broaden the modes such that they merge. Because of the correlations between masses and spins [152–154], multimodality in mass distributions may also translate to multiple peaks in the effective inspiral spin distribution. Multimodality can arise due to the complexity of the

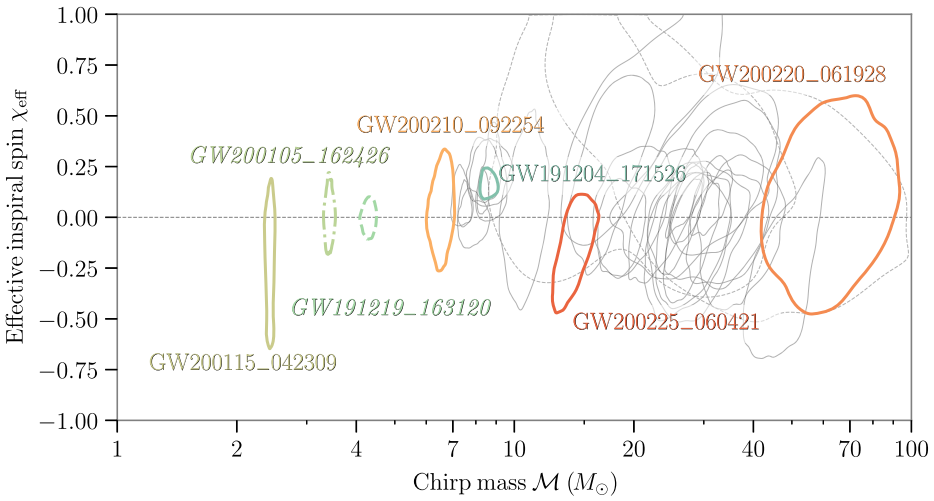

FIG. 9. Credible-region contours in the plane of chirp mass $\mathcal{M}$ and effective inspiral spin $\chi_{\rm eff}$ for O3b candidates with $p_{\rm astro} > 0.5$ plus GW200105_162426. Each contour represents the 90% credible region for a different candidate. Highlighted contours are for the NSBH candidates GW191219_163120, GW200105_162426, and GW200115_042309; the NSBH or low-mass BBH candidate GW200210_092254; GW191204_171526, which has inferred $\chi_{\rm eff} > 0$; GW200225_060421, which has 85% probability that $\chi_{\rm eff} < 0$, and GW200220_061928, which probably has the most massive source of the O3b candidates. We highlight with italics GW200105_162426 as it has $p_{\rm astro} < 0.5$, as well as GW191219_163120 because of significant uncertainty in its $p_{\rm astro}$ and because it has significant posterior support outside of mass ratios where the waveform models have been calibrated. Results for GW200308_173609 and GW200322_091133 are indicated with dashed lines to highlight that these include a low-likelihood mode at large distances and high masses, and are particularly prior sensitive.

likelihood surface when using waveform models that include higher-order multipole moments [19,155–157] and precession [158,159], noise fluctuations for quiet signals [160], the presence of glitches [161–163], or there being multiple overlapping signals in the data (which is unlikely given O3 sensitivity) [164]. Therefore, multimodality is expected in a few cases.

Cases with significant multimodality are GW200208_222617, GW200308_173609, and GW200322_091133. These candidates have modest significance with $p_{\rm astro} = 0.70$, 0.86, and 0.62, respectively, and are each identified with $p_{\rm astro} > 0.5$ by only one search analysis. They have low SNRs, and using `IMRPhenomXPHM` they are inferred to have $\rho = 7.4^{+1.4}_{-1.2}$, $4.7^{+2.5}_{-2.9}$, and $4.5^{+2.7}_{-3.0}$, respectively. For GW200208_222617, the two main modes have comparable likelihoods, indicating comparable fits to the data, while for GW200308_173609 and GW200322_091133, there are significant modes with lower likelihoods. The posterior probability distributions for GW200308_173609 and GW200322_091133 both have peaks at lower masses and lower distances, and another broader peak corresponding to higher masses and larger distances; this high-mass, large-distance peak is dominated by the prior. The default prior probability distribution (described in Appendix E 3) places significant weight at large distances and at high masses. This means that we can find significant posterior probability at large distances and high masses, even when the likelihood is low. Such low-likelihood peaks, corresponding to low SNRs, may arise due to a random noise fluctuation matching the signal template. For GW200308_173609 and GW200322_091133, the high-mass and high-distance peak has lower likelihood and posterior support for SNRs $\rho \sim 0$. For such candidates, the multimodality indicates that we cannot separate the possibility of a signal from a lower-mass, closer source from a weaker (potentially vanishing) signal from a higher-mass, more-distant source. However, this support for high masses and large distances is driven by our choice of prior, which is not designed to model the astrophysical population of sources. Therefore, we consider that the high-likelihood peaks for GW200308_173609 and GW200322_091133 yield a more plausible estimate of the source parameters, although we cannot exclude the possibility that the low-likelihood peaks describe the sources (assuming that the signals are astrophysical).

All results are given assuming our default priors. We highlight results for GW200308_173609 and GW200322_091133 in Table IV and the figures to indicate that these results may be especially sensitive to the choice of prior. Using a different prior, such as a population-informed prior [116,119,165–169], that has a stronger preference for masses more consistent with other GW observations, and a weaker preference for high masses and large distances, would alter results.

A. Masses

Masses are typically the best constrained binary parameters. They are the dominant properties in setting the frequency evolution of the signal, with lower- (higher-) mass systems merging at higher (lower) frequencies.

While we are typically interested in the source masses, it is the redshifted masses $(1+z)m_i$, where z is the source redshift, that are measured by the detectors [101]. The source masses are calculated by combining the inferred redshifted mass and luminosity distance (see Appendix E for the assumed cosmology).

Combinations of the two component masses (such as the chirp mass) may be more precisely measured than the individual component masses [152–154,170]. However, component masses are most informative about the nature of the source, and indicate whether the compact object is more likely to be a BH or a NS. The maximum NS mass is currently uncertain, with estimates ranging over 2.1–$2.7M_\odot$ [171–176]. We use $3M_\odot$ as a robust upper limit of the maximum NS mass [9,10], and split the candidates into two categories: unambiguous BBHs where, assuming that the signal is astrophysical, both components of the source were BHs ($m_2 > 3M_\odot$ at 99% probability), and potential-NS binaries (in our case, potential-NSBH binaries) where at least one component could have been a NS. Candidates from the two categories are discussed in Secs. V A 1 and V A 2, respectively. As shown in Fig. 8, all of the 35 candidates with $p_{\rm astro} > 0.5$ except GW191219_163120, GW200115_042309, and GW200210_092254 (plus GW200105_162426) have $m_2 > 3M_\odot$, and none of the candidates have posterior support for $m_1 < 3M_\odot$, which would be required for a BNS source. Therefore, we identify the majority of sources as BBHs.

1. Masses of sources with strictly $m_2 > 3M_\odot$: Unambiguous BBHs

The mass combination with greatest influence on a CBC signal's frequency evolution is the chirp mass $\mathcal{M}$ [98]. The chirp mass's influence on the inspiral means that it is more precisely measured in lower-mass systems, which have more of the inspiral signal in the sensitive frequency band of the detectors [177–181]. This is illustrated in Fig. 9, which also shows the effective inspiral spin (Sec. V B). The modestly significant ($p_{\rm astro} = 0.62$) GW200220_061928 probably has the highest chirp-mass source of the O3b candidates, with $\mathcal{M} = 62^{+23}_{-15}M_\odot$. Similarly, GW191129_134029's source probably has the lowest while still being an unambiguous-BBH ($m_2 > 3M_\odot$) candidate, with $\mathcal{M} = 7.31^{+0.43}_{-0.28}M_\odot$. The range of chirp masses for the O3b candidates is consistent with GWTC-2.1 [3,4].

The total mass of the binary M influences the merger and ringdown of the signal, which constitute a more significant proportion of the observed signal for higher-mass sources [13,182,183]. The O3b candidates with the highest M measurements, GW200220_061928 and (the multimodal) GW200308_173609, have lower median M measurements than GW190521 [4,184], of $M = 148^{+55}_{-33}M_\odot$ and $92^{+169}_{-48}M_\odot$, respectively. The lowest-mass O3b unambiguous-BBH candidate is GW191129_134029's source, with $M = 17.5^{+2.4}_{-1.2}M_\odot$. Posterior probability distributions for the total mass and mass ratio are shown in Fig. 8; the curving degeneracies seen at lower masses are where distributions follow a line of constant chirp mass.

Mass ratios are typically less precisely inferred from GW observations than the chirp mass or total mass. The mass ratio influences the phase evolution of the inspiral at the post-Newtonian (PN) order after the chirp mass [98,135,152,153]. Most measured mass ratios are consistent with the equal-mass limit $q = 1$, as shown in Fig. 7. For example, GW200129_065458 and GW200311_115853 have $q \geq 0.50$ and ≥ 0.61 at 90% probability, respectively. However, multiple BBH candidates have support for unequal masses. GW191113_071753's source has an inferred $q = 0.202^{+0.490}_{-0.087}$ ($q \leq 0.524$ at 90% probability) and GW200208_222617's source has $q = 0.21^{+0.67}_{-0.16}$ ($q \leq 0.79$ at 90% probability). Some posterior probability distributions extend outside the calibration range for current waveform models, and hence may be subject to additional systematic uncertainties [136,137]. Future analysis with waveforms with improved fidelity at more extreme mass ratios should lead to a more complete understanding of these sources. GW191113_071753 and GW200208_222617 have moderate significance ($p_{\rm astro} = 0.68$ and 0.70, respectively), and hence may not be a reflection of the true BBH population. Using a population-informed prior [116,119,165–169], in place of our default uninformative prior, may give greater weight to equal masses [5].

Considering individual BH masses, the unambiguous-BBH candidates have component masses ranging from approximately $5.9^{+4.4}_{-1.3}M_\odot$ to approximately $87^{+40}_{-23}M_\odot$. Primary masses range from $10.1^{+3.5}_{-1.4}M_\odot$ for GW200202_154313 to $87^{+40}_{-23}M_\odot$ and $60^{+166}_{-29}M_\odot$ for GW200220_061928 and GW200308_173609, while secondary masses range from $5.9^{+4.4}_{-1.3}M_\odot$ for GW191113_071753 to $61^{+26}_{-25}M_\odot$ for GW200220_061928. The distribution of component masses is analyzed and its astrophysical implications discussed in a companion paper [5].

Given our default prior assumptions, there is a 94% probability that the primary BH in GW200220_061928 has a mass $m_1 > 65M_\odot$; this is approximately the maximum mass of BHs expected to be formed from stellar collapse before encountering pair-instability supernovae [156,185–190], where the progenitor stars would be disrupted leaving no remnant behind, although there are many physical uncertainties that can impact this maximum mass [191–198]. GW191109_010717 has 51% probability that $m_1 > 65M_\odot$, while GW200208_222617 and GW191127_050227 have probabilities 42% and 30%, respectively. Similarly, GW200220_061928 has a 39% probability that its secondary has $m_2 > 65M_\odot$. GW200220_061928 and GW200208_222617 have 7% and 6% probabilities that $m_1 > 120M_\odot$, respectively, which

is expected to be approximately the mass where the pair-instability supernova mass gap ends [156,189,194,199,200].

Based upon x-ray binary observations, there is a hypothesized lower BH mass gap below $5M_\odot$ [201–204]. This may be a signature of the physics of core-collapse supernova explosions [205–209]. We infer that there are some BBHs that may have components in this mass gap. Given our standard prior assumptions, the candidate with the most posterior support for $m_2 < 5M_\odot$ is GW191113_071753 with 13% probability. None of the unambiguous-BBH candidates has a primary mass consistent with being in the lower mass gap.

The component BH masses overlap with those from previous GW and electromagnetic observations. The range is consistent with observations in GWTC-2.1 [4,184]. Non-LVK analysis of public GW data has led to other BBH candidates being reported [15–19,210]; these BBHs have inferred masses and mass ratios that are consistent with the systems found here. From these non-LVK searches, the marginal candidate GW170817A [18,211] may have the most massive source, with $m_1 = 56^{+16}_{-10}M_\odot$ and $m_2 = 40^{+10}_{-11}M_\odot$. While overlapping at lower masses, the BH masses inferred from GW observations extend above the masses seen in x-ray binaries [202,203,212–215]. However, these x-ray binaries are largely expected not to form merging BBHs [216,217]: For example, while Cygnus X-1 may form two BHs, predictions indicate that there is only a small probability that they would merge within a Hubble time [218]. Additionally, x-ray observations are typically drawn from binaries with near solar metallicity. Stellar mass loss due to winds increases with metallicity [219–221], so stars formed at solar metallicity leave less massive remnants than stars formed at lower metallicity with the same initial mass [189,222–226]. Studying the masses of BHs will provide insight into their formation and the lives of their progenitors [199,227–234].

The remnant BHs formed from the mergers have masses $M_f = M - E_{\rm rad}/c^2$ where $E_{\rm rad}$ is the energy radiated as GWs, which typically corresponds to a few percent of M [235–238]. The most massive remnant BH among the O3b candidates probably corresponds to GW200220_061928, with a final mass of $141^{+51}_{-31}M_\odot$. Using our default priors, there is a 99% probability of its final BH mass being above $100M_\odot$ (a conventional threshold for being considered an IMBH [26,239,240]). Several other systems are consistent with $M_f > 100M_\odot$, including GW191109_010717's remnant, which has a 78% probability of exceeding this threshold.

2. Masses of sources with support for $m_2 < 3M_\odot$: Potential-NS binaries

The candidates GW191219_163120, GW200115_042309, GW200210_092254, and GW200105_162426 are all consistent with originating from a source with $m_2 < 3M_\odot$. When a coalescing binary contains a NS, matter effects modify the waveform. If these effects can be measured, we can identify that the component is a NS rather than a BH. For O3b candidates, as discussed in Sec. V C, we find no measurable matter effects. Without this information, from the GW signal we can infer only the component type from their masses.

As illustrated by Figs. 7 and 8, the O3b candidates with potential-NS binary sources have more extreme mass ratios than the typical BBH candidates. At 90% probability, the sources of GW191219_163120, GW200105_162426, GW200115_042309, and GW200210_092254 have mass ratios $q \leq 0.041$, ≤ 0.258, ≤ 0.571, and ≤ 0.150, respectively. The mass ratio of GW200210_092254's source is $q = 0.118^{+0.048}_{-0.041}$, which is comparable to GW190814's $q = 0.11^{+0.01}_{-0.01}$ [4,241]. The mass ratio of GW191219_163120's source is inferred to be $0.038^{+0.005}_{-0.004}$, which is extremely challenging for waveform modeling, and thus, there may be systematic uncertainties in results for this candidate.

GW200115_042309's source is the lowest total mass O3b binary; this potential NSBH coalescence has $M = 7.4^{+1.7}_{-1.7}M_\odot$. Its chirp mass is well measured at $\mathcal{M} = 2.43^{+0.05}_{-0.07}M_\odot$. GW200115_042309's source has components with masses $m_1 = 5.9^{+2.0}_{-2.5}M_\odot$ and $m_2 = 1.44^{+0.85}_{-0.28}M_\odot$. These results are consistent with previous inferences [8], showing that the change in how the fast scattering glitches in Livingston data were mitigated (discussed in Appendix C) does not have a significant impact on this analysis. The primary is consistent with being a low-mass BH [8], and we infer a 29% probability that $m_1 < 5M_\odot$; the secondary is consistent with the masses of known Galactic NSs [173,242–244].

GW200105_162426's source corresponds to a higher-mass NSBH candidate, with $M = 11.0^{+1.5}_{-1.4}M_\odot$ and $\mathcal{M} = 3.42^{+0.08}_{-0.08}M_\odot$. The binary components have masses $m_1 = 9.1^{+1.7}_{-1.7}M_\odot$ and $m_2 = 1.91^{+0.33}_{-0.24}M_\odot$, which are consistent with a BH and a NS, respectively [8].

GW200210_092254's source has $M = 27.0^{+7.1}_{-4.3}M_\odot$ and $\mathcal{M} = 6.56^{+0.38}_{-0.40}M_\odot$, which sit within the range seen for the unambiguous-BBHs candidates discussed in Sec. V A 1. While the primary is clearly a BH with $m_1 = 24.1^{+7.5}_{-4.6}M_\odot$, its secondary has $m_2 = 2.83^{+0.47}_{-0.42}M_\odot$ with a 76% probability that $m_2 < 3M_\odot$. The secondary mass sits within the hypothesized lower mass gap between NSs and BHs [201–204]. The inferred m_2 is comparable to (i) the $3.3^{+2.8}_{-0.7}M_\odot$ (95% confidence) candidate BH in the non-interacting binary 2MASS J05215658+4359220 [245], (ii) the $3.04 \pm 0.06M_\odot$ (68% confidence) candidate BH binary companion to V723 Mon [246], although this binary has alternatively been interpreted as a stripped low-mass giant star with a subgiant companion [247], and (iii) potentially the pulsar J1748–2021B's estimated mass of $2.74 \pm 0.21M_\odot$ (68% confidence) if the assumption of purely relativistic precession (with no contributions from tidal or rotational distortion of the

companion) is accurate [248]. GW200210_092254's source is similar to GW190814's, where the component masses were inferred to be $m_1 = 23.3^{+1.4}_{-1.4} M_\odot$ and $m_2 = 2.6^{+0.1}_{-0.1} M_\odot$ [4,241]. GW200210_092254's source could either be a BBH or a NSBH system, but given the current understanding of the maximum NS mass [173,174,249–254], it is more probable that it is a BBH, similar to the case for GW190814 [241].

For GW191219_163120, we infer a source with $M = 32.3^{+2.2}_{-2.7} M_\odot$ and $\mathcal{M} = 4.31^{+0.12}_{-0.17} M_\odot$. It has $m_1 = 31.1^{+2.2}_{-2.8} M_\odot$ and $m_2 = 1.17^{+0.07}_{-0.06} M_\odot$, which would make the source a clear NSBH, assuming that the signal is astrophysical. The secondary is probably the least massive compact object among the O3b observations, and is comparable to the least massive of known NSs [173,242,255]: for example, the companion to pulsar J0453+1559 that has an estimated mass of $1.174 \pm 0.004 M_\odot$ (68% confidence) [256], although this object has also been suggested to be a white dwarf [257]; the pulsar J1802–2124 that has an estimated mass $1.24 \pm 0.11 M_\odot$ (68% confidence) [258], or the NSs in the high-mass x-ray binaries SMC X-1 and 4U 1538–522 that have inferred masses of $1.21 \pm 0.12 M_\odot$ and $1.02 \pm 0.17 M_\odot$ (68% confidence), respectively [259].

Measuring the mass distribution of NSs will illuminate the physical processes that form them. Determining the maximum NS mass provides a key insight into the properties of NS matter [250,253,254,260–264], while determining the spectrum of NS masses provides an insight into the physics of processes such as supernova explosions [209,257,265–270]. As the catalog of observations grows, it will be possible to better determine the NS mass distribution.

B. Spins

Spins leave a relatively subtle imprint on the GW signal, and so they are more difficult to measure from observations than the masses [13,152–154,170,271–273]. Typically, it is not possible to put strong constraints on individual components' spins, as the evolution of the system is primarily determined by mass-weighted combinations of the two component spins [274–278]. However, when a binary has unequal masses it may also be possible to constrain the primary spin because χ_1 dominates the spin contributions to the signal. To reflect how the two spins influence the signal, we quote results for two convenient spin parameters: the effective inspiral spin $\chi_{\rm eff}$ [99,100] and the effective precession spin χ_p [279,280].

The effective inspiral spin, as defined in Eq. (2), describes the mass-weighted projection of the component spins parallel to the orbital angular momentum, and is approximately conserved throughout the inspiral [281] while remaining important in determining evolution through the merger [236,282,283]. The effective inspiral spin influences the length of the inspiral and the transition to merger [236,275,282,284]. A nonzero $\chi_{\rm eff}$ indicates the definite presence of spins in the system, with positive values indicating that there is a net spin aligned with the orbital angular momentum, and negative values indicating that there is a net spin antialigned with the orbital angular momentum.

The effective precession spin,

$$\chi_p = \max\left\{\chi_{1,\perp}, \frac{q(4q+3)}{4+3q}\chi_{2,\perp}\right\}, \tag{4}$$

where $\chi_{i,\perp}$ is the component of spin perpendicular to the direction of the Newtonian orbital angular momentum $\hat{L}_N$, measures the mass-weighted in-plane spin component that contributes to spin precession [279,280,285,286]. With this parametrization, a value of $\chi_p = 0$ would indicate no spin precession, and a value of $\chi_p = 1$ indicates maximal precession; typically, only weak constraints are placed on χ_p, so the posterior covers a significant fraction of its prior range [3,287,288]. Since χ_p is weakly constrained, the shape of the χ_p prior often dominates the posterior. The χ_p prior tends to zero at $\chi_p = 0$ and peaks at a moderate value of χ_p that depends on the prior ranges of χ_1, χ_2, and q, and so an inferred nonzero value does not necessarily imply a measurement of precession.

As a consequence of orbital precession, χ_p changes throughout the inspiral. However, the tilt angles of a compact binary at a formally infinite separation are well defined [289]. We thus quote the tilt angles and the derived quantities ($\chi_{\rm eff}$ and χ_p) at a fiducial reference point of infinite separation. The spins are evolved to infinite separation [290] using precession-averaged evolution [289,291] with the orbital angular momentum calculated using higher-order PN expressions.

The spin orientations of a binary can provide clues to its formation channel [149,232,292–296]. Dynamically assembled binaries would have no preferred spin orientation, and therefore are expected to have an isotropic distribution of spin orientations (unless embedded in an environment like the disk of an active galactic nucleus where accretion or consecutive mergers can result in an anisotropic spin distribution [297–301]); on the other hand, binaries formed through isolated binary evolution are typically expected to have nearly aligned spins, with moderate misalignments arising due to supernova kicks [302–308]. Therefore, negative $\chi_{\rm eff}$ or large χ_p would be more common in dynamically formed binaries than those formed through isolated evolution.

Most of the candidates in O3b are consistent with $\chi_{\rm eff} = 0$. However, GW191204_171526's source has $\chi_{\rm eff} = 0.16^{-0.05}_{+0.08}$ with no posterior support at zero, while GW191103_012549, GW191126_115259, and GW191216_213338 have sources with $\chi_{\rm eff} = 0.21^{+0.16}_{-0.10}, 0.21^{+0.15}_{-0.11}$, and $0.11^{+0.13}_{-0.06}$, respectively, and negligible support for $\chi_{\rm eff} < 0$.

Other candidates with significant support for $\chi_{\rm eff} > 0$ include GW200316_215756, GW200208_222617, GW191129_134029, and GW200129_065458 with $\chi_{\rm eff} > 0$ at 98%, 95%, 91%, and 89% probability, respectively. The O3b candidates with the most significant support for $\chi_{\rm eff} < 0$ are GW191109_010717 and GW200225_060421 with $\chi_{\rm eff} < 0$ at 90% and 85% probability, respectively. As with previous catalogs, there are more systems with $\chi_{\rm eff} > 0$ than with $\chi_{\rm eff} < 0$ [3,4,116,211].

Figure 7 shows one-dimensional posterior probability distributions for $\chi_{\rm eff}$ and χ_p, and Fig. 9 shows two-dimensional posterior probability distributions for $\mathcal{M}$ and $\chi_{\rm eff}$. GW200208_222617 has a high inferred value of $\chi_{\rm eff} = 0.45^{+0.42}_{-0.46}$. This value is comparable to that inferred for GW190403_051519 ($p_{\rm astro} = 0.60$, as given in Table XV in Appendix D 7), which has $\chi_{\rm eff} = 0.68^{+0.16}_{-0.43}$ [4]. Both of these modest-significance candidates correspond to BBHs that have support for unequal masses. For example, GW190403_051519's source has $q = 0.23^{+0.57}_{-0.12}$. The O3b source with probably the lowest $\chi_{\rm eff}$ is GW191109_010717's, which has $\chi_{\rm eff} = -0.29^{+0.42}_{-0.31}$. Overall, the range of inferred $\chi_{\rm eff}$ values matches the range for previous LVK candidates [4] as well as candidates from non-LVK analyses (when adopting comparable prior assumptions) [17,19,309,310].

The in-plane spin components are less well constrained than those parallel to the orbital angular momentum. Given the constraint that spin magnitudes cannot exceed 1, a measurement of $\chi_{\rm eff}$ influences the permitted values of χ_p. This constraint means that the χ_p posterior probability distribution may appear different from its (unrestricted) prior distribution even in cases where the signal contains no measurable information on the in-plane spins [14,288]. Figure 10 shows the χ_p posterior probability distribution compared to the prior distribution after conditioning on the $\chi_{\rm eff}$ measurement for a selection of candidates [3]. These distributions would be the same if no information about the in-plane spin components had been extracted from the signal, and the selected candidates have the greatest difference between the two distributions. For many candidates, the χ_p posteriors are broad and uninformative. GW200129_065458 (the highest SNR O3b candidate) has probably the highest inferred χ_p of $0.52^{+0.41}_{-0.38}$. However, this inference is sensitive to the waveform model used, and is discussed in Sec. V E. GW191219_163120 has probably the lowest measurement of the O3b candidates, with $\chi_p \leq 0.14$ at 90% probability, which is between the measurements for GW200105_162426 [8] and GW190814 [4,241] of $\chi_p \leq 0.19$ and ≤ 0.07 at 90% probability, respectively. Since the mass ratio for this system is beyond the region of calibration for the waveforms, it is not clear how reliable this result is, and further work is needed to characterize the spin. For unequal-mass binaries, it is generally easier to observe the effects of precession (or lack thereof), enabling tighter constraints on χ_p [241,273,285,288].

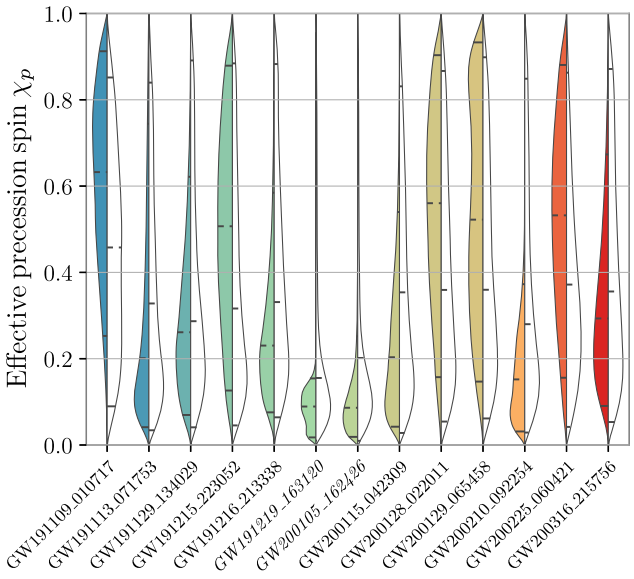

FIG. 10. Posterior (left; colored) and effective prior (right; white) probability distributions for the effective precession spin parameter χ_p of selected candidates. For each candidate, the prior distribution is conditioned on the posterior probability distribution for the effective inspiral spin $\chi_{\rm eff}$ to illustrate how measurement of this quantity is correlated with inference of χ_p. Horizontal lines mark the median and symmetric 90% interval for the distributions. The candidates selected show the greatest difference between the effective prior and posterior distributions. We highlight with italics GW200105_162426 as it has $p_{\rm astro} < 0.5$, as well as GW191219_163120 because of significant uncertainty in its $p_{\rm astro}$ and because it has significant posterior support outside of mass ratios where the waveform models are calibrated.

Figure 11 shows the posterior probability distributions for the dimensionless spin magnitude χ_i and tilt angle θ_{LS_i} for the binary components of a selection of six O3b candidates. In most cases, posteriors for the component spin magnitudes are largely uninformative, but for some of the unequal-mass binaries we may constrain χ_1 [241,278,311,312]. For GW191219_163120, GW200105_162426, and GW200210_092254, we find $\chi_1 \leq 0.15$, ≤ 0.26, and ≤ 0.38 at 90% probability, respectively. Like GW190814 [4,241], where we inferred $\chi_1 \leq 0.08$, these NSBHs or BBHs with low-mass secondaries have negligible support for maximal primary spins. Conversely, for the asymmetric BBH candidate GW200208_222617, we infer $\chi_1 \geq 0.30$ at 90% probability, with 51% probability that $\chi_1 > 0.8$. These inferred spins are not as extreme as they are for GW190403_051519's source [4]. With our default prior assumptions, only the O3a candidates GW190403_051519 [4], GW190412 [278,311], and GW190517_055101 [4] lack posterior support for a primary spin of zero.

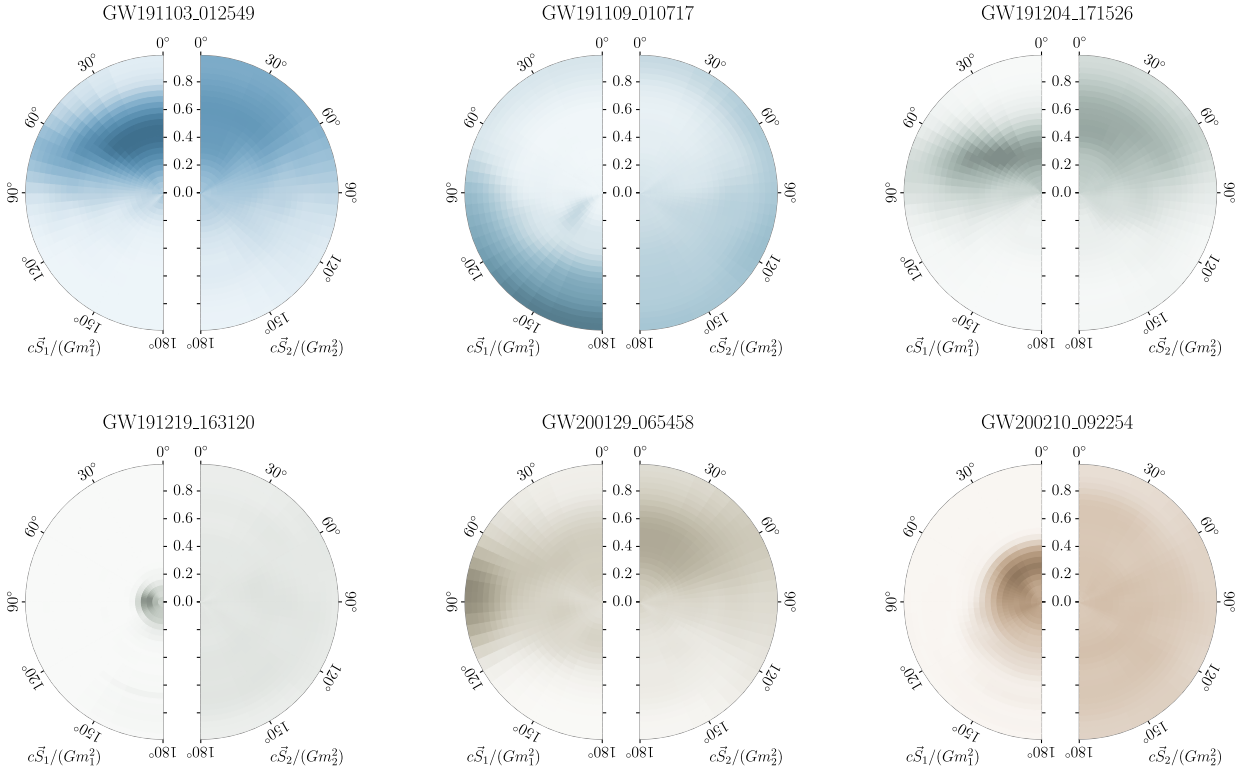

FIG. 11. Posterior probability distributions for the dimensionless component spins $\vec{\chi}_1 = c\vec{S}_1/(Gm_1^2)$ and $\vec{\chi}_2 = c\vec{S}_2/(Gm_2^2)$ relative to the orbital plane, marginalized over azimuthal angles, for candidates GW191103_012549, GW191109_010717, GW191204_171526, GW191219_163120, GW200129_065458, and GW200210_092254, ordered chronologically. BBH waveform models are used for all the results shown here. GW191103_012549 has $\chi_{\rm eff} = 0.21^{+0.16}_{-0.10}$ with negligible posterior support at zero. GW191109_010717 has $\chi_{\rm eff} < 0$ at 90% probability and $\chi_p = 0.63^{+0.28}_{-0.38}$. GW191204_171526 has $\chi_{\rm eff} = 0.16^{+0.08}_{-0.05}$ with no posterior support at zero. GW191219_163120 is a NSBH candidate with $\chi_p \leq 0.14$ at 90% probability; this candidate has significant uncertainty in its $p_{\rm astro}$ and has significant posterior support outside of mass ratios where the waveform models are calibrated. GW200129_065458 has $\chi_p = 0.52^{+0.41}_{-0.38}$. GW200210_092254 has $\chi_p \leq 0.32$ at 90% probability and mass ratio $q = 0.118^{+0.048}_{-0.041}$. In these plots, histogram bins are constructed linearly in spin magnitude and the cosine of the tilt angles such that they contain equal prior probability.

The final spin of the merger remnant χ_f is determined by conservation of angular momentum, and receives contributions from both the orbital angular momentum at merger and the component spins. For equal-mass, nonspinning BHs, the merger remnant has a spin of $\chi_f \sim 0.7$ [313–316]. As a consequence of the range of mass ratios and spins of the O3b candidates, there is a range of final spins from $\chi_f = 0.14^{+0.06}_{-0.06}$ for GW191219_163120 and $0.34^{+0.13}_{-0.08}$ for GW200210_092254 (assuming the BBH waveform models are accurate) to $0.83^{+0.14}_{-0.26}$ for GW200208_222617.

In comparison to GWTC-3 observations, spins of BHs in x-ray binaries span the full range of magnitudes, including near-maximal spins [215,317,318]. For low-mass x-ray binaries, it is possible that these spins are grown by accretion from their companion [319–321]; in contrast, for high-mass x-ray binaries there would be insufficient time for accretion to significantly change the spin [215,322,323]. The comparison between spins in x-ray binaries and coalescing BH binaries may highlight details of their formation and differences in their evolution.

Predictions for BH spin magnitudes vary, depending upon the formation channel and assumptions about stellar evolution such as stellar winds or the efficiency of stellar tides [193,230,306,324–326]. If angular momentum transport is efficient in stars, then BHs formed from stellar collapse may be born with low ($\lesssim$0.1) spins [327,328]; for binaries formed via isolated binary evolution, this may mean that the first-born BH is expected to have a low spin, although the second-born BH may have a larger spin due to tides spinning up its progenitor [329–331]. The situation may be different if progenitor stars have significant rotation rates, such as for close binary star systems, where tidal locking can lead to chemically homogeneous evolution [332–334]. In this case, predicted BH spins are typically approximately 0.3–0.5, and may extend up to the Kerr limit [232,335]. Spin could also be imparted by asymmetric supernova explosions [307]. For BBHs embedded in active galactic nuclei disks, accretion can grow spins if they are prograde with respect to the disk, while retrograde spins become smaller before flipping to become prograde,

with the rate of evolution depending upon the orientation of the orbit with respect to the disk [297,300,301]. Outside of stellar evolution, primordial BHs born in the early, radiation-dominated Universe are expected to have small ($\lesssim$0.01) spins at formation [336–338], but spins could increase through accretion [339,340]. Given the theoretical uncertainties on BH spin magnitudes, GW (and x-ray) observations may reveal details of BH formation; the distribution of spins is analyzed in a companion paper [5].

C. Tidal effects

If a binary contains at least one NS component, the GW signal from the inspiral is influenced by the deformability of NS matter. Tidal effects are quantified by the dimensionless quadrupole tidal deformability,

$$\Lambda_i = \frac{2}{3} k_{2,i} \left[\frac{c^2 R_i}{G m_i}\right]^5, \tag{5}$$

where $k_{2,i}$ is the second Love number and R_i is the component's radius [341,342]. Quasiuniversal relations [343] are used to parametrize the effects of NS spin-induced deformations in terms of Λ_i. Stiffer NS equations of state give larger values of Λ_i, which accelerates the rate of inspiral. BHs have $\Lambda_i = 0$ [344–347].

On account of their SNRs, we do not expect to be able to place a lower limit on the tidal deformability for any candidates from O3b [348–350]. Results confirm this, with no analysis showing strong support for matter effects. This is consistent with previous observations where it was not possible to determine the nature of the compact objects from the GW data alone, such as GW170817 [126,260] and GW190814 [241].

D. Localization

The distance to the source is inferred from the amplitude of the signal as the two are inversely related [131,135]. Posterior probability distributions for the luminosity distance are shown in Fig. 7. The closest source found in O3b is probably GW200105_162426, with an inferred distance of $D_L = 0.27^{+0.12}_{-0.11}$ Gpc and redshift $z = 0.06^{+0.02}_{-0.02}$. At 90% probability, GW200105_162426 has $D_L \leq 0.36$ Gpc. GW200308_173609 probably has the farthest source (including the high-distance, low-likelihood mode) at $D_L = 7.1^{+13.9}_{-4.4}$ Gpc ($D_L \geq 3.5$ Gpc at 90% probability), $z = 1.04^{+1.47}_{-0.57}$. This measurement is comparable to the probably most distant source reported in GWTC-2.1, which is for GW190403_051519 at $D_L = 8.28^{+6.72}_{-4.29}$ [3,4]. As our detectors become more sensitive, it will be possible to observe sources at greater distances.

The sky localization depends critically upon the number of observatories able to detect a signal [25,351,352]. With only a single detector observing, localizations may cover the entire sky. The most constrained localizations are achieved when all three observatories record a significant SNR. The O3b source with the best sky localization is GW200311_115853, with a 90% credible area of 35 deg^2, which was observed with all three detectors. As the detector network expands, the typical sky-localization precision will improve [25,353].

The volume localization depends upon both the distance and sky localization. The best three-dimensional localizations from O3b are for GW200202_154313 and GW200115_042309, which have 90% credible volumes of 0.0023 and 0.0063 Gpc^3, respectively. These correspond to two of the closest sources, with $D_L = 0.41^{+0.15}_{-0.16}$ and $0.29^{+0.15}_{-0.10}$ Gpc, respectively. Using the extended version of the Galaxy List for the Advanced Detector Era (GLADE+) [7,354,355], the 90% credible volume for GW200202_154313 contains approximately 1500 galaxies reported in the K band (approximately 10400 in the bJ band), where we estimate the completeness of the galaxy catalog to be 7%–59% (13%–66%). Similarly, the 90% credible volume for GW200115_042309 contains approximately 5400 galaxies in the K band (approximately 19100 in the bJ band), with estimated completeness of 19%–73% (85%–100%). As the typical distance to sources increases, so will the typical localization volume; however, improvements to detector sensitivity will mean that the localization precision for the best localized sources will improve [25,353,356].

The localization is crucial to multimessenger follow-up efforts. Previously reported candidates have been the target of dedicated follow-up observations. The details of currently reported follow-up observations are reviewed in Appendix A.

E. Waveform systematics

Our inference of the source properties is dependent on being able to accurately calculate the signal waveform given the source parameters [158,357–363]. The current generation of quasicircular BBH waveforms used here (`IMRPhenomXPHM` and `SEOBNRv4PHM`) include higher-order spherical harmonics and model spin precession. Since the waveforms include equivalent physical effects, we expect that any differences that exist are attributable to the particular modeling of the relevant physics. Additionally, `IMRPhenomXPHM` uses the stationary phase approximation to trade accuracy for faster waveform evaluation in the frequency domain, which produces less reliable descriptions of massive merger-ringdown-dominated signals. To assess the effects of waveform uncertainty on our inferences, and to identify discrepancies that require further study, we compare the results obtained with different waveforms.

The waveforms are calibrated to nonprecessing numerical relativity (NR) waveforms, and good agreement has been found between the two waveform models for nonprecessing systems [364]. However, the waveforms are not

calibrated to precessing NR waveforms and use different approximations to describe precession (discussed in Appendix E 2). The lack of accurate information about precession from NR also affects the merger and ringdown portions of the waveform, and the calculation of the quasinormal-mode frequencies. Additional issues regarding an accurate description of precessing systems arise for nearly antialigned spins, where approximations used to model spin effects can break down due to a wide opening angle of the precession cone (for more extreme mass ratios), or instabilities in the spin configuration [365]. Generally, waveforms tend to disagree in parts of the parameter space with higher spins and more extreme mass ratios [137,273,364,366], where the number of NR waveforms available for calibration are limited.

We find that for almost all the signals analyzed here, the differences between results obtained with the `IMRPhenomXPHM` and `SEOBNRv4PHM` are subdominant compared to the statistical uncertainty. As for previous observations, differences are typically small, and most noticeable for parameters like the spins [3,14,158,287]. In some cases, there are differences in the multimodality of the posterior probability distribution. Multimodality can be an indication of the complex structure of the waveform and highlight where subtle changes in the modeling may be important. Examples of candidates where there are differences between `IMRPhenomXPHM` and `SEOBNRv4PHM` are:

(i) GW191109_010717, which has significant support for negative $\chi_{\rm eff}$ and misaligned spins, where waveform differences may be expected [364,367]. There are differences in the spins and mass ratio inferred with the two waveforms. Both models show a structured, multimodal joint posterior distribution on $\chi_{\rm eff}$, q, orbital inclination θ_{JN} (the angle between the total angular momentum and the line of sight) and χ_p, although the modes are overlapping. `SEOBNRv4PHM` has a posterior probability distribution with two modes separated mostly in θ_{JN}, one face on and one face off. Both modes show similarly high values of χ_p, and both have $\chi_{\rm eff} < 0$ with high probability. `IMRPhenomXPHM`, however, finds a near-edge-on mode ($\theta_{JN} \sim \pi/2$) that prefers more equal component masses, and includes greater support for positive $\chi_{\rm eff}$. We infer $\chi_{\rm eff} = -0.31^{+0.53}_{-0.32}$ with `IMRPhenomXPHM` and $\chi_{\rm eff} = -0.28^{+0.26}_{-0.26}$ with `SEOBNRv4PHM`. When a binary is viewed edge on, any precession effects are maximally visible [271,288,360,367,368].

(ii) GW191219_163120, which has a large mass asymmetry, with the bulk of the posterior probability distribution outside the range of calibration of the waveforms. Despite this, the posteriors obtained with `SEOBNRv4PHM` and `IMRPhenomXPHM` show good agreement overall. While the waveforms produce consistent results, there are differences in the inferred inclination, with `IMRPhenomXPHM` showing less support for near edge-on orientations; total mass, with `IMRPhenomXPHM` preferring higher masses, and distance, with `IMRPhenomXPHM` having less support for larger distances. We infer $q = 0.037^{+0.004}_{-0.003}$ with `IMRPhenomXPHM` and $q = 0.038^{+0.006}_{-0.005}$ with `SEOBNRv4PHM`. Modeling of higher-order multipole moments is particularly important for inferring the properties of systems with unequal masses [275,311,368–371], and it may impact inference of parameters including the mass ratio, inclination, and distance [3,178,362,372–375].

(iii) GW200129_065458, which has a high SNR ($\rho = 26.8^{+0.2}_{-0.2}$ using `IMRPhenomXPHM`) and was detected in all three detectors. While both waveforms show approximately the same $\chi_{\rm eff}$, this candidate shows a high χ_p, as well as stronger support for unequal masses when analyzed with `IMRPhenomXPHM`, whereas with `SEOBNRv4PHM` it does not exhibit strong evidence for precession and shows more support for equal masses. We infer $\chi_p = 0.77^{+0.19}_{-0.44}$ and $q = 0.73^{+0.23}_{-0.30}$ with `IMRPhenomXPHM`, and $\chi_p = 0.36^{+0.31}_{-0.25}$ and $q = 0.901^{+0.083}_{-0.169}$ with `SEOBNRv4PHM`. Unlike GW191109_010717, the orbital plane is not viewed edge on to the line of sight, so amplitude modulations from precession of the orbital plane are likely to be less significant. However, GW200129_065458 has significant support for inclinations up to $\theta_{JN} \lesssim 1.06$, where precession and higher-order harmonic content may be important [178,271,288,360,368,371,374]. Waveform systematics become more important for higher SNR signals, where statistical uncertainties are smaller [131,361].

(iv) GW200208_222617, which has a multimodal mass posterior and low SNR. The preference for the different modes varies between waveforms. Of the two main modes, the lower-m_1-and-M mode is favored by `SEOBNRv4PHM`, while the higher-m_1-and-M mode is favored by `IMRPhenomXPHM`. Additionally, the `IMRPhenomXPHM` analysis finds an additional minor mode with $M \sim 175M_\odot$ (visible in Fig. 8 as a protuberance of the 90% contour). The `IMRPhenomXPHM` analysis also shows a greater preference for higher $\chi_{\rm eff}$: We infer $\chi_{\rm eff} = 0.62^{+0.26}_{-0.59}$ with `IMRPhenomXPHM`, and $\chi_{\rm eff} = 0.34^{+0.45}_{-0.38}$ with `SEOBNRv4PHM`.

Future analyses with enhanced waveforms will update our understanding of the source parameters for these candidates.

VI. WAVEFORM CONSISTENCY TESTS

Waveforms can be reconstructed from the data using two complementary approaches, either using parameter-estimation methods with templates [131,376]

or using minimal modeling [60,377,378]. While the parameter-estimation pipelines directly estimate the match between CBC model waveforms and data, BayesWave (Appendix C) and cWB (Appendix D 5) reconstruct waveforms making only minimal assumptions on the signal shape [60,377,378]. The waveform reconstruction performed by these pipelines uses time-frequency wavelets to identify coherent features in the data, filtering out incoherent noise from the detectors. Although there are similarities between the methods used by cWB [60,109] and BayesWave [377,379], their waveform reconstructions differ in some details. In particular, the point estimate returned by cWB is the constrained maximum-likelihood reconstruction, while for BayesWave we use the median of the time-domain waveform reconstructions from BayesWave's posterior probability distribution. Examples of both types of reconstruction were reported in GWTC-2 [3].

Starting from minimally modeled waveform reconstructions we can try to detect unexpected behavior by comparing these reconstructions with the CBC waveforms from parameter estimation [3,14,109,380,381]. To test the consistency (or lack thereof) between minimally modeled reconstructions and the CBC waveforms, we perform sets of dedicated injections of CBC waveform samples from the posterior distributions for the source parameters. In these simulations, the random waveforms are added to background data around the time of the candidates, and the simulated signal is analyzed by the minimally modeled pipelines. We call these off-source injected waveforms, while the reconstructed waveform of the candidate is our on-source result.

Here, as in GWTC-2 [3], we measure the waveform match (or overlap), defined by

$$\mathcal{O}(h_1, h_2) = \frac{\langle h_1 | h_2 \rangle}{\sqrt{\langle h_1 | h_1 \rangle \langle h_2 | h_2 \rangle}}, \tag{6}$$

where h_1 and h_2 are two waveforms, $\langle \cdot | \cdot \rangle$ represents the noise-weighted inner product [382], and the match is $-1 \leq \mathcal{O}(h_1, h_2) \leq 1$. The theoretical definition of match in Eq. (6) does not depend on the amplitude of each signal [3]. However, the addition of noise typically reduces the match value, and the calculated match does depend both on the SNR and, in more detail, on the distribution of signal power in time and frequency. A value of 1 indicates a perfect coincidence between waveforms, while a value close to 0 indicates that the correlation between waveforms is nil. A theoretically possible value of -1 would indicate an improbable perfect anticoincidence. The match is larger for signals corresponding to high-mass systems

TABLE V. List of candidates tested by BayesWave and cWB for consistency with the waveform templates used in the inference of source parameters. We quote the on-source match calculated using the waveform reconstructed for the candidate, and the median and 90% symmetric interval for off-source matches calculated for simulated signals with source parameters consistent with those inferred for the candidate signal. The values reported in the table correspond to those in Fig. 12. Three center dots $(\cdots)$ correspond to candidates not included in an analysis.

	BayesWave		cWB	
Candidate	On-source match	Off-source match	On-source match	Off-source match
GW191109_010717	0.93	$0.94^{+0.04}_{-0.10}$	0.90	$0.90^{+0.04}_{-0.05}$
GW191127_050227	···	···	0.86	$0.83^{+0.07}_{-0.10}$
GW191129_134029	0.57	$0.35^{+0.26}_{-0.28}$	···	···
GW191204_171526	0.82	$0.68^{+0.14}_{-0.30}$	0.91	$0.88^{+0.04}_{-0.07}$
GW191215_223052	0.79	$0.65^{+0.17}_{-0.49}$	0.86	$0.80^{+0.05}_{-0.10}$
GW191216_213338	0.73	$0.74^{+0.09}_{-0.42}$	···	···
GW191222_033537	0.90	$0.88^{+0.06}_{-0.16}$	0.86	$0.81^{+0.07}_{-0.13}$
GW191230_180458	···	···	0.85	$0.78^{+0.08}_{-0.11}$
GW200128_022011	···	···	0.87	$0.89^{+0.04}_{-0.05}$
GW200129_065458	0.96	$0.96^{+0.02}_{-0.06}$	0.80	$0.88^{+0.05}_{-0.09}$
GW200208_130117	0.73	$0.74^{+0.14}_{-0.50}$	0.78	$0.79^{+0.07}_{-0.13}$
GW200209_085452	···	···	0.82	$0.83^{+0.08}_{-0.09}$
GW200216_220804	···	···	0.73	$0.87^{+0.05}_{-0.13}$
GW200219_094415	0.81	$0.74^{+0.14}_{-0.35}$	0.81	$0.85^{+0.06}_{-0.08}$
GW200224_222234	0.96	$0.93^{+0.03}_{-0.09}$	0.83	$0.84^{+0.06}_{-0.10}$
GW200225_060421	0.85	$0.73^{+0.12}_{-0.38}$	0.77	$0.85^{+0.07}_{-0.13}$
GW200311_115853	0.94	$0.90^{+0.06}_{-0.43}$	0.93	$0.92^{+0.03}_{-0.04}$

[380,383–385]. The distribution of match values of the off-source injections defines a null distribution for each candidate; this distribution can be used both to estimate the uncertainty of the observed on-source match value and to obtain a p-value from the on-source match. For each candidate, the match is computed off source between injected waveforms and their reconstructions, while on source it is computed between the point estimate of the actual candidate and the maximum-likelihood estimate provided by source-parameter estimation.

The sets of candidates chosen for the BayesWave and cWB consistency tests are different. For the BayesWave analysis we consider candidates that are sufficiently loud and short for BayesWave to produce valid signal reconstructions. The candidates considered by cWB are those detected by the search analysis (reported in Table I), plus five additional candidates that were identified by other search analyses (also reported in Table I). These additional five candidates were reconstructed by the initial stages of the cWB search analysis, but did not pass the cWB postproduction cuts that are used to identify low-FAR candidates (described in Appendix D 5). Both lists are reported in Table V.

The waveform consistency tests are carried out with respect to the results calculated by the Bayesian inference library Bilby [144,146] using the `IMRPhenomXPHM` waveform [136] (details are presented in Appendix E). Figure 12 shows the on-source match values versus the median off-source match values (together with the 90% intervals). The match values move to lower values for smaller SNR, but the on-source value is still expected to be close to the median of the off-source distribution (blue dashed line in the figure) if the null hypothesis (that the minimally modeled reconstruction does not deviate significantly from the template-based reconstruction) holds.

Figure 13 shows the p-values sorted in increasing order [109,380]. When the null hypothesis holds, the sorted p-values are expected to remain close to the median value (orange dashed line); the 90% interval that surrounds the median line shows the size of the fluctuations that we expect to observe. Any significant deviations below the plot diagonal, corresponding to low p-values, point to a set of candidates that show potential disagreement with the waveform templates. However, the significance of several simultaneous deviations cannot be directly assessed from the 90% interval, which is calculated for single values [386]. Since the p-values are sorted in increasing order, the sorting induces a correlation between successive values, and this means that there may be a whole subset of points outside the interval. All of the 15 cWB p-values are within the 90% interval. This is not the case for BayesWave, where it is important to consider the finite-size effect due to the limited number of off-source samples in the match distribution. The posterior probability distribution for the p-value estimate due to the finite-size effect is $\mathrm{Beta}(n+1, N-n+1)$, where N is the total number of samples, and n is the number of samples with a match value less than the on-source match [6]. In addition to the 90% interval associated with the statistical distribution of p-values for the null hypothesis, the p-value plots in Fig. 13 also display the 90% interval from the finite-size effect: We see that after including this effect, there are four out of 12 incompatible p-values (where the 90% intervals

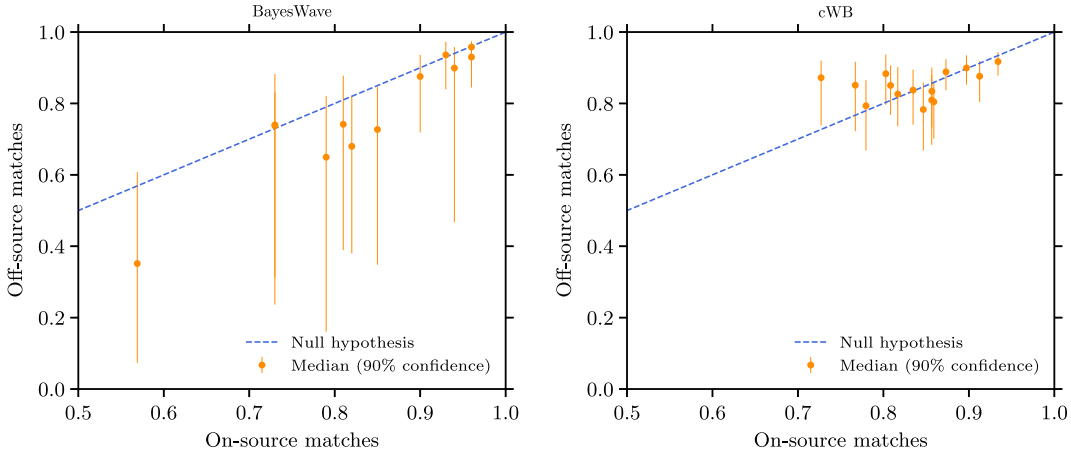

FIG. 12. Off-source versus on-source match values for the candidates in O3b. The left and right panels show the results of the BayesWave and cWB analyses, respectively. The on-source match is estimated comparing the inferred maximum-likelihood CBC waveform with point estimates from the minimally modeled waveform reconstructions. The off-source match is the median value of the match distribution estimated from off-source injection of sample waveforms from the template-based posterior distribution. The error bars in both panels are given by the symmetric (equal-tailed) 90% confidence interval, and they mark the distance from the null hypothesis (blue dashed line). The different sizes of the error bars in the two panels is due to the different numbers of off-source injections in the BayesWave and cWB analyses.

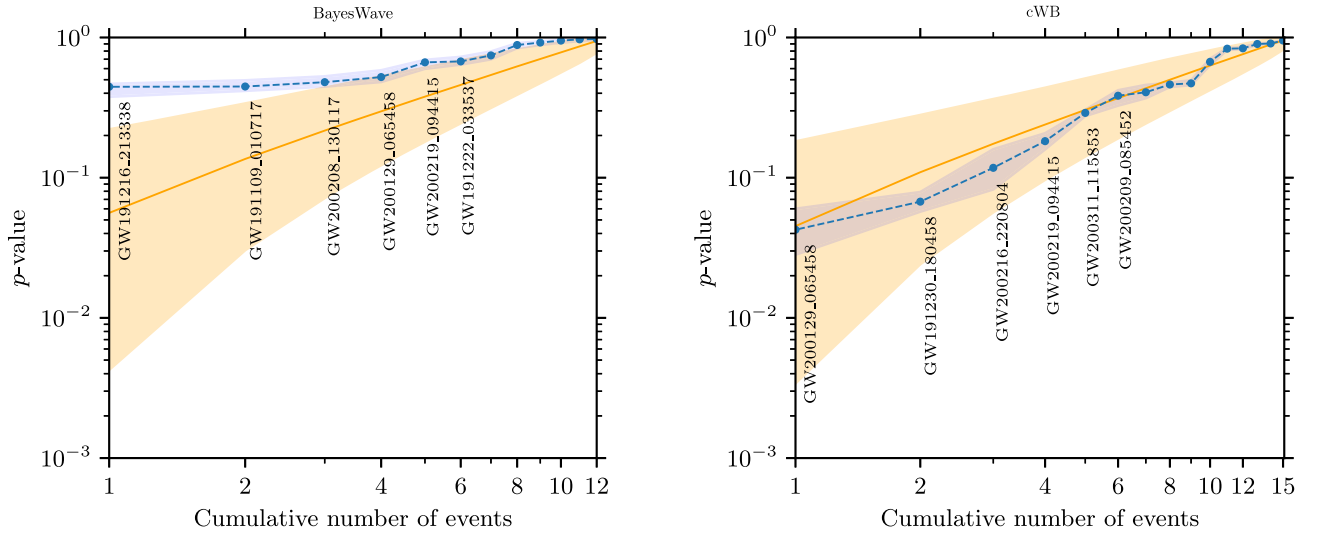

FIG. 13. Distribution of p-values for the O3b candidates reconstructed by the minimally modeled pipelines. The left and right panels report the BayesWave and cWB results, respectively. The p-values are sorted in increasing order and graphed against the order number (blue dashed line). Each p-value is estimated from the observed on-source match value and the related off-source distribution of the match values from off-source injections. The shadowed orange band is the symmetric 90% interval about the median, represented by the orange solid line. The blue band represents the symmetric 90% interval associated with the finite number of off-source injections.

do not overlap). Finding four incompatible p-values is not an unlikely event, it has approximately 4.1% probability of being due to chance. We conclude that both the match-match and the p-value plots indicate that there is no significant inconsistency between the minimally modeled waveform reconstruction and the results of the parameter-estimation analysis. Further checks of the consistency of the signals, focused on the predictions from general relativity, are given in a companion paper [6].

VII. CONCLUSION

We present the latest LVK catalog of GWs, which contains a total of 90 CBC candidate signals with an estimated probability of astrophysical origin $p_{\rm astro} > 0.5$. GWTC-3 builds upon past catalogs of GW candidates from O1 [13], O2 [14], and O3a [3,4], adding an additional 35 candidates from O3b with $p_{\rm astro} > 0.5$. These include the NSBH candidates GW191219_163120 and GW200115_042309, as well as the candidate GW200210_092254 that could potentially be either from a NSBH or a BBH. We additionally provide a list of candidates with $p_{\rm astro} < 0.5$ meeting a FAR threshold of $<2.0\ \mathrm{day}^{-1}$. This includes GW200105_162426, which is estimated to have $p_{\rm astro} = 0.36$ but is a clear outlier from our background noise distribution, and is inferred to have a NSBH source [8]. While we expect approximately four to six of the candidates with $p_{\rm astro} > 0.5$ to be false alarms, we also expect approximately seven candidates with $p_{\rm astro} < 0.5$ to be astrophysical GW signals. GW observations of CBCs provide new insight into diverse areas of physics ranging from binary stellar evolution to gravitation. Further analysis and interpretation of the GWTC-3 candidates is conducted in the companion papers [5–7]. As the population of GW observations grows, it will be possible to make increasingly detailed measurements of compact-object physics.

The growing catalog of GW sources has revealed a diversity of potential CBC sources. Among the candidates are a few with posterior support for high spins ($\chi_i \gtrsim 0.8$) and large mass asymmetries ($q \lesssim 0.1$). Creating waveform models in these regimes is challenging, as the need to maintain accuracy necessitates more complete prescriptions of the underlying physics, including effects such as spin-induced precession [387,388] plus higher-order multipole moments [178,357,362,374]. This task is further complicated by the lack of extensive NR waveform catalogs covering these regions of parameter space [389–392]. As sensitivity improves, waveform uncertainty may be a significant source of systematic uncertainty [360,361]. Therefore, to ensure reliable interpretation of GW observations in the future, it is imperative to develop improved waveform models that cover a wider range of source properties, and include potentially important additional physics such as orbital eccentricity [393–398].

Data products associated with GWTC-3 results are available through GWOSC [33] in addition to the full O3b detector strain data [399,400]. Release of previous observing runs' strain data [400,401] has enabled multiple independent analyses of LIGO and Virgo data, including identification of additional detection candidates [15–20,104,105,210,402–404]. Therefore, we anticipate that further discoveries may come from O3b data.

O3 saw the Advanced LIGO and Advanced Virgo detectors reach their greatest sensitivity to date, enabling

an unprecedented rate of discovery. Coupled to the longer duration of O3 compared to previous observing runs, this sensitivity has enabled the number of GW detections from O3 to significantly exceed that from O1 and O2. The Advanced LIGO and Advanced Virgo detectors are currently offline undergoing commissioning to further enhance their performance for O4. O4 will also see the joint operation of the KAGRA detector [405]. KAGRA successfully completed a joint observing run with GEO 600 following the end of O3 for Advanced LIGO and Advanced Virgo [406], and O4 will be the first opportunity for observations from the LIGO-Virgo-KAGRA detector network. The enhanced O4 global detector network will further increase the prospects for GW and multimessenger discoveries [25].

While the 90 probable GW candidates of GWTC-3 all correspond to CBC sources, we anticipate that there are other GW signals waiting to be found [407]. These could include new types of transient signal, such as from supernovae [408], cosmic strings [30], or previously unidentified sources [31,32]. Additionally, we may find long-lived signals such as continuous waves from rotating NSs [409–414] or stochastic backgrounds [415,416]. As detector sensitivity increases and we observe for longer, we expect more of the GW universe to reveal itself.

ACKNOWLEDGMENTS

Calibration of the LIGO strain data was performed with GstLAL-based calibration software pipeline [45]. Calibration of the Virgo strain data is performed with C-based software [53]. Data-quality products and event-validation results were computed using the DMT [417], DQR [76], DQSEGDB [418], GWDETCHAR [419], HVETO [420], iDQ [421], Omicron [65] and PYTHONVIRGOTOOLS [422] software packages and contributing software tools. Analyses in this catalog relied upon the LALSuite software library [423]. The detection of the signals and subsequent significance evaluations in this catalog were performed with the GstLAL-based inspiral software pipeline [78–81], with the MBTA pipeline [82,83], and with the PyCBC [86–88] and the cWB [60,89,90] packages. Estimates of the noise spectra and glitch models were obtained using BayesWave [377,379,383]. Noise subtraction for one candidate was also performed with gwsubtract [44]. Source-parameter estimation was performed with the Bilby and Parallel Bilby libraries [144–146] using the Dynesty nested sampling package [424], and the RIFT library [147–149], with the LALInference [376] libraries used for initial analyses. PESUMMARY was used to postprocess and collate parameter-estimation results [425]. The various stages of the parameter-estimation analysis were managed with the Asimov library [426]. Plots were prepared with MATPLOTLIB [427], SEABORN [428] and GWPy [429]. NumPy [430] and SciPy [431] were used in the preparation of the manuscript. This material is based upon work supported by NSF's LIGO Laboratory which is a major facility fully funded by the National Science Foundation. The authors also gratefully acknowledge the support of the Science and Technology Facilities Council (STFC) of the United Kingdom, the Max-Planck-Society, and the State of Niedersachsen/Germany for support of the construction of Advanced LIGO and construction and operation of the GEO 600 detector. Additional support for Advanced LIGO was provided by the Australian Research Council. The authors gratefully acknowledge the Italian Istituto Nazionale di Fisica Nucleare (INFN), the French Centre National de la Recherche Scientifique (CNRS), and the Netherlands Organization for Scientific Research, for the construction and operation of the Virgo detector and the creation and support of the EGO consortium. The authors also gratefully acknowledge research support from these agencies as well as by the Council of Scientific and Industrial Research of India, the Department of Science and Technology, India, the Science & Engineering Research Board, India, the Ministry of Human Resource Development, India, the Spanish Agencia Estatal de Investigación, the Vicepresidència i Conselleria d'Innovació, Recerca i Turisme, and the Conselleria d'Educació i Universitat del Govern de les Illes Balears, the Conselleria d'Innovació, Universitats, Ciència i Societat Digital de la Generalitat Valenciana, and the CERCA Programme Generalitat de Catalunya, Spain, the National Science Centre of Poland and the Foundation for Polish Science, the Swiss National Science Foundation, the Russian Foundation for Basic Research, the Russian Science Foundation, the European Commission, the European Regional Development Funds, the Royal Society, the Scottish Funding Council, the Scottish Universities Physics Alliance, the Hungarian Scientific Research Fund, the French Lyon Institute of Origins, the Belgian Fonds de la Recherche Scientifique, Actions de Recherche Concertées and Fonds Wetenschappelijk Onderzoek—Vlaanderen, Belgium, the Paris Île-de-France Region, the National Research, Development and Innovation Office Hungary, the National Research Foundation of Korea, the Natural Science and Engineering Research Council Canada, Canadian Foundation for Innovation, the Brazilian Ministry of Science, Technology, and Innovations, the International Center for Theoretical Physics South American Institute for Fundamental Research, the Research Grants Council of Hong Kong, the National Natural Science Foundation of China, the Leverhulme Trust, the Research Corporation, the Ministry of Science and Technology, Taiwan, the United States Department of Energy, and the Kavli Foundation. The authors gratefully acknowledge the support of the NSF, STFC, INFN, and CNRS for provision of computational resources. Computing was performed on the OzSTAR Australian national facility at Swinburne University of Technology, which receives funding in part from the Astronomy National Collaborative Research Infrastructure Strategy allocation

provided by the Australian Government. We thankfully acknowledge the computer resources at MareNostrum and the technical support provided by Barcelona Supercomputing Center (Grant No. RES-AECT-2021-2-0021). This work was supported by MEXT, JSPS Leading-edge Research Infrastructure Program, JSPS Grant-in-Aid for Specially Promoted Research, Grant No. 26000005, JSPS Grant-in-Aid for Scientific Research on Innovative Areas 2905: Grants No, JP17H06358, No. JP17H06361, and No. JP17H06364, JSPS Core-to-Core Program A. Advanced Research Networks, JSPS Grant-in-Aid for Scientific Research (S) Grant No. 17H06133, the joint research program of the Institute for Cosmic Ray Research, University of Tokyo, National Research Foundation and Computing Infrastructure Project of KISTI-GSDC in Korea, Academia Sinica, AS Grid Center and the Ministry of Science and Technology in Taiwan under grants including Grant No. AS-CDA-105-M06, Advanced Technology Center of NAOJ, and Mechanical Engineering Center of KEK. We thank the anonymous journal referees for helpful comments.

APPENDIX A: LOW-LATENCY ALERT SYSTEM AND MULTIMESSENGER FOLLOW-UP

Public alerts are issued for GW candidates identified by low-latency searches of the data. These candidates are cataloged in the Gravitational Candidate Event Database (GraceDB). Each entry into GraceDB is known as an event, and a collection of these within a specific time window is referred to as a superevent. The time window for CBC events is variable based on the spread of events, with a typical value of 1-s symmetric around the merger time. The duration of the time window for cWB is variable and is reported by the search pipeline for each event. One candidate event belonging to the superevent is identified as the preferred event, and its attributes (time, localization, significance, classification, and properties) [115,129,432] are inherited by the superevent. The HasRemnant property indicator is related to the probability of having an electromagnetic counterpart [432], and the p_{astro} classifier assigns a source-category-based astrophysical probability under the assumption that astrophysical and terrestrial triggers occur as independent Poisson processes [112,115]. The name of a superevent is its uniquely assigned identification in GraceDB consisting of three parts: the prefix S (for superevent), the six-digit UTC date of the event (YYMMDD), and a lowercase alphabetic suffix.

During O3, CBC superevents that passed a FAR threshold of one per two months and generic transient (Burst) superevents that passed a FAR threshold of one per year were distributed as public alerts. The individual FAR thresholds of each pipeline are corrected by a trials factor to account for the data being analyzed by multiple pipelines. Generally, multiple pipelines identify the candidate GW events distributed as public alerts.

When a preferred event candidate passes the public-alert threshold, a preliminary alert is queued, while new event candidates are still accepted to be added to the superevent. After the preliminary alert reception by the GCN broker, the preferred event is revised and a second preliminary Notice is issued, even if the preferred event candidate remains unchanged. The alerts are processed by the GWCelery distributed task queue software [11,433], which organizes basic data-quality checks, groups events from online searches, and initiates localization and inference of source properties.

As in O2 [434], human vetting of the superevents is a critical part of the online program, and is completed once the superevent passed the public-alert threshold. The rapid-response team consists of commissioning, computing, and calibration experts from each of the detector sites, search-pipeline experts, detector-characterization experts, and follow-up advocates in charge of the delivery of the initial GCN Notice and Circular. A data-quality report is also initiated by GWCelery, and consists of a semiautomated detector-characterization and data-quality investigation. It provides a variety of metrics based on auxiliary instrumental and environmental sensors to help the rapid-response team make a decision whether to confirm or retract a candidate. The preliminary alerts were typically issued within a few minutes of data collection, for which latency due to data transfer between sites and search investigation are largely dominated by the GWCelery task. The human vetting and delivery of initial alerts had a median duration of approximately 30 min.

There were 40 public alerts sent out via GCN during O3a and 39 during O3b. Of these, 33 from O3a and 23 from O3b were not retracted; the remaining were retracted on timescales from minutes to days. The majority of the retracted public alerts in O3b correspond to candidates with SNR $\rho > 5$ in only one detector. The online search pipelines collect background in real time, leaving them susceptible to new noise sources, and single-detector candidates are especially impacted by uncertainties in the background noise distribution since they cannot rely on coincidence to establish significance. Among the remaining O3b alerts, 22 involve CBC candidates, and one (S200114f) is a Burst candidate, as discussed in Sec. IV D 1. The unretracted O3a alerts are publicly distributed in 7.3^{+56}_{-2} min, and the O3b alerts in 5.8^{+377}_{-3} min (median and 90% symmetric interval). One O3b candidate, S200303ba, is retracted but never has a preliminary Notice sent out due to problems connecting to the GCN broker. The GW candidate alerts generated 1513 Circulars during O3 (44% of 3463 GCN Circulars in the same period), with 967 and 546 Circulars (64% and 36%) sent during O3a and O3b, respectively.

Follow-up observations were made by teams across the astronomical community, culminating in GCN Circulars and papers. The searches for multimessenger counterparts

TABLE VI. Public alerts and follow-up investigations of O3a GW candidates. The columns show the superevent identification (SID), the GW candidate name if in offline results [3,4], the GCN Circular, and references for follow-up publications. Candidates retracted following rapid event-validation checks are marked in italics. Candidates without superevent identifications were found only in the offline searches.

SID	Event	GCN	Follow-up publications
S190408an	GW190408_181802	[436]	[437–457]
S190412m	GW190412	[458]	[437–451,453,455–457,459–461]
	GW190413_052954		[437–439,441,446,448,453,457,459]
	GW190413_134308		[437–439,441,446,448,453,457,459]
S190421ar	GW190421_213856	[462]	[437–449,451,453,455–457,459]
	GW190424_180648		[437,441,446,448,453,457,459]
S190425z	GW190425	[463]	[437–449,451–453,455–457,459–461,464–472]
S190426c	GW190426_152155	[473]	[437,439–449,451–453,455–457,459–461,465–470,474–477]
S190503bf	GW190503_185404	[478]	[437–444,446,448–451,453,455,457,459]
S190510g		[479]	[440,443,444,447,449,451,455,456,460,461,466,467,474,480,481]
S190512at	GW190512_180714	[482]	[437–441,443,444,446–449,451,453,455,457,459,483–485]
S190513bm	GW190513_205428	[486]	[437–441,443–449,451,453,455,457,459]
	GW190514_065416		[437–439,441,446,448,453,457,459]
S190517h	GW190517_055101	[487]	[437–444,446–449,451,453,455,457,459]
S190518bb		[488]	
S190519bj	GW190519_153544	[489]	[437–439,441–443,446,448,451,453,457,459]
S190521g	GW190521	[490]	[437–449,451,453–455,457,459,491,492]
S190521r	GW190521_074359	[493]	[437–449,451,453,455–457,459]
S190524q		[494]	
	GW190527_092055		[437–439,441,446,448,453,457,459]
S190602aq	GW190602_175927	[495]	[437–444,446,448,449,451,453,455,457,459]
	GW190620_030421		[437–439,441,446,448,453,457,459]
S190630ag	GW190630_185205	[496]	[437–439,441–443,446,448,451,453,457,459]
S190701ah	GW190701_203306	[497]	[437–440,442–444,446,448,449,451,453,455,457,459]
S190706ai	GW190706_222641	[498]	[437–440,442–449,451,453,455,457,459]
S190707q	GW190707_093326	[499]	[437–440,442–444,446–449,451,453,455,457,459]
	GW190708_232457		[437–439,446,448,453,457,459]
S190718y		[500]	[440,443,444,447,449,451,455,460,461]
	GW190719_215514		[437–439,446,448,453,457,459]
S190720a	GW190720_000836	[501]	[437–440,443,444,446–449,451,453,455–457,459]
S190727h	GW190727_060333	[502]	[437–440,443,444,446–449,451,453,455,457,459]
S190728q	GW190728_064510	[503]	[437–440,443,444,446–449,451,453,455–457,460,483,484,504]
	GW190731_140936		[437–439,446,448,453,457,459]
	GW190803_022701		[437–439,446,448,453,457,459]
S190808ae		[505]	[460]
S190814bv	GW190814	[506]	[438–440,443–448,451,453,455,456,459–461,470,507–518]
S190816i		[519]	
S190822c		[520]	[460,461]
S190828j	GW190828_063405	[521]	[437–440,443–448,451,453,455,457,459]
S190828l	GW190828_065509	[522]	[437–440,443,444,446–448,451,453,455,457,459]
S190829u		[523]	
S190901ap		[524]	[440,443,444,447,451,454–456,466,468,470,510]

(Table continued)

TABLE VI. *(Continued)*

SID	Event	GCN	Follow-up publications
	GW190909_114149		[437,446,448,453,459]
S190910d		[525]	[440,443,444,447,451,455,457,468,470]
S190910h		[526]	[440,443,444,451,455,457,466,510]
	GW190910_112807		[437,439,446,453]
S190915ak	GW190915_235702	[527]	[437,440,443–448,451,453,455,457,459]
S190923y		[528]	[440,443,444,447,451,454–456,468,470]
S190924h	GW190924_021846	[529]	[437–440,443,444,446–448,451,453,455,459]
S190928c		[530]	
	GW190929_012149		[437–439,446,457,459]
S190930s	GW190930_133541	[531]	[437–440,443–448,451,453,455,456,459]
S190930t		[532]	[440,443,444,447,451,453–456,460,470]

employed the same variety of observing strategies used for previous observing runs [434], including archival analysis, prompt searches with all-sky instruments, wide-field tiled searches, targeted searches of potential host galaxies, and deep follow-up of individual sources. The follow-up effort mobilized a total of about 100 ground- and space-based instruments such as neutrino observatories, very-high-energy gamma-ray observatories, space-based gamma-ray and x-ray instruments, visible and infrared telescopes, and radio telescopes. The latency for follow-up observations, analyses, public reporting of results, and the process efficiency varied across the collaborations and the multi-messenger probe involved. Additionally, the public alerts enabled amateur astronomers to join professional astronomers in the search for electromagnetic counterparts [435]. Summaries of the O3a and O3b candidates with public alerts and follow-up investigations are reported in Tables VI and VII, respectively.

TABLE VII. Public alerts and follow-up investigations of O3b GW candidates. The columns show the superevent identification (SID), the GW candidate name if in the offline results (including GW200105_162426), the GCN Circular, and references for follow-up publications. Candidates retracted following rapid event-validation checks are marked in italics. Candidates without superevent identifications were found only in the offline searches.

SID	Event	GCN	Follow-up publications
S191105e	GW191105_143521	[533]	[435,437–440,443,445,448,451,453,455,456,459]
S191109d	GW191109_010717	[534]	[435,437–440,443,445,448,451,453,455,459]
S191110af		[535]	[460,461]
S191110x		[536]	
S191117j		[537]	
S191120aj		[538]	
S191120at		[539]	
S191124be		[540]	
S191129u	GW191129_134029	[541]	[435,437–440,443,448,451,453,455,459]
S191204r	GW191204_171526	[542]	[435,437–440,443,445,448,451,453,455,459]
S191205ah		[543]	[435,440,443,445,451,454,456,468,470]
S191212q		[544]	[437]
S191213g		[545]	[435,437,440,443,451,454,455,460,461,468,470,476]
S191213ai		[546]	
S191215w	GW191215_223052	[547]	[435,438–440,443,445,448,451,453,455,459]
S191216ap	GW191216_213338	[548]	[435,437–440,443,445,448,451,453,455,456,459–461,504,549]
S191220af		[550]	[466]
S191222n	GW191222_033537	[551]	[435,437,438,440,443,448,451,453,455,459]

(Table continued)

TABLE VII. *(Continued)*

SID	Event	GCN	Follow-up publications
S191225aq		[552]	
S200105ae	GW200105_162426	[553]	[435,437–440,443,448,451,454,455,457,459,470,484,554]
S200106au		[555]	
S200106av		[555]	
S200108v		[556]	
S200112r	GW200112_155838	[557]	[435,437–440,443,448,451,453,455,459]
S200114f		[558]	[440,443,445,451,454–456,460,461]
S200115j	GW200115_042309	[559]	[435,437–440,443,445,448,451,453–455,457,459–461,468,470,484,554,560]
S200116ah		[561]	
S200128d	GW200128_022011	[562]	[435,437–440,443,448,451,453,455,459]
S200129m	GW200129_065458	[563]	[435,437–440,443,448,451,453,455,459]
S200208q	GW200208_130117	[564]	[435,437–440,443,448,451,453,455,459]
S200213t		[565]	[435,437,440,443,445,451,455,456,460,461,468,470,476,504]
S200219ac	GW200219_094415	[566]	[435,437–440,443,445,448,451,453,455,456,459,567]
S200224ca	GW200224_222234	[568]	[435,437–440,443,445,448,451,453–456,459–461,483,569–571]
S200225q	GW200225_060421	[572]	[435,437–440,443,445,448,451,453,455,456,459–461]
S200302c	GW200302_015811	[573]	[435,437–440,443,448,451,453,455,459,574]
S200303ba		[575]	
S200308e		[576]	[439]
S200311bg	GW200311_115853	[577]	[435,437–440,443,448,451,453,455,459]
S200316bj	GW200316_215756	[578]	[435,437–440,443,445,448,451,453–455]

The two alerts with the largest number of GCN Circulars distributed during O3a are GW190814 (S190814bv), whose source is a potential NSBH or low-mass BBH coalescence [241,507–509,511,514,515,517,518] and the BNS GW190425 (S190425z) [159,469,510]. A potential association between GW190425 and the fast radio burst FRB 20190425A [579] occurring 2.5 h after the merger, has been suggested [580], but a late-time optical and radio search 2.5-yr postburst is negative [471]. S191213g, the first O3b BNS candidate, has the largest number of GCN Circulars during O3b, a total of 53 [545] (but it is only in fifth position considering the whole of O3). As discussed in Sec. IV D, S191213g was not identified as a significant candidate in the offline search results. The O3 candidates are predominantly BBHs, where counterparts are not typically expected unless the system has surrounding gas [581–586].

The neutrino follow-up involved searches of events with energies ranging from approximately 1 MeV to approximately 1 PeV. No confirmed neutrino counterpart has been found for any GW candidate [437–442,449,457,459,587].

The gamma- and x-ray observations involved energies extending up to approximately 1 TeV. The majority of high-energy searches report no candidates [443,461,472,483,484,492,504,518,569,588].

The optical and near-infrared teams focused mainly on the non-BBH systems or well-localized and nearby candidates. Often, multiple optical telescopes worked in synergy for the identification and characterization of counterparts [435,447,456,470,574]. Several surveys performed systematic prompt follow-up searches for counterparts for a large number of candidates [445,448,450–454,466,474]. No confirmed prompt optical or infrared counterpart has been detected for O3 candidates.

The follow-up in the radio domain was mostly focused on the characterization of specific candidate counterparts, either neutrino, x-ray, or optical candidates [464,512,549]. No confirmed radio counterparts have been reported, with the possible exception of the fast radio burst associated with GW190425 [580].

Nondetection of electromagnetic counterparts in follow-up searches for candidates where at least one component could be a NS can potentially set constraints on the ejected matter; however, current observations cannot provide strong constraints [467,589]. It has been suggested that due to their faintness and fast evolution, searches by optical surveys for kilonovas within a distance up to 200 Mpc require early observations down to magnitude 21 [590]. Future counterpart detections as soon as the next observing run are likely to place strong, multimessenger constraints on the equation of state of NSs, and the Hubble constant [591–595].

Additional specific counterpart searches have been performed after alerts, based on properties of the GW

candidates and using all-sky, multiwavelength data. As an illustration, GW190521, a signal from a high-mass BBH [4,184], generated interest due to the possible association with an observed flare of the active galactic nucleus AGN J124942.3+344929 [491]. This association, while still uncertain [19,596–598], highlights the potential discoveries that could be made by searching for counterparts to BBH coalescences, as well as the scope for detections of counterparts in archival searches.

APPENDIX B: OBSERVATORY EVOLUTION

From the start of the advanced-detector era in O1 through O3b, the network of GW observatories has undergone a variety of commissioning activities to improve performance [25]. The configurations of the detectors were different in O1 [13], O2 [14,304], and O3 [38,64]. O2 marked the first operation of the three-detector LIGO-Virgo network, and Fig. 14 shows the O2 and O3b sensitivities for all interferometers to illustrate the evolution in performance. Key parameters describing the LIGO detectors and Virgo are reported in Table VIII, specifically: input laser power (estimated at the power recycling mirror after exiting the input mode cleaner); power recycling gain (the ratio of stored power in the power recycling cavity to the input laser power, which depends on the reflectivities of the test masses and power recycling mirror, as well as the losses in the arms and the power recycling cavity [599]); the presence of signal recycling; adoption of squeezed light, and suspension type. The main upgrade from run to run for all interferometers was the increase in the input laser power, which is instrumental in reducing shot noise. Signal recycling mirrors [600] are presently installed only in the LIGO interferometers [1]. While in Hanford and Livingston, monolithic test-mass suspensions have been operating since O1, they were installed in Virgo only for O3, replacing the wire suspensions used during O2. Squeezing was implemented during O3 at all sites [601,602]. More details on the hardware and software changes that the LIGO Hanford, LIGO Livingston and Virgo observatories underwent from O3a to O3b are given below.

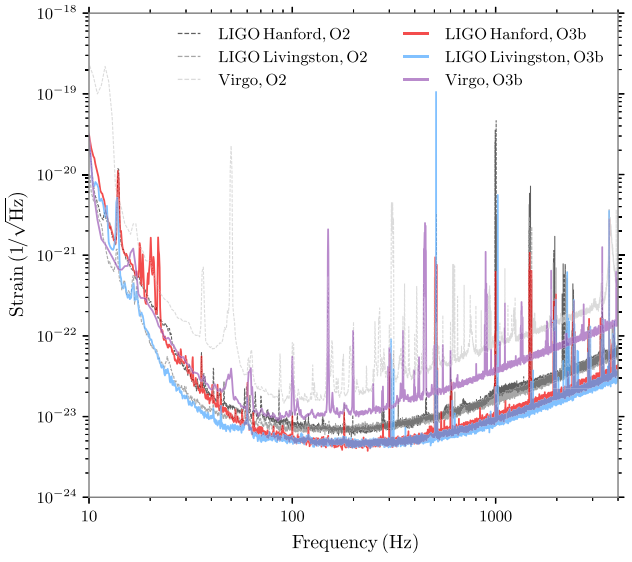

FIG. 14. Representative noise amplitude spectral densities for LIGO Livingston, LIGO Hanford, Virgo during O2 and O3b.

1. LIGO Hanford and Livingston Observatories

The sensitivities of the Hanford and Livingston interferometers during O3b were similar to during O3a [3,38]. The upgrades between O3a and O3b aimed to address not only noise couplings that affect the range, but also reduce light scattering that degrades data quality, and improve resilience against environmental conditions that affect duty cycle.

High optical power in the interferometer reduces the shot noise. The current limit on the maximum circulating power of both LIGO interferometers [599] is from point defects in the test-mass mirror optical coatings which absorb and scatter light. Point absorbers appear in both the LIGO Hanford and Livingston interferometers, and may be identified using Hartmann wave-front sensors, which can measure distortions created by point defects [603,604]. Prior to O3b, both end test masses at LIGO Livingston were inspected with a microscope to investigate potential defects. After this investigation, new point absorbers appeared on both of these end test masses [605,606] for reasons not yet known [599]. These new absorbers resulted in increased optical losses, a reduction in circulating power, and a consequent degradation of the Livingston interferometer's BNS inspiral range due to increased shot noise of approximately 5 Mpc.

Adjustments to the squeezing subsystem produced the largest range improvements during O3b shown in the left panel of Fig. 3. An in-vacuum squeezer was installed for the O3 run at both LIGO sites to improve detector sensitivity above approximately 55 Hz [601], below which radiation-pressure noise is larger with squeezing than the shot-noise level without squeezing. The squeezer works by optically pumping a nonlinear crystal to create correlated photons. The correlations modify the distribution of uncertainty in the quantum state that enters the interferometer [39,40]. The squeezer crystal has been found to degrade on timescales between a week and a month, reducing the pump light power and diminishing the squeezing below its optimal level. At LIGO Livingston, increased squeezing from moving the spot position on the crystal recovered approximately 3 Mpc in BNS inspiral range between O3a and O3b. At LIGO Hanford, a damaged fiber delivering pump light to the crystal was replaced between O3a and O3b, allowing a threefold increase in pump power and more squeezing. Adjustments done between O3a and O3b, in conjunction with moving the

TABLE VIII. Summary of selected optical and physical parameters of the LIGO Hanford (H), LIGO Livingston (L), and Virgo (V) interferometers in the advanced-detector era. The input laser power is an estimate for the maximum laser power level typically achieved during the observing period, and is the power that would be measured at the power recycling mirror (after the input mode cleaner). The suspension type is abbreviated as Silica for monolithic fused-silica fibers and Steel for steel wires.

	O1		O2			O3a			O3b		
Parameter	H	L	H	L	V	H	L	V	H	L	V
Input laser power	21 W	22 W	26 W	25 W	10 W	34 W	44 W	18 W	34 W	40 W	26 W
Power recycling gain	38	38	40	36	38	44	47	36	44	42	34
Signal recycling	✓	✓	✓	✓	✗	✓	✓	✗	✓	✓	✗
Squeezing	✗	✗	✗	✗	✗	✓	✓	✓	✓	✓	✓
Suspension type	Silica	Silica	Silica	Silica	Steel	Silica	Silica	Silica	Silica	Silica	Silica

crystal position and retuning the squeezer on 2 January 2020 during O3b (shown in Fig. 3), produced an improvement of approximately 7 Mpc in Hanford's BNS inspiral range.

O3b includes upgrades to the LIGO detectors to reduce scattered-light noise. Scattered-light noise occurs when a fraction of light gets scattered from its intended path, hits another moving surface, and a part of this light gets reflected back, rejoining the main interferometer beam with a noisy, varying phase [67,68]. This noise can be upconverted to higher harmonics of the surface motion frequencies, causing glitches. At LIGO Livingston, several locations at both end stations are outfitted with improved light baffles to prevent scattered light reflected off the vacuum envelope from recoupling with the main beam. A particularly important contribution was new baffles installed between O3a and O3b surrounding a suspended platform that relay a beam transmitted by one end test mass. At LIGO Hanford, a window in the output optic chain was replaced between O3a and O3b with one that has a larger incidence angle to ensure the back reflection from the window could not be a source of scattered light. Scattered-light noise is found to be correlated to microseismic activity, which is ground motion in the frequency band 0.1–0.5 Hz driven primarily by oceanic waves. During periods of high microseismic activity, both Hanford and Livingston interferometers suffer from large relative motion between the end test mass and the reaction mass that is immediately behind the test mass. This motion is found to produce a scattered-light noise path contributing to transient noise in the interferometer output [69]. This noise is mitigated by implementing reaction-chain tracking, a control loop that makes the reaction mass follow the end test mass, reducing the relative motion. Reaction-chain tracking was implemented on 7 January 2020 and 14 January 2020 at Livingston and Hanford, respectively. These efforts to reduce scattered-light noise had a significant effect on data quality by reducing transient noise as discussed in Sec. III B.

Finally, at LIGO Hanford, another source of environmental noise, ground tilt induced by wind on the buildings, was mitigated by installing wind fences that reduce the wind velocity at the end stations [607]. This has been shown to lower ground tilt. The effect on data quality and duty cycle is still being investigated.

While the Hanford and Livingston detectors are nominally the same design [1], differences in environment and implementation result in different sensitivity during O3b. Hanford has more unexplained noise from 30 to 100 Hz and more angular control noise below 30 Hz. The higher noise above 430 Hz in the Hanford spectrum is due to lower optical power causing increased shot noise as well as higher frequency-dependent losses that degrade the squeezing above the interferometer bandwidth [608].

2. Virgo Observatory

The one-month commissioning break between the two observing periods was used to get a better understanding of the Virgo sensitivity and of some of its main limiting noises. Throughout O3, work was continuously carried out to improve the Virgo sensitivity in parallel with the ongoing data taking. Dedicated tests were made during planned breaks in operation (commissioning, calibration, and maintenance), and in-depth data analysis of these tests was performed between breaks to ensure continual improvement. This effort culminated during the last three months of O3b, as shown by the step in the BNS inspiral range evolution in the left panel of Fig. 3, and by the bimodal BNS inspiral range distribution in the right panel.

The most significant change to the Virgo configuration between O3a and O3b was the increase of the input power from 18 to 26 W. As for the LIGO detectors, we find that the optical losses of the arms increase following the increase of the input power. The presence of absorbing points on the arm-cavity mirrors is suspected [599], and mitigation strategies will be implemented before O4.

The squeezing system in the Virgo interferometer was implemented before the start of O3a, and squeezing injection was maintained during the whole O3, with a gain in sensitivity at high frequency [602,609]. Prior to the start of O3a, new high-quantum-efficiency photodiodes were installed at the output (detection) port of the

interferometer. These diodes increased the electronics noise at low frequency, but were improved at the end of January 2020 during a maintenance period, by replacing preamplifiers. The electronic noise disappeared completely, leading to a BNS inspiral range gain of approximately 2 Mpc.

Shortly thereafter, an extended period of continuous and stable control of the Virgo detector allowed improvement to the performance of the etalon feedback system designed to reduce the residual asymmetry between the optical linewidths of the interferometer arm cavities [610]. To compensate for this asymmetry, the input mirrors of the Virgo Fabry-Perot cavities have parallel faces that create an optical resonator (the etalon) inside the substrate. To remain close to the optimized working point, it is necessary to reduce the temperature variations of the substrate by using heating belts in the input test-mass towers. The implemented feedback requires hours to reach equilibrium, but has a temperature accuracy of 6 mK, about 2% of a full etalon fringe (532 nm). The BNS inspiral range improvement from this etalon feedback control is approximately 2–3 Mpc.

During the same period, it was discovered that some channels used as input for the GW strain channel reconstruction were numerically limited by quantization errors. Changing their storage from float to double precision led to an immediate gain of approximately 2 Mpc for the BNS inspiral range.

Finally, in the period between the end of January to the beginning of February 2020, the alignment was improved for the injection of the squeezed light into the interferometer [602,609], a critical parameter of the low-frequency sensitivity. By mitigating scattered-light noise, the BNS inspiral range increased by approximately 1–2 Mpc.

All these quasisimultaneous hardware and software improvements led to a significant increase in the BNS inspiral range visible in the data after 28 January 2020 (Fig. 3, left panel). The median range improved from 49 Mpc (before 28 January 2020) to 56 Mpc (after 28 January 2020). The Virgo sensitivity improved over the whole frequency range, with a larger improvement below about 300 Hz, around the minimum of the sensitivity curve and at lower frequencies.

APPENDIX C: DATA-QUALITY METHODS

Information about the data quality of the detectors is repackaged into products used by astrophysical analyses, including data-quality flags, gating, and iDQ glitch likelihoods, as introduced and discussed below. Including this information in searches, as summarized in Table IX for each offline analysis, increases the total number of detectable signals [63,611,612]. The most egregious periods of light-scattering glitches in the LIGO detectors are vetoed from the astrophysical analyses through a combination of these veto products, but the rate of scattering glitches was so high in the beginning of O3b, especially in LIGO Hanford data, that current methods cannot effectively exclude these glitches without losing large stretches of data [63].

Data-quality flags are lists of time segments that identify the status of the detectors or the likely presence of a particular instrumental artifact. These flags are broken into three categories based on the severity of the data-quality issue and how the flag was designed [63,96,612]. The amount of time removed by data-quality flags in each detector is typically of order 1%. Table IX shows the cumulative fractional time removed by each category during O3b. The fractional time removed by individual data-quality flags can be found in a summary of flags

TABLE IX. Top: data-quality products used for noise mitigation by each offline search pipeline. Products listed here are publicly available from GWOSC [33]. Most analyses employ additional internal noise mitigation methods, including gating [79,83,93,110,613]. Bottom: the percent of single-detector time removed by each of the same veto categories for each detector during O3b. Veto time values for LIGO Hanford and LIGO Livingston are reproduced from studies of O3 detector characterization [63]. Three center dots (⋯) in a data-quality product's column indicates that it is not produced for the relevant detector, except for iDQ output; iDQ has no associated removed time as it is incorporated directly into the search-pipeline ranking statistic [611]. The listed removed time is in addition to the downtime associated with one or more detectors not being in a nominal observing state, as described in Sec. II, which is common to all searches.

Search pipeline	Category 1	CBC category 2	Burst category 2	Burst category 3	Gating	iDQ
cWB	✓	✗	✓	✓	✗	✗
GstLAL	✓	✗	✗	✗	✗	✓
MBTA	✓	✓	✗	✗	✗	✗
PyCBC	✓	✓	✗	✗	✓	✗

Detector	Category 1	CBC category 2	Burst category 2	Burst category 3	Gating	iDQ
LIGO Hanford	0.30%	0.02%	0.52%	0.41%	0.01%	⋯
LIGO Livingston	1.68%	0.28%	0.50%	0.17%	0.01%	⋯
Virgo	0.21%	⋯	⋯	⋯	⋯	⋯

applied during O3 for LIGO and Virgo [614,615]. Category 1 flags indicate time periods where data should not be analyzed due to either incorrect configuration of the detector, operator error, or egregious data-quality issues. All GW searches uniformly use category 1 flag information to exclude these time periods. Category 2 flags are designed to indicate segments that are predicted to contain non-Gaussian artifacts likely to trigger GW searches based on information from auxiliary channels [63]. While data during category 2 flags is still used in analyses to compute estimates of the power spectral density (PSD), searches that use category 2 vetoes do not consider any triggers during these time periods in estimates of significance. The set of category 2 flags that are used in analyses is different between the CBC analyses that use waveform templates and the Burst analyses that are more waveform agnostic. Similar to category 2 flags, category 3 flags are used to indicate periods of transient noise, but are constructed using estimates of statistically significant correlations between glitches in auxiliary channels and behavior of GW detector data [420]. Category 3 flags are produced only for use by the Burst analysis cWB.

The gating method removes short-duration artifacts from the data by smoothly rolling the data containing the artifact to zero with an inverse window function, as employed for LIGO data during previous observing runs [63]. The gating data product referenced in Table IX and available from GWOSC [33] was generated using times corresponding to a loud excursion in the data identified with auxiliary channel information. Most transient search algorithms also employ internal gating methods to exclude noise transients from analysis based only on the amplitude of the glitch.

The iDQ glitch likelihood uses machine learning to predict the probability that a non-Gaussian transient is present in detector data based only on information from auxiliary channels [421]. This likelihood is used by GstLAL as a part of the search-pipeline ranking statistic to penalize triggers near periods of high iDQ likelihood [611]. As shown in Table IX, GstLAL incorporates iDQ glitch likelihood information in lieu of applying category 2 or 3 data-quality flags.

Astrophysical analyses performed online use different data-quality products from those listed in Table IX. Online data-quality products describe the state of the detectors and the data using only products available within the low latency needed for the online search analyses and the sending of public alerts (as detailed in Appendix A). For example, the category 2 and 3 data-quality flags used by offline searches are often informed by follow-up investigations over the scale of weeks or months after data are initially collected. Table X lists the state vector and data-quality products available online, and which searches use each of these. Online data-quality products used in O3, including online detector state vectors, the LIGO data-quality vector, search-specific online Virgo vetoes, Virgo online category 1 products, and an online version of gating, are described in detail in related papers about LIGO [63] and Virgo detector characterization [77].

After the event-validation procedures described in Sec. III B, we assess whether excess power present within the target analysis time of any candidate is sufficiently nonstationary to require mitigation [44,617]. We compare the variance of the noise PSD in each identified time-frequency region for consistency with Gaussian noise. Time-frequency regions inconsistent with Gaussian noise ($p < 0.01$) are deglitched, as described below, before source-parameter estimation. Details of the candidates requiring mitigation are given in Appendix E 1.

The majority of glitch-subtracted data discussed in Appendix E 1 were produced with the BayesWave algorithm [377,379]. BayesWave models localized excess power as a sum of sine-Gaussian wavelets, using a multicomponent model that simultaneously fits signals, glitches, and the PSD of the Gaussian noise component using a transdimensional Bayesian inference, wherein the number of model components (wavelets, spectral lines, and spline control points for the smooth portion of the PSD) is allowed to vary, in addition to the parameters that describe each component.

The signal model reconstructs the plus and cross polarization states of a GW signal as a sum of wavelets, which are coherently projected onto the detector

TABLE X. State information and data-quality products used for noise mitigation by each online search pipeline. For each detector, the state vector defines the times the detector is online and the data are ready for analysis. The LIGO data-quality vector and Virgo online category 1 products flag known instrument artifacts during observing mode [63,616]. Information from online data-quality products is available in a different form for offline searches, e.g., the category 1 and 2 data-quality products, as part of the products listed in Table IX. Most analyses employ additional internal noise mitigation methods, including gating [79,83,93,110,613].

Search pipeline	State vector	LIGO data-quality vector	Virgo online category 1	Virgo PyCBC veto	Online gating
cWB	✓	✓	✓	✗	✗
GstLAL	✓	✓	✓	✗	✗
MBTAOnline	✓	✓	✓	✗	✗
PyCBC Live	✓	✓	✓	✓	✗
SPIIR	✓	✓	✓	✗	✓

network [379]. We use the waveform reconstruction produced by BayesWave in the waveform consistency tests as discussed in Sec. VI. The glitch model reconstructs noise transients separately in each detector. The spectral model adjusts to take into account the power that gets assigned to the signal and glitch models. Central to the BayesWave approach is that the model dimension is not fixed, with both the number of wavelets and their parameters explored using a transdimensional reversible jump Markov-chain Monte Carlo algorithm [618]. Louder signals generally demand more wavelets. In the case of CBC signals, high-mass, short-duration signals are generally reconstructed with fewer wavelets than low-mass, longer-duration signals.

The natural parsimony of Bayesian inference works to ensure that any coherent signal power is assigned to the signal model, while any incoherent noise transients are assigned to the glitch power, since fitting the data with a coherent model requires fewer parameters than fitting the data in each detector independently. Thus, this method allows us to remove glitches even if they overlap with a GW signal [126,379]. Going forward, it may be desirable to perform the glitch fitting and PSD estimation in concert with the CBC parameter estimation [162]. In the current analysis, the BayesWave algorithm is used to produce cleaned data and point estimates of the PSD that are then used in source-parameter estimation (Appendix E).

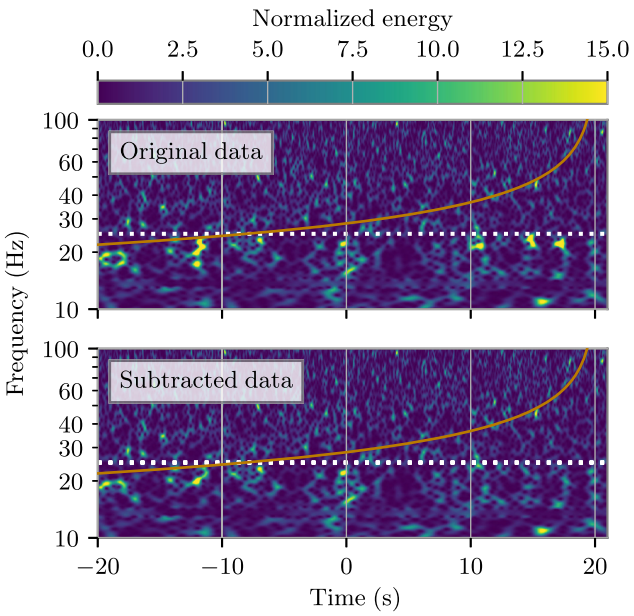

FIG. 15. A spectrogram [73] of LIGO Livingston data prior to the estimated merger time of GW200115_042309. The top plot shows the untreated data and the bottom shows the data with some excess power due to fast scattering subtracted [379]. The estimated signal track is represented as an orange line. A white dashed line shows the lower frequency used for source-parameter estimation for the original GW200115_042309 inference ($f_{\mathrm{low}} = 25$ Hz) [8].

An example of glitch subtraction by the BayesWave algorithm is illustrated in Fig. 15 for the case of analyzing GW200115_042309. The glitches removed here are fast scattering, one of the most common glitches observed in O3b LIGO Livingston data, as described in Sec. III B [63,70].

The mitigated data discussed in Appendix E 1 for GW200129_065458 are produced with the gwsubtract algorithm [44], which employs linear subtraction [59,619]. We use a photodiode monitoring an element of the LIGO Livingston detector's input optics (L1:LSC-POP_A_RF9_I_ERR_DQ) identified [620] as a linear witness of the glitch. The time of the subtracted glitch is also identified as correlated with an auxiliary witness channel by a CBC category 2 data-quality flag [59] defined as flag 1.24 (45 MHz sideband fluctuations) in the O3 LIGO data-quality flag summary [614].

In order to assess the efficacy of glitch subtraction by either method described above for O3b candidates, we compare the stationarity of the glitch-subtracted data within the targeted time-frequency window to Gaussian noise. Glitch-subtracted data consistent with Gaussian noise are deemed sufficiently stationary for parameter estimation.

Uncertainties related to the glitch modeling are not accounted for in source-parameter estimation. To do so would require glitches to be modeled simultaneously with inference of the source properties. Analyses estimating both the properties of glitches and signals have found that the glitch modeling uncertainty may impact the inferred source properties in specific parts of the parameter space [162,621,622]. However, joint glitch and source inference has not yet been incorporated into the inference algorithms used here. Both of the glitch-subtraction methods used in this work have different associated uncertainties, and may work better in different circumstances; for example, BayesWave works well when its coherent wavelet analysis accurately models the glitch, and gwsubtract works well when there is a reliable witness channel [44].

APPENDIX D: CANDIDATE-IDENTIFICATION METHODS

1. GstLAL

The GstLAL pipeline [78–81,623,624] uses matched filtering in the time domain to detect triggers and coincidences. We model signals and search for them in the data using the same template bank as for the GWTC-2 analysis [3]. The template bank covers waveforms with redshifted total masses from $2M_{\odot}$ to $758M_{\odot}$. The spins are assumed to be parallel (aligned or antialigned) to the orbital angular momentum; the spin magnitudes range from −0.05 to 0.05 for components with redshifted masses $<3M_{\odot}$, and from −0.999 to 0.999 for components with redshifted masses $>3M_{\odot}$. The template bank is constructed using a stochastic placement method in five different regions of the parameter space that are the same as those defined for the GWTC-2

analysis [3]. The SEOBNRv4_ROM waveform approximant [625] is used for templates with chirp mass $\geq 1.73 M_\odot$; this waveform is a frequency-domain reduced-order model [626] of the time-domain inspiral-merger-ringdown model SEOBNRv4 which models quasicircular, nonprecessing BBHs based upon the effective-one-body (EOB) equations of motion [625]. The TaylorF2 waveform approximant [98,627–635] is used for lower-mass systems; this waveform is a frequency-domain, inspiral-only model of aligned-spin CBC systems built from closed-form PN approximations. The template bank is constructed such that any template in the continuous parameter space is certain to match at least one template in the discrete space to greater than a chosen minimum match, where the match used is that given in Eq. (6), maximized over the phase and time of coalescence. The value of the minimum match is chosen to ensure that the SNR loss due to the templates not exactly matching the signals is acceptable while keeping the total number of templates small enough to be computationally feasible. The minimum match is dependent on the region of the parameter space, but is never smaller than 0.97 [3].

Triggers are defined by maximizing the matched-filter SNR for each template, in each detector, over 1-s time windows [78]. We use a SNR threshold of $\rho > 4.0$ to define triggers. Triggers from the same template that are time coincident in multiple detectors are grouped together to form events [78]. The GstLAL analysis uses single-detector triggers from HL coincident time (when either HL or HLV were operating) to estimate background statistics in bins according to template mass. This is due to the low probability of a real signal appearing above threshold in only LIGO Hanford or LIGO Livingston when both detectors are operating. Triggers from single-detector time, or times when only HV or Livingston-Virgo (LV) were operating, are excluded from the background estimation to avoid significant contamination by true astrophysical signals.

The likelihood ratio is informed by observables such as the matched-filter SNR from each detector, detector sensitivities at the time of coincidence, as well as the output of signal-based-veto tests, and time and phase differences between triggers [79]. The events are ranked by the likelihood-ratio statistic which compares the probability in the signal hypothesis of finding the given observables to the probability of the same observables in the noise hypothesis. In addition, the likelihood ratio includes a term from iDQ [611], a statistical inference framework that identifies short-duration non-Gaussian artifacts in the strain data [421] (described in Appendix C). As discussed in the GWTC-2.1 paper [4], iDQ time series were regenerated offline using an acausal binning scheme and a larger set of auxiliary witness channels, making its data products more sensitive in identifying noise artifacts compared to their online counterpart. An increased sampling rate in the offline configuration also allowed for better resolution of short-duration glitches. Because of these changes, iDQ had an improved performance in identifying glitches. Accordingly, starting in O3b, iDQ now has the capability to increase the significance of candidates during times in which no noise artifacts are identified: Whereas in the previous procedure used for GWTC-2 [3], the iDQ term in the GstLAL likelihood ratio was restricted to be positive, so that it could only decrease the significance of candidates [611], it may now be either positive or negative. Additionally, iDQ is now applied to both coincident and single-detector candidates.

Since O2, the GstLAL pipeline has allowed for the possibility of single-detector candidates [79]. This includes two cases: triggers from a time when only one detector was operational, and noncoincident triggers from one detector even when multiple detectors were operational. Single-detector candidates are required to pass the SNR threshold as well as a preliminary likelihood-ratio threshold. However, single-detector candidates are downweighted with a singles penalty in the likelihood-ratio statistic, depending on the detector in which it was observed and the sensitivities of the detectors which were on at the trigger time [4].

2. MBTA

MBTA [82,83] uses a template bank covering binaries with redshifted component masses ranging from $1 M_\odot$ to $195 M_\odot$, with the additional constraints that the maximum total mass is $200 M_\odot$, and if the secondary object has a mass lower than $2 M_\odot$, then the maximum mass of the primary object is $100 M_\odot$. Objects are assumed to have spins parallel to the orbital momentum with maximum dimensionless values 0.05 if their masses are below $2 M_\odot$, and 0.997 otherwise. The templates are generated in the time domain, using the SpinTaylorT4 waveform approximant [631,632,634,636–640] if both objects have masses below $2 M_\odot$, and the SEOBNRv4 waveform [625] otherwise. The SpinTaylorT4 waveform is an inspiral-only, time-domain model for CBC systems based on the PN equations of motion, while SEOBNRv4 is a full inspiral-merger-ringdown waveform appropriate for BBHs. The template bank is produced using a stochastic placement method.

The MBTA pipeline starts with a preprocessing step, where data are downsampled then gated at (externally or internally) identified times of bad data quality. To mitigate safety issues in the gating procedure, a subset of the template bank is also analyzed without applying the gating procedure, albeit with higher SNR thresholds ($\rho > 9.5$ in Hanford, 11.3 in Livingston, and 12 in Virgo). MBTA splits the parameter space into three regions treated as independent searches. The regions can be considered to cover the BNS, NSBH, and BBH source types, although the transition between NS and BH is conservatively taken to be $2 M_\odot$ (to allow for any heavier object to possibly have high spin) [4]. Single-detector triggers are ranked according to a

statistic based on the matched-filter SNR modified to take into account the consistency with an astrophysical signal (quantified from the quadratic average of the difference between the SNR time series around its maximum and the template autocorrelation) and the local data quality (quantified from the overall pipeline response). Coincidences are ranked according to a statistic based on the quadratic sum of the single-detector triggers ranking statistics modified to take into account the consistency of some parameters across the various detectors.

MBTA initially assigns a FAR to events depending on the coincidence type (whether HL, HV, LV, or HLV depending on which detectors provided a trigger), and the parameter-space region. The FAR is then modified to take into account trials factors from the various coincidence types and regions. For double coincidences, the FAR at a given ranking statistic threshold is estimated from the rate of false coincidences (built from single-detector triggers in that region) that are as loud or louder. Single-detector triggers that are known to be part of foreground coincidences with a combined ranking statistic above 10 are excluded from this process, as such statistic values typically correspond to low FARs (typically less than 0.2 yr^{-1} for HL coincidences) indicating a probable astrophysical origin. The FAR for triple coincidences is derived from that of double coincidences. Equal trials factors are applied for the three parameter-space regions, whereas for coincidence types, trials factors are applied according to the likelihood of astrophysical sources being detected as coincidences of each type, considering the relative detector sensitivities.

3. PyCBC

We employ two offline PyCBC configurations in this work [23,84–88,641]. The first, the PyCBC-broad analysis, is designed to search for as many different types of signal as possible, and probes a wide range of masses and spins. Following previous searches [3,4,17,19], we also perform an analysis focusing on the BBH region of the parameter space in which we have seen most of our signals so far, making use of a population prior [642]. This second approach is the PyCBC-BBH analysis.

The PyCBC-BBH analysis focuses on a region ranging in primary component mass from $5M_\odot$ to $350M_\odot$, with mass ratios from 1/3 to 1, and aligned, equal component spins ranging from −0.998 to 0.998. The PyCBC-broad template bank covers a similar parameter space as the GstLAL template bank, but with a few significant changes. Both the PyCBC-broad and PyCBC-BBH analyses use the `SEOBNRv4_ROM` [625] waveform approximant for templates with total mass above $4M_\odot$, and `TaylorF2` [98,627–635] for lower-mass systems. The templates within the template bank are placed using a hybrid geometric-random method [643,644], and no template is used that has a duration of less than 0.15 s [645], meaning there is an upper limit on the mass of the systems. If this duration limit is relaxed and additional vetoes on transient data artifacts are applied, higher sensitivity to high-mass systems may be obtained [26,646].

Both the PyCBC-broad and PyCBC-BBH analyses use data from all detectors, searching for coincident triggers in two or more detectors. For each coincident event, we calculate a ranking statistic which is compared to the background to calculate the significance, finally combining the significances from each possible combination of triggers from the available detectors (the coincidence type) into a single result.

The search in the three-detector network is done by performing coincident searches in each coincidence type, and then combining FAR depending on the available coincident combinations. For example, if an event is seen as a HL coincidence, the ranking statistic would be calculated, and the FAR estimated by counting higher-ranked events in a time-shifted background. If the Virgo detector is observing, then the FAR from the detected event would be added to the FAR at that ranking statistic from each of HV, HL, and HLV backgrounds. This method means that we effectively apply a trials factor where it is needed, but not when the coincidence type in which the candidate was found is the only one available such that a trials factor would be inappropriate.

The PyCBC pipelines use a ranking statistic based on the ratio of the expected signal rate and the measured noise rate [17,88]. This choice of ranking statistic has two consequences. First, we are able to incorporate more information about the detectors into our assessment of whether an apparent signal is real or not. For example, we now account for the sensitive volume of the detector network at the time of a candidate and combine the single-detector rates of noise triggers with the time window for coincidences in order to estimate the coincident-trigger rate. Second, we are able to directly combine FARs by summing the FARs at the ranking statistic of the event for each coincidence type available at the time; by adding the FARs rather than using a trials factor, we take into account the vastly different FARs for different coincidence types at the same ranking statistic.

The PyCBC-BBH ranking statistic uses a chirp-mass weighting designed to approximately model the BH population. In previous analyses [17], this weighting took a different functional form above a template chirp mass of $40M_\odot$, suppressing higher-mass triggers; however, in this analysis, due to an omission in implementation, the same functional form is continued over all templates. This change results in a higher background noise level than expected due to triggers in high-mass templates caused by glitches, potentially reducing the sensitivity of the search. From the sensitivity studies in Sec. IV E 1, we see that the sensitivity reduction is likely to be small.

Recent alterations to the PyCBC analysis allow the use of graphics processing unit (GPU) cores or distributed computing through the Open Science Grid [647,648] in order to perform matched filtering more quickly.

The PyCBC analysis used in this work did not analyze single-detector signals, though recent work allows this

feature [21,128]. Usually, triggers from significant signals are removed from the background of lower-ranked events within the analysis, in a process called hierarchical removal [649], but as we do not calculate single-detector significance, we have no metric by which to remove these triggers, and so signal triggers can remain in the background. As a result, these loud triggers from signals can match noise triggers in the time-shifted background and cause an excess of highly ranked background events. In order to prevent the contamination of the background, PyCBC analyses are performed twice: first with all triggers in place, and then again with the triggers removed from catalog candidates that do not form coincidences in the preliminary analysis. To ensure that this process matches the usual hierarchical removal procedure, we use the list of candidates from other analyses for this catalog that have a FAR of less than 10^{-2} yr^{-1}, and compare these to the list of coincident events in the PyCBC analyses. If no coincident event (of any significance) is found in the PyCBC pipeline, then a window of 1 s either side of each event is removed. The triggers removed from the background in the PyCBC-broad pipeline are from around GW200112_155838 and GW200202_154313, and from the PyCBC-BBH pipeline we remove the triggers from around GW200112_155838. The sensitive hypervolume estimates of Sec. IV E 1 use the analysis with the triggers from single-detector events removed. Only a small subset of the analysis chunks are significantly affected by this change, and this effect is particularly muted at the threshold we consider for $\langle VT \rangle$ estimates [21].

In addition to the offline analyses described above, we also use PyCBC Live [613,650] to search for signals in low latency. The PyCBC Live algorithm uses the data and data-quality information that are available in low latency (as described in Appendix C) without human vetting. PyCBC Live uses a more computationally simple ranking statistic than the one used in offline analyses. This simpler ranking statistic is used in order to maintain speed in a low-latency environment and does not contain all of the information used in the offline statistic. The reduced χ^2-reweighted SNR [23] and a sine-Gaussian veto [402,651] are used to assess significance of single-detector triggers. These single-detector triggers are then tested for coincidence, and the coincident ranking statistic is calculated. The ranking statistic is compared to the time-shifted background from five hours of data to estimate FAR.

4. SPIIR

The SPIIR pipeline [91–93] ran as an online low-latency modeled coherent search. SPIIR is a time-domain equivalent to matched filtering that uses infinite impulse response filters [93,652] to approximate waveforms with high accuracy and, in theory, constructs the SNR at zero latency. In O3 the pipeline operated in two low-latency, parallel modes: one to search using data from the two LIGO detectors, and another using data from all three detectors. SPIIR searches templates with primary component mass ranging from $1.1M_\odot$ to $100M_\odot$, a subset of the GstLAL template bank [93]. For online low-latency analyses, this method is more computationally efficient than traditional Fourier methods, with latency 7–10 s in O3 [93]. The filtering process [653–655] and coherent candidate selection [91] are accelerated using GPUs.

The pipeline ranks the triggers by a combination of the coherent network SNR and a χ^2-distributed signal-consistency statistic from the individual detectors [78,93]. It computes the background of the search by performing 100 time shifts per foreground trigger with SNR greater than 4. The k-nearest-neighbors technique is used to estimate the significance for triggers [93]. The FAR for each trigger is estimated over three timescales (two hours, one day, and one week) of collected background triggers for robustness, with the most conservative used for candidates.

5. cWB

The cWB pipeline detects and reconstructs transient signals with minimal assumptions [60,89,107–109] by coherently analyzing data from multiple observatories. The sensitivity of cWB approaches that of matched-filter methods for coalescing stellar-mass BBHs with high chirp masses [26,656], such that it can detect high-mass CBC sources, and also sources that are not well represented in current template banks such as eccentric systems or large mass asymmetry, precessing BBH systems [378]. It was used in previous CBC searches by the LVK [3,12,14,657].

The cWB algorithm analyzes whitened data using the Wilson-Daubechies-Meyer wavelet transform [89,108] to compute a time-frequency representation. The algorithm selects excess-energy data in the time-frequency representation and clusters them to define a trigger. Next, it identifies coherent signal power with the constrained maximum-likelihood method [60], and reconstructs the source sky location and the signal waveforms.

After identifying clusters of coherent data, cWB outputs several statistics. These include the total cluster energy for each detector, the coherent energy E_c of the reconstructed signal obtained by cross-correlating the normalized signal waveforms reconstructed in different detectors, the residual noise energy E_n estimated after the reconstructed waveforms are subtracted from the data, and the estimate of the coherent SNR in each detector. The residual noise energy is used to form a chi-squared statistic $\chi^2 = E_n/N_{\mathrm{DF}}$, where N_{DF} is the number of independent wavelet amplitudes describing the trigger. We estimate the signal SNRs from the reconstructed waveforms. Then, by combining the SNRs of the individual detectors, we calculate the network SNR. The network correlation coefficient $c_c = E_c/(E_c + E_n)$ is another derived statistic that compares coherent and null energies; it approaches 1 when coherence is high, as expected for real signals. The cWB detection statistic is

$\eta_c \propto [E_c/\max(\chi^2, 1)]^{1/2}$, where the χ^2 correction is applied to reduce the contribution of non-Gaussian noise.

For robustness against glitches and to reduce the FAR of the pipeline, cWB uses signal-independent vetoes, which include Burst category 2 data-quality flags in the processing step and category 3 in the postproduction phase [420,658]. To further reduce background, the cWB analysis applies cuts based on the network correlation coefficient c_c and on the χ^2, and employs signal-dependent vetoes based on basic properties of the time-frequency evolution of CBC signals [111,659].

A generic search for CBC systems covers a large parameter space, and it is not possible to design a search that is optimized for all such systems because of the wide frequency range in which the signals fall. With the setup used for this catalog, cWB can reconstruct GW signals with durations up to a few seconds in the detectors' frequency range, which makes it better suited to identify BBH signals than longer NSBH or BNS signals. A CBC signal has a peak frequency inversely proportional to the redshifted total mass, so that less massive binary systems merge at higher frequencies, while more massive systems merge at lower frequencies. Therefore, just as for the GWTC-2 analysis [3], the cWB analyses in this catalog are performed with two pipeline configurations targeting the detection of high-mass ($f_c < 80$ Hz) and low-mass ($f_c > 80$ Hz) BBH systems. These configurations use different signal-dependent vetoes defined *a priori* to alleviate the large variability of non-stationary noise in the detectors' bandwidth.

We estimate the FAR of triggers by time shifting the data of one detector with respect to the other in each detector pair, with time lags so large (typically multiples of 1 s) that actual astrophysical signals are excluded, and repeating this for a large number of different time lags over a total time $T_{\rm bkg}$ which is of the order of 10^3 yr. We count the number of triggers $N_{\rm bkg}$ due to background noise having a SNR (or another similar ranking statistic) that is at least as large as that of the trigger, and we compute the FAR as the $N_{\rm bkg}$ divided by $T_{\rm bkg}$ [660].

The detection significance of a trigger identified by either pipeline configuration in a single frequency range is determined by its FAR measured by the corresponding cWB configuration. In the end, each configuration reports the selected triggers and their FAR. Whenever the low-mass and high-mass configurations overlap, the trials factor of two (the Bonferroni adjustment for the false alarm probability [661]) is included to determine the final FAR [184].

The cWB algorithm can work with arbitrary detector networks, although the cWB analysis presented in this catalog is restricted to the HL, HV, and LV pairs. The HLV network is not included here because it does not improve the significance of the cWB candidates for the current sensitivity of the detector network [31]. Thanks to their near alignment, the two LIGO detectors select a well-defined GW polarization state, and cWB can efficiently exploit coherence to mitigate their glitches and make the remaining noise close to Gaussian. Conversely, the orientation of the Virgo detector differs considerably from that of the LIGO detectors so that, at the current sensitivity level, glitches in Virgo data cannot be mitigated as efficiently, and this reduces the discriminating power of current cWB HLV analyses with respect to HL analyses.

6. Search results

In Sec. IV D, we presented the $p_{\rm astro}$, FAR, and network SNR of candidates with CBC $p_{\rm astro} > 0.5$ or FAR $< 2.0\ {\rm yr}^{-1}$ in Tables I and II, respectively. Here, we additionally provide the single-detector SNRs of each candidate in Table XI. The single-detector SNRs are used as an initial criterion by pipelines to define triggers and determine coincidences, and therefore are an important component in calculating the significance of a detection candidate. The detectors listed in Table I are those that were operating at the time of each candidate, but whether a candidate was missed or found in a particular detector depends on the matched-filter SNR found by each pipeline in the detector's data. In particular, each of the single-detector candidates, GW200112_155838, GW200302_015811, and GW200105_162426, were found during times when either LIGO Livingston or LIGO Hanford were operating simultaneously with the Virgo detector. However, Table XI shows that these were still classified as single-detector candidates since in each case the SNR in Virgo was <4.0. Regardless of the number of detectors used for detection, data from all operating detectors are used for inference of the source parameters (described in Appendix E).

Candidates found by multiple analyses typically have comparable SNRs, but we do not expect the values to be identical because of differences in the template banks and how the pipelines select the most significant template when identifying a candidate. The most noticeable difference is in the Livingston SNR for GW200129_065458, as discussed in Sec. IV D 3; this is a result of the different analyses' handling of data-quality flags.

7. Search sensitivity and probability of astrophysical origin

To assess search sensitivity, we inject simulated signals into the data, and attempt to identify them with each search analysis. The details of the injected populations (which are the same as used for GWTC-2.1 [4]) are given in Table XII, and the injected distributions over redshift are defined assuming a flat Λ-cold-dark-matter cosmology such that

$$p(z) \propto \frac{dV_c}{dz}(1+z)^{\kappa-1}, \tag{D1}$$

where V_c is the comoving volume (see Appendix E for the assumed cosmology [662]). These injected populations are

TABLE XI. Individual-detector SNRs for all candidates in Tables I and II. LIGO Hanford, LIGO Livingston, and Virgo are indicated by H, L, and V, respectively. Numbers in italics indicate where a candidate is identified with probability of astrophysical origin $p_{\text{astro}} < 0.5$. Three center dots (···) indicate where no significant trigger is identified by a search analysis.

	cWB		GstLAL			MBTA			PyCBC-broad			PyCBC-BBH		
Name	H	L	H	L	V	H	L	V	H	L	V	H	L	V
GW191103_012549	···	···	···	···	···	*6.5*	*6.3*	···	6.3	6.8	···	6.2	6.9	···
GW191105_143521	···	···	*5.8*	*7.6*	*2.8*	6.1	8.2	3.1	5.9	7.8	···	5.9	7.8	···
GW191109_010717	9.8	12.1	8.5	13.3	···	8.6	12.6	···	8.7	9.9	···	9.0	11.3	···
GW191113_071753	···	···	···	···	···	6.3	6.4	2.2	*6.3*	*5.4*	···	*6.1*	*5.9*	···
GW191118_212859	···	···	···	···	···	···	*5.2*	*6.1*	···	*5.5*	*7.2*	···	···	···
GW191126_115259	···	···	*5.7*	*6.5*	···	*5.7*	*6.3*	···	*5.8*	*6.2*	···	5.8	6.2	···
GW191127_050227	···	···	*6.8*	*6.7*	*4.0*	6.7	6.4	3.2	*7.0*	*6.4*	···	6.1	6.2	···
GW191129_134029	···	···	8.8	10.0	···	8.5	9.4	···	8.6	9.6	···	8.6	9.6	···
GW191204_110529	···	···	*4.6*	*7.8*	···	*5.4*	*6.0*	···	*5.0*	*7.4*	···	5.0	7.4	···
GW191204_171526	9.0	14.5	8.9	12.8	···	10.0	13.8	···	9.8	13.8	···	9.8	13.8	···
GW191215_223052	6.6	7.3	7.0	7.8	3.0	6.7	7.9	3.0	7.2	7.5	···	7.0	7.5	···
GW191216_213338	···	···	17.8	···	5.6	17.1	···	5.4	17.6	···	5.2	17.6	···	5.2
GW191219_163120	···	···	···	···	···	···	···	···	4.8	7.5	···	···	···	···
GW191222_033537	7.9	7.8	8.8	8.2	···	8.3	7.0	···	8.4	7.9	···	8.4	7.9	···
GW191230_180458	7.4	7.1	7.2	7.0	1.9	*7.4*	*5.9*	*2.4*	*7.2*	*6.2*	···	7.3	6.6	···
GW200105_162426	···	···	···	*13.6*	*2.6*	···	···	···	···	···	···	···	···	···
GW200112_155838	···	···	···	17.5	2.1	···	···	···	···	···	···	···	···	···
GW200115_042309	···	···	6.7	8.9	2.8	6.6	8.6	2.6	6.3	8.8	···	···	···	···
200121_031748	···	···	*8.2*	···	*4.0*	*9.5*	···	*4.9*	···	···	···	*7.3*	···	*4.0*
GW200128_022011	6.7	5.7	7.4	6.9	···	6.9	6.4	···	7.0	6.9	···	7.2	6.9	···
GW200129_065458	···	···	14.6	21.2	6.3	···	···	···	14.7	···	7.1	14.6	···	7.0
GW200201_203549	···	···	*6.2*	*5.9*	*2.9*	*6.1*	*5.7*	*3.0*	*6.1*	*5.5*	···	···	···	···
GW200202_154313	···	···	4.6	10.0	2.4	···	···	···	···	···	···	4.8	9.6	···
GW200208_130117	···	···	6.5	7.4	4.1	6.8	6.6	4.3	6.6	7.0	···	6.6	7.3	4.5
GW200208_222617	···	···	*5.6*	*5.7*	*2.1*	*5.8*	*6.0*	*3.2*	···	···	···	5.7	5.4	···
GW200209_085452	···	···	7.5	6.0	2.8	7.1	6.2	2.4	*7.0*	*6.1*	···	7.0	6.1	···
GW200210_092254	···	···	*4.3*	*8.0*	*2.9*	···	···	···	4.9	7.5	···	4.9	7.5	···
200214_224526	7.1	11.0	···	···	···	···	···	···	···	···	···	···	···	···
GW200216_220804	···	···	6.9	5.9	2.4	*6.4*	*5.7*	*2.2*	*7.1*	*5.6*	···	6.3	6.0	···
GW200219_094415	5.8	7.7	5.8	8.7	2.5	5.3	8.8	2.6	5.8	8.0	···	5.8	8.1	···
200219_201407	···	···	···	···	···	*12.2*	*5.1*	*3.3*	···	···	···	···	···	···
GW200220_061928	···	···	···	···	···	···	···	···	···	···	···	4.4	6.0	···
GW200220_124850	···	···	*6.1*	*5.5*	···	6.1	5.5	···	···	···	···	*5.8*	*5.2*	···
GW200224_222234	13.3	13.4	12.5	12.9	5.8	12.6	13.0	5.5	12.7	12.9	6.4	12.2	12.5	6.3
GW200225_060421	9.6	8.9	9.9	8.2	···	9.8	7.8	···	9.4	7.9	···	9.4	7.9	···
GW200302_015811	···	···	10.4	···	1.9	···	···	···	···	···	···	···	···	···
GW200306_093714	···	···	···	···	···	5.9	6.1	···	*5.7*	*5.4*	···	*5.5*	*5.8*	···
GW200308_173609	···	···	*4.9*	*6.1*	*2.1*	*5.1*	*5.7*	*3.2*	*5.1*	*6.1*	···	5.1	6.1	···
GW200311_103121	···	···	*5.4*	*7.2*	···	*5.7*	*7.0*	···	*5.7*	*7.2*	···	···	···	···
GW200311_115853	12.0	11.0	12.1	10.7	7.0	10.7	10.4	6.9	11.9	10.2	6.7	11.9	10.7	6.9
GW200316_215756	···	···	5.4	7.9	3.1	*5.1*	*7.2*	*3.5*	5.6	7.4	···	5.5	7.5	···
GW200322_091133	···	···	···	···	···	6.0	5.8	3.5	*5.8*	*5.6*	···	*5.5*	*5.4*	···

TABLE XII. Parameter distributions used to generate injections and to compute the probability of astrophysical origin $p_{\rm astro}$ for each pipeline. The BNS injections are generated using the `SpinTaylorT4` waveform model [631,632,634,636–640], while the BBH and NSBH injections are generated using the `SEOBNRv4PHM` model [137], or the `SEOBNRv4P` model [137,625,663] for injections corresponding to binaries with redshifted total mass below $9M_\odot$. We always use the convention that $m_1 \geq m_2$; this constraint means that the marginalized one-dimensional distributions for the masses will not match the distributions used to define the two-dimensional distributions (as given here) in cases where the m_1 and m_2 distributions overlap. Masses are in the source frame, except for the PyCBC rows, where the measured (redshifted) chirp mass is considered. The redshift-evolution parameter κ controls the injected distribution as described in Eq. (D1). The injection sets are used to estimate sensitive hypervolumes, with weights to match the populations assumed within each $\langle VT \rangle$ calculation, including updating the mass, spin, and redshift distributions where appropriate.

		Mass distribution	Mass range ($M_\odot$)	Spin range	Spin orientations	Redshift evolution	Maximum redshift
Injections	BBH	$p(m_1) \propto {m_1}^{-2.35}$ $p(m_2\|m_1) \propto m_2$	$2 < m_1 < 100$ $2 < m_2 < 100$	$\|\chi_{1,2}\| < 0.998$	Isotropic	$\kappa = 1$	1.9
	NSBH	$p(m_1) \propto {m_1}^{-2.35}$ Uniform	$2.5 < m_1 < 60$ $1 < m_2 < 2.5$	$\|\chi_1\| < 0.998$ $\|\chi_2\| < 0.4$	Isotropic	$\kappa = 0$	0.25
	BNS	Uniform	$1 < m_1 < 2.5$ $1 < m_2 < 2.5$	$\|\chi_{1,2}\| < 0.4$	Isotropic	$\kappa = 0$	0.15
cWB $p_{\rm astro}$	BBH	Same as injections					
GstLAL $p_{\rm astro}$	BBH	Log-uniform	$3 < m_1 < 300$ $3 < m_2 < 300$	$\|\chi_{1,2}\| < 0.99$	Aligned	$\kappa = 0$	3.76
	NSBH	Log-uniform	$3 < m_1 < 300$ $1 < m_2 < 3$	$\|\chi_1\| < 0.99$ $\|\chi_2\| < 0.4$	Aligned	$\kappa = 0$	0.80
	BNS	Log-uniform	$1 < m_1 < 3$ $1 < m_2 < 3$	$\|\chi_{1,2}\| < 0.05$	Aligned	$\kappa = 0$	0.16
MBTA $p_{\rm astro}$	BBH	POWER LAW+PEAK [116] with $\alpha = 2.5$, $\beta_q = 1.5$, $m_{\rm min} = 5M_\odot$, $m_{\rm max} = 80M_\odot$, $\lambda_{\rm peak} = 0.1$, $\mu_m = 34M_\odot$, $\sigma_m = 5M_\odot$, $\delta_m = 3.5M_\odot$	$5 < m_1 < 80$ $5 < m_2 < 80$	$\|\chi_{1,2}\| < 0.998$	Isotropic	$\kappa = 0$	1.9
	NSBH	Same as injections					
	BNS	Same as injections					
PyCBC-broad $p_{\rm astro}$	BBH		$\mathcal{M} > 4.353$				
	NSBH		$2.176 < \mathcal{M} < 4.353$				
	BNS		$\mathcal{M} < 2.176$				
PyCBC-BBH $p_{\rm astro}$	BBH		$\mathcal{M} > 4.353$				

reweighted to obtain estimates of the sensitive hypervolumes presented in Table III such that the injected distributions in Table XII do not represent the assumed populations used to estimate search sensitivity.

The probability of astrophysical origin $p_{\rm astro}$ for a candidate is estimated directly from the ranking statistics x that are used to assess the FAR. By comparing the distributions of ranking statistics under the assumptions of foreground $p(x|\text{signal})$ or background $p(x|\text{noise})$, we can calculate a signal-versus-noise Bayes factor for each event. This Bayes factor acts as a likelihood in the $p_{\rm astro}$ computation for each event. The normalization of the astrophysical x distributions depends on merger rates, which are jointly estimated in the calculation, assuming that the triggers are drawn from independent Poisson processes [112]. For a given FAR, $p_{\rm astro}$ will be larger if the true alarm rate is higher.

The construction of the foreground (signal) and background (noise) distributions is specific to individual detection pipelines:

(i) The PyCBC analyses use time-shifted triggers to empirically estimate the rates of background events and their distributions over the search ranking statistic, while foreground distributions are estimated using recovered simulated signals. As in GWTC-2.1 [4], we allow these background and foreground distributions to differ between different combinations of detectors in coincidence, and also allow for a dependence of the foreground distribution and signal rate on which detectors are observing at a given time [664]. In order to model variation of the signal rate over binary masses, the foreground and background estimates are obtained separately over the ranges of template chirp mass given in

Table XII; the rate of astrophysical signals is also estimated separately in each range.

(ii) For GstLAL, the ratio of the foreground-to-background distributions (the signal-to-noise Bayes factor that enters into the p_{astro} calculation) is proportional to the likelihood ratio which is the ranking statistic x. Details of the GstLAL background collection method are given in Appendix D 1. The time-volume sensitivity of the pipeline used in this calculation is estimated based on simulated sources injected into the pipeline and is rescaled to the astrophysical distribution [665]. We use time-volume ratios to combine triggers from various observation runs and perform the multicomponent analysis yielding p_{astro} and merger rates [112,115] inferred from the entire set of available data (from O1 to O3b).

(iii) The MBTA analysis uses a template bank split into 165 bins in the chirp-mass–mass-ratio parameter space to compute p_{astro} values of events [117]. The fine binning has the main benefit of allowing the proper tracking over the parameter space of the assumed CBCs populations used in the foreground distribution. It also provides a more tailored estimate of the background rate compared to the FAR reported by the analysis, which uses a coarse estimate of the background (integrated over one of the three search regions) that is conservative for signals from high-mass sources. It can therefore result in events being assigned a significant p_{astro} in population-rich regions of the parameter space even though they were assigned a high FAR value (examples are GW200220_124850, GW200306_093714, and GW200322_091133). For instance, GW200220_124850 is in an $\mathcal{M}$-q bin that captures 11% of the expected astrophysical signal while it contains only 0.008% of the BBH templates. For the combined ranking statistics of this candidate, the expected foreground rate density (per unit interval of the ranking statistic squared) is 0.109 yr^{-1}, while the local background rate density is 0.023 yr^{-1}. For each of the bins, the background is constructed by making random coincidences of single-detector triggers for each coincidence type (HL, LV, HV, or HLV) using the templates of the bin considered, but only during HL and HLV coincidence time to remove single-detector events from the background estimation [82,83]. This means that the background assigned to an event depends on its coincidence type and on the bin which triggered the associated template. The foreground for the BNS and NSBH categories is estimated using the populations described in Table XII. The foreground estimate for the BBH uses the POWER LAW+PEAK population model used to describe the GWTC-2 population [116,666].

(iv) Just as PyCBC, cWB also uses time-shifted analysis for significance assessment of background and foreground triggers. The distribution of the coherent network SNR ranking statistic for the time-shifted triggers is used to estimate the background, and consequently to assign the FAR. The foreground is derived from the recovered simulated signals. Since cWB is significantly more sensitive to BBH systems, only these sources are considered.

The precise p_{astro} value depends upon the assumed true population, and hence may be subject to change as we learn more about the astrophysical population of CBCs. The population models used by the various pipelines in their computation of p_{astro} are summarized in Table XII.

When estimating p_{astro} for each candidate, we do so separately for each category of source, as p_{astro} is dependent on the underlying BNS, NSBH, and BBH populations. We separate the candidates based on their component masses; rather than a rigorous statement of the nature of the component, the NS label is used only to identify components whose masses are below $3M_{\odot}$. BBH-category candidates are any for which component masses are both above $3M_{\odot}$, BNS-category candidates are the ones for which both component masses fall below this value, and we consider a candidate a part of the NSBH category if the primary component mass was above this boundary, and the secondary below it. The category chosen for each source is based on the masses of the template found by the search pipeline, rather than a detailed inference of source properties (Sec. V); this may lead to p_{astro} estimates that are biased relative to an ideal calculation using the full information available for the signals.

In Table XIII, we give the calculated probabilities that a candidate comes from a system in our BBH category p_{BBH}, our NSBH category p_{NSBH}, or our BNS category p_{BNS}. The probability that a candidate belongs to a specific astrophysical source category (p_{BNS}, p_{NSBH}, or p_{BBH}) is evaluated from source-class-specific Bayes factors by redistributing the foreground probabilities across astrophysical source classes. This redistribution makes use of the template-based estimate of the component masses of the candidate, as well as the response of the template bank to an assumed population of BNS, NSBH and BBH signals. The computation of the probability that a candidate comes from a system in one of the three astrophysical categories requires the choice of a prior on the counts in each category [114]. GstLAL used a uniform prior for the BNS and NSBH categories and a Poisson-Jeffreys prior for the BBH category, MBTA used a uniform prior for the BNS category and a Poisson-Jeffreys prior for the NSBH and BBH categories, PyCBC used a Poisson-Jeffreys prior for all three categories, and cWB used a Poisson-Jeffreys prior. Given the number of candidates, the prior choice does not significantly impact the BBH results, but can influence the BNS and NSBH p_{astro} values (e.g., variations of 0.045 for GW200105_162426).

TABLE XIII. Multicomponent $p_{\rm astro}$ values for candidates with $p_{\rm astro} > 0.5$ and marginal candidates with FAR $< 2.0\ {\rm yr}^{-1}$ where the probability of a BNS or NSBH category is nonzero in any search analysis. Since cWB does not calculate separate source probabilities, all sources are treated as BBHs for the purposes of $p_{\rm astro}$ calculation. Results in italics indicate where an analysis found the candidate with $p_{\rm astro} < 0.5$, and three center dots (⋯) indicate that a candidate was not found by an analysis. Source probability for BNS is not given for PyCBC-BBH, as the search is not sensitive to redshifted chirp masses below $4.353M_\odot$. This would require extremely high redshifts, to which LIGO and Virgo are not sensitive, to correspond to a BNS source. The BNS, NSBH, and BBH categories are defined by the masses associated with the candidate from the search results (as defined in Table XII), and do not necessarily correspond to the true astrophysical population of sources.

	cWB	GstLAL				MBTA				PyCBC-broad				PyCBC-BBH		
Name	$p_{\rm astro}$	$p_{\rm BBH}$	$p_{\rm NSBH}$	$p_{\rm BNS}$	$p_{\rm astro}$	$p_{\rm BBH}$	$p_{\rm NSBH}$	$p_{\rm BNS}$	$p_{\rm astro}$	$p_{\rm BBH}$	$p_{\rm NSBH}$	$p_{\rm BNS}$	$p_{\rm astro}$	$p_{\rm BBH}$	$p_{\rm NSBH}$	$p_{\rm astro}$
GW191118_212859	⋯	⋯	⋯	⋯	⋯	*<0.01*	*<0.01*	*<0.01*	*<0.01*	*<0.01*	*0.04*	*<0.01*	*0.05*	⋯	⋯	⋯
GW200105_162426	⋯	*<0.01*	*0.36*	*<0.01*	*0.36*	⋯	⋯	⋯	⋯	⋯	⋯	⋯	⋯	⋯	⋯	⋯
200121_031748	⋯	*0.02*	*<0.01*	*<0.01*	*0.02*	*0.22*	*0.01*	*<0.01*	*0.23*	⋯	⋯	⋯	⋯	*<0.01*	*<0.01*	*<0.01*
GW200201_203549	⋯	*<0.01*	*0.12*	*<0.01*	*0.12*	*<0.01*	*<0.01*	*<0.01*	*<0.01*	*<0.01*	*<0.01*	*<0.01*	*<0.01*	⋯	⋯	⋯
200219_201407	⋯	⋯	⋯	⋯	⋯	*0.45*	*0.03*	*<0.01*	*0.48*	⋯	⋯	⋯	⋯	⋯	⋯	⋯
GW200311_103121	⋯	*<0.01*	*<0.01*	*<0.01*	*<0.01*	*<0.01*	*<0.01*	*0.03*	*0.03*	*<0.01*	*<0.01*	*0.19*	*0.19*	⋯	⋯	⋯
GW191103_012549	⋯	⋯	⋯	⋯	⋯	*0.13*	*<0.01*	*<0.01*	*0.13*	0.67	0.10	<0.01	0.77	0.81	0.14	0.94
GW191105_143521	⋯	*0.07*	*<0.01*	*<0.01*	*0.07*	>0.99	<0.01	<0.01	>0.99	0.81	0.19	<0.01	>0.99	0.81	0.19	>0.99
GW191126_115259	⋯	*0.02*	*<0.01*	*<0.01*	*0.02*	*0.30*	*<0.01*	*<0.01*	*0.30*	*0.38*	*<0.01*	*<0.01*	*0.39*	0.69	0.01	0.70
GW191127_050227	⋯	*0.34*	*0.14*	*<0.01*	*0.49*	0.73	<0.01	<0.01	0.73	*0.47*	*<0.01*	*<0.01*	*0.47*	0.74	<0.01	0.74
GW191129_134029	⋯	>0.99	<0.01	<0.01	>0.99	>0.99	<0.01	<0.01	>0.99	0.72	0.28	<0.01	>0.99	0.72	0.28	>0.99
GW191204_171526	>0.99	>0.99	<0.01	<0.01	>0.99	>0.99	<0.01	<0.01	>0.99	0.98	0.02	<0.01	>0.99	0.98	0.02	>0.99
GW191216_213338	⋯	>0.99	<0.01	<0.01	>0.99	>0.99	<0.01	<0.01	>0.99	0.91	0.09	<0.01	>0.99	0.91	0.09	>0.99
GW191219_163120	⋯	⋯	⋯	⋯	⋯	⋯	⋯	⋯	⋯	0.20	0.63	<0.01	0.82	⋯	⋯	⋯
GW191222_033537	>0.99	>0.99	<0.01	<0.01	>0.99	>0.99	<0.01	<0.01	>0.99	>0.99	<0.01	<0.01	>0.99	>0.99	<0.01	>0.99
GW200115_042309	⋯	<0.01	>0.99	<0.01	>0.99	<0.01	>0.99	<0.01	>0.99	<0.01	0.93	0.07	>0.99	⋯	⋯	⋯
GW200202_154313	⋯	>0.99	<0.01	<0.01	>0.99	⋯	⋯	⋯	⋯	⋯	⋯	⋯	⋯	0.67	0.33	>0.99
GW200210_092254	⋯	*0.40*	*0.03*	*<0.01*	*0.42*	⋯	⋯	⋯	⋯	0.31	0.22	<0.01	0.53	0.31	0.23	0.54
GW200316_215756	⋯	>0.99	<0.01	<0.01	>0.99	*0.30*	*<0.01*	*<0.01*	*0.30*	0.98	<0.01	<0.01	0.98	0.95	0.03	0.98

In addition to the choice of prior on count, $p_{\rm BNS}$, $p_{\rm NSBH}$, and $p_{\rm BBH}$ also depend upon the assumed foreground and background. The methods to redistribute the foreground probabilities across astrophysical source classes are specific to individual detection pipelines:

(i) GstLAL classifies signals into BNS, NSBH, and BBH using a semianalytic template weighting scheme [667], which is needed for a multicomponent $p_{\rm astro}$ calculation [115]. The response of each template to signals from the different categories is computed assuming Gaussian noise [667] instead of using simulated signals. For a given trigger, the template identified for this classification is the one which has the highest SNR divided by the value of the signal-based-veto test, rather than the one with the highest likelihood ratio.

(ii) For MBTA, the fraction of recovered simulated signals from each category is used to infer the probabilities [117]. Following GWTC-2.1 [4], this analysis assumes an astrophysical population where BNSs have a maximum component mass of $2.5M_\odot$, NSBHs have one component above $2.5M_\odot$ and one below $2.5M_\odot$, and BBHs have both components above $5M_\odot$. While this division between NSs and BHs does not match the other analyses, it should preserve our goal of the BBH category only including confident BHs with masses above $3M_\odot$, while the BNS and NSBH categories include any systems that could contain a NS (as well as potentially some low-mass BHs).

(iii) For PyCBC, categories are assigned based on the source chirp mass. This is estimated by correcting the redshifted template masses using a luminosity distance derived from the SNRs [613]. As the PyCBC-BBH analysis is not sensitive to redshifted chirp masses below $4.353M_\odot$ (corresponding to an equal-mass binary with components of $5M_\odot$), we do not calculate $p_{\rm BNS}$ for this analysis.

(iv) As discussed above, cWB is most sensitive to BBH signals, and, in this analysis, BBHs are the only astrophysical source class considered for this pipeline. The assumption that all signals identified by cWB correspond to CBCs is discussed further in Appendix F.

Given our current uncertainties on the maximum NS mass and minimum BH mass, the three categories do not necessarily reflect the true nature of the source, but should serve to highlight candidates of interest if looking for potential BNSs or NSBHs, or a clean sample of BBHs.

The precise values of astrophysical source-class probabilities are generally insensitive to assumptions for candidates confidently identified as noise ($p_{\rm astro} \sim 0$) or signal ($p_{\rm astro} \sim 1$). However, marginal $p_{\rm astro}$ estimates ($p_{\rm astro} \sim 0.5$) tend to fluctuate by $\mathcal{O}(0.1)$ based on various choices made [117]:

(i) The choice of distribution of masses used to estimate the foreground model. Since the true distribution of BNSs, NSBHs, and BBHs is unknown, the marginal $p_{\rm astro}$ values are subject to this uncertainty.

(ii) The choice of injection distributions used to assess the response of the template banks to different astrophysical source classes. Given our lack of knowledge of the true distribution of intrinsic parameters for BNS, NSBH, and BBH systems, uncertainties germane to this choice are especially pertinent to the MBTA estimations of $p_{\rm astro}$. For GstLAL, the classification is most sensitive to the choice of upper limit on the NS mass distribution, as only triggers falling close to this threshold will have an ambiguous classification. For PyCBC, the corresponding uncertainty comes from the choice of threshold on $\mathcal{M}$ used to assign a candidate to the BBH source class. Using the response of the template as a means to account for biases in the template-based estimate of intrinsic parameters is itself expected to be suboptimal as compared to a full inference of these parameters, and is therefore itself a source of uncertainty.

(iii) The location of the boundary between source classes in mass space. The upper limit on the NS mass is set at $3M_\odot$, although the true boundary is unknown. Marginal candidates with components close to this boundary could have significantly different $p_{\rm astro}$ depending on which side of the boundary the template estimates of their masses put them. For example, a marginal candidate categorized as BBH would have a larger $p_{\rm astro}$ than the same candidate categorized as NSBH, since $p_{\rm astro}$ depends on the number of foreground candidates pertaining to these source categories; this is the case of GW191219_163120.

(iv) Specifically for single-detector candidates, the background distribution must be extrapolated to evaluate the background probability. For coincident candidates, the background models are built from random coincidences from data between pairs of detectors time shifted with respect to each other, which is not possible for single-detector candidates.

While the above captures some of the primary factors that affect the values of marginal $p_{\rm astro}$, the list is not exhaustive. Marginal $p_{\rm astro}$ values also depend on other factors which are specific to the analysis methods used by different detection pipelines. Additionally, we expect that the estimated values of $p_{\rm astro}$ may change as we learn more about the various astrophysical populations.

TABLE XIV. Sensitive hypervolume $\langle VT \rangle$ for the various search analyses for all of O3 at the assessed points in the mass parameter space. The Any results come from calculating the sensitive hypervolume for injections found by at least one search analysis. The sets of binary masses and distribution of injections found in this bin are the same as given in Table III. As in Table III, where insufficient numbers of injections are recovered such that the sensitive hypervolume cannot be accurately estimated; these cases are indicated by three center dots $(\cdots)$.

Binary masses ($M_\odot$)			Sensitive hypervolume (Gpc^3 yr)					
m_1	m_2	$\mathcal{M}$	cWB	GstLAL	MBTA	PyCBC-broad	PyCBC-BBH	Any
35.0	35.0	30.5	$5.5^{+0.1}_{-0.2}$	$8.8^{+0.2}_{-0.2}$	$7.4^{+0.2}_{-0.2}$	$6.9^{+0.1}_{-0.2}$	$9.2^{+0.2}_{-0.2}$	$11.2^{+0.2}_{-0.2}$
35.0	20.0	22.9	$2.7^{+0.1}_{-0.2}$	$4.9^{+0.2}_{-0.2}$	$3.9^{+0.2}_{-0.1}$	$3.9^{+0.2}_{-0.1}$	$5.3^{+0.2}_{-0.2}$	$6.4^{+0.2}_{-0.2}$
35.0	1.5	5.2	$\cdots$	$3.8^{+0.3}_{-0.4} \times 10^{-2}$	$3.7^{+0.4}_{-0.4} \times 10^{-2}$	$6.2^{+0.4}_{-0.5} \times 10^{-2}$	$\cdots$	$6.6^{+0.5}_{-0.5} \times 10^{-2}$
20.0	20.0	17.4	$1.19^{+0.05}_{-0.05}$	$2.82^{+0.08}_{-0.08}$	$2.41^{+0.07}_{-0.08}$	$2.38^{+0.07}_{-0.08}$	$2.99^{+0.09}_{-0.08}$	$3.57^{+0.09}_{-0.09}$
20.0	10.0	12.2	$0.48^{+0.05}_{-0.05}$	$1.25^{+0.07}_{-0.07}$	$1.10^{+0.06}_{-0.07}$	$1.14^{+0.07}_{-0.07}$	$1.32^{+0.07}_{-0.08}$	$1.56^{+0.08}_{-0.08}$
20.0	1.5	4.2	$\cdots$	$3.9^{+0.2}_{-0.3} \times 10^{-2}$	$3.4^{+0.3}_{-0.2} \times 10^{-2}$	$5.4^{+0.3}_{-0.3} \times 10^{-2}$	$\cdots$	$6.0^{+0.3}_{-0.4} \times 10^{-2}$
10.0	10.0	8.7	$0.15^{+0.01}_{-0.01}$	$0.59^{+0.02}_{-0.03}$	$0.53^{+0.02}_{-0.02}$	$0.56^{+0.03}_{-0.02}$	$0.59^{+0.03}_{-0.02}$	$0.72^{+0.02}_{-0.03}$
10.0	5.0	6.1	$3.6^{+0.9}_{-0.8} \times 10^{-2}$	$0.25^{+0.02}_{-0.03}$	$0.23^{+0.02}_{-0.02}$	$0.27^{+0.02}_{-0.03}$	$0.26^{+0.02}_{-0.02}$	$0.31^{+0.02}_{-0.02}$
10.0	1.5	3.1	$\cdots$	$3.5^{+0.1}_{-0.2} \times 10^{-2}$	$3.3^{+0.2}_{-0.1} \times 10^{-2}$	$3.8^{+0.1}_{-0.2} \times 10^{-2}$	$\cdots$	$4.5^{+0.1}_{-0.2} \times 10^{-2}$
5.0	5.0	4.4	$1.1^{+0.2}_{-0.2} \times 10^{-2}$	$0.129^{+0.007}_{-0.006}$	$9.8^{+0.6}_{-0.6} \times 10^{-2}$	$0.138^{+0.007}_{-0.007}$	$0.108^{+0.006}_{-0.006}$	$0.158^{+0.008}_{-0.007}$
5.0	1.5	2.3	$\cdots$	$2.34^{+0.08}_{-0.08} \times 10^{-2}$	$2.41^{+0.08}_{-0.08} \times 10^{-2}$	$2.47^{+0.08}_{-0.08} \times 10^{-2}$	$\cdots$	$2.96^{+0.09}_{-0.09} \times 10^{-2}$
1.5	1.5	1.3	$\cdots$	$5.8^{+0.2}_{-0.1} \times 10^{-3}$	$7.0^{+0.2}_{-0.2} \times 10^{-3}$	$7.3^{+0.2}_{-0.2} \times 10^{-3}$	$\cdots$	$8.2^{+0.2}_{-0.2} \times 10^{-3}$

Using the expanded list of candidates including the subthreshold candidates, it is possible to use updated population models to reevaluate $p_{\rm astro}$ and compile revised lists of probable GW candidates.

a. Results for all of O3

Here we present results from all of O3, giving sensitivity estimates for the points in parameter space discussed in Sec. IV E 1 from injections covering all of O3, and the updated $p_{\rm astro}$ for candidates in O3a given the updated event-rate information inclusive of O3b.

The sensitive hypervolume $\langle VT\rangle$ for each search analysis for all of O3 is presented in Table XIV. These results show the same trends as shown in Table III and Fig. 6 for O3b. However, the values are naturally larger on account of the greater observing time.

Finally, in Table XV we provide updated calculations of $p_{\rm astro}$ for O3a candidates which were published in GWTC-2.1 [4] with $p_{\rm astro} > 0.5$ using data from all of O3. For the first time for these candidates, we also report $p_{\rm astro}$ as calculated by the cWB pipeline. While there are small changes in value compared to the calculation using only O3a data, there are no changes in the list of candidates with $p_{\rm astro} > 0.5$. The change in $p_{\rm astro}$ for GW190425, from 0.78 in GWTC-2.1 to 0.69 here, stems from the increased $\langle VT\rangle$ with no new confirmed BNS detection in O3b, and illustrates how medium-range $p_{\rm astro}$ values are subject to vary with our knowledge of source populations.

TABLE XV. Updated probability of astrophysical origin $p_{\rm astro}$, FAR, and SNR values for candidates from O3a using data from the whole of O3. We include $p_{\rm astro}$ values for any candidates that were published in GWTC-2.1 [4] with $p_{\rm astro} > 0.5$. Using all of the O3 data, there are no changes to the list of candidates with $p_{\rm astro} > 0.5$. As in Table I, results in italics indicate where an analysis found the candidate with $p_{\rm astro} < 0.5$, and three center dots (…) indicate that a candidate was not found by an analysis. Although cWB contributed to the analysis of GW190814 [241], it is not included in the cWB column because it was not detected with LV alone with the standard data-quality vetoes, but required a manual override of the LIGO Hanford vetoes. This table updates Table I of GWTC-2.1 [4].

	cWB			GstLAL			MBTA			pyCBC-broad			pyCBC-BBH		
Name	FAR (yr^{-1})	SNR	$p_{\rm astro}$	FAR (yr^{-1})	SNR	$p_{\rm astro}$	FAR (yr^{-1})	SNR	$p_{\rm astro}$	FAR (yr^{-1})	SNR	$p_{\rm astro}$	FAR (yr^{-1})	SNR	$p_{\rm astro}$
GW190403_051519	…	…	…	…	…	…	…	…	…	…	…	…	7.7	8.0	0.60
GW190408_181802	9.5×10^{-4}	14.8	>0.99	$<1.0\times10^{-5}$	15	>0.99	8.7×10^{-5}	14	>0.99	2.5×10^{-4}	13	>0.99	$<1.2\times10^{-4}$	14	>0.99
GW190412	9.5×10^{-4}	19.7	>0.99	$<1.0\times10^{-5}$	19	>0.99	1.0×10^{-5}	18	>0.99	$<1.1\times10^{-4}$	17	>0.99	$<1.2\times10^{-4}$	18	>0.99
GW190413_052954	…	…	…	…	…	…	…	…	…	*170*	*8.5*	*0.12*	0.82	8.5	0.92
GW190413_134308	…	…	…	*39*	*10*	*0.03*	0.34	10	0.99	*21*	*9.3*	*0.47*	0.18	8.9	0.99
GW190421_213856	0.30	9.3	0.90	0.0028	10	>0.99	1.2	9.7	0.99	5.9	10	0.74	0.014	10	>0.99
GW190425	…	…	…	0.034	13	0.69	…	…	…	…	…	…	…	…	…
GW190426_190642	…	…	…	…	…	…	…	…	…	…	…	…	4.1	9.6	0.73
GW190503_185404	0.0018	11.5	>0.99	$<1.0\times10^{-5}$	12	>0.99	0.013	13	>0.99	0.038	12	>0.99	0.0026	12	>0.99
GW190512_180714	0.88	10.7	0.75	$<1.0\times10^{-5}$	12	>0.99	0.038	12	0.98	1.1×10^{-4}	12	>0.99	$<1.1\times10^{-4}$	12	>0.99
GW190513_205428	…	…	…	1.3×10^{-5}	12	>0.99	0.11	13	0.99	*19*	*12*	*0.48*	0.044	12	>0.99
GW190514_065416	…	…	…	*450*	*8.3*	*<0.01*	…	…	…	…	…	…	2.8	8.4	0.75
GW190517_055101	0.0065	10.7	>0.99	0.0045	11	>0.99	0.11	11	>0.99	0.0095	10	>0.99	3.5×10^{-4}	10	>0.99
GW190519_153544	3.1×10^{-4}	14.0	>0.99	$<1.0\times10^{-5}$	12	>0.99	7.0×10^{-5}	14	>0.99	$<1.0\times10^{-4}$	13	>0.99	$<1.1\times10^{-4}$	13	>0.99
GW190521	2.0×10^{-4}	14.4	>0.99	0.20	13	0.77	0.042	13	0.96	0.44	14	0.96	0.0013	14	>0.99
GW190521_074359	1.0×10^{-4}	24.7	>0.99	$<1.0\times10^{-5}$	24	>0.99	1.0×10^{-5}	22	>0.99	$<1.8\times10^{-5}$	24	>0.99	$<2.3\times10^{-5}$	24	>0.99
GW190527_092055	…	…	…	0.23	8.7	0.83	…	…	…	…	…	…	*19*	*8.4*	*0.31*
GW190602_175927	0.015	11.1	>0.99	$<1.0\times10^{-5}$	12	>0.99	3.0×10^{-4}	13	>0.99	0.29	12	0.98	0.013	12	>0.99
GW190620_030421	…	…	…	0.011	11	0.99	…	…	…	…	…	…	…	…	…
GW190630_185205	…	…	…	$<1.0\times10^{-5}$	15	>0.99	…	…	…	…	…	…	0.24	15	>0.99
GW190701_203306	0.32	10.2	0.89	0.0057	12	>0.99	35	11	0.85	0.064	12	>0.99	0.56	12	>0.99
GW190706_222641	0.0010	12.7	>0.99	5.0×10^{-5}	13	>0.99	0.0015	12	>0.99	3.7×10^{-4}	12	>0.99	0.34	13	>0.99
GW190707_093326	…	…	…	$<1.0\times10^{-5}$	13	>0.99	0.032	13	>0.99	$<1.0\times10^{-5}$	13	>0.99	$<1.9\times10^{-5}$	13	>0.99
GW190708_232457	…	…	…	3.1×10^{-4}	13	>0.99	…	…	…	…	…	…	…	…	…
GW190719_215514	…	…	…	…	…	…	…	…	…	…	…	…	0.63	8.0	0.91
GW190720_000836	…	…	…	$<1.0\times10^{-5}$	12	>0.99	0.094	12	>0.99	1.4×10^{-4}	11	>0.99	$<7.8\times10^{-5}$	11	>0.99

(Table continued)

TABLE XV. *(Continued)*

	cWB			GstLAL			MBTA			pyCBC-broad			pyCBC-BBH		
Name	FAR (yr^{-1})	SNR	p_{astro}	FAR (yr^{-1})	SNR	p_{astro}	FAR (yr^{-1})	SNR	p_{astro}	FAR (yr^{-1})	SNR	p_{astro}	FAR (yr^{-1})	SNR	p_{astro}
GW190725_174728	···	···	···	···	···	···	3.1	9.8	0.56	0.46	9.1	0.96	2.9	8.8	0.80
GW190727_060333	0.088	11.4	0.95	$<1.0\times10^{-5}$	12	>0.99	0.023	12	>0.99	0.0056	11	>0.99	2.0×10^{-4}	11	>0.99
GW190728_064510	···	···	···	$<1.0\times10^{-5}$	13	>0.99	7.5×10^{-4}	13	>0.99	$<8.2\times10^{-5}$	13	>0.99	$<7.8\times10^{-5}$	13	>0.99
GW190731_140936	···	···	···	0.33	8.5	0.76	6.1	9.1	0.78	···	···	···	1.9	7.8	0.83
GW190803_022701	···	···	···	0.073	9.1	0.93	77	9.0	0.95	*81*	*8.7*	*0.16*	0.39	8.7	0.97
GW190805_211137	···	···	···	···	···	···	···	···	···	···	···	···	0.63	8.3	0.95
GW190814	···	···	···	$<1.0\times10^{-5}$	22	>0.99	2.0×10^{-4}	20	>0.99	0.17	19	>0.99	···	···	···
GW190828_063405	9.6×10^{-4}	16.6	>0.99	$<1.0\times10^{-5}$	16	>0.99	1.0×10^{-5}	15	>0.99	$<8.5\times10^{-5}$	14	>0.99	$<7.0\times10^{-5}$	16	>0.99
GW190828_065509	···	···	···	3.5×10^{-5}	11	>0.99	0.16	11	0.96	2.8×10^{-4}	11	>0.99	1.1×10^{-4}	11	>0.99
GW190910_112807	···	···	···	0.0029	13	>0.99	···	···	···	···	···	···	···	···	···
GW190915_235702	0.0010	12.3	>0.99	$<1.0\times10^{-5}$	13	>0.99	0.0055	13	>0.99	6.8×10^{-4}	13	>0.99	$<7.0\times10^{-5}$	13	>0.99
GW190916_200658	···	···	···	*12*	*8.2*	*0.08*	6.9×10^{3}	8.2	0.62	···	···	···	4.7	7.9	0.62
GW190917_114630	···	···	···	0.66	9.5	0.74	···	···	···	···	···	···	···	···	···
GW190924_021846	···	···	···	$<1.0\times10^{-5}$	13	>0.99	0.0049	12	>0.99	$<8.2\times10^{-5}$	12	>0.99	8.3×10^{-5}	12	>0.99
GW190925_232845	···	···	···	···	···	···	*100*	*9.4*	*0.32*	*73*	*9.0*	*0.03*	0.0072	9.9	0.99
GW190926_050336	···	···	···	1.1	9.0	0.51	···	···	···	···	···	···	*87*	*7.8*	*0.09*
GW190929_012149	···	···	···	0.16	10	0.86	2.9	10	0.61	*120*	*9.4*	*0.14*	*14*	*8.5*	*0.40*
GW190930_133541	···	···	···	0.43	10	0.74	0.34	10.0	0.86	0.018	9.8	>0.99	0.012	10	>0.99

APPENDIX E: PARAMETER-ESTIMATION METHODS

To determine the astrophysical parameters of each signal's source, we employ statistical inference techniques on the data from the interferometers. We calculate the posterior probability distribution $p(\vec{\theta}|d)$ for the source parameters $\vec{\theta}$ using Bayes's theorem [668],

$$p(\vec{\theta}|d) \propto p(d|\vec{\theta})p(\vec{\theta}), \tag{E1}$$

where the posterior is proportional to the prior probability distributions on the parameters $p(\vec{\theta})$, and the likelihood $p(d|\vec{\theta})$, which is the probability the data d would be observed given a model with parameters $\vec{\theta}$. Our analysis matches that performed for GWTC-2.1 [4].

Results from a number of analysis pipelines are presented in this work, but the principles used to construct the likelihood are the same for each [131]. The data from each interferometer are analyzed coherently, making the assumption that the noise can be treated as stationary, Gaussian, and independent between each of the interferometers used in the analysis over the duration analyzed for each signal [96,669]. These assumptions result in a Gaussian likelihood [135] for a single interferometer,

$$p(d^k|\vec{\theta}) \propto \exp\left[-\frac{1}{2}\langle d^k - h^k_M | d^k - h^k_M\rangle\right], \tag{E2}$$

where d^k is the data and h^k_M the waveform model evaluated at $\vec{\theta}$ as measured by the interferometer (incorporating the detector response [670,671] and adjusted for detector calibration). The operation $\langle\cdot|\cdot\rangle$ represents the noise-weighted inner product [382], which requires the precalculation of the PSD of the noise, and a choice of frequency ranges over which the product should be calculated:

(i) The minimum frequency f_{low} for the inner product is chosen to be 20 Hz.

(ii) The maximum frequency is set as $f_{\mathrm{high}} = \alpha^{\text{roll-off}}(f_s/2)$, where f_s is the sampling frequency ($f_s/2$ is the Nyquist frequency), and $\alpha^{\text{roll-off}}$ is included to avoid power loss due to the application of a window function. We limit power loss to 1%, which for the adopted Butterworth filter [146,376] requires $\alpha^{\text{roll-off}} = 0.875$. To limit computational cost, the sampling rate is typically limited to $f_s = 4096$ Hz or $f_s = 8192$ Hz, and a lower rate is used when f_{high} is high enough to fully resolve the $(\ell, |m|) = (3, 3)$ multipole moments. Given current detector sensitivity, we do not expect to gain significant information by using sampling rates above $f_s \sim 4096$ Hz.

(iii) The noise PSD for each candidate is estimated using BayesWave [379,672]. The PSD is either estimated using the same data used for the likelihood calculation or for an equivalent length of adjacent data. We use the median inferred PSD value at each frequency [673,674]. The various PSDs are precalculated for each candidate and used in each of the parameter-estimation studies for that candidate.

TABLE XVI. List of data used and mitigation methods applied to data surrounding each candidate prior to source-parameter estimation. We list the candidates for which we perform mitigation of instrumental artifacts; there are seven candidates reported in Table I and the previously reported GW200105_162426 [8]. For all analyses using Virgo data, calibration error at approximately 50 Hz is mitigated by notching out the relevant frequency range. The noise-subtraction methods (BayesWave [377,379] glitch modeling and gwsubtract linear subtraction using a witness [44,59]) used for these candidates are detailed in Appendix C.

Candidate	Affected detectors	Mitigation
GW191105_143521	Virgo	BayesWave deglitching
GW191109_010717	Hanford, Livingston	BayesWave deglitching
GW191113_071753	Hanford	BayesWave deglitching
GW191127_050227	Hanford	BayesWave deglitching
GW191219_163120	Hanford, Livingston	BayesWave deglitching
GW200105_162426	Livingston	BayesWave deglitching
GW200115_042309	Livingston	BayesWave deglitching
GW200129_065458	Livingston	Linear subtraction

The duration of the data analyzed for each candidate is chosen such that the evolution of the signal from $f_{\rm low}$ to merger and ringdown is captured, and that there is 2 s of data postmerger [4]. The overall likelihood of data from across the detector network is obtained by multiplying together the single-detector likelihoods for the given set of parameters.

As described in Appendix E 3, we marginalize over the uncertainty in the strain calibration. The frequency and phase calibration uncertainties are modeled using frequency-dependent splines. The coefficients of these splines are allowed to vary alongside the signal parameters with prior distributions on each spline node informed by the measured uncertainty at each node [131]. Preliminary studies [675,676] have shown that, given the SNR of the candidates during O3, the calibration systematic errors are expected to have negligible impact on the estimation of the astrophysical parameters.

1. Data-quality mitigation

For candidates affected by transient, non-Gaussian detector noise, as part of the event-validation process described in Sec. III B, we perform data-quality mitigation prior to performing source-parameter estimation, as summarized in Table XVI. Where possible, noise transients are modeled and subtracted with the BayesWave algorithm [377,379], or with the gwsubtract algorithm using a witness time series [44,59], as described in Appendix C. Such subtraction is first used to mitigate the effects of a glitch that appear in data from the LIGO Livingston detector overlapping GW170817 [126,677].

When analyzing Virgo data, the systematic error in calibration around 50 Hz described in Sec. III A is mitigated by setting the PSD to a large value ($1\ \mathrm{Hz}^{-1/2}$) for 46–51 Hz, such that the affected data do not influence the results.

2. Waveforms

The waveform models used to analyze each candidate are selected depending upon the most likely source for the signal. Each candidate undergoes an initial parameter-estimation analysis shortly after the candidate is first identified. This is used to roughly infer the component masses (and other properties) of the binary source of the candidate signal, which are used to verify analysis settings. A further, more exhaustive set of parameter-estimation analyses are conducted to produce final results. To assess potential systematic uncertainties from waveform modeling, we perform analyses with two waveform families [131].

In cases with component masses in excess of $3M_{\odot}$, analyses are conducted using the `SEOBNRv4PHM` [137] and `IMRPhenomXPHM` [136] waveform models. The `NRSur7dq4` NR surrogate model [678], previously used in a subset of analyses in GWTC-2 [3], is restricted in its length to only approximately 20 orbits before the merger, and so not generally applicable for analysis of the candidates in this catalog. The `SEOBNRv4PHM` waveform is part of the `SEOBNR` waveform family [625,663]. It is a time-domain model that is constructed by first deriving a time-dependent rotation from the coprecessing to the inertial frame using the EOB equations of motion [679,680] for the spins and orbital angular momentum, and then applying this rotation to the nonprecessing (incorporating only spins parallel to the orbital angular momentum) `SEOBNRv4HM` waveform. The `SEOBNRv4HM` model is computed by solving the EOB equations obtained by resumming PN corrections and incorporating information from NR simulations and BH perturbation theory [141]. To model spin precession, `SEOBNRv4PHM` numerically evolves the EOB dynamics of the system, including the spins in the time domain [137]. Since `SEOBNRv4PHM` inherits its higher-order multipole moment content from `SEOBNRv4HM`, it

includes the modes $(\ell, |m|) = \{(2,2), (2,1), (3,3), (4,4), (5,5)\}$ in the coprecessing frame. The `IMRPhenomXPHM` model is the latest in the `Phenom` family of phenomenological, frequency-domain GW models, and is built upon the higher-order multipole model `IMRPhenomXHM` [140]. Each of the available higher-order multipole moments modeled in `IMRPhenomXHM`, $(\ell, |m|) = \{(2,2), (2,1), (3,3), (3,2), (4,4)\}$, is tuned to NR and is rapidly generated through the use of frequency multibanding [681]. `IMRPhenomXPHM` includes precession effects by performing a frequency-dependent rotation on the nonprecessing GW waveform `IMRPhenomXHM` [140,279,363,682,683]. The angles used arise from a multiscale expansion of the PN equations of motion [291]. Neither waveform models the asymmetry between spherical harmonic modes with positive and negative spherical harmonic index m [684], and neither is tuned to NR in the precessing sector, but both are validated by comparing to a large set of BBH waveforms [136,137].

When the initial parameter estimation provides evidence that the secondary mass is below $3M_\odot$, then the signal may arise from a NSBH. In these cases, waveforms that include matter effects can be used to try to identify their imprint on the signal. We use the `SEOBNRv4_ROM_NRTidalv2_NSBH` [139] and `IMRPhenomNSBH` [138] waveforms. Both are nonprecessing, frequency-domain NSBH waveforms built upon previous nonprecessing, frequency-domain BBH waveform models: `SEOBNRv4_ROM` [625] for `SEOBNRv4_ROM_NRTidalv2_NSBH`, and a combination of the `IMRPhenomC` [283] amplitude and `IMRPhenomD` [685] phase for `IMRPhenomNSBH`. These models include corrections to the phase arising from matter effects as in `IMRPhenomPv2_NRTidalv2`, but have additional corrections to the amplitude tuned to NSBH NR waveforms.

For BBHs, the mass and spin of the final BH are calculated from the initial masses and spins using fits to NR results [237,238,304,686,687]. When using NSBH waveforms, the mass and spin of the final BH are calculated from the initial masses, the initial BH spin, and the NS tidal deformability Λ_2 using fits to NR results [688]. These fits are calibrated to BBH fits [238] in order to recover the BBH values in the test-mass limit ($m_2 \to 0$) and in the absence of tides ($\Lambda_2 \to 0$).

None of the waveform models employed for the analyses presented here include the effects of orbital eccentricity, and instead assume that all binaries follow quasicircular orbits. An eccentric source can be interpreted by a quasicircular analysis to be both higher mass and more equal mass than it truly is [393,396–398,689]. Consequently, if any sources analyzed here have eccentric orbits, their true masses may be lower and their mass ratios more unequal than our inferred values. Eccentricity may also influence the inferred spins [396–398,690]. Significant eccentricity is not expected for the majority of sources considered here [97,691].

3. Priors and sampling algorithms

To ensure that the parameter space for each candidate is explored adequately, each candidate is analyzed independently, with a choice of prior ranges for parameters that balance the required analysis time with the total volume of parameter space to be sampled. For all candidates, we choose a uniform prior over spin magnitudes and redshifted component masses, and an isotropic prior over spin orientation, sky location, and binary orientation [3,14]. The default mass-ratio prior is $q \in [0.05, 1]$ to reflect the range of calibration for our waveform models [136,137]. However, some candidates show strong support for mass ratios outside of this range (such as GW191219_163120). In these cases, we extend the priors, as biases due to any waveform inaccuracies are likely subdominant to those from truncating the prior, and we consider prior ranges as wide as $q \in [0.02, 1]$. Following GWTC-2 [3], we reweight posteriors to have a luminosity-distance prior corresponding to a uniform merger rate in the source's comoving frame for a Λ-cold-dark-matter cosmology with $H_0 = 67.9\ \mathrm{km\,s^{-1}\,Mpc^{-1}}$ and $\Omega_m = 0.3065$ [662].

We employ a number of different sampling techniques and their associated parameter-estimation pipelines for the candidate signals presented in this work. For the majority of candidates, the Bilby [144,146] and RIFT [147–149] pipelines are used to generate samples from the posterior distributions for each signal.

Bilby provides support for both Markov-chain Monte Carlo samplers and nested sampling techniques [144]. We use the Dynesty [424] sampler, which uses nested sampling to sample the posterior probability distribution. Analyses are organized using BilbyPipe which enables greater automation and reproducibility of analysis pipeline construction [146]. We use Bilby for inferences using the `IMRPhenomXPHM` [136] model.

For candidates where more computationally expensive analyses are required, for example, using waveforms that include matter effects, we use the Parallel Bilby code [145]. This employs a highly parallel distributed approach to nested sampling that can be run over a large number of processing cores, reducing the wall time of the required computation.

To improve the sampling performance of Bilby and Parallel Bilby, the posterior distribution is analytically marginalized over luminosity distance [129] and geocenter time [146,692] prior to sampling. We reconstruct posterior distributions for marginalized parameters in postprocessing: For each sample, we interpolate over a one-dimensional likelihood computed at discrete points within the prior of the marginalized parameter, and draw one value from this posterior probability curve [146,150].

For time-domain, computationally expensive waveforms, we use RIFT [693]. This algorithm constructs the posterior probability distribution iteratively with two alternating steps. First, for a grid of intrinsic-parameter

points, a marginalized likelihood is evaluated by integrating over extrinsic parameters (source position, orientation, and coalescence time) [147]. From this discrete grid of likelihoods, a continuous likelihood distribution is constructed via Gaussian-process regression. A new grid is then sampled from the resulting posterior probability distribution; this process is repeated until convergence is reached. RIFT's grid-based approach has been shown to produce results consistent with our stochastic sampling algorithms [693].

To marginalize over calibration uncertainty [131,694], the calibration coefficients are sampled alongside the source parameters in inferences performed by Bilby and Parallel Bilby [146], whereas for RIFT, this marginalization is done using likelihood reweighting (with the same spline calibration model) after the inference of the source parameters [675].

All sampling algorithms return posterior samples in the same format, and these are postprocessed using PESUMMARY [425] to produce uniform HDF5 results. In the preparation of GWTC-2 [3], we employ some automation to assist with monitoring the parameter-estimation processes as they run. For GWTC-2.1 and GWTC-3, we further develop this automation into the Asimov [426] code. This allows the creation of analysis pipeline configurations to be fully automated, with the intention of ensuring consistency between analysis settings used for different algorithms.

The settings for the Bilby and RIFT analyses are designed to be as consistent as possible, aside from the differences in waveforms used. However, there do exist a number of differences between the analyses, such as the marginalization over time and the tapering applied to time-domain waveforms, that may lead to differences in results. Any differences should be negligible for intrinsic parameters such as the masses. In cases where the Bilby and RIFT parameters agree, we can be more confident in the robustness of results.

APPENDIX F: UNCONFIRMED cWB-ONLY CANDIDATES

The minimally modeled cWB pipeline (described in Sec. IV B) can identify a range of signal morphologies, including signals unrelated to CBC sources [31]. Since cWB does not exploit the rich prior information provided by CBC waveform templates, its flexibility in identifying many potential signals comes with a reduced sensitivity to CBC signals that match such templates as compared to the matched-filter analyses. However, for the O3 analyses, we find that the efficiency of detection of cWB becomes comparable to that of matched-filter pipelines for systems with $(1+z)\mathcal{M} \gtrsim 150M_{\odot}$, and it is possible for cWB to identify CBC signals that would otherwise be omitted from the candidate list. In selecting candidates for Table I, we use a criterion that the probability of astrophysical origin assuming a CBC source is $p_{\rm astro} > 0.5$; as explained in Sec. IV D, because we cannot assume that a candidate identified by the cWB pipeline is consistent with a CBC origin, we require independent support from a template-based search pipeline.

Here we discuss three candidates from cWB that would have $p_{\rm astro} > 0.5$ assuming a CBC source, but for which we do not have the counterpart from the matched-filter search pipelines required to corroborate the CBC source assumption. The candidates 190804_083543 and 190930_234652 were found during O3a, and 200214_224526 was found during O3b. These three candidates have FAR $< 2.0\ \mathrm{yr}^{-1}$, meeting the threshold for marginal candidates. The candidate 190804_083543 was also studied in the O3 minimally modeled search for short-duration transient signals [31], and the candidate 200214_224526 was further studied in the O3 search for IMBH binaries [26]. In each case, we find that the analysis and interpretation of the data is made more difficult by the presence of glitches, as illustrated in Fig. 16. The detailed reconstructed signal morphology is shown in Fig. 17, which displays the time-frequency map [89,108]. For a CBC signal, we would typically expect the reconstructed signal to show a chirp from lower to higher frequencies, with higher-mass sources being limited to lower frequencies and shorter durations [109,657]. However, we find that the three candidates have a range of signal morphologies.

The candidate 190804_083543 was identified in low latency by the cWB BBH search analyzing HL network data, and in the offline analysis its SNR is 13.3 and FAR is $0.024\ \mathrm{yr}^{-1}$. It occurs less than a second after a loud series of glitches in the LIGO Livingston detector. The time around these glitches is vetoed by a Burst category 2 flag that measures length sensing and control channels [63]. Similar sequences of glitches have been observed at other times for both the LIGO Livingston and LIGO Hanford detectors [695]. In O3, it was observed that times around these loud glitches produced a higher rate of background triggers in the cWB analysis, and we consider this candidate of likely instrumental origin.

The candidate 190930_234652 was identified in low latency by the cWB BBH search analyzing HL network data, and in the offline analysis its SNR is 8.6 and FAR is $1.0\ \mathrm{yr}^{-1}$. Slow scattering glitches [69] are present in the LIGO Hanford data at the time of the candidate. These glitches correlate with the observed motion of the suspension systems and directly overlap the candidate. At LIGO Livingston, excess motion was measured by accelerometers at the time of the candidate that may also account for the observed signal in that detector's data. We consider this candidate of likely instrumental origin.

The candidate 200214_224526 was identified in low latency by the cWB BBH search analyzing HL network data, and in the offline analysis its SNR is 13.1 and FAR is $0.13\ \mathrm{yr}^{-1}$. In LIGO Livingston, the candidate is associated

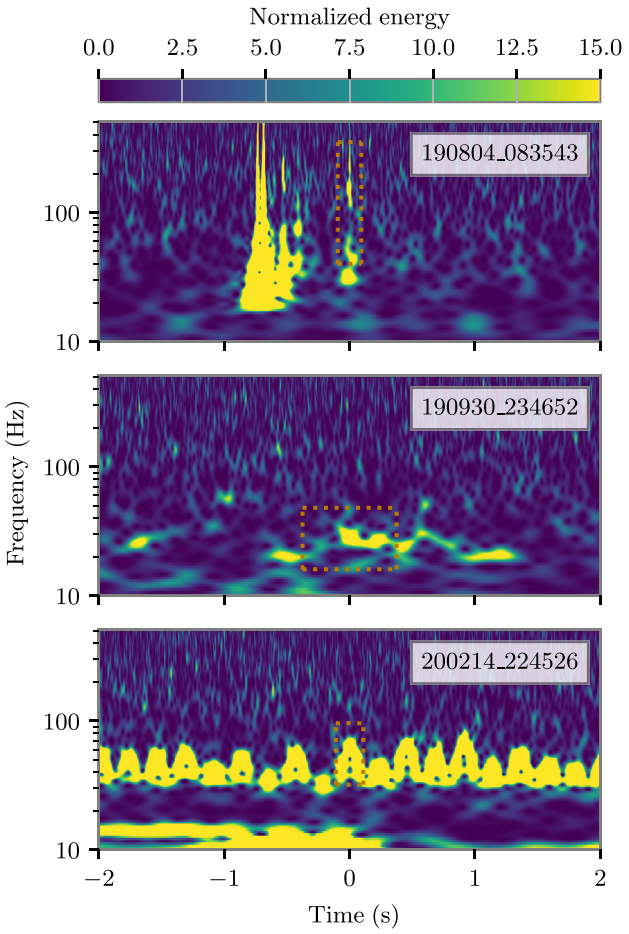

FIG. 16. Spectrograms [73] of data surrounding 190804_083543, 190930_234652, and 200214_224526. Time is plotted relative to the central time of each trigger. The plotted data are from LIGO Hanford for 190930_234652 and from LIGO Livingston for 190804_083543 and 200214_224526. The red box represents the bandwidth and duration of the candidate identified by cWB. In all three cases, the data are affected by transient noise at the time of the trigger, and additional excess power is present in the data that is not accounted for as part of the trigger identified by cWB. Although there is power present in the other detectors, the evidence for instrumental origin of the candidate in one detector makes it likely that this is just a chance coincidence.

with a fast scattering glitch [69]; a sequence of such glitches is observed for multiple seconds before and after the candidate. As shown in Fig. 16, the glitch overlaps the candidate in LIGO Livingston. In LIGO Hanford, we find evidence of a weak scattering arch that starts approximately 0.5 s before the trigger and lasts approximately 2 s in the frequency range 20–30 Hz. The candidate was studied in the search for IMBH binaries [26], where it was listed as the third-ranked candidate (the first ranked being GW190521). However, it was not corroborated by any matched-filter search analysis, and it was concluded that the trigger was due to noise.

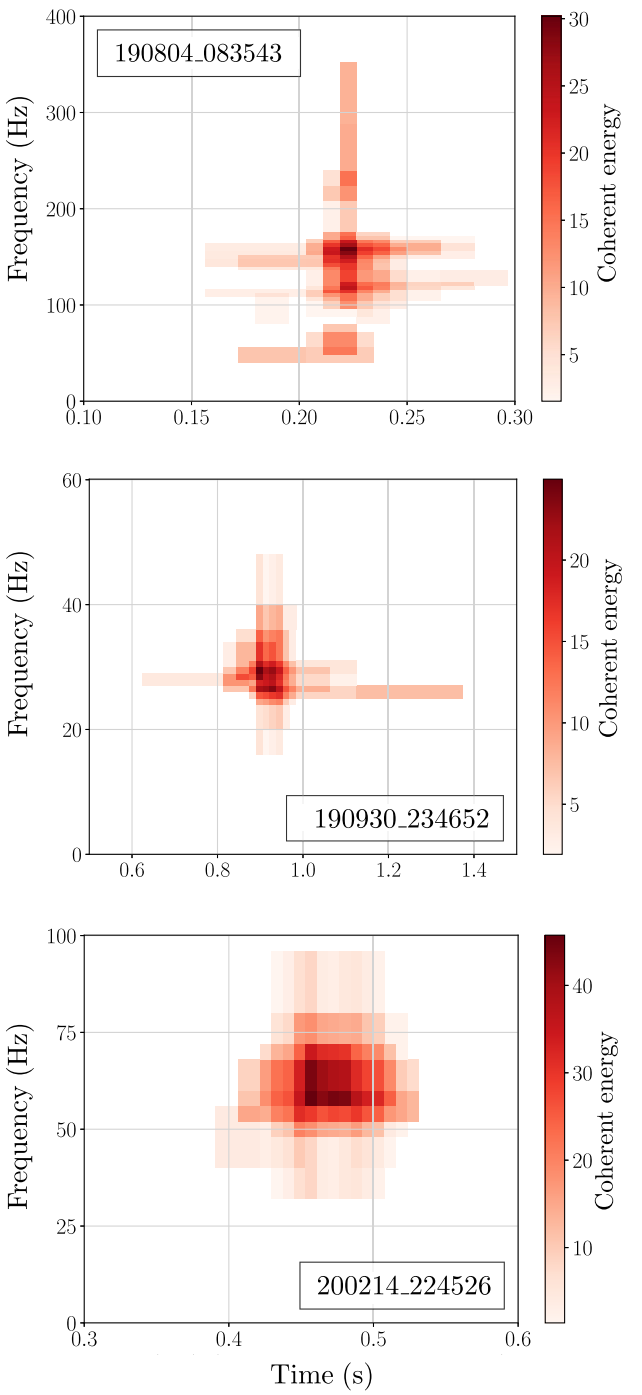

FIG. 17. The coherent-energy time–frequency maps of the three candidates identified by only the cWB analysis. These time-frequency maps are scalograms of the Wilson-Daubechies-Meyer wavelet transform of the candidate signal, where the scale is represented by frequency [89,108], for the coherent energy E_c (see Appendix D 5). The normalization of the coherent energy scale is such that the sum of all the pixel values times their area is equal to the power SNR. The time axis corresponds to GPS times after adding the appropriate offset. For 190804_083543, the offset is 1 248 942 961 s, for 190930_234652, the offset is 1 253 922 430 s, and for 200214_224526, the offset is 1 265 75 5 544 s.

For each of 190804_083543, 190930_234652, and 200214_224526 there is plausible evidence that the candidate is of instrumental origin. Regardless of the instrumental or astrophysical origin of these candidates, their morphologies (as shown in Fig. 17) do not resemble the CBC signals so far detected. The versatility of cWB in identifying potential signals without a template means that a variety of sources could be detected, such that the assumption of a CBC source is not assured and must be verified. Under the alternative assumption of a non-CBC source, the probability of astrophysical origin would be reduced, making any candidates less plausible as GW signals. Detection of new source types, and inference of their rates, would enable calculation of p_{astro} for a range of sources in addition to CBCs.

[1] J. Aasi *et al.* (LIGO Scientific Collaboration), *Advanced LIGO*, Classical Quantum Gravity **32**, 074001 (2015).

[2] F. Acernese *et al.* (Virgo Collaboration), *Advanced Virgo: A Second-Generation Interferometric Gravitational Wave Detector*, Classical Quantum Gravity **32**, 024001 (2015).

[3] R. Abbott *et al.* (LIGO Scientific Collaboration and Virgo Collaboration), *GWTC-2: Compact Binary Coalescences Observed by LIGO and Virgo during the First Half of the Third Observing Run*, Phys. Rev. X **11**, 021053 (2021).

[4] R. Abbott *et al.* (LIGO Scientific Collaboration and Virgo Collaboration), *GWTC-2.1: Deep Extended Catalog of Compact Binary Coalescences Observed by LIGO and Virgo during the First Half of the Third Observing Run*, arXiv:2108.01045.

[5] R. Abbott *et al.* (LIGO Scientific Collaboration, Virgo Collaboration, and KAGRA Collaboration), *The Population of Merging Compact Binaries Inferred Using Gravitational Waves through GWTC-3*, arXiv:2111.03634.

[6] R. Abbott *et al.* (LIGO Scientific Collaboration, Virgo Collaboration, and KAGRA Collaboration), *Tests of General Relativity with GWTC-3*, arXiv:2112.06861.

[7] R. Abbott *et al.* (LIGO Scientific Collaboration, Virgo Collaboration, and KAGRA Collaboration), *Constraints on the Cosmic Expansion History from GWTC-3*, arXiv:2111.03604.

[8] R. Abbott *et al.* (LIGO Scientific Collaboration, Virgo Collaboration, and KAGRA Collaboration), *Observation of Gravitational Waves from Two Neutron Star–Black Hole Coalescences*, Astrophys. J. Lett. **915**, L5 (2021).

[9] C. E. Rhoades, Jr. and R. Ruffini, *Maximum Mass of a Neutron Star*, Phys. Rev. Lett. **32**, 324 (1974).

[10] V. Kalogera and G. Baym, *The Maximum Mass of a Neutron Star*, Astrophys. J. Lett. **470**, L61 (1996).

[11] LIGO Scientific Collaboration and Virgo Collaboration, *LIGO/Virgo Public Alerts User Guide*, LIGO Report No. DCC-P1900171, 2019, https://emfollow.docs.ligo.org/userguide/.

[12] B. P. Abbott *et al.* (LIGO Scientific Collaboration and Virgo Collaboration), *Observation of Gravitational Waves from a Binary Black Hole Merger*, Phys. Rev. Lett. **116**, 061102 (2016).

[13] B. P. Abbott *et al.* (LIGO Scientific Collaboration and Virgo Collaboration), *Binary Black Hole Mergers in the First Advanced LIGO Observing Run*, Phys. Rev. X **6**, 041015 (2016); **8**, 039903(E) (2018).

[14] B. P. Abbott *et al.* (LIGO Scientific Collaboration and Virgo Collaboration), *GWTC-1: A Gravitational-Wave Transient Catalog of Compact Binary Mergers Observed by LIGO and Virgo during the First and Second Observing Runs*, Phys. Rev. X **9**, 031040 (2019).

[15] B. Zackay, T. Venumadhav, L. Dai, J. Roulet, and M. Zaldarriaga, *Highly Spinning and Aligned Binary Black Hole Merger in the Advanced LIGO First Observing Run*, Phys. Rev. D **100**, 023007 (2019).

[16] T. Venumadhav, B. Zackay, J. Roulet, L. Dai, and M. Zaldarriaga, *New Binary Black Hole Mergers in the Second Observing Run of Advanced LIGO and Advanced Virgo*, Phys. Rev. D **101**, 083030 (2020).

[17] A. H. Nitz, T. Dent, G. S. Davies, S. Kumar, C. D. Capano, I. Harry, S. Mozzon, L. Nuttall, A. Lundgren, and M. Tápai, *2-OGC: Open Gravitational-Wave Catalog of Binary Mergers from Analysis of Public Advanced LIGO and Virgo Data*, Astrophys. J. **891**, 123 (2020).

[18] B. Zackay, L. Dai, T. Venumadhav, J. Roulet, and M. Zaldarriaga, *Detecting Gravitational Waves with Disparate Detector Responses: Two New Binary Black Hole Mergers*, Phys. Rev. D **104**, 063030 (2021).

[19] A. H. Nitz, C. D. Capano, S. Kumar, Y.-F. Wang, S. Kastha, M. Schäfer, R. Dhurkunde, and M. Cabero, *3-OGC: Catalog of Gravitational Waves from Compact-Binary Mergers*, Astrophys. J. **922**, 76 (2021).

[20] S. Olsen, T. Venumadhav, J. Mushkin, J. Roulet, B. Zackay, and M. Zaldarriaga, *New Binary Black Hole Mergers in the LIGO-Virgo O3a Data*, Phys. Rev. D **106**, 043009 (2022).

[21] G. S. Cabourn Davies and I. W. Harry, *Establishing Significance of Gravitational-Wave Signals from a Single Observatory in the PyCBC Offline Search*, Classical Quantum Gravity **39**, 215012 (2022).

[22] L. S. Finn and D. F. Chernoff, *Observing Binary Inspiral in Gravitational Radiation: One Interferometer*, Phys. Rev. D **47**, 2198 (1993).

[23] B. Allen, W. G. Anderson, P. R. Brady, D. A. Brown, and J. D. E. Creighton, *FINDCHIRP: An Algorithm for Detection of Gravitational Waves from Inspiraling Compact Binaries*, Phys. Rev. D **85**, 122006 (2012).

[24] H.-Y. Chen, D. E. Holz, J. Miller, M. Evans, S. Vitale, and J. Creighton, *Distance Measures in Gravitational-Wave Astrophysics and Cosmology*, Classical Quantum Gravity **38**, 055010 (2021).

[25] B. P. Abbott *et al.* (KAGRA Collaboration, LIGO Scientific Collaboration, and Virgo Collaboration), *Prospects for Observing and Localizing Gravitational-Wave Transients with Advanced LIGO, Advanced Virgo and KAGRA*, Living Rev. Relativity **23**, 3 (2020).

[26] R. Abbott *et al.* (LIGO Scientific Collaboration, Virgo Collaboration, and KAGRA Collaboration), *Search for Intermediate-Mass Black Hole Binaries in the Third Observing Run of Advanced LIGO and Advanced Virgo*, Astron. Astrophys. **659**, A84 (2022).

[27] R. Abbott *et al.* (LIGO Scientific Collaboration, Virgo Collaboration, and KAGRA Collaboration), *Search for Subsolar-Mass Black Hole Binaries in the Second Part of Advanced LIGO's and Advanced Virgo's Third Observing Run*, arXiv:2212.01477.

[28] R. Abbott *et al.* (LIGO Scientific Collaboration, Virgo Collaboration, and KAGRA Collaboration), *Search for Gravitational-Lensing Signatures in the Full Third Observing Run of the LIGO-Virgo Network*, arXiv:2304.08393.

[29] R. Abbott *et al.* (LIGO Scientific Collaboration, Virgo Collaboration, and KAGRA Collaboration), *Search for Gravitational Waves Associated with Gamma-Ray Bursts Detected by Fermi and Swift during the LIGO–Virgo Run O3b*, Astrophys. J. **928**, 186 (2022).

[30] R. Abbott *et al.* (LIGO Scientific Collaboration, Virgo Collaboration, and KAGRA Collaboration), *Constraints on Cosmic Strings Using Data from the Third Advanced LIGO–Virgo Observing Run*, Phys. Rev. Lett. **126**, 241102 (2021).

[31] R. Abbott *et al.* (LIGO Scientific Collaboration, Virgo Collaboration, and KAGRA Collaboration), *All-Sky Search for Short Gravitational-Wave Bursts in the Third Advanced LIGO and Advanced Virgo Run*, Phys. Rev. D **104**, 122004 (2021).

[32] R. Abbott *et al.* (LIGO Scientific Collaboration, Virgo Collaboration, and KAGRA Collaboration), *All-Sky Search for Long-Duration Gravitational-Wave Bursts in the Third Advanced LIGO and Advanced Virgo Run*, Phys. Rev. D **104**, 102001 (2021).

[33] LIGO Scientific Collaboration, Virgo Collaboration, and KAGRA Collaboration, GWTC-3 Data Release (2021), https://www.gw-openscience.org/GWTC-3/.

[34] C. Bond, D. Brown, A. Freise, and K. Strain, *Interferometer Techniques for Gravitational-Wave Detection*, Living Rev. Relativity **19**, 3 (2016).

[35] M. Pitkin, S. Reid, S. Rowan, and J. Hough, *Gravitational Wave Detection by Interferometry (Ground and Space)*, Living Rev. Relativity **14**, 5 (2011).

[36] G. Vajente, E. K. Gustafson, and D. H. Reitze, *Precision Interferometry for Gravitational Wave Detection: Current Status and Future Trends*, Adv. At. Mol. Opt. Phys. **68**, 75 (2019).

[37] D. V. Martynov *et al.*, *Sensitivity of the Advanced LIGO Detectors at the Beginning of Gravitational Wave Astronomy*, Phys. Rev. D **93**, 112004 (2016); **97**, 059901(E) (2018).

[38] A. Buikema *et al.* (LIGO Instrument Science Collaboration), *Sensitivity and Performance of the Advanced LIGO Detectors in the Third Observing Run*, Phys. Rev. D **102**, 062003 (2020).

[39] C. M. Caves, *Quantum Mechanical Noise in an Interferometer*, Phys. Rev. D **23**, 1693 (1981).

[40] L. Barsotti, J. Harms, and R. Schnabel, *Squeezed Vacuum States of Light for Gravitational Wave Detectors*, Rep. Prog. Phys. **82**, 016905 (2019).

[41] G. Vajente, Y. Huang, M. Isi, J. C. Driggers, J. S. Kissel, M. J. Szczepańczyk, and S. Vitale, *Machine-Learning Nonstationary Noise Out of Gravitational-Wave Detectors*, Phys. Rev. D **101**, 042003 (2020).

[42] F. Acernese *et al.* (Virgo Collaboration), *Calibration of Advanced Virgo and Reconstruction of the Gravitational Wave Signal $h(t)$ during the Observing Run O2*, Classical Quantum Gravity **35**, 205004 (2018).

[43] A. Viets and M. Wade, *Subtracting Narrow-Band Noise from LIGO Strain Data in the Third Observing Run*, LIGO Report No. DCC-T2100058, 2021, https://dcc.ligo.org/LIGO-T2100058/public.

[44] D. Davis, T. B. Littenberg, I. M. Romero-Shaw, M. Millhouse, J. McIver, F. Di Renzo, and G. Ashton, *Subtracting Glitches from Gravitational-Wave Detector Data during the Third LIGO-Virgo Observing Run*, Classical Quantum Gravity **39**, 245013 (2022).

[45] A. D. Viets *et al.*, *Reconstructing the Calibrated Strain Signal in the Advanced LIGO Detectors*, Classical Quantum Gravity **35**, 095015 (2018).

[46] I. Bartos, R. Bork, M. Factourovich, J. Heefner, S. Márka, Z. Márka, Z. Raics, P. Schwinberg, and D. Sigg, *The Advanced LIGO Timing System*, Classical Quantum Gravity **27**, 084025 (2010).

[47] B. P. Abbott *et al.* (LIGO Scientific Collaboration), *Calibration of the Advanced LIGO Detectors for the Discovery of the Binary Black-Hole Merger GW150914*, Phys. Rev. D **95**, 062003 (2017).

[48] D. Tuyenbayev *et al.*, *Improving LIGO Calibration Accuracy by Tracking and Compensating for Slow Temporal Variations*, Classical Quantum Gravity **34**, 015002 (2017).

[49] L. Sun *et al.*, *Characterization of Systematic Error in Advanced LIGO Calibration*, Classical Quantum Gravity **37**, 225008 (2020).

[50] L. Sun *et al.*, *Characterization of Systematic Error in Advanced LIGO Calibration in the Second Half of O3*, arXiv:2107.00129.

[51] D. Estevez, B. Mours, L. Rolland, and D. Verkindt, *Online $h(t)$ Reconstruction for Virgo O3 Data: Start of O3*, Virgo Report No. VIR-0652B-19, 2019, https://tds.ego-gw.it/ql/?c=14486.

[52] L. Rolland, D. Estevez, B. Mours, T. Pradier, M. Seglar Arroyo, and D. Verkindt, *Update on $h(t)$ Uncertainties during O3*, Virgo Report No. VIR-0688A-20, 2020, https://tds.virgo-gw.eu/ql/?c=15813.

[53] F. Acernese *et al.* (Virgo Collaboration), *Calibration of Advanced Virgo and Reconstruction of Detector Strain $h(t)$ during the Observing Run O3*, Classical Quantum Gravity **39**, 045006 (2022).

[54] S. Karki *et al.*, *The Advanced LIGO Photon Calibrators*, Rev. Sci. Instrum. **87**, 114503 (2016).

[55] D. Bhattacharjee, Y. Lecoeuche, S. Karki, J. Betzwieser, V. Bossilkov, S. Kandhasamy, E. Payne, and R. L. Savage, *Fiducial Displacements with Improved Accuracy for the Global Network of Gravitational Wave Detectors*, Classical Quantum Gravity **38**, 015009 (2021).

[56] D. Estevez, P. Lagabbe, A. Masserot, L. Rolland, M. Seglar-Arroyo, and D. Verkindt, *The Advanced Virgo Photon Calibrators*, Classical Quantum Gravity **38**, 075007 (2021).

[57] V. Tiwari *et al.*, *Regression of Environmental Noise in LIGO Data*, Classical Quantum Gravity **32**, 165014 (2015).

[58] J. C. Driggers *et al.* (LIGO Instrument Science Collaboration), *Improving Astrophysical Parameter Estimation via Offline Noise Subtraction for Advanced LIGO*, Phys. Rev. D **99**, 042001 (2019).
[59] D. Davis, T. Massinger, A. Lundgren, J. C. Driggers, A. L. Urban, and L. Nuttall, *Improving the Sensitivity of Advanced LIGO Using Noise Subtraction*, Classical Quantum Gravity **36**, 055011 (2019).
[60] S. Klimenko *et al.*, *Method for Detection and Reconstruction of Gravitational Wave Transients with Networks of Advanced Detectors*, Phys. Rev. D **93**, 042004 (2016).
[61] B. P. Abbott *et al.* (LIGO Scientific Collaboration and Virgo Collaboration), *Characterization of Transient Noise in Advanced LIGO Relevant to Gravitational Wave Signal GW150914*, Classical Quantum Gravity **33**, 134001 (2016).
[62] L. K. Nuttall, *Characterizing Transient Noise in the LIGO Detectors*, Phil. Trans. R. Soc. A **376**, 20170286 (2018).
[63] D. Davis *et al.* (LIGO Instrument Science Collaboration), *LIGO Detector Characterization in the Second and Third Observing Runs*, Classical Quantum Gravity **38**, 135014 (2021).
[64] F. Acernese *et al.* (Virgo Collaboration), *Virgo Detector Characterization and Data Quality: Results from the O3 Run*, arXiv:2210.15633.
[65] F. Robinet, N. Arnaud, N. Leroy, A. Lundgren, D. Macleod, and J. McIver, *Omicron: A Tool to Characterize Transient Noise in Gravitational-Wave Detectors*, SoftwareX **12**, 100620 (2020).
[66] F. Acernese *et al.* (Virgo Collaboration), *The Virgo O3 Run and the Impact of the Environment*, Classical Quantum Gravity **39**, 235009 (2022).
[67] T. Accadia *et al.* (Virgo Collaboration), *Noise from Scattered Light in Virgo's Second Science Run Data*, Classical Quantum Gravity **27**, 194011 (2010).
[68] D. J. Ottaway, P. Fritschel, and S. J. Waldman, *Impact of Upconverted Scattered Light on Advanced Interferometric Gravitational Wave Detectors*, Opt. Express **20**, 8329 (2012).
[69] S. Soni *et al.* (LIGO Instrument Science Collaboration), *Reducing Scattered Light in LIGO's Third Observing Run*, Classical Quantum Gravity **38**, 025016 (2021).
[70] S. Soni *et al.*, *Discovering Features in Gravitational-Wave Data through Detector Characterization, Citizen Science and Machine Learning*, Classical Quantum Gravity **38**, 195016 (2021).
[71] R. Schofield, *aLIGO LHO Logbook*, Report No. 54298, 2020, https://alog.ligo-wa.caltech.edu/aLOG/index.php?callRep=54298.
[72] A. Effler, *aLIGO LLO Logbook*, Report No. 50851, 2020, https://alog.ligo-la.caltech.edu/aLOG/index.php?callRep=50851.
[73] S. Chatterji, L. Blackburn, G. Martin, and E. Katsavounidis, *Multiresolution Techniques for the Detection of Gravitational-Wave Bursts*, Classical Quantum Gravity **21**, S1809 (2004).
[74] A. Effler, *aLIGO LLO Logbook*, Report No. 53025, 2020, https://alog.ligo-la.caltech.edu/aLOG/index.php?callRep=53025.
[75] A. Effler, *aLIGO LLO Logbook*, Report No. 53364, 2020, https://alog.ligo-la.caltech.edu/aLOG/index.php?callRep=53364.
[76] LIGO Scientific Collaboration and Virgo Collaboration, *Data Quality Report User Documentation* (2018), https://docs.ligo.org/detchar/data-quality-report/.
[77] F. Acernese *et al.* (Virgo Collaboration), *Virgo Detector Characterization and Data Quality: Tools*, arXiv:2210.15634.
[78] C. Messick *et al.*, *Analysis Framework for the Prompt Discovery of Compact Binary Mergers in Gravitational-Wave Data*, Phys. Rev. D **95**, 042001 (2017).
[79] S. Sachdev *et al.*, *The GstLAL Search Analysis Methods for Compact Binary Mergers in Advanced LIGO's Second and Advanced Virgo's First Observing Runs*, arXiv:1901.08580.
[80] C. Hanna *et al.*, *Fast Evaluation of Multidetector Consistency for Real-Time Gravitational Wave Searches*, Phys. Rev. D **101**, 022003 (2020).
[81] K. Cannon *et al.*, *GstLAL: A Software Framework for Gravitational Wave Discovery*, SoftwareX **14**, 100680 (2021).
[82] T. Adams, D. Buskulic, V. Germain, G. M. Guidi, F. Marion, M. Montani, B. Mours, F. Piergiovanni, and G. Wang, *Low-Latency Analysis Pipeline for Compact Binary Coalescences in the Advanced Gravitational Wave Detector Era*, Classical Quantum Gravity **33**, 175012 (2016).
[83] F. Aubin *et al.*, *The MBTA Pipeline for Detecting Compact Binary Coalescences in the Third LIGO-Virgo Observing Run*, Classical Quantum Gravity **38**, 095004 (2021).
[84] B. Allen, χ^2 *Time-Frequency Discriminator for Gravitational Wave Detection*, Phys. Rev. D **71**, 062001 (2005).
[85] T. Dal Canton *et al.*, *Implementing a Search for Aligned-Spin Neutron Star-Black Hole Systems with Advanced Ground Based Gravitational Wave Detectors*, Phys. Rev. D **90**, 082004 (2014).
[86] S. A. Usman *et al.*, *The PyCBC Search for Gravitational Waves from Compact Binary Coalescence*, Classical Quantum Gravity **33**, 215004 (2016).
[87] A. H. Nitz, T. Dent, T. Dal Canton, S. Fairhurst, and D. A. Brown, *Detecting Binary Compact-Object Mergers with Gravitational Waves: Understanding and Improving the Sensitivity of the PyCBC Search*, Astrophys. J. **849**, 118 (2017).
[88] G. S. Davies, T. Dent, M. Tápai, I. Harry, C. McIsaac, and A. H. Nitz, *Extending the PyCBC Search for Gravitational Waves from Compact Binary Mergers to a Global Network*, Phys. Rev. D **102**, 022004 (2020).
[89] S. Klimenko and G. Mitselmakher, *A Wavelet Method for Detection of Gravitational Wave Bursts*, Classical Quantum Gravity **21**, S1819 (2004).
[90] S. Klimenko, G. Vedovato, M. Drago, G. Mazzolo, G. Mitselmakher, C. Pankow, G. Prodi, V. Re, F. Salemi, and I. Yakushin, *Localization of Gravitational Wave Sources with Networks of Advanced Detectors*, Phys. Rev. D **83**, 102001 (2011).
[91] J. Luan, S. Hooper, L. Wen, and Y. Chen, *Towards Low-Latency Real-Time Detection of Gravitational Waves from Compact Binary Coalescences in the Era of Advanced Detectors*, Phys. Rev. D **85**, 102002 (2012).

[92] Q. Chu, *Low-Latency Detection and Localization of Gravitational Waves from Compact Binary Coalescences*, Ph.D. thesis, The University of Western Australia, 2017, 10.4225/23/5987feb0a789c.

[93] Q. Chu *et al.*, *SPIIR Online Coherent Pipeline to Search for Gravitational Waves from Compact Binary Coalescences*, Phys. Rev. D **105**, 024023 (2022).

[94] B. P. Abbott *et al.* (LIGO Scientific Collaboration and Virgo Collaboration), *All-Sky Search for Short Gravitational-Wave Bursts in the First Advanced LIGO Run*, Phys. Rev. D **95**, 042003 (2017).

[95] L. A. Wainstein and V. D. Zubakov, *Extraction of Signals from Noise*, Dover Books on Physics and Mathematical Physics (Prentice-Hall, Englewood Cliffs, NJ, 1962).

[96] B. P. Abbott *et al.* (LIGO Scientific Collaboration and Virgo Collaboration), *A Guide to LIGO–Virgo Detector Noise and Extraction of Transient Gravitational-Wave Signals*, Classical Quantum Gravity **37**, 055002 (2020).

[97] P. C. Peters, *Gravitational Radiation and the Motion of Two Point Masses*, Phys. Rev. **136**, B1224 (1964).

[98] L. Blanchet, T. Damour, B. R. Iyer, C. M. Will, and A. G. Wiseman, *Gravitational Radiation Damping of Compact Binary Systems to Second Post-Newtonian Order*, Phys. Rev. Lett. **74**, 3515 (1995).

[99] P. Ajith *et al.*, *Inspiral-Merger-Ringdown Waveforms for Black-Hole Binaries with Non-Precessing Spins*, Phys. Rev. Lett. **106**, 241101 (2011).

[100] L. Santamaria *et al.*, *Matching Post-Newtonian and Numerical Relativity Waveforms: Systematic Errors and a New Phenomenological Model for Non-Precessing Black Hole Binaries*, Phys. Rev. D **82**, 064016 (2010).

[101] A. Krolak and B. F. Schutz, *Coalescing Binaries—Probe of the Universe*, Gen. Relativ. Gravit. **19**, 1163 (1987).

[102] B. P. Abbott *et al.* (LIGO Scientific Collaboration and Virgo Collaboration), *Search for Subsolar-Mass Ultracompact Binaries in Advanced LIGO's First Observing Run*, Phys. Rev. Lett. **121**, 231103 (2018).

[103] B. P. Abbott *et al.* (LIGO Scientific Collaboration and Virgo Collaboration), *Search for Subsolar Mass Ultracompact Binaries in Advanced LIGO's Second Observing Run*, Phys. Rev. Lett. **123**, 161102 (2019).

[104] A. H. Nitz and Y.-F. Wang, *Search for Gravitational Waves from High-Mass-Ratio Compact-Binary Mergers of Stellar Mass and Subsolar Mass Black Holes*, Phys. Rev. Lett. **126**, 021103 (2021).

[105] A. H. Nitz and Y.-F. Wang, *Search for Gravitational Waves from the Coalescence of Sub-Solar Mass and Eccentric Compact Binaries*, Astrophys. J. **915**, 54 (2021).

[106] R. Abbott *et al.* (LIGO Scientific Collaboration, Virgo Collaboration, and KAGRA Collaboration), *Search for Subsolar-Mass Binaries in the First Half of Advanced LIGO's and Advanced Virgo's Third Observing Run*, Phys. Rev. Lett. **129**, 061104 (2022).

[107] S. Klimenko, I. Yakushin, A. Mercer, and G. Mitselmakher, *A Coherent Method for Detection of Gravitational Wave Bursts*, Classical Quantum Gravity **25**, 114029 (2008).

[108] V. Necula, S. Klimenko, and G. Mitselmakher, *Transient analysis with Fast Wilson-Daubechies Time-Frequency Transform*, J. Phys. Conf. Ser. **363**, 012032 (2012).

[109] F. Salemi, E. Milotti, G. A. Prodi, G. Vedovato, C. Lazzaro, S. Tiwari, S. Vinciguerra, M. Drago, and S. Klimenko, *Wider Look at the Gravitational-Wave Transients from GWTC-1 Using an Unmodeled Reconstruction Method*, Phys. Rev. D **100**, 042003 (2019).

[110] M. Drago *et al.*, *coherent WaveBurst, A Pipeline for Unmodeled Gravitational-Wave Data Analysis*, SoftwareX **14**, 100678 (2021).

[111] M. Szczepańczyk *et al.*, *Observing an Intermediate-Mass Black Hole GW190521 with Minimal Assumptions*, Phys. Rev. D **103**, 082002 (2021).

[112] W. M. Farr, J. R. Gair, I. Mandel, and C. Cutler, *Counting and Confusion: Bayesian Rate Estimation with Multiple Populations*, Phys. Rev. D **91**, 023005 (2015).

[113] B. P. Abbott *et al.* (LIGO Scientific Collaboration and Virgo Collaboration), *The Rate of Binary Black Hole Mergers Inferred from Advanced LIGO Observations Surrounding GW150914*, Astrophys. J. Lett. **833**, L1 (2016).

[114] B. P. Abbott *et al.* (LIGO Scientific Collaboration and Virgo Collaboration), *Supplement: The Rate of Binary Black Hole Mergers Inferred from Advanced LIGO Observations Surrounding GW150914*, Astrophys. J. Suppl. Ser. **227**, 14 (2016).

[115] S. J. Kapadia *et al.*, *A Self-Consistent Method to Estimate the Rate of Compact Binary Coalescences with a Poisson Mixture Model*, Classical Quantum Gravity **37**, 045007 (2020).

[116] R. Abbott *et al.* (LIGO Scientific Collaboration and Virgo Collaboration), *Population Properties of Compact Objects from the Second LIGO-Virgo Gravitational-Wave Transient Catalog*, Astrophys. J. Lett. **913**, L7 (2021).

[117] N. Andres *et al.*, *Assessing the Compact-Binary Merger Candidates Reported by the MBTA Pipeline in the LIGO–Virgo O3 Run: Probability of Astrophysical Origin, Classification, and Associated Uncertainties*, Classical Quantum Gravity **39**, 055002 (2022).

[118] S. M. Gaebel, J. Veitch, T. Dent, and W. M. Farr, *Digging the Population of Compact Binary Mergers out of the Noise*, Mon. Not. R. Astron. Soc. **484**, 4008 (2019).

[119] S. Galaudage, C. Talbot, and E. Thrane, *Gravitational-Wave Inference in the Catalog Era: Evolving Priors and Marginal Events*, Phys. Rev. D **102**, 083026 (2020).

[120] J. Roulet, T. Venumadhav, B. Zackay, L. Dai, and M. Zaldarriaga, *Binary Black Hole Mergers from LIGO/Virgo O1 and O2: Population Inference Combining Confident and Marginal Events*, Phys. Rev. D **102**, 123022 (2020).

[121] R. Abbott *et al.* (LIGO Scientific Collaboration, Virgo Collaboration, KAGRA Collaboration, and CHIME/FRB Collaboration), *Search for Gravitational Waves Associated with Fast Radio Bursts Detected by CHIME/FRB during the LIGO–Virgo Observing Run O3a*, arXiv:2203.12038.

[122] S. Banagiri, C. P. L. Berry, G. S. Cabourn Davies, L. Tsukada, and Z. Doctor, *A Unified p_{astro} for Gravitational Waves: Consistently Combining Information from Multiple Search Pipelines*, arXiv:2305.00071.

[123] P. J. Sutton, *Upper Limits from Counting Experiments with Multiple Pipelines*, Classical Quantum Gravity **26**, 245007 (2009).

[124] R. Biswas *et al.*, *Detecting Transient Gravitational Waves in Non-Gaussian Noise with Partially Redundant Analysis Methods*, Phys. Rev. D **85**, 122009 (2012).
[125] M. Cabero *et al.*, *Blip Glitches in Advanced LIGO Data*, Classical Quantum Gravity **36**, 155010 (2019).
[126] B. P. Abbott *et al.* (LIGO Scientific Collaboration and Virgo Collaboration), *GW170817: Observation of Gravitational Waves from a Binary Neutron Star Inspiral*, Phys. Rev. Lett. **119**, 161101 (2017).
[127] N. Farrow, X.-J. Zhu, and E. Thrane, *The Mass Distribution of Galactic Double Neutron Stars*, Astrophys. J. **876**, 18 (2019).
[128] A. H. Nitz, T. Dent, G. S. Davies, and I. Harry, *A Search for Gravitational Waves from Binary Mergers with a Single Observatory*, Astrophys. J. **897**, 169 (2020).
[129] L. P. Singer and L. R. Price, *Rapid Bayesian Position Reconstruction for Gravitational-Wave Transients*, Phys. Rev. D **93**, 024013 (2016).
[130] L. P. Singer *et al.*, *Going the Distance: Mapping Host Galaxies of LIGO and Virgo Sources in Three Dimensions Using Local Cosmography and Targeted Follow-Up*, Astrophys. J. Lett. **829**, L15 (2016).
[131] B. P. Abbott *et al.* (LIGO Scientific Collaboration and Virgo Collaboration), *Properties of the Binary Black Hole Merger GW150914*, Phys. Rev. Lett. **116**, 241102 (2016).
[132] M. Fishbach and D. E. Holz, *Where Are LIGO's Big Black Holes?*, Astrophys. J. Lett. **851**, L25 (2017).
[133] M. Fishbach, Z. Doctor, T. A. Callister, B. Edelman, J. Ye, R. Essick, W. M. Farr, B. Farr, and D. E. Holz, *When Are LIGO/Virgo's Big Black Hole Mergers?*, Astrophys. J. **912**, 98 (2021).
[134] J. Creighton, *Certain Identities in FGMC*, LIGO Report No. DCC-T1700029, 2017, https://dcc.ligo.org/LIGO-T1700029/public.
[135] C. Cutler and É. E. Flanagan, *Gravitational Waves from Merging Compact Binaries: How Accurately Can One Extract the Binary's Parameters from the Inspiral Wave Form?*, Phys. Rev. D **49**, 2658 (1994).
[136] G. Pratten *et al.*, *Computationally Efficient Models for the Dominant and Subdominant Harmonic Modes of Precessing Binary Black Holes*, Phys. Rev. D **103**, 104056 (2021).
[137] S. Ossokine *et al.*, *Multipolar Effective-One-Body Waveforms for Precessing Binary Black Holes: Construction and Validation*, Phys. Rev. D **102**, 044055 (2020).
[138] J. E. Thompson, E. Fauchon-Jones, S. Khan, E. Nitoglia, F. Pannarale, T. Dietrich, and M. Hannam, *Modeling the Gravitational Wave Signature of Neutron Star Black Hole Coalescences*, Phys. Rev. D **101**, 124059 (2020).
[139] A. Matas *et al.*, *Aligned-Spin Neutron-Star–Black-Hole Waveform Model Based on the Effective-One-Body Approach and Numerical-Relativity Simulations*, Phys. Rev. D **102**, 043023 (2020).
[140] C. García-Quirós, M. Colleoni, S. Husa, H. Estellés, G. Pratten, A. Ramos-Buades, M. Mateu-Lucena, and R. Jaume, *Multimode Frequency-Domain Model for the Gravitational Wave Signal from Nonprecessing Black-Hole Binaries*, Phys. Rev. D **102**, 064002 (2020).
[141] R. Cotesta, A. Buonanno, A. Bohé, A. Taracchini, I. Hinder, and S. Ossokine, *Enriching the Symphony of Gravitational Waves from Binary Black Holes by Tuning Higher Harmonics*, Phys. Rev. D **98**, 084028 (2018).
[142] C. P. L. Berry *et al.*, *Quoting Parameter-Estimation Results*, LIGO Report No. DCC-T1500597, 2015, https://dcc.ligo.org/LIGO-T1500597/public.
[143] G. Ashton and S. Khan, *Multiwaveform Inference of Gravitational Waves*, Phys. Rev. D **101**, 064037 (2020).
[144] G. Ashton *et al.*, *Bilby: A User-Friendly Bayesian Inference Library for Gravitational-Wave Astronomy*, Astrophys. J. Suppl. Ser. **241**, 27 (2019).
[145] R. J. E. Smith, G. Ashton, A. Vajpeyi, and C. Talbot, *Massively Parallel Bayesian Inference for Transient Gravitational-Wave Astronomy*, Mon. Not. R. Astron. Soc. **498**, 4492 (2020).
[146] I. M. Romero-Shaw *et al.*, *Bayesian Inference for Compact Binary Coalescences with Bilby: Validation and Application to the First LIGO–Virgo Gravitational-Wave Transient Catalogue*, Mon. Not. R. Astron. Soc. **499**, 3295 (2020).
[147] C. Pankow, P. Brady, E. Ochsner, and R. O'Shaughnessy, *Novel Scheme for Rapid Parallel Parameter Estimation of Gravitational Waves from Compact Binary Coalescences*, Phys. Rev. D **92**, 023002 (2015).
[148] J. Lange *et al.*, *Parameter Estimation Method that Directly Compares Gravitational Wave Observations to Numerical Relativity*, Phys. Rev. D **96**, 104041 (2017).
[149] D. Wysocki, R. O'Shaughnessy, J. Lange, and Y.-L. L. Fang, *Accelerating Parameter Inference with Graphics Processing Units*, Phys. Rev. D **99**, 084026 (2019).
[150] E. Thrane and C. Talbot, *An Introduction to Bayesian Inference in Gravitational-Wave Astronomy: Parameter Estimation, Model Selection, and Hierarchical Models*, Pub. Astron. Soc. Aust. **36**, e010 (2019); **37**, e036(E) (2020).
[151] T. A. Callister, *A Thesaurus for Common Priors in Gravitational-Wave Astronomy*, arXiv:2104.09508.
[152] E. Poisson and C. M. Will, *Gravitational Waves from Inspiraling Compact Binaries: Parameter Estimation Using Second Post-Newtonian Wave Forms*, Phys. Rev. D **52**, 848 (1995).
[153] E. Baird, S. Fairhurst, M. Hannam, and P. Murphy, *Degeneracy between Mass and Spin in Black-Hole-Binary Waveforms*, Phys. Rev. D **87**, 024035 (2013).
[154] B. Farr *et al.*, *Parameter Estimation on Gravitational Waves from Neutron-Star Binaries with Spinning Components*, Astrophys. J. **825**, 116 (2016).
[155] H. Estellés *et al.*, *A Detailed Analysis of GW190521 with Phenomenological Waveform Models*, Astrophys. J. **924**, 79 (2022).
[156] A. K. Mehta, A. Buonanno, J. Gair, M. C. Miller, E. Farag, R. J. deBoer, M. Wiescher, and F. X. Timmes, *Observing Intermediate-Mass Black Holes and the Upper Stellar-Mass Gap with LIGO and Virgo*, Astrophys. J. **924**, 39 (2022).
[157] H. S. Chia, S. Olsen, J. Roulet, L. Dai, T. Venumadhav, B. Zackay, and M. Zaldarriaga, *Signs of Higher Multipoles and Orbital Precession in GW151226*, Phys. Rev. D **106**, 024009 (2022).

[158] B. P. Abbott *et al.* (LIGO Scientific Collaboration and Virgo Collaboration), *Properties of the Binary Neutron Star Merger GW170817*, Phys. Rev. X **9**, 011001 (2019).
[159] B. P. Abbott *et al.* (LIGO Scientific Collaboration and Virgo Collaboration), *GW190425: Observation of a Compact Binary Coalescence with Total* Mass $\sim 3.4M_{\odot}$, Astrophys. J. Lett. **892**, L3 (2020).
[160] Y. Huang, H. Middleton, K. K. Y. Ng, S. Vitale, and J. Veitch, *Characterization of Low-Significance Gravitational-Wave Compact Binary Sources*, Phys. Rev. D **98**, 123021 (2018).
[161] J. Powell, *Parameter Estimation and Model Selection of Gravitational Wave Signals Contaminated by Transient Detector Noise Glitches*, Classical Quantum Gravity **35**, 155017 (2018).
[162] K. Chatziioannou, N. Cornish, M. Wijngaarden, and T. B. Littenberg, *Modeling Compact Binary Signals and Instrumental Glitches in Gravitational Wave Data*, Phys. Rev. D **103**, 044013 (2021).
[163] G. Ashton, S. Thiele, Y. Lecoeuche, J. McIver, and L. K. Nuttall, *Parameterised Population Models of Transient Non-Gaussian Noise in the LIGO Gravitational-Wave Detectors*, Classical Quantum Gravity **39**, 175004 (2022).
[164] P. Relton and V. Raymond, *Parameter Estimation Bias from Overlapping Binary Black Hole Events in Second Generation Interferometers*, Phys. Rev. D **104**, 084039 (2021).
[165] I. Mandel, *Parameter Estimation on Gravitational Waves from Multiple Coalescing Binaries*, Phys. Rev. D **81**, 084029 (2010).
[166] M. Fishbach, W. M. Farr, and D. E. Holz, *The Most Massive Binary Black Hole Detections and the Identification of Population Outliers*, Astrophys. J. Lett. **891**, L31 (2020).
[167] S. Miller, T. A. Callister, and W. Farr, *The Low Effective Spin of Binary Black Holes and Implications for Individual Gravitational-Wave Events*, Astrophys. J. **895**, 128 (2020).
[168] C. Kimball, C. Talbot, C. P. L. Berry, M. Carney, M. Zevin, E. Thrane, and V. Kalogera, *Black Hole Genealogy: Identifying Hierarchical Mergers with Gravitational Waves*, Astrophys. J. **900**, 177 (2020).
[169] T. A. Callister, C.-J. Haster, K. K. Y. Ng, S. Vitale, and W. M. Farr, *Who Ordered That? Unequal-Mass Binary Black Hole Mergers Have Larger Effective Spins*, Astrophys. J. Lett. **922**, L5 (2021).
[170] S. Vitale, R. Lynch, V. Raymond, R. Sturani, J. Veitch, and P. Graff, *Parameter Estimation for Heavy Binary-Black Holes with Networks of Second-Generation Gravitational-Wave Detectors*, Phys. Rev. D **95**, 064053 (2017).
[171] B. Margalit and B. D. Metzger, *Constraining the Maximum Mass of Neutron Stars From Multi-Messenger Observations of GW170817*, Astrophys. J. Lett. **850**, L19 (2017).
[172] S. Ai, H. Gao, and B. Zhang, *What Constraints on the Neutron Star Maximum Mass Can One Pose from GW170817 Observations?*, Astrophys. J. **893**, 146 (2020).
[173] D.-S. Shao, S.-P. Tang, J.-L. Jiang, and Y.-Z. Fan, *Maximum Mass Cutoff in the Neutron Star Mass Distribution and the Prospect of Forming Supramassive Objects in the Double Neutron Star Mergers*, Phys. Rev. D **102**, 063006 (2020).
[174] Y. Lim, A. Bhattacharya, J. W. Holt, and D. Pati, *Radius and Equation of State Constraints from Massive Neutron Stars and GW190814*, Phys. Rev. C **104**, L032802 (2021).
[175] M. C. Miller *et al.*, *The Radius of PSR J0740+6620 from NICER and XMM-Newton Data*, Astrophys. J. Lett. **918**, L28 (2021).
[176] G. Raaijmakers, S. K. Greif, K. Hebeler, T. Hinderer, S. Nissanke, A. Schwenk, T. E. Riley, A. L. Watts, J. M. Lattimer, and W. C. G. Ho, *Constraints on the Dense Matter Equation of State and Neutron Star Properties from NICER's Mass–Radius Estimate of PSR J0740+6620 and Multimessenger Observations*, Astrophys. J. Lett. **918**, L29 (2021).
[177] P. Ajith and S. Bose, *Estimating the Parameters of Non-Spinning Binary Black Holes Using Ground-Based Gravitational-Wave Detectors: Statistical Errors*, Phys. Rev. D **79**, 084032 (2009).
[178] P. B. Graff, A. Buonanno, and B. S. Sathyaprakash, *Missing Link: Bayesian Detection and Measurement of Intermediate-Mass Black-Hole Binaries*, Phys. Rev. D **92**, 022002 (2015).
[179] C.-J. Haster, Z. Wang, C. P. L. Berry, S. Stevenson, J. Veitch, and I. Mandel, *Inference on Gravitational Waves from Coalescences of Stellar-Mass Compact Objects and Intermediate-Mass Black Holes*, Mon. Not. R. Astron. Soc. **457**, 4499 (2016).
[180] J. Veitch, M. Pürrer, and I. Mandel, *Measuring Intermediate Mass Black Hole Binaries with Advanced Gravitational Wave Detectors*, Phys. Rev. Lett. **115**, 141101 (2015).
[181] T. Islam, S. E. Field, C.-J. Haster, and R. Smith, *High Precision Source Characterization of Intermediate Mass-Ratio Black Hole Coalescences with Gravitational Waves: The Importance of Higher Order Multipoles*, Phys. Rev. D **104**, 084068 (2021).
[182] F. Echeverria, *Gravitational Wave Measurements of the Mass and Angular Momentum of a Black Hole*, Phys. Rev. D **40**, 3194 (1989).
[183] E. Berti, V. Cardoso, and C. M. Will, *On Gravitational-Wave Spectroscopy of Massive Black Holes with the Space Interferometer LISA*, Phys. Rev. D **73**, 064030 (2006).
[184] R. Abbott *et al.* (LIGO Scientific Collaboration and Virgo Collaboration), *GW190521: A Binary Black Hole Merger with a Total Mass of* $150M_{\odot}$, Phys. Rev. Lett. **125**, 101102 (2020).
[185] W. A. Fowler and F. Hoyle, *Neutrino Processes and Pair Formation in Massive Stars and Supernovae*, Astrophys. J. Suppl. Ser. **9**, 201 (1964).
[186] Z. Barkat, G. Rakavy, and N. Sack, *Dynamics of Supernova Explosion Resulting from Pair Formation*, Phys. Rev. Lett. **18**, 379 (1967).
[187] C. L. Fryer, S. E. Woosley, and A. Heger, *Pair Instability Supernovae, Gravity Waves, and Gamma-Ray Transients*, Astrophys. J. **550**, 372 (2001).
[188] K. Belczynski *et al.*, *The Effect of Pair-Instability Mass Loss on Black Hole Mergers*, Astron. Astrophys. **594**, A97 (2016).
[189] M. Spera and M. Mapelli, *Very Massive Stars, Pair-Instability Supernovae and Intermediate-Mass Black*

Holes with the SEVN Code, Mon. Not. R. Astron. Soc. **470**, 4739 (2017).

[190] S. Stevenson, M. Sampson, J. Powell, A. Vigna-Gómez, C. J. Neijssel, D. Szécsi, and I. Mandel, *The Impact of Pair-Instability Mass Loss on the Binary Black Hole Mass Distribution*, Astrophys. J. **882**, 121 (2019).

[191] R. Farmer, M. Renzo, S. E. de Mink, P. Marchant, and S. Justham, *Mind the Gap: The Location of the Lower Edge of the Pair Instability Supernovae Black Hole Mass Gap*, Astrophys. J. **887**, 53 (2019).

[192] L. A. C. van Son, S. E. de Mink, F. S. Broekgaarden, M. Renzo, S. Justham, E. Laplace, J. Morán-Fraile, D. D. Hendriks, and R. Farmer, *Polluting the Pair-Instability Mass Gap for Binary Black Holes through Super-Eddington Accretion in Isolated Binaries*, Astrophys. J. **897**, 100 (2020).

[193] P. Marchant and T. Moriya, *The Impact of Stellar Rotation on the Black Hole Mass-Gap from Pair-Instability Supernovae*, Astron. Astrophys. **640**, L18 (2020).

[194] G. Costa, A. Bressan, M. Mapelli, P. Marigo, G. Iorio, and M. Spera, *Formation of GW190521 from Stellar Evolution: The Impact of the Hydrogen-Rich Envelope, Dredge-Up and* $^{12}C(\alpha,\gamma)^{16}O$ *Rate on the Pair-Instability Black Hole Mass Gap*, Mon. Not. R. Astron. Soc. **501**, 4514 (2021).

[195] A. Tanikawa, T. Kinugawa, T. Yoshida, K. Hijikawa, and H. Umeda, *Population III Binary Black Holes: Effects of Convective Overshooting on Formation of GW190521*, Mon. Not. R. Astron. Soc. **505**, 2170 (2020).

[196] H. Umeda, T. Yoshida, C. Nagele, and K. Takahashi, *Pulsational Pair-Instability and the Mass Gap of Population III Black Holes: Effects of Overshooting*, Astrophys. J. Lett. **905**, L21 (2020).

[197] J. S. Vink, E. R. Higgins, A. A. C. Sander, and G. N. Sabhahit, *Maximum Black Hole Mass across Cosmic Time*, Mon. Not. R. Astron. Soc. **504**, 146 (2021).

[198] S. E. Woosley and A. Heger, *The Pair-Instability Mass Gap for Black Holes*, Astrophys. J. Lett. **912**, L31 (2021).

[199] R. Farmer, M. Renzo, S. de Mink, M. Fishbach, and S. Justham, *Constraints from Gravitational Wave Detections of Binary Black Hole Mergers on the* $^{12}C(\alpha,\gamma)^{16}O$ *Rate*, Astrophys. J. Lett. **902**, L36 (2020).

[200] M. Renzo, R. Farmer, S. Justham, Y. Götberg, S. E. de Mink, E. Zapartas, P. Marchant, and N. Smith, *Predictions for the Hydrogen-Free Ejecta of Pulsational Pair-Instability Supernovae*, Astron. Astrophys. **640**, A56 (2020).

[201] C. D. Bailyn, R. K. Jain, P. Coppi, and J. A. Orosz, *The Mass Distribution of Stellar Black Holes*, Astrophys. J. **499**, 367 (1998).

[202] F. Özel, D. Psaltis, R. Narayan, and J. E. McClintock, *The Black Hole Mass Distribution in the Galaxy*, Astrophys. J. **725**, 1918 (2010).

[203] W. M. Farr, N. Sravan, A. Cantrell, L. Kreidberg, C. D. Bailyn, I. Mandel, and V. Kalogera, *The Mass Distribution of Stellar-Mass Black Holes*, Astrophys. J. **741**, 103 (2011).

[204] L. Kreidberg, C. D. Bailyn, W. M. Farr, and V. Kalogera, *Mass Measurements of Black Holes in X-Ray Transients: Is There a Mass Gap?*, Astrophys. J. **757**, 36 (2012).

[205] C. L. Fryer, K. Belczynski, G. Wiktorowicz, M. Dominik, V. Kalogera, and D. E. Holz, *Compact Remnant Mass Function: Dependence on the Explosion Mechanism and Metallicity*, Astrophys. J. **749**, 91 (2012).

[206] I. Mandel and B. Müller, *Simple Recipes for Compact Remnant Masses and Natal Kicks*, Mon. Not. R. Astron. Soc. **499**, 3214 (2020).

[207] M. Zevin, M. Spera, C. P. L. Berry, and V. Kalogera, *Exploring the Lower Mass Gap and Unequal Mass Regime in Compact Binary Evolution*, Astrophys. J. Lett. **899**, L1 (2020).

[208] T. Liu, Y.-F. Wei, L. Xue, and M.-Y. Sun, *Final Compact Remnants in Core-Collapse Supernovae from 20 to* $40M_\odot$*: The Lower Mass Gap*, Astrophys. J. **908**, 106 (2021).

[209] R. A. Patton, T. Sukhbold, and J. J. Eldridge, *Comparing Compact Object Distributions from Mass- and Presupernova Core Structure-Based Prescriptions*, Mon. Not. R. Astron. Soc. **511**, 903 (2022).

[210] T. Venumadhav, B. Zackay, J. Roulet, L. Dai, and M. Zaldarriaga, *New Search Pipeline for Compact Binary Mergers: Results for Binary Black Holes in the First Observing Run of Advanced LIGO*, Phys. Rev. D **100**, 023011 (2019).

[211] J. Roulet, H. S. Chia, S. Olsen, L. Dai, T. Venumadhav, B. Zackay, and M. Zaldarriaga, *On the Distribution of Effective Spins and Masses of Binary Black Holes from the LIGO and Virgo O1-O3a Observing Runs*, Phys. Rev. D **104**, 083010 (2021).

[212] J. Casares and P. G. Jonker, *Mass Measurements of Stellar and Intermediate Mass Black-Holes*, Space Sci. Rev. **183**, 223 (2014).

[213] J. Casares, I. Negueruela, M. Ribó, I. Ribas, J. M. Paredes, A. Herrero, and S. Simón-Díaz, *A Be-Type Star with a Black-Hole Companion*, Nature (London) **505**, 378 (2014).

[214] J. M. Corral-Santana, J. Casares, T. Muñoz-Darias, F. E. Bauer, I. G. Martinez-Pais, and D. M. Russell, *BlackCAT: A Catalogue of Stellar-Mass Black Holes in X-Ray Transients*, Astron. Astrophys. **587**, A61 (2016).

[215] J. C. A. Miller-Jones *et al.*, *Cygnus X-1 Contains a 21–Solar Mass Black Hole—Implications for Massive Star Winds*, Science **371**, 1046 (2021).

[216] K. Belczynski, T. Bulik, and C. L. Fryer, *High Mass X-Ray Binaries: Future Evolution and Fate*, arXiv:1208.2422.

[217] B. P. Abbott *et al.* (LIGO Scientific Collaboration and Virgo Collaboration), *Astrophysical Implications of the Binary Black-Hole Merger GW150914*, Astrophys. J. Lett. **818**, L22 (2016).

[218] C. J. Neijssel, S. Vinciguerra, A. Vigna-Gomez, R. Hirai, J. C. A. Miller-Jones, A. Bahramian, T. J. Maccarone, and I. Mandel, *Wind Mass-Loss Rates of Stripped Stars Inferred from Cygnus X-1*, Astrophys. J. **908**, 118 (2021).

[219] J. Puls, J. S. Vink, and F. Najarro, *Mass Loss from Hot Massive Stars*, Astron. Astrophys. Rev. **16**, 209 (2008).

[220] N. Smith, *Mass Loss: Its Effect on the Evolution and Fate of High-Mass Stars*, Annu. Rev. Astron. Astrophys. **52**, 487 (2014).

[221] J. S. Vink and A. A. C. Sander, *Metallicity-Dependent Wind Parameter Predictions for OB Stars*, Mon. Not. R. Astron. Soc. **504**, 2051 (2021).

[222] K. Belczynski, T. Bulik, C. L. Fryer, A. Ruiter, J. S. Vink, and J. R. Hurley, *On the Maximum Mass of Stellar Black Holes*, Astrophys. J. **714**, 1217 (2010).
[223] J. J. Eldridge, E. R. Stanway, L. Xiao, L. A. S. McClelland, G. Taylor, M. Ng, S. M. L. Greis, and J. C. Bray, *Binary Population and Spectral Synthesis Version 2.1: Construction, Observational Verification, and New Results*, Pub. Astron. Soc. Aust. **34**, e058 (2017).
[224] N. Giacobbo, M. Mapelli, and M. Spera, *Merging Black Hole Binaries: The Effects of Progenitor's Metallicity, Mass-Loss Rate and Eddington Factor*, Mon. Not. R. Astron. Soc. **474**, 2959 (2018).
[225] C. J. Neijssel, A. Vigna-Gómez, S. Stevenson, J. W. Barrett, S. M. Gaebel, F. Broekgaarden, S. E. de Mink, D. Szécsi, S. Vinciguerra, and I. Mandel, *The Effect of the Metallicity-Specific Star Formation History on Double Compact Object Mergers*, Mon. Not. R. Astron. Soc. **490**, 3740 (2019).
[226] E. R. Higgins, A. A. C. Sander, J. S. Vink, and R. Hirschi, *Evolution of Wolf–Rayet Stars as Black Hole Progenitors*, Mon. Not. R. Astron. Soc. **505**, 4874 (2021).
[227] S. Stevenson, F. Ohme, and S. Fairhurst, *Distinguishing Compact Binary Population Synthesis Models Using Gravitational-Wave Observations of Coalescing Binary Black Holes*, Astrophys. J. **810**, 58 (2015).
[228] J. W. Barrett, S. M. Gaebel, C. J. Neijssel, A. Vigna-Gómez, S. Stevenson, C. P. L. Berry, W. M. Farr, and I. Mandel, *Accuracy of Inference on the Physics of Binary Evolution from Gravitational-Wave Observations*, Mon. Not. R. Astron. Soc. **477**, 4685 (2018).
[229] A. Hall, A. D. Gow, and C. T. Byrnes, *Bayesian Analysis of LIGO-Virgo Mergers: Primordial versus Astrophysical Black Hole Populations*, Phys. Rev. D **102**, 123524 (2020).
[230] S. S. Bavera *et al.*, *The Impact of Mass-Transfer Physics on the Observable Properties of Field Binary Black Hole Populations*, Astron. Astrophys. **647**, A153 (2021).
[231] Y. Bouffanais, M. Mapelli, F. Santoliquido, N. Giacobbo, G. Iorio, and G. Costa, *Constraining Accretion Efficiency in Massive Binary Stars with LIGO–Virgo Black Holes*, Mon. Not. R. Astron. Soc. **505**, 3873 (2021).
[232] M. Zevin, S. S. Bavera, C. P. L. Berry, V. Kalogera, T. Fragos, P. Marchant, C. L. Rodriguez, F. Antonini, D. E. Holz, and C. Pankow, *One Channel to Rule Them All? Constraining the Origins of Binary Black Holes Using Multiple Formation Pathways*, Astrophys. J. **910**, 152 (2021).
[233] G. Franciolini, V. Baibhav, V. De Luca, K. K. Y. Ng, K. W. K. Wong, E. Berti, P. Pani, A. Riotto, and S. Vitale, *Searching for a Subpopulation of Primordial Black Holes in LIGO-Virgo Gravitational-Wave Data*, Phys. Rev. D **105**, 083526 (2022).
[234] M. Mapelli, Y. Bouffanais, F. Santoliquido, M. A. Sedda, and M. C. Artale, *The Cosmic Evolution of Binary Black Holes in Young, Globular, and Nuclear Star Clusters: Rates, Masses, Spins, and Mixing Fractions*, Mon. Not. R. Astron. Soc. **511**, 5797 (2022).
[235] J. G. Baker, W. D. Boggs, J. Centrella, B. J. Kelly, S. T. McWilliams, and J. R. van Meter, *Mergers of Non-Spinning Black-Hole Binaries: Gravitational Radiation Characteristics*, Phys. Rev. D **78**, 044046 (2008).
[236] C. Reisswig, S. Husa, L. Rezzolla, E. N. Dorband, D. Pollney, and J. Seiler, *Gravitational-Wave Detectability of Equal-Mass Black-Hole Binaries with Aligned Spins*, Phys. Rev. D **80**, 124026 (2009).
[237] J. Healy and C. O. Lousto, *Remnant of Binary Black-Hole Mergers: New Simulations and Peak Luminosity Studies*, Phys. Rev. D **95**, 024037 (2017).
[238] X. Jiménez-Forteza, D. Keitel, S. Husa, M. Hannam, S. Khan, and M. Pürrer, *Hierarchical Data-Driven Approach to Fitting Numerical Relativity Data for Nonprecessing Binary Black Holes with an Application to Final Spin and Radiated Energy*, Phys. Rev. D **95**, 064024 (2017).
[239] M. C. Miller and E. J. M. Colbert, *Intermediate-Mass Black Holes*, Int. J. Mod. Phys. D **13**, 1 (2004).
[240] J. E. Greene, J. Strader, and L. C. Ho, *Intermediate-Mass Black Holes*, Annu. Rev. Astron. Astrophys. **58**, 257 (2020).
[241] R. Abbott *et al.* (LIGO Scientific Collaboration and Virgo Collaboration), *GW190814: Gravitational Waves from the Coalescence of a 23 Solar Mass Black Hole with a 2.6 Solar Mass Compact Object*, Astrophys. J. Lett. **896**, L44 (2020).
[242] J. Alsing, H. O. Silva, and E. Berti, *Evidence for a Maximum Mass Cut-Off in the Neutron Star Mass Distribution and Constraints on the Equation of State*, Mon. Not. R. Astron. Soc. **478**, 1377 (2018).
[243] E. Fonseca *et al.*, *Refined Mass and Geometric Measurements of the High-Mass PSR J0740+6620*, Astrophys. J. Lett. **915**, L12 (2021).
[244] D. J. Reardon *et al.*, *The Parkes Pulsar Timing Array Second Data Release: Timing Analysis*, Mon. Not. R. Astron. Soc. **507**, 2137 (2021).
[245] T. A. Thompson *et al.*, *A Noninteracting Low-Mass Black Hole-Giant Star Binary System*, Science **366**, 637 (2019).
[246] T. Jayasinghe *et al.*, *A Unicorn in Monoceros: The $3M_\odot$ Dark Companion to the Bright, Nearby Red Giant V723 Mon Is a Non-Interacting, Mass-Gap Black Hole Candidate*, Mon. Not. R. Astron. Soc. **504**, 2577 (2021).
[247] K. El-Badry, R. Seeburger, T. Jayasinghe, H.-W. Rix, S. Almada, C. Conroy, A. M. Price-Whelan, and K. Burdge, *Unicorns and Giraffes in the Binary Zoo: Stripped Giants with Subgiant Companions*, Mon. Not. R. Astron. Soc. **512**, 5620 (2022).
[248] P. C. C. Freire, S. M. Ransom, S. Begin, I. H. Stairs, J. W. T. Hessels, L. H. Frey, and F. Camilo, *Eight New Millisecond Pulsars in NGC 6440 and NGC 6441*, Astrophys. J. **675**, 670 (2008).
[249] R. Essick and P. Landry, *Discriminating between Neutron Stars and Black Holes with Imperfect Knowledge of the Maximum Neutron Star Mass*, Astrophys. J. **904**, 80 (2020).
[250] D. A. Godzieba, D. Radice, and S. Bernuzzi, *On the Maximum Mass of Neutron Stars and GW190814*, Astrophys. J. **908**, 122 (2021).
[251] K. Huang, J. Hu, Y. Zhang, and H. Shen, *The Possibility of the Secondary Object in GW190814 as a Neutron Star*, Astrophys. J. **904**, 39 (2020).
[252] E. R. Most, L. J. Papenfort, L. R. Weih, and L. Rezzolla, *A Lower Bound on the Maximum Mass if the Secondary in*

GW190814 Was Once a Rapidly Spinning Neutron Star, Mon. Not. R. Astron. Soc. **499**, L82 (2020).
[253] A. Tsokaros, M. Ruiz, and S. L. Shapiro, *GW190814: Spin and Equation of State of a Neutron Star Companion*, Astrophys. J. **905**, 48 (2020).
[254] I. Tews, P. T. H. Pang, T. Dietrich, M. W. Coughlin, S. Antier, M. Bulla, J. Heinzel, and L. Issa, *On the Nature of GW190814 and Its Impact on the Understanding of Supranuclear Matter*, Astrophys. J. Lett. **908**, L1 (2021).
[255] F. Özel and P. Freire, *Masses, Radii, and the Equation of State of Neutron Stars*, Annu. Rev. Astron. Astrophys. **54**, 401 (2016).
[256] J. G. Martinez, K. Stovall, P. C. C. Freire, J. S. Deneva, F. A. Jenet, M. A. McLaughlin, M. Bagchi, S. D. Bates, and A. Ridolfi, *Pulsar J0453+1559: A Double Neutron Star System with a Large Mass Asymmetry*, Astrophys. J. **812**, 143 (2015).
[257] T. M. Tauris and H.-T. Janka, *J0453+1559: A Neutron Star–White Dwarf Binary from a Thermonuclear Electron-Capture Supernova?*, Astrophys. J. Lett. **886**, L20 (2019).
[258] R. D. Ferdman *et al.*, *A Precise Mass Measurement of the Intermediate-Mass Binary Pulsar PSR J1802–2124*, Astrophys. J. **711**, 764 (2010).
[259] M. Falanga, E. Bozzo, A. Lutovinov, J. M. Bonnet-Bidaud, Y. Fetisova, and J. Puls, *Ephemeris, Orbital Decay, and Masses of Ten Eclipsing High-Mass X-Ray Binaries*, Astron. Astrophys. **577**, A130 (2015).
[260] B. P. Abbott *et al.* (LIGO Scientific Collaboration and Virgo Collaboration), *Model Comparison from LIGO–Virgo Data on GW170817's Binary Components and Consequences for the Merger Remnant*, Classical Quantum Gravity **37**, 045006 (2020).
[261] R. Essick, P. Landry, and D. E. Holz, *Nonparametric Inference of Neutron Star Composition, Equation of State, and Maximum Mass with GW170817*, Phys. Rev. D **101**, 063007 (2020).
[262] K. Chatziioannou and W. M. Farr, *Inferring the Maximum and Minimum Mass of Merging Neutron Stars with Gravitational Waves*, Phys. Rev. D **102**, 064063 (2020).
[263] D. Wysocki, R. O'Shaughnessy, L. Wade, and J. Lange, *Inferring the Neutron Star Equation of State Simultaneously with the Population of Merging Neutron Stars*, arXiv:2001.01747.
[264] J. Golomb and C. Talbot, *Hierarchical Inference of Binary Neutron Star Mass Distribution and Equation of State with Gravitational Waves*, Astrophys. J. **926**, 79 (2022).
[265] T. M. Tauris, N. Langer, and Ph. Podsiadlowski, *Ultra-Stripped Supernovae: Progenitors and Fate*, Mon. Not. R. Astron. Soc. **451**, 2123 (2015).
[266] B. Müller, T. M. Tauris, A. Heger, P. Banerjee, Y. Z. Qian, J. Powell, C. Chan, D. W. Gay, and N. Langer, *Three-Dimensional Simulations of Neutrino-Driven Core-Collapse Supernovae from Low-Mass Single and Binary Star Progenitors*, Mon. Not. R. Astron. Soc. **484**, 3307 (2019).
[267] A. Vigna-Gómez *et al.*, *On the Formation History of Galactic Double Neutron Stars*, Mon. Not. R. Astron. Soc. **481**, 4009 (2018).
[268] Y. Suwa, T. Yoshida, M. Shibata, H. Umeda, and K. Takahashi, *On the Minimum Mass of Neutron Stars*, Mon. Not. R. Astron. Soc. **481**, 3305 (2018).
[269] A. Burrows, D. Radice, D. Vartanyan, H. Nagakura, M. A. Skinner, and J. Dolence, *The Overarching Framework of Core-Collapse Supernova Explosions as Revealed by 3D Fornax Simulations*, Mon. Not. R. Astron. Soc. **491**, 2715 (2020).
[270] T. Ertl, S. E. Woosley, T. Sukhbold, and H. T. Janka, *The Explosion of Helium Stars Evolved with Mass Loss*, Astrophys. J. **890**, 51 (2020).
[271] S. Vitale, R. Lynch, J. Veitch, V. Raymond, and R. Sturani, *Measuring the Spin of Black Holes in Binary Systems Using Gravitational Waves*, Phys. Rev. Lett. **112**, 251101 (2014).
[272] K. Chatziioannou, N. Cornish, A. Klein, and N. Yunes, *Spin-Precession: Breaking the Black Hole–Neutron Star Degeneracy*, Astrophys. J. Lett. **798**, L17 (2015).
[273] G. Pratten, P. Schmidt, R. Buscicchio, and L. M. Thomas, *Measuring Precession in Asymmetric Compact Binaries*, Phys. Rev. Res. **2**, 043096 (2020).
[274] T. Damour, *Coalescence of Two Spinning Black Holes: An Effective One-Body Approach*, Phys. Rev. D **64**, 124013 (2001).
[275] L. Blanchet, *Gravitational Radiation from Post-Newtonian Sources and Inspiralling Compact Binaries*, Living Rev. Relativity **17**, 2 (2014).
[276] M. Pürrer, M. Hannam, and F. Ohme, *Can We Measure Individual Black-Hole Spins from Gravitational-Wave Observations?*, Phys. Rev. D **93**, 084042 (2016).
[277] K. K. Y. Ng, S. Vitale, A. Zimmerman, K. Chatziioannou, D. Gerosa, and C.-J. Haster, *Gravitational-Wave Astrophysics with Effective-Spin Measurements: Asymmetries and Selection Biases*, Phys. Rev. D **98**, 083007 (2018).
[278] M. Zevin, C. P. L. Berry, S. Coughlin, K. Chatziioannou, and S. Vitale, *You Can't Always Get What You Want: The Impact of Prior Assumptions on Interpreting GW190412*, Astrophys. J. Lett. **899**, L17 (2020).
[279] M. Hannam, P. Schmidt, A. Bohé, L. Haegel, S. Husa, F. Ohme, G. Pratten, and M. Pürrer, *Simple Model of Complete Precessing Black-Hole-Binary Gravitational Waveforms*, Phys. Rev. Lett. **113**, 151101 (2014).
[280] P. Schmidt, F. Ohme, and M. Hannam, *Towards Models of Gravitational Waveforms from Generic Binaries II: Modelling Precession Effects with a Single Effective Precession Parameter*, Phys. Rev. D **91**, 024043 (2015).
[281] É. Racine, *Analysis of Spin Precession in Binary Black Hole Systems Including Quadrupole-Monopole Interaction*, Phys. Rev. D **78**, 044021 (2008).
[282] M. Campanelli, C. O. Lousto, and Y. Zlochower, *Spinning-Black-Hole Binaries: The Orbital Hang Up*, Phys. Rev. D **74**, 041501 (2006).
[283] M. Pürrer, M. Hannam, P. Ajith, and S. Husa, *Testing the Validity of the Single-Spin Approximation in Inspiral-Merger-Ringdown Waveforms*, Phys. Rev. D **88**, 064007 (2013).
[284] J. Roulet and M. Zaldarriaga, *Constraints on Binary Black Hole Populations from LIGO–Virgo Detections*, Mon. Not. R. Astron. Soc. **484**, 4216 (2019).

[285] T. A. Apostolatos, C. Cutler, G. J. Sussman, and K. S. Thorne, *Spin Induced Orbital Precession and Its Modulation of the Gravitational Wave Forms from Merging Binaries*, Phys. Rev. D **49**, 6274 (1994).

[286] L. E. Kidder, *Coalescing Binary Systems of Compact Objects to (post)$^{5/2}$-Newtonian Order. V. Spin Effects*, Phys. Rev. D **52**, 821 (1995).

[287] B. P. Abbott *et al.* (LIGO Scientific Collaboration and Virgo Collaboration), *Improved Analysis of GW150914 Using a Fully Spin-Precessing Waveform Model*, Phys. Rev. X **6**, 041014 (2016).

[288] R. Green, C. Hoy, S. Fairhurst, M. Hannam, F. Pannarale, and C. Thomas, *Identifying when Precession Can Be Measured in Gravitational Waveforms*, Phys. Rev. D **103**, 124023 (2021).

[289] D. Gerosa, M. Kesden, U. Sperhake, E. Berti, and R. O'Shaughnessy, *Multi-Timescale Analysis of Phase Transitions in Precessing Black-Hole Binaries*, Phys. Rev. D **92**, 064016 (2015).

[290] N. K. Johnson-McDaniel, S. Kulkarni, and A. Gupta, *Inferring Spin Tilts at Formation from Gravitational Wave Observations of Binary Black Holes: Interfacing Precession-Averaged and Orbit-Averaged Spin Evolution*, Phys. Rev. D **106**, 023001 (2022).

[291] K. Chatziioannou, A. Klein, N. Yunes, and N. Cornish, *Constructing Gravitational Waves from Generic Spin-Precessing Compact Binary Inspirals*, Phys. Rev. D **95**, 104004 (2017).

[292] I. Mandel and R. O'Shaughnessy, *Compact Binary Coalescences in the Band of Ground-Based Gravitational-Wave Detectors*, Classical Quantum Gravity **27**, 114007 (2010).

[293] S. Vitale, R. Lynch, R. Sturani, and P. Graff, *Use of Gravitational Waves to Probe the Formation Channels of Compact Binaries*, Classical Quantum Gravity **34**, 03LT01 (2017).

[294] S. Stevenson, C. P. L. Berry, and I. Mandel, *Hierarchical Analysis of Gravitational-Wave Measurements of Binary Black Hole Spin–Orbit Misalignments*, Mon. Not. R. Astron. Soc. **471**, 2801 (2017).

[295] M. Fishbach, D. E. Holz, and B. Farr, *Are LIGO's Black Holes Made from Smaller Black Holes?*, Astrophys. J. Lett. **840**, L24 (2017).

[296] C. Talbot and E. Thrane, *Determining the Population Properties of Spinning Black Holes*, Phys. Rev. D **96**, 023012 (2017).

[297] B. Mckernan *et al.*, *Constraining Stellar-Mass Black Hole Mergers in AGN Disks Detectable with LIGO*, Astrophys. J. **866**, 66 (2018).

[298] Y. Yang *et al.*, *Hierarchical Black Hole Mergers in Active Galactic Nuclei*, Phys. Rev. Lett. **123**, 181101 (2019).

[299] B. McKernan, K. E. S. Ford, R. O'Shaughnessy, and D. Wysocki, *Monte Carlo Simulations of Black Hole Mergers in AGN Discs: Low $\chi_{\rm eff}$ Mergers and Predictions for LIGO*, Mon. Not. R. Astron. Soc. **494**, 1203 (2020).

[300] A. Secunda, J. Bellovary, M.-M. Mac Low, K. E. S. Ford, B. McKernan, N. W. C. Leigh, W. Lyra, Z. Sandor, and J. I. Adorno, *Orbital Migration of Interacting Stellar Mass Black Holes in Disks around Supermassive Black Holes II. Spins and Incoming Objects*, Astrophys. J. **903**, 133 (2020).

[301] H. Tagawa, Z. Haiman, I. Bartos, and B. Kocsis, *Spin Evolution of Stellar-Mass Black Hole Binaries in Active Galactic Nuclei*, Astrophys. J. **899**, 26 (2020).

[302] V. Kalogera, *Spin Orbit Misalignment in Close Binaries with Two Compact Objects*, Astrophys. J. **541**, 319 (2000).

[303] C. L. Rodriguez, M. Zevin, C. Pankow, V. Kalogera, and F. A. Rasio, *Illuminating Black Hole Binary Formation Channels with Spins in Advanced LIGO*, Astrophys. J. Lett. **832**, L2 (2016).

[304] B. P. Abbott *et al.* (LIGO Scientific Collaboration and Virgo Collaboration), *GW170104: Observation of a 50-Solar-Mass Binary Black Hole Coalescence at Redshift 0.2*, Phys. Rev. Lett. **118**, 221101 (2017); **121**, 129901(E) (2018).

[305] T. A. Callister, W. M. Farr, and M. Renzo, *State of the Field: Binary Black Hole Natal Kicks and Prospects for Isolated Field Formation after GWTC-2*, Astrophys. J. **920**, 157 (2021).

[306] N. Steinle and M. Kesden, *Pathways for Producing Binary Black Holes with Large Misaligned Spins in the Isolated Formation Channel*, Phys. Rev. D **103**, 063032 (2021).

[307] C. Chan, B. Müller, and A. Heger, *The Impact of Fallback on the Compact Remnants and Chemical Yields of Core-Collapse Supernovae*, Mon. Not. R. Astron. Soc. **495**, 3751 (2020).

[308] G. Fragione, A. Loeb, and F. A. Rasio, *Impact of Natal Kicks on Merger Rates and Spin–Orbit Misalignments of Black Hole–Neutron Star Mergers*, Astrophys. J. Lett. **918**, L38 (2021).

[309] Y. Huang, C.-J. Haster, S. Vitale, A. Zimmerman, J. Roulet, T. Venumadhav, B. Zackay, L. Dai, and M. Zaldarriaga, *Source Properties of the Lowest Signal-to-Noise-Ratio Binary Black Hole Detections*, Phys. Rev. D **102**, 103024 (2020).

[310] G. Pratten and A. Vecchio, *Assessing Gravitational-Wave Binary Black Hole Candidates with Bayesian Odds*, Phys. Rev. D **104**, 124039 (2021).

[311] R. Abbott *et al.* (LIGO Scientific Collaboration and Virgo Collaboration), *GW190412: Observation of a Binary-Black-Hole Coalescence with Asymmetric Masses*, Phys. Rev. D **102**, 043015 (2020).

[312] S. Biscoveanu, M. Isi, S. Vitale, and V. Varma, *New Spin on LIGO-Virgo Binary Black Holes*, Phys. Rev. Lett. **126**, 171103 (2021).

[313] F. Pretorius, *Evolution of Binary Black Hole Spacetimes*, Phys. Rev. Lett. **95**, 121101 (2005).

[314] J. A. González, U. Sperhake, B. Brügmann, M. Hannam, and S. Husa, *The Maximum Kick from Nonspinning Black-Hole Binary Inspiral*, Phys. Rev. Lett. **98**, 091101 (2007).

[315] A. Buonanno, L. E. Kidder, and L. Lehner, *Estimating the Final Spin of a Binary Black Hole Coalescence*, Phys. Rev. D **77**, 026004 (2008).

[316] J. T. Gálvez Ghersi and L. C. Stein, *A Fixed Point for Black Hole Distributions*, Classical Quantum Gravity **38**, 045012 (2021).

[317] M. C. Miller and J. M. Miller, *The Masses and Spins of Neutron Stars and Stellar-Mass Black Holes*, Phys. Rep. **548**, 1 (2014).

[318] C. S. Reynolds, *Observational Constraints on Black Hole Spin*, Annu. Rev. Astron. Astrophys. **59**, 117 (2021).
[319] Ph. Podsiadlowski, S. Rappaport, and Z. Han, *On the Formation and Evolution of Black Hole Binaries*, Mon. Not. R. Astron. Soc. **341**, 385 (2003).
[320] T. Fragos and J. E. McClintock, *The Origin of Black Hole Spin in Galactic Low-Mass X-Ray Binaries*, Astrophys. J. **800**, 17 (2015).
[321] M. Sørensen, T. Fragos, J. F. Steiner, V. Antoniou, G. Meynet, and F. Dosopoulou, *Unraveling the Formation History of the Black Hole X-Ray Binary LMC X-3 from the Zero Age Main Sequence to the Present*, Astron. Astrophys. **597**, A12 (2017).
[322] F. Valsecchi, E. Glebbeek, W. M. Farr, T. Fragos, B. Willems, J. A. Orosz, J. Liu, and V. Kalogera, *Formation of the Black-Hole Binary M33 X-7 via Mass-Exchange in a Tight Massive System*, Nature (London) **468**, 77 (2010).
[323] Y. Qin, P. Marchant, T. Fragos, G. Meynet, and V. Kalogera, *On the Origin of Black-Hole Spin in High-Mass X-Ray Binaries*, Astrophys. J. Lett. **870**, L18 (2019).
[324] D. Kushnir, M. Zaldarriaga, J. A. Kollmeier, and R. Waldman, *GW150914: Spin Based Constraints on the Merger Time of the Progenitor System*, Mon. Not. R. Astron. Soc. **462**, 844 (2016).
[325] K. Hotokezaka and T. Piran, *Implications of the Low Binary Black Hole Aligned Spins Observed by LIGO*, Astrophys. J. **842**, 111 (2017).
[326] K. Belczynski *et al.*, *Evolutionary Roads Leading to Low Effective Spins, High Black Hole Masses, and O1/O2 Rates for LIGO/Virgo Binary Black Holes*, Astron. Astrophys. **636**, A104 (2020).
[327] Y. Qin, T. Fragos, G. Meynet, J. Andrews, M. Sørensen, and H. F. Song, *The Spin of the Second-Born Black Hole in Coalescing Binary Black Holes*, Astron. Astrophys. **616**, A28 (2018).
[328] J. Fuller and L. Ma, *Most Black Holes Are Born Very Slowly Rotating*, Astrophys. J. Lett. **881**, L1 (2019).
[329] S. S. Bavera, T. Fragos, Y. Qin, E. Zapartas, C. J. Neijssel, I. Mandel, A. Batta, S. M. Gaebel, C. Kimball, and S. Stevenson, *The Origin of Spin in Binary Black Holes: Predicting the Distributions of the Main Observables of Advanced LIGO*, Astron. Astrophys. **635**, A97 (2020).
[330] I. Mandel and T. Fragos, *An Alternative Interpretation of GW190412 as a Binary Black Hole Merger with a Rapidly Spinning Secondary*, Astrophys. J. Lett. **895**, L28 (2020).
[331] A. Olejak and K. Belczynski, *The Implications of High Black Hole Spins for the Origin of Binary Black Hole Mergers*, Astrophys. J. Lett. **921**, L2 (2021).
[332] S. E. de Mink, M. Cantiello, N. Langer, O. R. Pols, I. Brott, and S.-Ch. Yoon, *Rotational Mixing in Massive Binaries: Detached Short-Period Systems*, Astron. Astrophys. **497**, 243 (2009).
[333] I. Mandel and S. E. de Mink, *Merging Binary Black Holes Formed through Chemically Homogeneous Evolution in Short-Period Stellar Binaries*, Mon. Not. R. Astron. Soc. **458**, 2634 (2016).
[334] L. du Buisson, P. Marchant, Ph. Podsiadlowski, C. Kobayashi, F. B. Abdalla, P. Taylor, I. Mandel, S. E. de Mink, T. J. Moriya, and N. Langer, *Cosmic Rates of Black Hole Mergers and Pair-Instability Supernovae from Chemically Homogeneous Binary Evolution*, Mon. Not. R. Astron. Soc. **499**, 5941 (2020).
[335] P. Marchant, N. Langer, Ph. Podsiadlowski, T. M. Tauris, and T. J. Moriya, *A New Route towards Merging Massive Black Holes*, Astron. Astrophys. **588**, A50 (2016).
[336] M. Mirbabayi, A. Gruzinov, and J. Noreña, *Spin of Primordial Black Holes*, J. Cosmol. Astropart. Phys. 03 (2020) 017.
[337] V. De Luca, V. Desjacques, G. Franciolini, A. Malhotra, and A. Riotto, *The Initial Spin Probability Distribution of Primordial Black Holes*, J. Cosmol. Astropart. Phys. 05 (2019) 018.
[338] T. Harada, C.-M. Yoo, K. Kohri, Y. Koga, and T. Monobe, *Spins of Primordial Black Holes Formed in the Radiation-Dominated Phase of the Universe: First-Order Effect*, Astrophys. J. **908**, 140 (2021).
[339] E. Berti and M. Volonteri, *Cosmological Black Hole Spin Evolution by Mergers and Accretion*, Astrophys. J. **684**, 822 (2008).
[340] V. De Luca, G. Franciolini, P. Pani, and A. Riotto, *The Evolution of Primordial Black Holes and Their Final Observable Spins*, J. Cosmol. Astropart. Phys. 04 (2020) 052.
[341] T. Damour, M. Soffel, and C. Xu, *General Relativistic Celestial Mechanics. 2. Translational Equations of Motion*, Phys. Rev. D **45**, 1017 (1992).
[342] É. É. Flanagan and T. Hinderer, *Constraining Neutron Star Tidal Love Numbers with Gravitational Wave Detectors*, Phys. Rev. D **77**, 021502 (2008).
[343] K. Yagi and N. Yunes, *Approximate Universal Relations for Neutron Stars and Quark Stars*, Phys. Rep. **681**, 1 (2017).
[344] A. Le Tiec and M. Casals, *Spinning Black Holes Fall in Love*, Phys. Rev. Lett. **126**, 131102 (2021).
[345] H. S. Chia, *Tidal Deformation and Dissipation of Rotating Black Holes*, Phys. Rev. D **104**, 024013 (2021).
[346] W. D. Goldberger, J. Li, and I. Z. Rothstein, *Non-Conservative Effects on Spinning Black Holes from World-Line Effective Field Theory*, J. High Energy Phys. 06 (2021) 053.
[347] P. Charalambous, S. Dubovsky, and M. M. Ivanov, *On the Vanishing of Love Numbers for Kerr Black Holes*, J. High Energy Phys. 05 (2021) 038.
[348] P. Kumar, M. Pürrer, and H. P. Pfeiffer, *Measuring Neutron Star Tidal Deformability with Advanced LIGO: A Bayesian Analysis of Neutron Star-Black Hole Binary Observations*, Phys. Rev. D **95**, 044039 (2017).
[349] Y. Huang, C.-J. Haster, S. Vitale, V. Varma, F. Foucart, and S. Biscoveanu, *Statistical and Systematic Uncertainties in Extracting the Source Properties of Neutron Star-Black Hole Binaries with Gravitational Waves*, Phys. Rev. D **103**, 083001 (2021).
[350] S. M. Brown, C. D. Capano, and B. Krishnan, *Using Gravitational Waves to Distinguish between Neutron Stars and Black Holes in Compact Binary Mergers*, Astrophys. J. **941**, 98 (2022).
[351] L. Wen and Y. Chen, *Geometrical Expression for the Angular Resolution of a Network of Gravitational-Wave Detectors*, Phys. Rev. D **81**, 082001 (2010).

[352] L. P. Singer *et al.*, *The First Two Years of Electromagnetic Follow-Up with Advanced LIGO and Virgo*, Astrophys. J. **795**, 105 (2014).

[353] C. Pankow, M. Rizzo, K. Rao, C. P. L. Berry, and V. Kalogera, *Localization of Compact Binary Sources with Second Generation Gravitational-Wave Interferometer Networks*, Astrophys. J. **902**, 71 (2020).

[354] G. Dálya, G. Galgóczi, L. Dobos, Z. Frei, I. S. Heng, R. Macas, C. Messenger, P. Raffai, and R. S. de Souza, *GLADE: A Galaxy Catalogue for Multimessenger Searches in the Advanced Gravitational-Wave Detector Era*, Mon. Not. R. Astron. Soc. **479**, 2374 (2018).

[355] G. Dálya *et al.*, *GLADE+: An Extended Galaxy Catalogue for Multimessenger Searches with Advanced Gravitational-Wave Detectors*, Mon. Not. R. Astron. Soc. **514**, 1403 (2022).

[356] W. Del Pozzo, C. P. L. Berry, A. Ghosh, T. S. F. Haines, L. P. Singer, and A. Vecchio, *Dirichlet Process Gaussian-Mixture Model: An Application to Localizing Coalescing Binary Neutron Stars with Gravitational-Wave Observations*, Mon. Not. R. Astron. Soc. **479**, 601 (2018).

[357] T. B. Littenberg, J. G. Baker, A. Buonanno, and B. J. Kelly, *Systematic Biases in Parameter Estimation of Binary Black-Hole Mergers*, Phys. Rev. D **87**, 104003 (2013).

[358] V. Varma, P. Ajith, S. Husa, J. Calderon Bustillo, M. Hannam, and M. Pürrer, *Gravitational-Wave Observations of Binary Black Holes: Effect of Nonquadrupole Modes*, Phys. Rev. D **90**, 124004 (2014).

[359] P. Kumar, T. Chu, H. Fong, H. P. Pfeiffer, M. Boyle, D. A. Hemberger, L. E. Kidder, M. A. Scheel, and B. Szilagyi, *Accuracy of Binary Black Hole Waveform Models for Aligned-Spin Binaries*, Phys. Rev. D **93**, 104050 (2016).

[360] B. P. Abbott *et al.* (LIGO Scientific Collaboration and Virgo Collaboration), *Effects of Waveform Model Systematics on the Interpretation of GW150914*, Classical Quantum Gravity **34**, 104002 (2017).

[361] M. Pürrer and C.-J. Haster, *Gravitational Waveform Accuracy Requirements for Future Ground-Based Detectors*, Phys. Rev. Res. **2**, 023151 (2020).

[362] F. H. Shaik, J. Lange, S. E. Field, R. O'Shaughnessy, V. Varma, L. E. Kidder, H. P. Pfeiffer, and D. Wysocki, *Impact of Subdominant Modes on the Interpretation of Gravitational-Wave Signals from Heavy Binary Black Hole Systems*, Phys. Rev. D **101**, 124054 (2020).

[363] A. Ramos-Buades, P. Schmidt, G. Pratten, and S. Husa, *Validity of Common Modeling Approximations for Precessing Binary Black Holes with Higher-Order Modes*, Phys. Rev. D **101**, 103014 (2020).

[364] M. Colleoni, M. Mateu-Lucena, H. Estellés, C. García-Quirós, D. Keitel, G. Pratten, A. Ramos-Buades, and S. Husa, *Towards the Routine Use of Subdominant Harmonics in Gravitational-Wave Inference: Reanalysis of GW190412 with Generation X Waveform Models*, Phys. Rev. D **103**, 024029 (2021).

[365] D. Gerosa, M. Kesden, R. O'Shaughnessy, A. Klein, E. Berti, U. Sperhake, and D. Trifirò, *Precessional Instability in Binary Black Holes with Aligned Spins*, Phys. Rev. Lett. **115**, 141102 (2015).

[366] H. Estellés, M. Colleoni, C. García-Quirós, S. Husa, D. Keitel, M. Mateu-Lucena, M. d. L. Planas, and A. Ramos-Buades, *New Twists in Compact Binary Waveform Modeling: A Fast Time-Domain Model for Precession*, Phys. Rev. D **105**, 084040 (2022).

[367] S. Biscoveanu, M. Isi, V. Varma, and S. Vitale, *Measuring the Spins of Heavy Binary Black Holes*, Phys. Rev. D **104**, 103018 (2021).

[368] N. V. Krishnendu and F. Ohme, *Interplay of Spin-Precession and Higher Harmonics in the Parameter Estimation of Binary Black Holes*, Phys. Rev. D **105**, 064012 (2022).

[369] V. Varma and P. Ajith, *Effects of Nonquadrupole Modes in the Detection and Parameter Estimation of Black Hole Binaries with Nonprecessing Spins*, Phys. Rev. D **96**, 124024 (2017).

[370] E. Payne, C. Talbot, and E. Thrane, *Higher Order Gravitational-Wave Modes with Likelihood Reweighting*, Phys. Rev. D **100**, 123017 (2019).

[371] C. Mills and S. Fairhurst, *Measuring Gravitational-Wave Higher-Order Multipoles*, Phys. Rev. D **103**, 024042 (2021).

[372] P. Kumar, J. Blackman, S. E. Field, M. Scheel, C. R. Galley, M. Boyle, L. E. Kidder, H. P. Pfeiffer, B. Szilagyi, and S. A. Teukolsky, *Constraining the Parameters of GW150914 and GW170104 with Numerical Relativity Surrogates*, Phys. Rev. D **99**, 124005 (2019).

[373] K. Chatziioannou *et al.*, *On the Properties of the Massive Binary Black Hole Merger GW170729*, Phys. Rev. D **100**, 104015 (2019).

[374] C. Kalaghatgi, M. Hannam, and V. Raymond, *Parameter Estimation with a Spinning Multimode Waveform Model*, Phys. Rev. D **101**, 103004 (2020).

[375] S. Khan, F. Ohme, K. Chatziioannou, and M. Hannam, *Including Higher Order Multipoles in Gravitational-Wave Models for Precessing Binary Black Holes*, Phys. Rev. D **101**, 024056 (2020).

[376] J. Veitch *et al.*, *Parameter Estimation for Compact Binaries with Ground-Based Gravitational-Wave Observations Using the* LALInference *Software Library*, Phys. Rev. D **91**, 042003 (2015).

[377] N. J. Cornish and T. B. Littenberg, *BayesWave: Bayesian Inference for Gravitational Wave Bursts and Instrument Glitches*, Classical Quantum Gravity **32**, 135012 (2015).

[378] B. P. Abbott *et al.* (LIGO Scientific Collaboration and Virgo Collaboration), *Search for Eccentric Binary Black Hole Mergers with Advanced LIGO and Advanced Virgo during Their First and Second Observing Runs*, Astrophys. J. **883**, 149 (2019).

[379] N. J. Cornish, T. B. Littenberg, B. Bécsy, K. Chatziioannou, J. A. Clark, S. Ghonge, and M. Millhouse, *BayesWave Analysis Pipeline in the Era of Gravitational Wave Observations*, Phys. Rev. D **103**, 044006 (2021).

[380] S. Ghonge, K. Chatziioannou, J. A. Clark, T. Littenberg, M. Millhouse, L. Cadonati, and N. Cornish, *Reconstructing Gravitational Wave Signals from Binary Black Hole Mergers with Minimal Assumptions*, Phys. Rev. D **102**, 064056 (2020).

[381] N. K. Johnson-McDaniel, A. Ghosh, S. Ghonge, M. Saleem, N. V. Krishnendu, and J. A. Clark, *Investigating the Relation between Gravitational Wave Tests of General Relativity*, Phys. Rev. D **105**, 044020 (2022).

[382] L. S. Finn, *Detection, Measurement and Gravitational Radiation*, Phys. Rev. D **46**, 5236 (1992).
[383] T. B. Littenberg, J. B. Kanner, N. J. Cornish, and M. Millhouse, *Enabling High Confidence Detections of Gravitational-Wave Bursts*, Phys. Rev. D **94**, 044050 (2016).
[384] B. Bécsy, P. Raffai, N. J. Cornish, R. Essick, J. Kanner, E. Katsavounidis, T. B. Littenberg, M. Millhouse, and S. Vitale, *Parameter Estimation for Gravitational-Wave Bursts with the BayesWave Pipeline*, Astrophys. J. **839**, 15 (2017).
[385] F. Pannarale, R. Macas, and P. J. Sutton, *Bayesian Inference Analysis of Unmodelled Gravitational-Wave Transients*, Classical Quantum Gravity **36**, 035011 (2019).
[386] J. Abadie *et al.* (LIGO Scientific Collaboration), *Search for Gravitational Waves Associated with Gamma-Ray Bursts during LIGO Science Run 6 and Virgo Science Runs 2 and 3*, Astrophys. J. **760**, 12 (2012).
[387] A. R. Williamson, J. Lange, R. O'Shaughnessy, J. A. Clark, P. Kumar, J. Calderón Bustillo, and J. Veitch, *Systematic Challenges for Future Gravitational Wave Measurements of Precessing Binary Black Holes*, Phys. Rev. D **96**, 124041 (2017).
[388] A. Samajdar and T. Dietrich, *Waveform Systematics for Binary Neutron Star Gravitational Wave Signals: Effects of Spin, Precession, and the Observation of Electromagnetic Counterparts*, Phys. Rev. D **100**, 024046 (2019).
[389] K. Jani, J. Healy, J. A. Clark, L. London, P. Laguna, and D. Shoemaker, *Georgia Tech Catalog of Gravitational Waveforms*, Classical Quantum Gravity **33**, 204001 (2016).
[390] M. Boyle *et al.*, *The SXS Collaboration Catalog of Binary Black Hole Simulations*, Classical Quantum Gravity **36**, 195006 (2019).
[391] J. Healy and C. O. Lousto, *Third RIT Binary Black Hole Simulations Catalog*, Phys. Rev. D **102**, 104018 (2020).
[392] C. O. Lousto and J. Healy, *Exploring the Small Mass Ratio Binary Black Hole Merger via Zeno's Dichotomy Approach*, Phys. Rev. Lett. **125**, 191102 (2020).
[393] M. E. Lower, E. Thrane, P. D. Lasky, and R. Smith, *Measuring Eccentricity in Binary Black Hole Inspirals with Gravitational Waves*, Phys. Rev. D **98**, 083028 (2018).
[394] B. Moore and N. Yunes, *Data Analysis Implications of Moderately Eccentric Gravitational Waves*, Classical Quantum Gravity **37**, 225015 (2020).
[395] I. M. Romero-Shaw, P. D. Lasky, and E. Thrane, *Searching for Eccentricity: Signatures of Dynamical Formation in the First Gravitational-Wave Transient Catalogue of LIGO and Virgo*, Mon. Not. R. Astron. Soc. **490**, 5210 (2019).
[396] A. K. Lenon, A. H. Nitz, and D. A. Brown, *Measuring the Eccentricity of GW170817 and GW190425*, Mon. Not. R. Astron. Soc. **497**, 1966 (2020).
[397] E. O'Shea and P. Kumar, *Correlations in Parameter Estimation of Low-Mass Eccentric Binaries: GW151226 & GW170608*, arXiv:2107.07981.
[398] M. Favata, C. Kim, K. G. Arun, J. Kim, and H. W. Lee, *Constraining the Orbital Eccentricity of Inspiralling Compact Binary Systems with Advanced LIGO*, Phys. Rev. D **105**, 023003 (2022).
[399] LIGO Scientific Collaboration, Virgo Collaboration, and KAGRA Collaboration, *The O3b Data Release* (2021), 10.7935/pr1e-j706.
[400] R. Abbott *et al.* (LIGO Scientific Collaboration, Virgo Collaboration, and KAGRA Collaboration), *Open Data from the Third Observing Run of LIGO, Virgo, KAGRA and GEO*, Astrophys. J. Suppl. Ser. **267**, 29 (2023).
[401] R. Abbott *et al.* (LIGO Scientific Collaboration and Virgo Collaboration), *Open Data from the First and Second Observing Runs of Advanced LIGO and Advanced Virgo*, SoftwareX **13**, 100658 (2021).
[402] A. H. Nitz, C. Capano, A. B. Nielsen, S. Reyes, R. White, D. A. Brown, and B. Krishnan, *1-OGC: The First Open Gravitational-Wave Catalog of Binary Mergers from Analysis of Public Advanced LIGO Data*, Astrophys. J. **872**, 195 (2019).
[403] R. Magee *et al.*, *Sub-Threshold Binary Neutron Star Search in Advanced LIGO's First Observing Run*, Astrophys. J. Lett. **878**, L17 (2019).
[404] K. Chandra, J. Calderón Bustillo, A. Pai, and I. W. Harry, *First Gravitational-Wave Search for Intermediate-Mass Black Hole Mergers with Higher-Order Harmonics*, Phys. Rev. D **106**, 123003 (2022).
[405] T. Akutsu *et al.* (KAGRA Collaboration), *KAGRA: 2.5 Generation Interferometric Gravitational Wave Detector*, Nat. Astron. **3**, 35 (2019).
[406] R. Abbott *et al.* (LIGO Scientific Collaboration, Virgo Collaboration, and KAGRA Collaboration), *First Joint Observation by the Underground Gravitational-Wave Detector KAGRA with GEO 600*, Prog. Theor. Exp. Phys. **2022**, 063F01 (2022).
[407] B. S. Sathyaprakash and B. F. Schutz, *Physics, Astrophysics and Cosmology with Gravitational Waves*, Living Rev. Relativity **12**, 2 (2009).
[408] B. P. Abbott *et al.* (LIGO Scientific Collaboration and Virgo Collaboration), *Optically Targeted Search for Gravitational Waves Emitted by Core-Collapse Supernovae during the First and Second Observing Runs of Advanced LIGO and Advanced Virgo*, Phys. Rev. D **101**, 084002 (2020).
[409] R. Abbott *et al.* (LIGO Scientific Collaboration and Virgo Collaboration), *All-Sky Search in Early O3 LIGO Data for Continuous Gravitational-Wave Signals from Unknown Neutron Stars in Binary Systems*, Phys. Rev. D **103**, 064017 (2021).
[410] R. Abbott *et al.* (LIGO Scientific Collaboration, Virgo Collaboration, and KAGRA Collaboration), *Constraints from LIGO O3 Data on Gravitational-Wave Emission Due to R-Modes in the Glitching Pulsar PSR J0537–6910*, Astrophys. J. **922**, 71 (2021).
[411] R. Abbott *et al.* (LIGO Scientific Collaboration, Virgo Collaboration, and KAGRA Collaboration), *Searches for Continuous Gravitational Waves from Young Supernova Remnants in the Early Third Observing Run of Advanced LIGO and Virgo*, Astrophys. J. **921**, 80 (2021).
[412] R. Abbott *et al.* (LIGO Scientific Collaboration, Virgo Collaboration, and KAGRA Collaboration), *Narrow-band Searches for Continuous and Long-Duration Transient Gravitational Waves from Known Pulsars in the*

LIGO-Virgo Third Observing Run, Astrophys. J. **932**, 133 (2022).

[413] R. Abbott *et al.* (LIGO Scientific Collaboration, Virgo Collaboration, and KAGRA Collaboration), *All-Sky Search for Continuous Gravitational Waves from Isolated Neutron Stars Using Advanced LIGO and Advanced Virgo O3 Data*, Phys. Rev. D **106**, 102008 (2022).

[414] R. Abbott *et al.* (LIGO Scientific Collaboration, Virgo Collaboration, and KAGRA Collaboration), *Search for Gravitational Waves from Scorpius X-1 with a Hidden Markov Model in O3 LIGO Data*, Phys. Rev. D **106**, 062002 (2022).

[415] R. Abbott *et al.* (LIGO Scientific Collaboration, Virgo Collaboration, and KAGRA Collaboration), *Upper Limits on the Isotropic Gravitational-Wave Background from Advanced LIGO and Advanced Virgo's Third Observing Run*, Phys. Rev. D **104**, 022004 (2021).

[416] R. Abbott *et al.* (LIGO Scientific Collaboration, Virgo Collaboration, and KAGRA Collaboration), *Search for Anisotropic Gravitational-Wave Backgrounds Using Data from Advanced LIGO and Advanced Virgo's First Three Observing Runs*, Phys. Rev. D **104**, 022005 (2021).

[417] John Zweizig, *The Data Monitor Tool Project* (2006), https://labcit.ligo.caltech.edu/~jzweizig/DMT-Project.html.

[418] R. P. Fisher, G. Hemming, M.-A. Bizouard, D. A. Brown, P. F. Couvares, F. Robinet, and D. Verkindt, *DQSEGDB: A Time-Interval Database for Storing Gravitational Wave Observatory Metadata*, SoftwareX **14**, 100677 (2021).

[419] A. L. Urban *et al.*, *gwdetchar/gwdetchar* (2021), 10.5281/zenodo.2575786.

[420] J. R. Smith, T. Abbott, E. Hirose, N. Leroy, D. Macleod, J. McIver, P. Saulson, and P. Shawhan, *A Hierarchical Method for Vetoing Noise Transients in Gravitational-Wave Detectors*, Classical Quantum Gravity **28**, 235005 (2011).

[421] R. Essick, P. Godwin, C. Hanna, L. Blackburn, and E. Katsavounidis, *iDQ: Statistical Inference of Non-Gaussian Noise with Auxiliary Degrees of Freedom in Gravitational-Wave Detectors*, Mach. Learn. Sci. Technol. **2**, 015004 (2020).

[422] Virgo Collaboration, PythonVirgotools, https://git.ligo.org/virgo/virgoapp/PythonVirgoTools (2021).

[423] LIGO Scientific Collaboration, *LIGO Algorithm Library*, 10.7935/GT1W-FZ16 (2018).

[424] J. S. Speagle, *Dynesty: A Dynamic Nested Sampling Package for Estimating Bayesian Posteriors and Evidences*, Mon. Not. R. Astron. Soc. **493**, 3132 (2020).

[425] C. Hoy and V. Raymond, *PESummary: The Code Agnostic Parameter Estimation Summary Page Builder*, SoftwareX **15**, 100765 (2021).

[426] D. Williams, J. Veitch, M. L. Chiofalo, P. Schmidt, R. P. Udall, A. Vajpeji, and C. Hoy, *Asimov: A Framework for Coordinating Parameter Estimation Workflows*, J. Open Source Softwaare **8**, 4170 (2023).

[427] J. D. Hunter, *MATPLOTLIB: A 2D Graphics Environment*, Comput. Sci. Eng. **9**, 90 (2007).

[428] M. L. Waskom, *seaborn: Statistical Data Visualization*, J. Open Source Softwaare **6**, 3021 (2021).

[429] D. Macleod *et al.*, *gwpy/gwpy* (2021), 10.5281/zenodo.597016.

[430] C. R. Harris *et al.*, *Array Programming with NumPy*, Nature (London) **585**, 357 (2020).

[431] P. Virtanen *et al.*, *SciPy 1.0–Fundamental Algorithms for Scientific Computing in PYTHON*, Nat. Methods **17**, 261 (2020).

[432] D. Chatterjee, S. Ghosh, P. R. Brady, S. J. Kapadia, A. L. Miller, S. Nissanke, and F. Pannarale, *A Machine Learning Based Source Property Inference for Compact Binary Mergers*, Astrophys. J. **896**, 54 (2020).

[433] R. Magee *et al.*, *First Demonstration of Early Warning Gravitational Wave Alerts*, Astrophys. J. Lett. **910**, L21 (2021).

[434] B. P. Abbott *et al.* (LIGO Scientific Collaboration and Virgo Collaboration), *Low-Latency Gravitational-Wave Alerts for Multimessenger Astronomy during the Second Advanced LIGO and Virgo Observing Run*, Astrophys. J. **875**, 161 (2019).

[435] S. Antier *et al.*, *GRANDMA Observations of Advanced LIGO's and Advanced Virgo's Third Observational Campaign*, Mon. Not. R. Astron. Soc. **497**, 5518 (2020).

[436] LIGO Scientific Collaboration and Virgo Collaboration, GCN 24069, 2019, https://gcn.gsfc.nasa.gov/other/S190408an.gcn3.

[437] R. Abbasi *et al.* (IceCube Collaboration), *Probing Neutrino Emission at GeV Energies from Compact Binary Mergers with the IceCube Neutrino Observatory*, arXiv:2105.13160.

[438] R. Abbasi *et al.* (IceCube Collaboration), *IceCube Search for Neutrinos Coincident with Gravitational Wave Events from LIGO/Virgo Run O3*, Astrophys. J. **944**, 80 (2023).

[439] R. Abbasi *et al.* (IceCube Collaboration), *A Search for IceCube Sub-TeV Neutrinos Correlated with Gravitational-Wave Events Detected By LIGO/Virgo*, arXiv:2303.15970.

[440] S. Abe *et al.* (KamLAND Collaboration), *Search for Low-Energy Electron Antineutrinos in KamLAND Associated with Gravitational Wave Events*, Astrophys. J. **909**, 116 (2021).

[441] K. Abe *et al.* (Super-Kamiokande Collaboration), *Search for Neutrinos in Coincidence with Gravitational Wave Events from the LIGO-Virgo O3a Observing Run with the Super-Kamiokande Detector*, Astrophys. J. **918**, 78 (2021).

[442] M. A. Acero *et al.* (NOvA Collaboration), *Search for Multimessenger Signals in NOvA Coincident with LIGO/Virgo Detections*, Phys. Rev. D **101**, 112006 (2020).

[443] O. Adriani *et al.*, *CALET Search for Electromagnetic Counterparts of Gravitational Waves during the LIGO/Virgo O3 Run*, Astrophys. J. **933**, 85 (2022).

[444] S. Antier *et al.*, *The First Six Months of the Advanced LIGO's and Advanced Virgo's Third Observing Run with GRANDMA*, Mon. Not. R. Astron. Soc. **492**, 3904 (2020).

[445] R. L. Becerra *et al.*, *DDOTI Observations of Gravitational-Wave Sources Discovered in O3*, Mon. Not. R. Astron. Soc. **507**, 1401 (2021).

[446] C. Cai *et al.*, *Search for Gamma-Ray Bursts and Gravitational Wave Electromagnetic Counterparts with High Energy X-Ray Telescope of Insight-HXMT*, Mon. Not. R. Astron. Soc. **508**, 3910 (2021).

[447] B. P. Gompertz *et al.*, *Searching for Electromagnetic Counterparts to Gravitational-wave Merger Events with the Prototype Gravitational-Wave Optical Transient Observer (GOTO-4)*, Mon. Not. R. Astron. Soc. **497**, 726 (2020).

[448] M. J. Graham *et al.*, *A Light in the Dark: Searching for Electromagnetic Counterparts to Black Hole–Black Hole Mergers in LIGO/Virgo O3 with the Zwicky Transient Facility*, Astrophys. J. **942**, 99 (2023).

[449] R. Hussain, J. Vandenbroucke, and J. Wood (IceCube Collaboration), *A Search for IceCube Neutrinos from the First 33 Detected Gravitational Wave Events*, Proc. Sci., ICRC2019 (**2020**) 918 [arXiv:1908.07706].

[450] J. Kim *et al.*, *GECKO Optical Follow-Up Observation of Three Binary Black Hole Merger Events: GW190408_181802, GW190412, and GW190503_185404*, Astrophys. J. **916**, 47 (2021).

[451] V. Lipunov *et al.*, *Strategy and Results of MASTER Network Follow-Up Observations of LIGO and Virgo Gravitational Wave Events within the Observational Sets O1, O2, and O3*, Astron. Rep. **66**, 1118 (2022).

[452] M. J. Lundquist *et al.*, *Searches after Gravitational Waves Using ARizona Observatories (SAGUARO): System Overview and First Results from Advanced LIGO/Virgo's Third Observing Run*, Astrophys. J. Lett. **881**, L26 (2019).

[453] G. Mo, R. Jayaraman, M. Fausnaugh, E. Katsavounidis, G. R. Ricker, and R. Vanderspek, *Searching for Gravitational-Wave Counterparts Using the Transiting Exoplanet Survey Satellite*, Astrophys. J. Lett. **948**, L3 (2023).

[454] K. Paterson *et al.*, *Searches after Gravitational Waves Using ARizona Observatories (SAGUARO): Observations and Analysis from Advanced LIGO/Virgo's Third Observing Run*, Astrophys. J. **912**, 128 (2021).

[455] A. Ridnaia, D. Svinkin, and D. Frederiks, *A Search for Gamma-Ray Counterparts to Gravitational Wave Events in Konus-Wind Data*, J. Phys. Conf. Ser. **1697**, 012030 (2020).

[456] M. Sasada *et al.* (J-GEM Collaboration), *J-GEM Optical and Near-Infrared Follow-Up of Gravitational Wave Events during LIGO's and Virgo's Third Observing Run*, Prog. Theor. Exp. Phys. **2021**, 05A104 (2021).

[457] I. B. Unatlokov, I. M. Dzaparova, M. G. Kostyuk, M. M. Kochkarov, A. N. Kurenya, Y. F. Novoseltsev, R. V. Novoseltseva, V. B. Petkov, P. S. Striganov, and A. F. Yanin, *Search for Neutrino Counterparts of LIGO/Virgo Gravitational-Wave Events*, J. Phys. Conf. Ser. **2156**, 012142 (2021).

[458] LIGO Scientific Collaboration and Virgo Collaboration, GCN 24098, 2019, https://gcn.gsfc.nasa.gov/other/S190412m.gcn3.

[459] A. Albert *et al.* (ANTARES Collaboration), *Search for Neutrino Counterparts to the Gravitational Wave Sources from LIGO/Virgo O3 Run with the ANTARES Detector*, J. Cosmol. Astropart. Phys. 04 (2023) 004.

[460] S. R. Oates *et al.*, *Swift/UVOT Follow-Up of Gravitational Wave Alerts in the O3 Era*, Mon. Not. R. Astron. Soc. **507**, 1296 (2021).

[461] K. L. Page *et al.*, *Swift-XRT Follow-Up of Gravitational Wave Triggers during the Third aLIGO/Virgo Observing Run*, Mon. Not. R. Astron. Soc. **499**, 3459 (2020).

[462] LIGO Scientific Collaboration and Virgo Collaboration, GCN 24141, 2019, https://gcn.gsfc.nasa.gov/other/S190421ar.gcn3.

[463] LIGO Scientific Collaboration and Virgo Collaboration, GCN 24168, 2019, https://gcn.gsfc.nasa.gov/other/S190425z.gcn3.

[464] O. M. Boersma *et al.*, *A Search for Radio Emission from Double-Neutron Star Merger GW190425 Using Apertif*, Astron. Astrophys. **650**, A131 (2021).

[465] D. Basilico *et al.* (Borexino Collaboration), *Borexino's Search for Low-Energy Neutrinos Associated with Gravitational Wave Events from GWTC-3 Database*, Eur. Phys. J. C **83**, 538 (2023).

[466] S.-W. Chang, C. A. Onken, C. Wolf, L. Luvaul, A. Möller, R. Scalzo, B. P. Schmidt, S. M. Scott, N. Sura, and F. Yuan, *SkyMapper Optical Follow-Up of Gravitational Wave Triggers: Alert Science Data Pipeline and LIGO/Virgo O3 Run*, Pub. Astron. Soc. Aust. **38**, e024 (2021).

[467] M. W. Coughlin *et al.*, *Implications of the Search for Optical Counterparts during the Second Part of the Advanced LIGO's and Advanced Virgo's Third Observing Run: Lessons Learned for Future Follow-Up Observations*, Mon. Not. R. Astron. Soc. **497**, 1181 (2020).

[468] T. de Jaeger, B. J. Shappee, C. S. Kochanek, K. Z. Stanek, J. F. Beacom, T. W.-S. Holoien, T. A. Thompson, A. Franckowiak, and S. Holmbo, *ASAS-SN Search for Optical Counterparts of Gravitational-Wave Events from the Third Observing Run of Advanced LIGO/Virgo*, Mon. Not. R. Astron. Soc. **509**, 3427 (2022).

[469] G. Hosseinzadeh *et al.*, *Follow-Up of the Neutron Star Bearing Gravitational Wave Candidate Events S190425z and S190426c with MMT and SOAR*, Astrophys. J. Lett. **880**, L4 (2019).

[470] M. M. Kasliwal *et al.*, *Kilonova Luminosity Function Constraints Based on Zwicky Transient Facility Searches for 13 Neutron Star Merger Triggers during O3*, Astrophys. J. **905**, 145 (2020).

[471] F. H. Panther *et al.*, *The Most Probable Host of CHIME FRB 190425A, Associated with Binary Neutron Star Merger GW190425, and a Late-Time Transient Search*, Mon. Not. R. Astron. Soc. **519**, 2235 (2023).

[472] A. S. Pozanenko, P. Yu. Minaev, S. A. Grebenev, and I. V. Chelovekov, *Observation of the Second LIGO/Virgo Event Connected with a Binary Neutron Star Merger S190425z in the Gamma-Ray Range*, Astron. Lett. **45**, 710 (2020).

[473] LIGO Scientific Collaboration and Virgo Collaboration, GCN 24237, 2019, https://gcn.gsfc.nasa.gov/other/S190426c.gcn3.

[474] S. Anand *et al.*, *DECam-GROWTH Search for the Faint and Distant Binary Neutron Star and Neutron Star-Black Hole Mergers in O3a*, Rev. Mex. Astron. Astrofis. **53**, 91 (2021).

[475] D. A. Goldstein *et al.*, *GROWTH on S190426c: Real-Time Search for a Counterpart to the Probable Neutron Star–Black Hole Merger Using an Automated Difference Imaging Pipeline for DECam*, Astrophys. J. Lett. **881**, L7 (2019).

[476] K. Gourdji, A. Rowlinson, R. Wijers, J. Broderick, and A. Shulevski, *LOFAR Observations of Gravitational Wave*

Merger Events: O3 Results and O4 Strategy, Mon. Not. R. Astron. Soc. **523**, 4748 (2023).
[477] H. Kumar *et al.*, *GROWTH on S190426c II: GROWTH-India Telescope Search for an Optical Counterpart with a Custom Image Reduction and Candidate Vetting Pipeline*, Mon. Not. R. Astron. Soc. **516**, 4517 (2022).
[478] LIGO Scientific Collaboration and Virgo Collaboration, GCN 24377, 2019, https://gcn.gsfc.nasa.gov/other/S190503bf.gcn3.
[479] LIGO Scientific Collaboration and Virgo Collaboration, GCN 24442, 2019, https://gcn.gsfc.nasa.gov/other/S190510g.gcn3.
[480] I. Andreoni *et al.*, *GROWTH on S190510g: DECam Observation Planning and Follow-Up of a Distant Binary Neutron Star Merger Candidate*, Astrophys. J. Lett. **881**, L16 (2019).
[481] A. Garcia *et al.* (DES Collaboration), *A DESGW Search for the Electromagnetic Counterpart to the LIGO/Virgo Gravitational Wave Binary Neutron Star Merger Candidate S190510g*, Astrophys. J. **903**, 75 (2020).
[482] LIGO Scientific Collaboration and Virgo Collaboration, GCN 24503, 2019, https://gcn.gsfc.nasa.gov/other/S190512at.gcn3.
[483] H. Abdalla *et al.* (H.E.S.S. Collaboration), *H.E.S.S. Follow-Up Observations of Binary Black Hole Coalescence Events during the Second and Third Gravitational-Wave Observing Runs of Advanced LIGO and Advanced Virgo*, Astrophys. J. **923**, 109 (2021).
[484] H. Ashkar, F. Brun, M. Füßling, C. Hoischen, S. Ohm, H. Prokoph, P. Reichherzer, F. Schüssler, and M. Seglar-Arroyo, *The H.E.S.S. Gravitational Wave Rapid Follow-Up Program*, J. Cosmol. Astropart. Phys. 03 (2021) 045.
[485] T. Ohgami *et al.*, *Optical Follow-Up Observation for GW Event S190510g Using Subaru/Hyper Suprime-Cam*, Publ. Astron. Soc. Jpn. **73**, 350 (2021).
[486] LIGO Scientific Collaboration and Virgo Collaboration, GCN 24522, 2019, https://gcn.gsfc.nasa.gov/other/S190513bm.gcn3.
[487] LIGO Scientific Collaboration and Virgo Collaboration, GCN 24570, 2019, https://gcn.gsfc.nasa.gov/other/S190517h.gcn3.
[488] LIGO Scientific Collaboration and Virgo Collaboration, GCN 24591, 2019, https://gcn.gsfc.nasa.gov/other/S190518bb.gcn3.
[489] LIGO Scientific Collaboration and Virgo Collaboration, GCN 24598, 2019, https://gcn.gsfc.nasa.gov/other/S190519bj.gcn3.
[490] LIGO Scientific Collaboration and Virgo Collaboration, GCN 24621, 2019, https://gcn.gsfc.nasa.gov/other/S190521g.gcn3.
[491] M. J. Graham *et al.*, *Candidate Electromagnetic Counterpart to the Binary Black Hole Merger Gravitational Wave Event S190521g*, Phys. Rev. Lett. **124**, 251102 (2020).
[492] E. Podlesnyi and T. Dzhatdoev, *Search for High Energy γ-Rays from the Direction of the Candidate Electromagnetic Counterpart to the Binary Black Hole Merger Gravitational-Wave Event S190521g*, Results Phys. **19**, 103579 (2020).
[493] LIGO Scientific Collaboration and Virgo Collaboration, GCN 24632, 2019, https://gcn.gsfc.nasa.gov/other/S190521r.gcn3.
[494] LIGO Scientific Collaboration and Virgo Collaboration, GCN 24656, 2019, https://gcn.gsfc.nasa.gov/other/S190524q.gcn3.
[495] LIGO Scientific Collaboration and Virgo Collaboration, GCN 24717, 2019, https://gcn.gsfc.nasa.gov/other/S190602aq.gcn3.
[496] LIGO Scientific Collaboration and Virgo Collaboration, GCN 24922, 2019, https://gcn.gsfc.nasa.gov/other/S190630ag.gcn3.
[497] LIGO Scientific Collaboration and Virgo Collaboration, GCN 24950, 2019, https://gcn.gsfc.nasa.gov/other/S190701ah.gcn3.
[498] LIGO Scientific Collaboration and Virgo Collaboration, GCN 24998, 2019, https://gcn.gsfc.nasa.gov/other/S190706ai.gcn3.
[499] LIGO Scientific Collaboration and Virgo Collaboration, GCN 25012, 2019, https://gcn.gsfc.nasa.gov/other/S190707q.gcn3.
[500] LIGO Scientific Collaboration and Virgo Collaboration, GCN 25087, 2019, https://gcn.gsfc.nasa.gov/other/S190718y.gcn3.
[501] LIGO Scientific Collaboration and Virgo Collaboration, GCN 25115, 2019, https://gcn.gsfc.nasa.gov/other/S190720a.gcn3.
[502] LIGO Scientific Collaboration and Virgo Collaboration, GCN 25164, 2019, https://gcn.gsfc.nasa.gov/other/S190727h.gcn3.
[503] LIGO Scientific Collaboration and Virgo Collaboration, GCN 25187, 2019, https://gcn.gsfc.nasa.gov/other/S190728q.gcn3.
[504] A. Keivani *et al.*, *Swift Follow-up Observations of Gravitational-Wave and High-energy Neutrino Coincident Signals*, Astrophys. J. **909**, 126 (2021).
[505] LIGO Scientific Collaboration and Virgo Collaboration, GCN 25296, 2019, https://gcn.gsfc.nasa.gov/other/S190808ae.gcn3.
[506] LIGO Scientific Collaboration and Virgo Collaboration, GCN 25324, 2019, https://gcn.gsfc.nasa.gov/other/S190814bv.gcn3.
[507] K. Ackley *et al.*, *Observational Constraints on the Optical and Near-Infrared Emission from the Neutron Star-Black Hole Binary Merger Candidate S190814bv*, Astron. Astrophys. **643**, A113 (2020).
[508] K. D. Alexander *et al.*, *A Late-Time Galaxy-Targeted Search for the Radio Counterpart of GW190814*, Astrophys. J. **923**, 66 (2021).
[509] I. Andreoni *et al.*, *GROWTH on S190814bv: Deep Synoptic Limits on the Optical/Near-Infrared Counterpart to a Neutron Star-Black Hole Merger*, Astrophys. J. **890**, 131 (2020).
[510] M. W. Coughlin *et al.*, *GROWTH on S190425z: Searching Thousands of Square Degrees to Identify an Optical or Infrared Counterpart to a Binary Neutron Star Merger with the Zwicky Transient Facility and Palomar Gattini IR*, Astrophys. J. Lett. **885**, L19 (2019).

[511] S. de Wet *et al.*, *GW190814 Follow-Up with the Optical Telescope MeerLICHT*, Astron. Astrophys. **649**, A72 (2021).
[512] D. Dobie *et al.*, *An ASKAP Search for a Radio Counterpart to the First High-Significance Neutron Star–Black Hole Merger LIGO/Virgo S190814bv*, Astrophys. J. Lett. **887**, L13 (2019).
[513] S. Gomez *et al.*, *A Galaxy-Targeted Search for the Optical Counterpart of the Candidate NS–BH Merger S190814bv with Magellan*, Astrophys. J. Lett. **884**, L55 (2019).
[514] C. D. Kilpatrick *et al.*, *The Gravity Collective: A Search for the Electromagnetic Counterpart to the Neutron Star–Black Hole Merger GW190814*, Astrophys. J. **923**, 258 (2021).
[515] A. L. Thakur *et al.*, *A Search for Optical and Near-Infrared Counterparts of the Compact Binary Merger GW190814*, Mon. Not. R. Astron. Soc. **499**, 3868 (2020); **501**, 2821(E) (2021).
[516] D. Tucker *et al.* (DES Collaboration), *SOAR/Goodman Spectroscopic Assessment of Candidate Counterparts of the LIGO/Virgo Event GW190814**, Astrophys. J. **929**, 115 (2022).
[517] N. Vieira *et al.*, *A Deep CFHT Optical Search for a Counterpart to the Possible Neutron Star-Black Hole Merger GW190814*, Astrophys. J. **895**, 96 (2020).
[518] A. M. Watson *et al.*, *Limits on the Electromagnetic Counterpart to S190814bv*, Mon. Not. R. Astron. Soc. **492**, 5916 (2020).
[519] LIGO Scientific Collaboration and Virgo Collaboration, GCN 25367, 2019, https://gcn.gsfc.nasa.gov/gcn/gcn3/25367.gcn3.
[520] LIGO Scientific Collaboration and Virgo Collaboration, GCN 25442, 2019, https://gcn.gsfc.nasa.gov/other/S190822c.gcn3.
[521] LIGO Scientific Collaboration and Virgo Collaboration, GCN 25497, 2019, https://gcn.gsfc.nasa.gov/other/S190828j.gcn3.
[522] LIGO Scientific Collaboration and Virgo Collaboration, GCN 25503, 2019, https://gcn.gsfc.nasa.gov/other/S190828l.gcn3.
[523] LIGO Scientific Collaboration and Virgo Collaboration, GCN 25554, 2019, https://gcn.gsfc.nasa.gov/other/S190829u.gcn3.
[524] LIGO Scientific Collaboration and Virgo Collaboration, GCN 25606, 2019, https://gcn.gsfc.nasa.gov/other/S190901ap.gcn3.
[525] LIGO Scientific Collaboration and Virgo Collaboration, GCN 25695, 2019, https://gcn.gsfc.nasa.gov/other/S190910d.gcn3.
[526] LIGO Scientific Collaboration and Virgo Collaboration, GCN 25707, 2019, https://gcn.gsfc.nasa.gov/other/S190910h.gcn3.
[527] LIGO Scientific Collaboration and Virgo Collaboration, GCN 25753, 2019, https://gcn.gsfc.nasa.gov/other/S190915ak.gcn3.
[528] LIGO Scientific Collaboration and Virgo Collaboration, GCN 25814, 2019, https://gcn.gsfc.nasa.gov/other/S190923y.gcn3.
[529] LIGO Scientific Collaboration and Virgo Collaboration, GCN 25829, 2019, https://gcn.gsfc.nasa.gov/other/S190924h.gcn3.
[530] LIGO Scientific Collaboration and Virgo Collaboration, GCN 25883, 2019, https://gcn.gsfc.nasa.gov/other/S190928c.gcn3.
[531] LIGO Scientific Collaboration and Virgo Collaboration, GCN 25871, 2019, https://gcn.gsfc.nasa.gov/other/S190930s.gcn3.
[532] LIGO Scientific Collaboration and Virgo Collaboration, GCN 25876, 2019, https://gcn.gsfc.nasa.gov/other/S190930t.gcn3.
[533] LIGO Scientific Collaboration and Virgo Collaboration, GCN 26182, 2019, https://gcn.gsfc.nasa.gov/other/S191105e.gcn3.
[534] LIGO Scientific Collaboration and Virgo Collaboration, GCN 26202, 2019, https://gcn.gsfc.nasa.gov/other/S191109d.gcn3.
[535] LIGO Scientific Collaboration and Virgo Collaboration, GCN 26222, 2019, https://gcn.gsfc.nasa.gov/other/S191110af.gcn3.
[536] LIGO Scientific Collaboration and Virgo Collaboration, GCN 26218, 2019, https://gcn.gsfc.nasa.gov/other/S191110x.gcn3.
[537] LIGO Scientific Collaboration and Virgo Collaboration, GCN 26254, 2019, https://gcn.gsfc.nasa.gov/other/S191117j.gcn3.
[538] LIGO Scientific Collaboration and Virgo Collaboration, GCN 26263, 2019, https://gcn.gsfc.nasa.gov/other/S191120aj.gcn3.
[539] LIGO Scientific Collaboration and Virgo Collaboration, GCN 26265, 2019, https://gcn.gsfc.nasa.gov/other/S191120at.gcn3.
[540] LIGO Scientific Collaboration and Virgo Collaboration, GCN 26288, 2019, https://gcn.gsfc.nasa.gov/other/S191124be.gcn3.
[541] LIGO Scientific Collaboration and Virgo Collaboration, GCN 26303, 2019, https://gcn.gsfc.nasa.gov/other/S191129u.gcn3.
[542] LIGO Scientific Collaboration and Virgo Collaboration, GCN 26334, 2019, https://gcn.gsfc.nasa.gov/other/S191204r.gcn3.
[543] LIGO Scientific Collaboration and Virgo Collaboration, GCN 26350, 2019, https://gcn.gsfc.nasa.gov/other/S191205ah.gcn3.
[544] LIGO Scientific Collaboration and Virgo Collaboration, GCN 26395, 2019, https://gcn.gsfc.nasa.gov/other/S191212q.gcn3.
[545] LIGO Scientific Collaboration and Virgo Collaboration, GCN 26402, 2019, https://gcn.gsfc.nasa.gov/other/S191213g.gcn3.
[546] LIGO Scientific Collaboration and Virgo Collaboration, GCN 26413, 2019, https://gcn.gsfc.nasa.gov/other/S191213ai.gcn3.
[547] LIGO Scientific Collaboration and Virgo Collaboration, GCN 26441, 2019, https://gcn.gsfc.nasa.gov/other/S191215w.gcn3.
[548] LIGO Scientific Collaboration and Virgo Collaboration, GCN 26454, 2019, https://gcn.gsfc.nasa.gov/other/S191216ap.gcn3.

[549] D. Bhakta, K. P. Mooley, A. Corsi, A. Balasubramanian, D. Dobie, D. A. Frail, G. Hallinan, D. L. Kaplan, S. T. Myers, and L. P. Singer, *The JAGWAR Prowls LIGO/Virgo O3 Paper I: Radio Search of a Possible Multimessenger Counterpart of the Binary Black Hole Merger Candidate S191216ap*, Astrophys. J. **911**, 77 (2021).
[550] LIGO Scientific Collaboration and Virgo Collaboration, GCN 26513, 2019, https://gcn.gsfc.nasa.gov/other/S191220af.gcn3.
[551] LIGO Scientific Collaboration and Virgo Collaboration, GCN 26543, 2019, https://gcn.gsfc.nasa.gov/other/S191222n.gcn3.
[552] LIGO Scientific Collaboration and Virgo Collaboration, GCN 26585, 2019, https://gcn.gsfc.nasa.gov/other/S191225aq.gcn3.
[553] LIGO Scientific Collaboration and Virgo Collaboration, GCN 26640, 2020, https://gcn.gsfc.nasa.gov/other/S200105ae.gcn3.
[554] S. Anand *et al.*, *Optical Follow-Up of the Neutron Star-Black Hole Mergers S200105ae and S200115j*, Nat. Astron. **5**, 46 (2021).
[555] LIGO Scientific Collaboration and Virgo Collaboration, GCN 26641, 2020, https://gcn.gsfc.nasa.gov/other/S200106au.gcn3.
[556] LIGO Scientific Collaboration and Virgo Collaboration, GCN 26665, 2020, https://gcn.gsfc.nasa.gov/other/S200108v.gcn3.
[557] LIGO Scientific Collaboration and Virgo Collaboration, GCN 26715, 2020, https://gcn.gsfc.nasa.gov/other/S200112r.gcn3.
[558] LIGO Scientific Collaboration and Virgo Collaboration, GCN 26734, 2020, https://gcn.gsfc.nasa.gov/other/S200114f.gcn3.
[559] LIGO Scientific Collaboration and Virgo Collaboration, GCN 26759, 2020, https://gcn.gsfc.nasa.gov/other/S200115j.gcn3.
[560] S. Dichiara *et al.*, *Constraints on the Electromagnetic Counterpart of the Neutron-Star–Black-Hole Merger GW200115*, Astrophys. J. Lett. **923**, L32 (2021).
[561] LIGO Scientific Collaboration and Virgo Collaboration, GCN 26785, 2020, https://gcn.gsfc.nasa.gov/other/S200116ah.gcn3.
[562] LIGO Scientific Collaboration and Virgo Collaboration, GCN 26906, 2020, https://gcn.gsfc.nasa.gov/other/S200128d.gcn3.
[563] LIGO Scientific Collaboration and Virgo Collaboration, GCN 26926, 2020, https://gcn.gsfc.nasa.gov/other/S200129m.gcn3.
[564] LIGO Scientific Collaboration and Virgo Collaboration, GCN 27014, 2020, https://gcn.gsfc.nasa.gov/other/S200208q.gcn3.
[565] LIGO Scientific Collaboration and Virgo Collaboration, GCN 27042, 2020, https://gcn.gsfc.nasa.gov/other/S200213t.gcn3.
[566] LIGO Scientific Collaboration and Virgo Collaboration, GCN 27130, 2020, https://gcn.gsfc.nasa.gov/other/S200219ac.gcn3.
[567] V. Lipunov *et al.*, *Optical Transients Found by MASTER during the Observation of LIGO/VIRGO S200219ac Gravitational-Wave Event*, Res. Notes AAS **4**, 194 (2020).
[568] LIGO Scientific Collaboration and Virgo Collaboration, GCN 27184, 2020, https://gcn.gsfc.nasa.gov/other/S200224ca.gcn3.
[569] N. J. Klingler *et al.*, *Swift Multiwavelength Follow-Up of LVC S200224ca and the Implications for Binary Black Hole Mergers*, Astrophys. J. **907**, 97 (2021).
[570] V. Lipunov *et al.*, *MASTER Optical Observation of LIGO/VIRGO S200224ca Error-Box*, Res. Notes AAS **4**, 225 (2020).
[571] T. Ohgami *et al.* (J-GEM Collaboration), *Follow-Up Survey for the Binary Black Hole Merger GW200224_222234 Using Subaru/HSC and GTC/OSIRIS*, Astrophys. J. **947**, 9 (2023).
[572] LIGO Scientific Collaboration and Virgo Collaboration, GCN 27193, 2020, https://gcn.gsfc.nasa.gov/other/S200225q.gcn3.
[573] LIGO Scientific Collaboration and Virgo Collaboration, GCN 27278, 2020, https://gcn.gsfc.nasa.gov/other/S200302c.gcn3.
[574] V. Lipunov *et al.*, *MASTER Optical Observation of LIGO/VIRGO S200302c Event*, Res. Notes AAS **4**, 230 (2020).
[575] LIGO Scientific Collaboration and Virgo Collaboration, GCN 27306, 2020, https://gcn.gsfc.nasa.gov/other/S200303ba.gcn3.
[576] LIGO Scientific Collaboration and Virgo Collaboration, GCN 27347, 2020, https://gcn.gsfc.nasa.gov/other/S200308e.gcn3.
[577] LIGO Scientific Collaboration and Virgo Collaboration, GCN 27358, 2020, https://gcn.gsfc.nasa.gov/other/S200311bg.gcn3.
[578] LIGO Scientific Collaboration and Virgo Collaboration, GCN 27388, 2020, https://gcn.gsfc.nasa.gov/other/S200316bj.gcn3.
[579] M. Amiri *et al.* (CHIME/FRB Collaboration), *The First CHIME/FRB Fast Radio Burst Catalog*, Astrophys. J. Suppl. Ser. **257**, 59 (2021).
[580] A. Moroianu, L. Wen, C. W. James, S. Ai, M. Kovalam, F. H. Panther, and B. Zhang, *An Assessment of the Association between a Fast Radio Burst and Binary Neutron Star Merger*, Nat. Astron. **7**, 579 (2023).
[581] R. Perna, D. Lazzati, and B. Giacomazzo, *Short Gamma-Ray Bursts from the Merger of Two Black Holes*, Astrophys. J. Lett. **821**, L18 (2016).
[582] N. C. Stone, B. D. Metzger, and Z. Haiman, *Assisted Inspirals of Stellar Mass Black Holes Embedded in AGN Discs: Solving the 'Final au Problem'* Mon. Not. R. Astron. Soc. **464**, 946 (2017).
[583] K. Murase, K. Kashiyama, P. Mészáros, I. Shoemaker, and N. Senno, *Ultrafast Outflows from Black Hole Mergers with a Minidisk*, Astrophys. J. Lett. **822**, L9 (2016).
[584] S. E. de Mink and A. King, *Electromagnetic Signals Following Stellar-Mass Black Hole Mergers*, Astrophys. J. Lett. **839**, L7 (2017).
[585] B. McKernan, K. E. S. Ford, I. Bartos, M. J. Graham, W. Lyra, S. Marka, Z. Marka, N. P. Ross, D. Stern, and Y. Yang, *Ram-Pressure Stripping of a Kicked Hill Sphere: Prompt Electromagnetic Emission from the Merger of Stellar Mass Black Holes in an AGN Accretion Disk*, Astrophys. J. Lett. **884**, L50 (2019).

[586] T. Bogdanovic, M. C. Miller, and L. Blecha, *Electromagnetic Counterparts to Massive Black-Hole Mergers*, Living Rev. Relativity **25**, 3 (2022).
[587] V. B. Petkov, I. M. Dzaparova, M. M. Kochkarov, M. G. Kostyuk, A. N. Kurenya, Y. F. Novoseltsev, R. V. Novoseltseva, P. S. Striganov, I. B. Unatlokov, and A. F. Yanin, *Searching for Muon Neutrinos from Regions of the Localization of Gravitational-Wave Events*, Bull. Russ. Acad. Sci. Phys. **85**, 444 (2021).
[588] R. Abbott *et al.* (LIGO Scientific Collaboration and Virgo Collaboration), *Search for Gravitational Waves Associated with Gamma-Ray Bursts Detected by Fermi and Swift During the LIGO-Virgo Run O3a*, Astrophys. J. **915**, 86 (2021).
[589] M. W. Coughlin, T. Dietrich, S. Antier, M. Bulla, F. Foucart, K. Hotokezaka, G. Raaijmakers, T. Hinderer, and S. Nissanke, *Implications of the Search for Optical Counterparts during the First Six Months of the Advanced LIGO's and Advanced Virgo's Third Observing Run: Possible Limits on the Ejecta Mass and Binary Properties*, Mon. Not. R. Astron. Soc. **492**, 863 (2020).
[590] A. Sagués Carracedo, M. Bulla, U. Feindt, and A. Goobar, *Detectability of Kilonovae in Optical Surveys: Post-Mortem Examination of the LVC O3 Run Follow-Up*, Mon. Not. R. Astron. Soc. **504**, 1294 (2021).
[591] M. W. Coughlin, T. Dietrich, B. Margalit, and B. D. Metzger, *Multimessenger Bayesian Parameter Inference of a Binary Neutron Star Merger*, Mon. Not. R. Astron. Soc. **489**, L91 (2019).
[592] T. Dietrich, M. W. Coughlin, P. T. H. Pang, M. Bulla, J. Heinzel, L. Issa, I. Tews, and S. Antier, *Multimessenger Constraints on the Neutron-Star Equation of State and the Hubble Constant*, Science **370**, 1450 (2020).
[593] M. W. Coughlin, *Lessons from Counterpart Searches in LIGO and Virgo's Third Observing Campaign*, Nat. Astron. **4**, 550 (2020).
[594] M. Nicholl, B. Margalit, P. Schmidt, G. P. Smith, E. J. Ridley, and J. Nuttall, *Tight Multimessenger Constraints on the Neutron Star Equation of State from GW170817 and a Forward Model for Kilonova Light-Curve Synthesis*, Mon. Not. R. Astron. Soc. **505**, 3016 (2021).
[595] G. Raaijmakers *et al.*, *The Challenges Ahead for Multimessenger Analyses of Gravitational Waves and Kilonova: A Case Study on GW190425*, Astrophys. J. **922**, 269 (2021).
[596] G. Ashton, K. Ackley, I. Magaña Hernandez, and B. Piotrzkowski, *Current Observations Are Insufficient to Confidently Associate the Binary Black Hole Merger GW190521 with AGN J124942.3+344929*, Classical Quantum Gravity **38**, 235004 (2021).
[597] A. Palmese, M. Fishbach, C. J. Burke, J. T. Annis, and X. Liu, *Do LIGO/Virgo Black Hole Mergers Produce AGN Flares? The Case of GW190521 and Prospects for Reaching a Confident Association*, Astrophys. J. Lett. **914**, L34 (2021).
[598] F. De Paolis, A. A. Nucita, F. Strafella, D. Licchelli, and G. Ingrosso, *A Quasar Microlensing Event towards J1249+3449?*, Mon. Not. R. Astron. Soc. **499**, L87 (2020).
[599] A. F. Brooks *et al.* (LIGO Instrument Science Collaboration), *Point Absorbers in Advanced LIGO*, Appl. Opt. **60**, 4047 (2021).
[600] B. J. Meers, *Recycling in Laser Interferometric Gravitational Wave Detectors*, Phys. Rev. D **38**, 2317 (1988).
[601] M. Tse *et al.*, *Quantum-Enhanced Advanced LIGO Detectors in the Era of Gravitational-Wave Astronomy*, Phys. Rev. Lett. **123**, 231107 (2019).
[602] F. Acernese *et al.* (Virgo Collaboration), *Increasing the Astrophysical Reach of the Advanced Virgo Detector via the Application of Squeezed Vacuum States of Light*, Phys. Rev. Lett. **123**, 231108 (2019).
[603] A. F. Brooks *et al.*, *Direct Measurement of Absorption-Induced Wavefront Distortion in High Optical Power Systems*, Appl. Opt. **48**, 355 (2009).
[604] A. F. Brooks *et al.*, *Overview of Advanced LIGO Adaptive Optics*, Appl. Opt. **55**, 8256 (2016).
[605] A. Brooks, *aLIGO LLO Logbook*, Report No. 49535, 2019, https://alog.ligo-la.caltech.edu/aLOG/index.php?callRep=49535.
[606] A. Brooks, *aLIGO LLO Logbook*, Report No. 49564, 2019, https://alog.ligo-la.caltech.edu/aLOG/index.php?callRep=49564.
[607] P. Nguyen *et al.* (LIGO Instrument Science Collaboration), *Environmental Noise in Advanced LIGO Detectors*, Classical Quantum Gravity **38**, 145001 (2021).
[608] L. McCuller *et al.*, *LIGO's Quantum Response to Squeezed States*, Phys. Rev. D **104**, 062006 (2021).
[609] F. Acernese *et al.* (Virgo Collaboration), *Quantum Backaction on kg-Scale Mirrors: Observation of Radiation Pressure Noise in the Advanced Virgo Detector*, Phys. Rev. Lett. **125**, 131101 (2020).
[610] J. Brooks, M. Mantovani, A. Allocca, J. Casanueva Diaz, V. Dattilo, A. Masserot, and P. Ruggi, *Temperature Control for an Intra-Mirror Etalon in Interferometric Gravitational Wave Detector Fabry–Perot Cavities*, Galaxies **8**, 80 (2020).
[611] P. Godwin *et al.*, *Incorporation of Statistical Data Quality Information into the GstLAL Search Analysis*, arXiv:2010.15282.
[612] B. P. Abbott *et al.* (LIGO Scientific Collaboration and Virgo Collaboration), *Effects of Data Quality Vetoes on a Search for Compact Binary Coalescences in Advanced LIGO's First Observing Run*, Classical Quantum Gravity **35**, 065010 (2018).
[613] T. Dal Canton, A. H. Nitz, B. Gadre, G. S. Cabourn Davies, V. Villa-Ortega, T. Dent, I. Harry, and L. Xiao, *Real-Time Search for Compact Binary Mergers in Advanced LIGO and Virgo's Third Observing Run Using PyCBC Live*, Astrophys. J. **923**, 254 (2021).
[614] D. Davis *et al.*, *Data Quality Vetoes Applied to the Analysis of LIGO Data from the Third Observing Run*, LIGO Report No. DCC-T2100045, 2021, https://dcc.ligo.org/LIGO-T2100045/public.
[615] N. Arnaud *et al.*, *Category 1 (CAT1) Data Quality Vetoes Applied to the Analysis of the O3 Run Virgo Data*, Virgo Report No. VIR-0560A-21, 2021, https://tds.virgo-gw.eu/?content=3&r=18844.

[616] F. Acernese *et al.* (Virgo Collaboration), *Virgo Detector Characterization and Data Quality during the O3 Run*, arXiv:2205.01555.

[617] S. Mozzon, L. K. Nuttall, A. Lundgren, T. Dent, S. Kumar, and A. H. Nitz, *Dynamic Normalization for Compact Binary Coalescence Searches in Non-Stationary Noise*, Classical Quantum Gravity **37**, 215014 (2020).

[618] P. J. Green, *Reversible Jump Markov Chain Monte Carlo Computation and Bayesian Model Determination*, Biometrika **82**, 711 (1995).

[619] B. Allen, W. Hua, and A. C. Ottewill, *Automatic Cross Talk Removal from Multichannel Data*, arXiv:gr-qc/9909083.

[620] A. Lundgren, *aLIGO LLO Logbook*, Report No. 47707, 2019, https://alog.ligo-la.caltech.edu/aLOG/index.php?callRep=47707.

[621] S. Hourihane, K. Chatziioannou, M. Wijngaarden, D. Davis, T. Littenberg, and N. Cornish, *Accurate Modeling and Mitigation of Overlapping Signals and Glitches in Gravitational-Wave Data*, Phys. Rev. D **106**, 042006 (2022).

[622] E. Payne, S. Hourihane, J. Golomb, R. Udall, D. Davis, and K. Chatziioannou, *Curious Case of GW200129: Interplay between Spin-Precession Inference and Data-Quality Issues*, Phys. Rev. D **106**, 104017 (2022).

[623] K. Cannon *et al.*, *Toward Early-Warning Detection of Gravitational Waves from Compact Binary Coalescence*, Astrophys. J. **748**, 136 (2012).

[624] S. Privitera, S. R. P. Mohapatra, P. Ajith, K. Cannon, N. Fotopoulos, M. A. Frei, C. Hanna, A. J. Weinstein, and J. T. Whelan, *Improving the Sensitivity of a Search for Coalescing Binary Black Holes with Nonprecessing Spins in Gravitational Wave Data*, Phys. Rev. D **89**, 024003 (2014).

[625] A. Bohé *et al.*, *Improved Effective-One-Body Model of Spinning, Nonprecessing Binary Black Holes for the Era of Gravitational-Wave Astrophysics with Advanced Detectors*, Phys. Rev. D **95**, 044028 (2017).

[626] M. Pürrer, *Frequency Domain Reduced Order Model of Aligned-Spin Effective-One-Body Waveforms with Generic Mass-Ratios and Spins*, Phys. Rev. D **93**, 064041 (2016).

[627] E. Poisson, *Gravitational Waves from Inspiraling Compact Binaries: The Quadrupole Moment Term*, Phys. Rev. D **57**, 5287 (1998).

[628] T. Damour, P. Jaranowski, and G. Schaefer, *Dimensional Regularization of the Gravitational Interaction of Point Masses*, Phys. Lett. B **513**, 147 (2001).

[629] B. Mikóczi, M. Vasúth, and L. Á. Gergely, *Self-Interaction Spin Effects in Inspiralling Compact Binaries*, Phys. Rev. D **71**, 124043 (2005).

[630] L. Blanchet, T. Damour, G. Esposito-Farèse, and B. R. Iyer, *Dimensional Regularization of the Third Post-Newtonian Gravitational Wave Generation from Two Point Masses*, Phys. Rev. D **71**, 124004 (2005).

[631] K. G. Arun, A. Buonanno, G. Faye, and E. Ochsner, *Higher-Order Spin Effects in the Amplitude and Phase of Gravitational Waveforms Emitted by Inspiraling Compact Binaries: Ready-to-Use Gravitational Waveforms*, Phys. Rev. D **79**, 104023 (2009); **84**, 049901(E) (2011).

[632] A. Buonanno, B. Iyer, E. Ochsner, Y. Pan, and B. S. Sathyaprakash, *Comparison of Post-Newtonian Templates for Compact Binary Inspiral Signals in Gravitational-Wave Detectors*, Phys. Rev. D **80**, 084043 (2009).

[633] A. Bohé, S. Marsat, and L. Blanchet, *Next-to-Next-to-Leading Order Spin–Orbit Effects in the Gravitational Wave Flux and Orbital Phasing of Compact Binaries*, Classical Quantum Gravity **30**, 135009 (2013).

[634] A. Bohé, G. Faye, S. Marsat, and E. K. Porter, *Quadratic-in-Spin Effects in the Orbital Dynamics and Gravitational-Wave Energy Flux of Compact Binaries at the 3PN Order*, Classical Quantum Gravity **32**, 195010 (2015).

[635] C. K. Mishra, A. Kela, K. G. Arun, and G. Faye, *Ready-to-Use Post-Newtonian Gravitational Waveforms for Binary Black Holes with Nonprecessing Spins: An Update*, Phys. Rev. D **93**, 084054 (2016).

[636] A. Buonanno, Y. Chen, and M. Vallisneri, *Detecting Gravitational Waves from Precessing Binaries of Spinning Compact Objects: Adiabatic Limit*, Phys. Rev. D **67**, 104025 (2003); **74**, 029904(E) (2006).

[637] É. Racine, A. Buonanno, and L. E. Kidder, *Recoil Velocity at 2PN Order for Spinning Black Hole Binaries*, Phys. Rev. D **80**, 044010 (2009).

[638] J. Vines, É. É. Flanagan, and T. Hinderer, *Post-1-Newtonian Tidal Effects in the Gravitational Waveform from Binary Inspirals*, Phys. Rev. D **83**, 084051 (2011).

[639] S. Marsat, A. Bohé, L. Blanchet, and A. Buonanno, *Next-to-Leading Tail-Induced Spin–Orbit Effects in the Gravitational Radiation Flux of Compact Binaries*, Classical Quantum Gravity **31**, 025023 (2014).

[640] S. Marsat, *Cubic Order Spin Effects in the Dynamics and Gravitational Wave Energy Flux of Compact Object Binaries*, Classical Quantum Gravity **32**, 085008 (2015).

[641] A. Nitz *et al.*, *gwastro/pycbc: PyCBC Release v1.16.13*, 10.5281/zenodo.4309869 (2020).

[642] T. Dent and J. Veitch, *Optimizing Gravitational-Wave Searches for a Population of Coalescing Binaries: Intrinsic Parameters*, Phys. Rev. D **89**, 062002 (2014).

[643] S. Roy, A. S. Sengupta, and N. Thakor, *Hybrid Geometric-Random Template-Placement Algorithm for Gravitational Wave Searches from Compact Binary Coalescences*, Phys. Rev. D **95**, 104045 (2017).

[644] S. Roy, A. S. Sengupta, and P. Ajith, *Effectual Template Banks for Upcoming Compact Binary Searches in Advanced-LIGO and Virgo Data*, Phys. Rev. D **99**, 024048 (2019).

[645] T. Dal Canton and I. W. Harry, *Designing a Template Bank to Observe Compact Binary Coalescences in Advanced LIGO's Second Observing Run*, arXiv:1705.01845.

[646] K. Chandra, V. Villa-Ortega, T. Dent, C. McIsaac, A. Pai, I. W. Harry, G. S. Cabourn Davies, and K. Soni, *An Optimized PyCBC Search for Gravitational Waves from Intermediate-Mass Black Hole Mergers*, Phys. Rev. D **104**, 042004 (2021).

[647] R. Pordes *et al.* (OSG Consortium), *The Open Science Grid*, J. Phys. Conf. Ser. **78**, 012057 (2007).

[648] I. Sfiligoi, D. C. Bradley, B. Holzman, P. Mhashilkar, S. Padhi, and F. Wurthwrin, *The Pilot Way to Grid Resources Using glideinWMS*, WRI World Congr. **2**, 428 (2009).

[649] C. Capano, T. Dent, Y.-M. Hu, M. Hendry, C. Messenger, and J. Veitch, *Systematic Errors in Estimation of Gravitational-Wave Candidate Significance*, arXiv:1601.00130.
[650] A. H. Nitz, T. Dal Canton, D. Davis, and S. Reyes, *Rapid Detection of Gravitational Waves from Compact Binary Mergers with PyCBC Live*, Phys. Rev. D **98**, 024050 (2018).
[651] A. H. Nitz, *Distinguishing Short Duration Noise Transients in LIGO Data to Improve the PyCBC Search for Gravitational Waves from High Mass Binary Black Hole Mergers*, Classical Quantum Gravity **35**, 035016 (2018).
[652] S. Hooper, S. K. Chung, J. Luan, D. Blair, Y. Chen, and L. Wen, *Summed Parallel Infinite Impulse Response Filters for Low-Latency Gravitational Wave Detection*, Phys. Rev. D **86**, 024012 (2012).
[653] Y. Liu, Z. Du, S. K. Chung, S. Hooper, D. Blair, and L. Wen, *GPU-Accelerated Low-Latency Real-Time Searches for Gravitational Waves from Compact Binary Coalescence*, Classical Quantum Gravity **29**, 235018 (2012).
[654] X. Guo, Q. Chu, S. K. Chung, Z. Du, L. Wen, and Y. Gu, *GPU-Acceleration on a Low-Latency Binary-Coalescence Gravitational Wave Search Pipeline*, Comput. Phys. Commun. **231**, 62 (2018).
[655] X. Guo, Q. Chu, Z. Du, and L. Went, *GPU-Optimised Low-Latency Online Search for Gravitational Waves from Binary Coalescences*, in *Proceedings of the 2018 26th European Signal Processing Conference (EUSIPCO)* (IEEE, New York, 2018), pp. 2638–2642, 10.23919/eusipco.2018.8553574.
[656] J. Calderón Bustillo, F. Salemi, T. Dal Canton, and K. P. Jani, *Sensitivity of Gravitational Wave Searches to the Full Signal of Intermediate-Mass Black Hole Binaries during the First Observing Run of Advanced LIGO*, Phys. Rev. D **97**, 024016 (2018).
[657] B. P. Abbott *et al.* (LIGO Scientific Collaboration and Virgo Collaboration), *Observing Gravitational-Wave Transient GW150914 with Minimal Assumptions*, Phys. Rev. D **93**, 122004 (2016); **94**, 069903(E) (2016).
[658] J. Aasi *et al.* (Virgo Collaboration), *The Characterization of Virgo Data and Its Impact on Gravitational-Wave Searches*, Classical Quantum Gravity **29**, 155002 (2012).
[659] V. Tiwari, S. Klimenko, V. Necula, and G. Mitselmakher, *Reconstruction of Chirp Mass in Searches for Gravitational Wave Transients*, Classical Quantum Gravity **33**, 01LT01 (2016).
[660] M. Was, M.-A. Bizouard, V. Brisson, F. Cavalier, M. Davier, P. Hello, N. Leroy, F. Robinet, and M. Vavoulidis, *On the Background Estimation by Time Slides in a Network of Gravitational Wave Detectors*, Classical Quantum Gravity **27**, 015005 (2010).
[661] S. P. Wright, *Adjusted P-Values for Simultaneous Inference*, Biometrics **48**, 1005 (1992).
[662] P. A. R. Ade *et al.* (Planck Collaboration), *Planck 2015 Results. XIII. Cosmological Parameters*, Astron. Astrophys. **594**, A13 (2016).
[663] S. Babak, A. Taracchini, and A. Buonanno, *Validating the Effective-One-Body Model of Spinning, Precessing Binary Black Holes against Numerical Relativity*, Phys. Rev. D **95**, 024010 (2017).
[664] T. Dent, *Extending the PyCBC Pastro Calculation to a Global Network*, LIGO Report No. DCC-T2100060, 2021, https://dcc.ligo.org/LIGO-T2100060/public.
[665] V. Tiwari, *Estimation of the Sensitive Volume for Gravitational-Wave Source Populations Using Weighted Monte Carlo Integration*, Classical Quantum Gravity **35**, 145009 (2018).
[666] C. Talbot and E. Thrane, *Measuring the Binary Black Hole Mass Spectrum with an Astrophysically Motivated Parameterization*, Astrophys. J. **856**, 173 (2018).
[667] H. K. Y. Fong, *From Simulations to Signals: Analyzing Gravitational Waves from Compact Binary Coalescences*, Ph. D. thesis, Toronto University, 2018.
[668] T. Bayes, *An Essay toward Solving a Problem in the Doctrine of Chances*, Phil. Trans. R. Soc. London **53**, 370 (1763).
[669] C. P. L. Berry *et al.*, *Parameter Estimation for Binary Neutron-Star Coalescences with Realistic Noise during the Advanced LIGO Era*, Astrophys. J. **804**, 114 (2015).
[670] R. L. Forward, *Wide Band Laser Interferometer Gravitational Radiation Experiment*, Phys. Rev. D **17**, 379 (1978).
[671] K. S. Thorne, *Gravitational Radiation*, in *Three Hundred Years of Gravitation*, edited by S. W. Hawking and W. Israel (Cambridge University Press, Cambridge, England, 1987), Chap. 9, pp. 330–458.
[672] T. B. Littenberg and N. J. Cornish, *Bayesian Inference for Spectral Estimation of Gravitational Wave Detector Noise*, Phys. Rev. D **91**, 084034 (2015).
[673] K. Chatziioannou, C.-J. Haster, T. B. Littenberg, W. M. Farr, S. Ghonge, M. Millhouse, J. A. Clark, and N. Cornish, *Noise Spectral Estimation Methods and Their Impact on Gravitational Wave Measurement of Compact Binary Mergers*, Phys. Rev. D **100**, 104004 (2019).
[674] S. Biscoveanu, C.-J. Haster, S. Vitale, and J. Davies, *Quantifying the Effect of Power Spectral Density Uncertainty on Gravitational-Wave Parameter Estimation for Compact Binary Sources*, Phys. Rev. D **102**, 023008 (2020).
[675] E. Payne, C. Talbot, P. D. Lasky, E. Thrane, and J. S. Kissel, *Gravitational-Wave Astronomy with a Physical Calibration Model*, Phys. Rev. D **102**, 122004 (2020).
[676] S. Vitale, C.-J. Haster, L. Sun, B. Farr, E. Goetz, J. Kissel, and C. Cahillane, *Physical Approach to the Marginalization of LIGO Calibration Uncertainties*, Phys. Rev. D **103**, 063016 (2021).
[677] C. Pankow *et al.*, *Mitigation of the Instrumental Noise Transient in Gravitational-Wave Data Surrounding GW170817*, Phys. Rev. D **98**, 084016 (2018).
[678] V. Varma, S. E. Field, M. A. Scheel, J. Blackman, D. Gerosa, L. C. Stein, L. E. Kidder, and H. P. Pfeiffer, *Surrogate Models for Precessing Binary Black Hole Simulations with Unequal Masses*, Phys. Rev. Res. **1**, 033015 (2019).
[679] A. Buonanno and T. Damour, *Effective One-Body Approach to General Relativistic Two-Body Dynamics*, Phys. Rev. D **59**, 084006 (1999).
[680] A. Buonanno and T. Damour, *Transition from Inspiral to Plunge in Binary Black Hole Coalescences*, Phys. Rev. D **62**, 064015 (2000).

[681] C. García-Quirós, S. Husa, M. Mateu-Lucena, and A. Borchers, *Accelerating the Evaluation of Inspiral–Merger–Ringdown waveforms with Adapted Grids*, Classical Quantum Gravity **38**, 015006 (2021).

[682] P. Schmidt, M. Hannam, S. Husa, and P. Ajith, *Tracking the Precession of Compact Binaries from Their Gravitational-Wave Signal*, Phys. Rev. D **84**, 024046 (2011).

[683] P. Schmidt, M. Hannam, and S. Husa, *Towards Models of Gravitational Waveforms from Generic Binaries: A Simple Approximate Mapping between Precessing and Non-Precessing Inspiral Signals*, Phys. Rev. D **86**, 104063 (2012).

[684] B. Brügmann, J. A. González, M. Hannam, S. Husa, and U. Sperhake, *Exploring Black Hole Superkicks*, Phys. Rev. D **77**, 124047 (2008).

[685] S. Khan, S. Husa, M. Hannam, F. Ohme, M. Pürrer, X. Jiménez Forteza, and A. Bohé, *Frequency-Domain Gravitational Waves from Nonprecessing Black-Hole Binaries. II. A Phenomenological Model for the Advanced Detector Era*, Phys. Rev. D **93**, 044007 (2016).

[686] F. Hofmann, E. Barausse, and L. Rezzolla, *The Final Spin from Binary Black Holes in Quasi-Circular Orbits*, Astrophys. J. Lett. **825**, L19 (2016).

[687] N. K. Johnson-McDaniel, A. Gupta, P. Ajith, D. Keitel, O. Birnholtz, and F. Ohme, *Determining the Final Spin of a Binary Black Hole System Including In-Plane Spins: Method and Checks of Accuracy*, LIGO Report No. DCC-T1600168, 2016, https://dcc.ligo.org/LIGO-T1600168/public.

[688] F. Zappa, S. Bernuzzi, F. Pannarale, M. Mapelli, and N. Giacobbo, *Black-Hole Remnants from Black-Hole–Neutron-Star Mergers*, Phys. Rev. Lett. **123**, 041102 (2019).

[689] K. Martel and E. Poisson, *Gravitational Waves from Eccentric Compact Binaries: Reduction in Signal-to-Noise Ratio due to Nonoptimal Signal Processing*, Phys. Rev. D **60**, 124008 (1999).

[690] I. M. Romero-Shaw, P. D. Lasky, E. Thrane, and J. Calderón Bustillo, *GW190521: Orbital Eccentricity and Signatures of Dynamical Formation in a Binary Black Hole Merger Signal*, Astrophys. J. Lett. **903**, L5 (2020).

[691] A. Tucker and C. M. Will, *Residual Eccentricity of Inspiralling Orbits at the Gravitational-Wave Detection Threshold: Accurate Estimates Using Post-Newtonian Theory*, Phys. Rev. D **104**, 104023 (2021).

[692] W. Farr, *Marginalisation of the Time and Phase Parameters in CBC Parameter Estimation*, LIGO Report No. DCC-T1400460, 2014, https://dcc.ligo.org/LIGO-T1400460/public.

[693] J. Lange, R. O'Shaughnessy, and M. Rizzo, *Rapid and Accurate Parameter Inference for Coalescing, Precessing Compact Binaries*, arXiv:1805.10457.

[694] W. Farr, B. Farr, and T. Littenberg, *Modelling Calibration Errors in CBC Waveforms*, LIGO Report No. DCC-T1400682, 2014, https://dcc.ligo.org/LIGO-T1400682/public.

[695] M. Zevin *et al.*, *Gravity Spy: Integrating Advanced LIGO Detector Characterization, Machine Learning, and Citizen Science*, Classical Quantum Gravity **34**, 064003 (2017).

R. Abbott,[1] T. D. Abbott,[2] F. Acernese,[3,4] K. Ackley,[5] C. Adams,[6] N. Adhikari,[7] R. X. Adhikari,[1] V. B. Adya,[8] C. Affeldt,[9,10] D. Agarwal,[11] M. Agathos,[12,13] K. Agatsuma,[14] N. Aggarwal,[15] O. D. Aguiar,[16] L. Aiello,[17] A. Ain,[18] P. Ajith,[19] S. Akcay,[13,20] T. Akutsu,[21,22] S. Albanesi,[23] A. Allocca,[24,4] P. A. Altin,[8] A. Amato,[25] C. Anand,[5] S. Anand,[1] A. Ananyeva,[1] S. B. Anderson,[1] W. G. Anderson,[7] M. Ando,[26,27] T. Andrade,[28] N. Andres,[29] T. Andrić,[30] S. V. Angelova,[31] S. Ansoldi,[32,33] J. M. Antelis,[34] S. Antier,[35] S. Appert,[1] Koji Arai,[1] Koya Arai,[36] Y. Arai,[36] S. Araki,[37] A. Araya,[38] M. C. Araya,[1] J. S. Areeda,[39] M. Arène,[35] N. Aritomi,[26] N. Arnaud,[40,41] M. Arogeti,[42] S. M. Aronson,[2] K. G. Arun,[43] H. Asada,[44] Y. Asali,[45] G. Ashton,[5] Y. Aso,[46,47] M. Assiduo,[48,49] S. M. Aston,[6] P. Astone,[50] F. Aubin,[29] C. Austin,[2] S. Babak,[35] F. Badaracco,[51] M. K. M. Bader,[52] C. Badger,[53] S. Bae,[54] Y. Bae,[55] A. M. Baer,[56] S. Bagnasco,[23] Y. Bai,[1] L. Baiotti,[57] J. Baird,[35] R. Bajpai,[58] M. Ball,[59] G. Ballardin,[41] S. W. Ballmer,[60] A. Balsamo,[56] G. Baltus,[61] S. Banagiri,[62] D. Bankar,[11] J. C. Barayoga,[1] C. Barbieri,[63,64,65] B. C. Barish,[1] D. Barker,[66] P. Barneo,[28] F. Barone,[67,4] B. Barr,[68] L. Barsotti,[69] M. Barsuglia,[35] D. Barta,[70] J. Bartlett,[66] M. A. Barton,[68,21] I. Bartos,[71] R. Bassiri,[72] A. Basti,[73,18] M. Bawaj,[74,75] J. C. Bayley,[68] A. C. Baylor,[7] M. Bazzan,[76,77] B. Bécsy,[78] V. M. Bedakihale,[79] M. Bejger,[80] I. Belahcene,[40] V. Benedetto,[81] D. Beniwal,[82] T. F. Bennett,[83] J. D. Bentley,[14] M. BenYaala,[31] F. Bergamin,[9,10] B. K. Berger,[72] S. Bernuzzi,[13] C. P. L. Berry,[15,68] D. Bersanetti,[84] A. Bertolini,[52] J. Betzwieser,[6] D. Beveridge,[85] R. Bhandare,[86] U. Bhardwaj,[87,52] D. Bhattacharjee,[88] S. Bhaumik,[71] I. A. Bilenko,[89] G. Billingsley,[1] S. Bini,[90,91] R. Birney,[92] O. Birnholtz,[93] S. Biscans,[1,69] M. Bischi,[48,49] S. Biscoveanu,[69] A. Bisht,[9,10] B. Biswas,[11] M. Bitossi,[41,18] M.-A. Bizouard,[94] J. K. Blackburn,[1] C. D. Blair,[85,6] D. G. Blair,[85] R. M. Blair,[66] F. Bobba,[95,96] N. Bode,[9,10] M. Boer,[94] G. Bogaert,[94] M. Boldrini,[97,50] L. D. Bonavena,[76] F. Bondu,[98] E. Bonilla,[72] R. Bonnand,[29] P. Booker,[9,10] B. A. Boom,[52] R. Bork,[1] V. Boschi,[18] N. Bose,[99] S. Bose,[11] V. Bossilkov,[85] V. Boudart,[61] Y. Bouffanais,[76,77] A. Bozzi,[41] C. Bradaschia,[18] P. R. Brady,[7] A. Bramley,[6] A. Branch,[6] M. Branchesi,[30,100] J. Brandt,[42] J. E. Brau,[59] M. Breschi,[13] T. Briant,[101] J. H. Briggs,[68] A. Brillet,[94] M. Brinkmann,[9,10] P. Brockill,[7] A. F. Brooks,[1] J. Brooks,[41] D. D. Brown,[82] S. Brunett,[1] G. Bruno,[51] R. Bruntz,[56] J. Bryant,[14]

T. Bulik,[102] H. J. Bulten,[52] A. Buonanno,[103,104] R. Buscicchio,[14] D. Buskulic,[29] C. Buy,[105] R. L. Byer,[72] G. S. Cabourn Davies,[106] L. Cadonati,[42] G. Cagnoli,[25] C. Cahillane,[66] J. Calderón Bustillo,[107,108] J. D. Callaghan,[68] T. A. Callister,[109,110] E. Calloni,[24,4] J. Cameron,[85] J. B. Camp,[111] M. Canepa,[112,84] S. Canevarolo,[113] M. Cannavacciuolo,[95] K. C. Cannon,[27] H. Cao,[82] Z. Cao,[114] E. Capocasa,[21] E. Capote,[60] G. Carapella,[95,96] F. Carbognani,[41] J. B. Carlin,[115] M. F. Carney,[15] M. Carpinelli,[116,117,41] G. Carrillo,[59] G. Carullo,[73,18] T. L. Carver,[17] J. Casanueva Diaz,[41] C. Casentini,[118,119] G. Castaldi,[120] S. Caudill,[52,113] M. Cavaglià,[88] F. Cavalier,[40] R. Cavalieri,[41] M. Ceasar,[121] G. Cella,[18] P. Cerdá-Durán,[122] E. Cesarini,[119] W. Chaibi,[94] K. Chakravarti,[11] S. Chalathadka Subrahmanya,[123] E. Champion,[124] C.-H. Chan,[125] C. Chan,[27] C. L. Chan,[108] K. Chan,[108] M. Chan,[126] K. Chandra,[99] P. Chanial,[41] S. Chao,[125] C. E. A. Chapman-Bird,[68] P. Charlton,[127] E. A. Chase,[15] E. Chassande-Mottin,[35] C. Chatterjee,[85] Debarati Chatterjee,[11] Deep Chatterjee,[7] M. Chaturvedi,[86] S. Chaty,[35] K. Chatziioannou,[1] C. Chen,[128,129] H. Y. Chen,[69] J. Chen,[125] K. Chen,[130] X. Chen,[85] Y.-B. Chen,[131] Y.-R. Chen,[132] Z. Chen,[17] H. Cheng,[71] C. K. Cheong,[108] H. Y. Cheung,[108] H. Y. Chia,[71] F. Chiadini,[133,96] C-Y. Chiang,[134] G. Chiarini,[77] R. Chierici,[135] A. Chincarini,[84] M. L. Chiofalo,[73,18] A. Chiummo,[41] G. Cho,[136] H. S. Cho,[137] R. K. Choudhary,[85] S. Choudhary,[11] N. Christensen,[94] H. Chu,[130] Q. Chu,[85] Y-K. Chu,[134] S. Chua,[8] K. W. Chung,[53] G. Ciani,[76,77] P. Ciecielag,[80] M. Cieślar,[80] M. Cifaldi,[118,119] A. A. Ciobanu,[82] R. Ciolfi,[138,77] F. Cipriano,[94] A. Cirone,[112,84] F. Clara,[66] E. N. Clark,[139] J. A. Clark,[1,42] L. Clarke,[140] P. Clearwater,[141] S. Clesse,[142] F. Cleva,[94] E. Coccia,[30,100] E. Codazzo,[30] P.-F. Cohadon,[101] D. E. Cohen,[40] L. Cohen,[2] M. Colleoni,[143] C. G. Collette,[144] A. Colombo,[63] M. Colpi,[63,64] C. M. Compton,[66] M. Constancio Jr.,[16] L. Conti,[77] S. J. Cooper,[14] P. Corban,[6] T. R. Corbitt,[2] I. Cordero-Carrión,[145] S. Corezzi,[75,74] K. R. Corley,[45] N. Cornish,[78] D. Corre,[40] A. Corsi,[146] S. Cortese,[41] C. A. Costa,[16] R. Cotesta,[104] M. W. Coughlin,[62] J.-P. Coulon,[94] S. T. Countryman,[45] B. Cousins,[147] P. Couvares,[1] D. M. Coward,[85] M. J. Cowart,[6] D. C. Coyne,[1] R. Coyne,[148] J. D. E. Creighton,[7] T. D. Creighton,[149] A. W. Criswell,[62] M. Croquette,[101] S. G. Crowder,[150] J. R. Cudell,[61] T. J. Cullen,[2] A. Cumming,[68] R. Cummings,[68] L. Cunningham,[68] E. Cuoco,[41,151,18] M. Curyło,[102] P. Dabadie,[25] T. Dal Canton,[40] S. Dall'Osso,[30] G. Dálya,[152] A. Dana,[72] L. M. DaneshgaranBajastani,[83] B. D'Angelo,[112,84] B. Danila,[153] S. Danilishin,[154,52] S. D'Antonio,[119] K. Danzmann,[9,10] C. Darsow-Fromm,[123] A. Dasgupta,[79] L. E. H. Datrier,[68] V. Dattilo,[41] I. Dave,[86] M. Davier,[40] D. Davis,[1] M. C. Davis,[121] E. J. Daw,[155] P. F. de Alarcón,[143] R. Dean,[121] D. DeBra,[72] M. Deenadayalan,[11] J. Degallaix,[156] M. De Laurentis,[24,4] S. Deléglise,[101] V. Del Favero,[124] F. De Lillo,[51] N. De Lillo,[68] W. Del Pozzo,[73,18] L. M. DeMarchi,[15] F. De Matteis,[118,119] V. D'Emilio,[17] N. Demos,[69] T. Dent,[107] A. Depasse,[51] R. De Pietri,[157,158] R. De Rosa,[24,4] C. De Rossi,[41] R. DeSalvo,[120] R. De Simone,[133] S. Dhurandhar,[11] M. C. Díaz,[149] M. Diaz-Ortiz Jr.,[71] N. A. Didio,[60] T. Dietrich,[104,52] L. Di Fiore,[4] C. Di Fronzo,[14] C. Di Giorgio,[95,96] F. Di Giovanni,[122] M. Di Giovanni,[30] T. Di Girolamo,[24,4] A. Di Lieto,[73,18] B. Ding,[144] S. Di Pace,[97,50] I. Di Palma,[97,50] F. Di Renzo,[73,18] A. K. Divakarla,[71] A. Dmitriev,[14] Z. Doctor,[59] L. D'Onofrio,[24,4] F. Donovan,[69] K. L. Dooley,[17] S. Doravari,[11] I. Dorrington,[17] M. Drago,[97,50] J. C. Driggers,[66] Y. Drori,[1] J.-G. Ducoin,[40] P. Dupej,[68] O. Durante,[95,96] D. D'Urso,[116,117] P.-A. Duverne,[40] S. E. Dwyer,[66] C. Eassa,[66] P. J. Easter,[5] M. Ebersold,[159] T. Eckhardt,[123] G. Eddolls,[68] B. Edelman,[59] T. B. Edo,[1] O. Edy,[106] A. Effler,[6] S. Eguchi,[126] J. Eichholz,[8] S. S. Eikenberry,[71] M. Eisenmann,[29] R. A. Eisenstein,[69] A. Ejlli,[17] E. Engelby,[39] Y. Enomoto,[26] L. Errico,[24,4] R. C. Essick,[160] H. Estellés,[143] D. Estevez,[161] Z. Etienne,[162] T. Etzel,[1] M. Evans,[69] T. M. Evans,[6] B. E. Ewing,[147] V. Fafone,[118,119,30] H. Fair,[60] S. Fairhurst,[17] A. M. Farah,[160] S. Farinon,[84] B. Farr,[59] W. M. Farr,[109,110] N. W. Farrow,[5] E. J. Fauchon-Jones,[17] G. Favaro,[76] M. Favata,[163] M. Fays,[61] M. Fazio,[164] J. Feicht,[1] M. M. Fejer,[72] E. Fenyvesi,[70,165] D. L. Ferguson,[166] A. Fernandez-Galiana,[69] I. Ferrante,[73,18] T. A. Ferreira,[16] F. Fidecaro,[73,18] P. Figura,[102] I. Fiori,[41] M. Fishbach,[15] R. P. Fisher,[56] R. Fittipaldi,[167,96] V. Fiumara,[168,96] R. Flaminio,[29,21] E. Floden,[62] H. Fong,[27] J. A. Font,[122,169] B. Fornal,[170] P. W. F. Forsyth,[8] A. Franke,[123] S. Frasca,[97,50] F. Frasconi,[18] C. Frederick,[171] J. P. Freed,[34] Z. Frei,[152] A. Freise,[172] R. Frey,[59] P. Fritschel,[69] V. V. Frolov,[6] G. G. Fronzé,[23] Y. Fujii,[173] Y. Fujikawa,[174] M. Fukunaga,[36] M. Fukushima,[22] P. Fulda,[71] M. Fyffe,[6] H. A. Gabbard,[68] W. E. Gabella,[175] B. U. Gadre,[104] J. R. Gair,[104] J. Gais,[108] S. Galaudage,[5] R. Gamba,[13] D. Ganapathy,[69] A. Ganguly,[19] D. Gao,[176] S. G. Gaonkar,[11] B. Garaventa,[84,112] F. García,[35] C. García-Núñez,[92] C. García-Quirós,[143] F. Garufi,[24,4] B. Gateley,[66] S. Gaudio,[34] V. Gayathri,[71] G.-G. Ge,[176] G. Gemme,[84] A. Gennai,[18] J. George,[86] R. N. George,[166] O. Gerberding,[123] L. Gergely,[153] P. Gewecke,[123] S. Ghonge,[42] Abhirup Ghosh,[104] Archisman Ghosh,[177] Shaon Ghosh,[7,163] Shrobana Ghosh,[17] B. Giacomazzo,[63,64,65] L. Giacoppo,[97,50] J. A. Giaime,[2,6] K. D. Giardina,[6] D. R. Gibson,[92] C. Gier,[31] M. Giesler,[178] P. Giri,[18,73] F. Gissi,[81] J. Glanzer,[2] A. E. Gleckl,[39] P. Godwin,[147] E. Goetz,[179] R. Goetz,[71] N. Gohlke,[9,10] J. Golomb,[1] B. Goncharov,[5,30] G. González,[2] A. Gopakumar,[180] M. Gosselin,[41] R. Gouaty,[29] D. W. Gould,[8] B. Grace,[8] A. Grado,[181,4] M. Granata,[156] V. Granata,[95] A. Grant,[68] S. Gras,[69] P. Grassia,[1] C. Gray,[66] R. Gray,[68] G. Greco,[74] A. C. Green,[71] R. Green,[17] A. M. Gretarsson,[34] E. M. Gretarsson,[34] D. Griffith,[1]

W. Griffiths,[17] H. L. Griggs,[42] G. Grignani,[75,74] A. Grimaldi,[90,91] S. J. Grimm,[30,100] H. Grote,[17] S. Grunewald,[104] P. Gruning,[40] D. Guerra,[122] G. M. Guidi,[48,49] A. R. Guimaraes,[2] G. Guixé,[28] H. K. Gulati,[79] H.-K. Guo,[170] Y. Guo,[52] Anchal Gupta,[1] Anuradha Gupta,[182] P. Gupta,[52,113] E. K. Gustafson,[1] R. Gustafson,[183] F. Guzman,[184] S. Ha,[185] L. Haegel,[35] A. Hagiwara,[36,186] S. Haino,[134] O. Halim,[33,187] E. D. Hall,[69] E. Z. Hamilton,[159] G. Hammond,[68] W.-B. Han,[188] M. Haney,[159] J. Hanks,[66] C. Hanna,[147] M. D. Hannam,[17] O. Hannuksela,[113,52] H. Hansen,[66] T. J. Hansen,[34] J. Hanson,[6] T. Harder,[94] T. Hardwick,[2] K. Haris,[52,113] J. Harms,[30,100] G. M. Harry,[189] I. W. Harry,[106] D. Hartwig,[123] K. Hasegawa,[36] B. Haskell,[80] R. K. Hasskew,[6] C.-J. Haster,[69] K. Hattori,[190] K. Haughian,[68] H. Hayakawa,[191] K. Hayama,[126] F. J. Hayes,[68] J. Healy,[124] A. Heidmann,[101] A. Heidt,[9,10] M. C. Heintze,[6] J. Heinze,[9,10] J. Heinzel,[192] H. Heitmann,[94] F. Hellman,[193] P. Hello,[40] A. F. Helmling-Cornell,[59] G. Hemming,[41] M. Hendry,[68] I. S. Heng,[68] E. Hennes,[52] J. Hennig,[194] M. H. Hennig,[194] A. G. Hernandez,[83] F. Hernandez Vivanco,[5] M. Heurs,[9,10] S. Hild,[154,52] P. Hill,[31] Y. Himemoto,[195] A. S. Hines,[184] Y. Hiranuma,[196] N. Hirata,[21] E. Hirose,[36] S. Hochheim,[9,10] D. Hofman,[156] J. N. Hohmann,[123] D. G. Holcomb,[121] N. A. Holland,[8] K. Holley-Bockelmann,[175] I. J. Hollows,[155] Z. J. Holmes,[82] K. Holt,[6] D. E. Holz,[160] Z. Hong,[197] P. Hopkins,[17] J. Hough,[68] S. Hourihane,[131] E. J. Howell,[85] C. G. Hoy,[17] D. Hoyland,[14] A. Hreibi,[9,10] B-H. Hsieh,[36] Y. Hsu,[125] G-Z. Huang,[197] H-Y. Huang,[134] P. Huang,[176] Y-C. Huang,[132] Y.-J. Huang,[134] Y. Huang,[69] M. T. Hübner,[5] A. D. Huddart,[140] B. Hughey,[34] D. C. Y. Hui,[198] V. Hui,[29] S. Husa,[143] S. H. Huttner,[68] R. Huxford,[147] T. Huynh-Dinh,[6] S. Ide,[199] B. Idzkowski,[102] A. Iess,[118,119] B. Ikenoue,[22] S. Imam,[197] K. Inayoshi,[200] C. Ingram,[82] Y. Inoue,[130] K. Ioka,[201] M. Isi,[69] K. Isleif,[123] K. Ito,[202] Y. Itoh,[203,204] B. R. Iyer,[19] K. Izumi,[205] V. JaberianHamedan,[85] T. Jacqmin,[101] S. J. Jadhav,[206] S. P. Jadhav,[11] A. L. James,[17] A. Z. Jan,[124] K. Jani,[175] J. Janquart,[113,52] K. Janssens,[207,94] N. N. Janthalur,[206] P. Jaranowski,[208] D. Jariwala,[71] R. Jaume,[143] A. C. Jenkins,[53] K. Jenner,[82] C. Jeon,[209] M. Jeunon,[62] W. Jia,[69] H.-B. Jin,[210,211] G. R. Johns,[56] N. K. Johnson-McDaniel,[182] A. W. Jones,[85] D. I. Jones,[212] J. D. Jones,[66] P. Jones,[14] R. Jones,[68] R. J. G. Jonker,[52] L. Ju,[85] P. Jung,[55] K. Jung,[185] J. Junker,[9,10] V. Juste,[161] K. Kaihotsu,[202] T. Kajita,[213] M. Kakizaki,[190] C. V. Kalaghatgi,[17,113] V. Kalogera,[15] B. Kamai,[1] M. Kamiizumi,[191] N. Kanda,[203,204] S. Kandhasamy,[11] G. Kang,[214] J. B. Kanner,[1] Y. Kao,[125] S. J. Kapadia,[19] D. P. Kapasi,[8] S. Karat,[1] C. Karathanasis,[215] S. Karki,[88] R. Kashyap,[147] M. Kasprzack,[1] W. Kastaun,[9,10] S. Katsanevas,[41] E. Katsavounidis,[69] W. Katzman,[6] T. Kaur,[85] K. Kawabe,[66] K. Kawaguchi,[36] N. Kawai,[216] T. Kawasaki,[26] F. Kéfélian,[94] D. Keitel,[143] J. S. Key,[217] S. Khadka,[72] F. Y. Khalili,[89] S. Khan,[17] E. A. Khazanov,[218] N. Khetan,[30,100] M. Khursheed,[86] N. Kijbunchoo,[8] C. Kim,[219] J. C. Kim,[220] J. Kim,[221] K. Kim,[222] W. S. Kim,[223] Y.-M. Kim,[224] C. Kimball,[15] N. Kimura,[186] M. Kinley-Hanlon,[68] R. Kirchhoff,[9,10] J. S. Kissel,[66] N. Kita,[26] H. Kitazawa,[202] L. Kleybolte,[123] S. Klimenko,[71] A. M. Knee,[179] T. D. Knowles,[162] E. Knyazev,[69] P. Koch,[9,10] G. Koekoek,[52,154] Y. Kojima,[225] K. Kokeyama,[226] S. Koley,[30] P. Kolitsidou,[17] M. Kolstein,[215] K. Komori,[69,26] V. Kondrashov,[1] A. K. H. Kong,[227] A. Kontos,[228] N. Koper,[9,10] M. Korobko,[123] K. Kotake,[126] M. Kovalam,[85] D. B. Kozak,[1] C. Kozakai,[46] R. Kozu,[191] V. Kringel,[9,10] N. V. Krishnendu,[9,10] A. Królak,[229,230] G. Kuehn,[9,10] F. Kuei,[125] P. Kuijer,[52] S. Kulkarni,[182] A. Kumar,[206] P. Kumar,[178] Rahul Kumar,[66] Rakesh Kumar,[79] J. Kume,[27] K. Kuns,[69] C. Kuo,[130] H-S. Kuo,[197] Y. Kuromiya,[202] S. Kuroyanagi,[231,232] K. Kusayanagi,[216] S. Kuwahara,[27] K. Kwak,[185] P. Lagabbe,[29] D. Laghi,[73,18] E. Lalande,[233] T. L. Lam,[108] A. Lamberts,[94,234] M. Landry,[66] B. B. Lane,[69] R. N. Lang,[69] J. Lange,[166] B. Lantz,[72] I. La Rosa,[29] A. Lartaux-Vollard,[40] P. D. Lasky,[5] M. Laxen,[6] A. Lazzarini,[1] C. Lazzaro,[76,77] P. Leaci,[97,50] S. Leavey,[9,10] Y. K. Lecoeuche,[179] H. K. Lee,[235] H. M. Lee,[136] H. W. Lee,[220] J. Lee,[136] K. Lee,[236] R. Lee,[132] J. Lehmann,[9,10] A. Lemaître,[237] M. Leonardi,[21] N. Leroy,[40] N. Letendre,[29] C. Levesque,[233] Y. Levin,[5] J. N. Leviton,[183] K. Leyde,[35] A. K. Y. Li,[1] B. Li,[125] J. Li,[15] K. L. Li,[238] T. G. F. Li,[108] X. Li,[131] C-Y. Lin,[239] F-K. Lin,[134] F-L. Lin,[197] H. L. Lin,[130] L. C.-C. Lin,[185] F. Linde,[240,52] S. D. Linker,[83] J. N. Linley,[68] T. B. Littenberg,[241] G. C. Liu,[128] J. Liu,[9,10] K. Liu,[125] X. Liu,[7] F. Llamas,[149] M. Llorens-Monteagudo,[122] R. K. L. Lo,[1] A. Lockwood,[242] M. Loh,[39] L. T. London,[69] A. Longo,[243,244] D. Lopez,[159] M. Lopez Portilla,[113] M. Lorenzini,[118,119] V. Loriette,[245] M. Lormand,[6] G. Losurdo,[18] T. P. Lott,[42] J. D. Lough,[9,10] C. O. Lousto,[124] G. Lovelace,[39] J. F. Lucaccioni,[171] H. Lück,[9,10] D. Lumaca,[118,119] A. P. Lundgren,[106] L.-W. Luo,[134] J. E. Lynam,[56] R. Macas,[106] M. MacInnis,[69] D. M. Macleod,[17] I. A. O. MacMillan,[1] A. Macquet,[94] I. Magaña Hernandez,[7] C. Magazzù,[18] R. M. Magee,[1] R. Maggiore,[14] M. Magnozzi,[84,112] S. Mahesh,[162] E. Majorana,[97,50] C. Makarem,[1] I. Maksimovic,[245] S. Maliakal,[1] A. Malik,[86] N. Man,[94] V. Mandic,[62] V. Mangano,[97,50] J. L. Mango,[246] G. L. Mansell,[66,69] M. Manske,[7] M. Mantovani,[41] M. Mapelli,[76,77] F. Marchesoni,[247,74,248] M. Marchio,[21] F. Marion,[29] Z. Mark,[131] S. Márka,[45] Z. Márka,[45] C. Markakis,[12] A. S. Markosyan,[72] A. Markowitz,[1] E. Maros,[1] A. Marquina,[145] S. Marsat,[35] F. Martelli,[48,49] I. W. Martin,[68] R. M. Martin,[163] M. Martinez,[215] V. A. Martinez,[71] V. Martinez,[25] K. Martinovic,[53] D. V. Martynov,[14] E. J. Marx,[69] H. Masalehdan,[123] K. Mason,[69] E. Massera,[155] A. Masserot,[29] T. J. Massinger,[69] M. Masso-Reid,[68]

S. Mastrogiovanni,[35] A. Matas,[104] M. Mateu-Lucena,[143] F. Matichard,[1,69] M. Matiushechkina,[9,10] N. Mavalvala,[69] J. J. McCann,[85] R. McCarthy,[66] D. E. McClelland,[8] P. K. McClincy,[147] S. McCormick,[6] L. McCuller,[69] G. I. McGhee,[68] S. C. McGuire,[249] C. McIsaac,[106] J. McIver,[179] T. McRae,[8] S. T. McWilliams,[162] D. Meacher,[7] M. Mehmet,[9,10] A. K. Mehta,[104] Q. Meijer,[113] A. Melatos,[115] D. A. Melchor,[39] G. Mendell,[66] A. Menendez-Vazquez,[215] C. S. Menoni,[164] R. A. Mercer,[7] L. Mereni,[156] K. Merfeld,[59] E. L. Merilh,[6] J. D. Merritt,[59] M. Merzougui,[94] S. Meshkov,[1,†] C. Messenger,[68] C. Messick,[166] P. M. Meyers,[115] F. Meylahn,[9,10] A. Mhaske,[11] A. Miani,[90,91] H. Miao,[14] I. Michaloliakos,[71] C. Michel,[156] Y. Michimura,[26] H. Middleton,[115] L. Milano,[24] A. L. Miller,[51] A. Miller,[83] B. Miller,[87,52] M. Millhouse,[115] J. C. Mills,[17] E. Milotti,[187,33] O. Minazzoli,[94,250] Y. Minenkov,[119] N. Mio,[251] Ll. M. Mir,[215] M. Miravet-Tenés,[122] C. Mishra,[252] T. Mishra,[71] T. Mistry,[155] S. Mitra,[11] V. P. Mitrofanov,[89] G. Mitselmakher,[71] R. Mittleman,[69] O. Miyakawa,[191] A. Miyamoto,[203] Y. Miyazaki,[26] K. Miyo,[191] S. Miyoki,[191] Geoffrey Mo,[69] L. M. Modafferi,[143] E. Moguel,[171] K. Mogushi,[88] S. R. P. Mohapatra,[69] S. R. Mohite,[7] I. Molina,[39] M. Molina-Ruiz,[193] M. Mondin,[83] M. Montani,[48,49] C. J. Moore,[14] D. Moraru,[66] F. Morawski,[80] A. More,[11] C. Moreno,[34] G. Moreno,[66] Y. Mori,[202] S. Morisaki,[7] Y. Moriwaki,[190] G. Morrás,[231] B. Mours,[161] C. M. Mow-Lowry,[14,172] S. Mozzon,[106] F. Muciaccia,[97,50] Arunava Mukherjee,[253] D. Mukherjee,[147] Soma Mukherjee,[149] Subroto Mukherjee,[79] Suvodip Mukherjee,[87] N. Mukund,[9,10] A. Mullavey,[6] J. Munch,[82] E. A. Muñiz,[60] P. G. Murray,[68] R. Musenich,[84,112] S. Muusse,[82] S. L. Nadji,[9,10] K. Nagano,[205] S. Nagano,[254] A. Nagar,[23,255] K. Nakamura,[21] H. Nakano,[256] M. Nakano,[36] R. Nakashima,[216] Y. Nakayama,[202] V. Napolano,[41] I. Nardecchia,[118,119] T. Narikawa,[36] L. Naticchioni,[50] B. Nayak,[83] R. K. Nayak,[257] R. Negishi,[196] B. F. Neil,[85] J. Neilson,[81,96] G. Nelemans,[258] T. J. N. Nelson,[6] M. Nery,[9,10] P. Neubauer,[171] A. Neunzert,[217] K. Y. Ng,[69] S. W. S. Ng,[82] C. Nguyen,[35] P. Nguyen,[59] T. Nguyen,[69] L. Nguyen Quynh,[259] W.-T. Ni,[210,176,132] S. A. Nichols,[2] A. Nishizawa,[27] S. Nissanke,[87,52] E. Nitoglia,[135] F. Nocera,[41] M. Norman,[17] C. North,[17] S. Nozaki,[190] J. F. Nuño Siles,[231] L. K. Nuttall,[106] J. Oberling,[66] B. D. O'Brien,[71] Y. Obuchi,[22] J. O'Dell,[140] E. Oelker,[68] W. Ogaki,[36] G. Oganesyan,[30,100] J. J. Oh,[223] K. Oh,[198] S. H. Oh,[223] M. Ohashi,[191] N. Ohishi,[46] M. Ohkawa,[174] F. Ohme,[9,10] H. Ohta,[27] M. A. Okada,[16] Y. Okutani,[199] K. Okutomi,[191] C. Olivetto,[41] K. Oohara,[196] C. Ooi,[26] R. Oram,[6] B. O'Reilly,[6] R. G. Ormiston,[62] N. D. Ormsby,[56] L. F. Ortega,[71] R. O'Shaughnessy,[124] E. O'Shea,[178] S. Oshino,[191] S. Ossokine,[104] C. Osthelder,[1] S. Otabe,[216] D. J. Ottaway,[82] H. Overmier,[6] A. E. Pace,[147] G. Pagano,[73,18] M. A. Page,[85] G. Pagliaroli,[30,100] A. Pai,[99] S. A. Pai,[86] J. R. Palamos,[59] O. Palashov,[218] C. Palomba,[50] H. Pan,[125] K. Pan,[132,227] P. K. Panda,[206] H. Pang,[130] P. T. H. Pang,[52,113] C. Pankow,[15] F. Pannarale,[97,50] B. C. Pant,[86] F. H. Panther,[85] F. Paoletti,[18] A. Paoli,[41] A. Paolone,[50,260] A. Parisi,[128] H. Park,[7] J. Park,[261] W. Parker,[6,249] D. Pascucci,[52] A. Pasqualetti,[41] R. Passaquieti,[73,18] D. Passuello,[18] M. Patel,[56] M. Pathak,[82] B. Patricelli,[41,18] A. S. Patron,[2] S. Paul,[59] E. Payne,[5] M. Pedraza,[1] M. Pegoraro,[77] A. Pele,[6] F. E. Peña Arellano,[191] S. Penn,[262] A. Perego,[90,91] A. Pereira,[25] T. Pereira,[263] C. J. Perez,[66] C. Périgois,[29] C. C. Perkins,[71] A. Perreca,[90,91] S. Perriès,[135] J. Petermann,[123] D. Petterson,[1] H. P. Pfeiffer,[104] K. A. Pham,[62] K. S. Phukon,[52,240] O. J. Piccinni,[50] M. Pichot,[94] M. Piendibene,[73,18] F. Piergiovanni,[48,49] L. Pierini,[97,50] V. Pierro,[81,96] G. Pillant,[41] M. Pillas,[40] F. Pilo,[18] L. Pinard,[156] I. M. Pinto,[81,96,264] M. Pinto,[41] B. Piotrzkowski,[7] K. Piotrzkowski,[51] M. Pirello,[66] M. D. Pitkin,[265] E. Placidi,[97,50] L. Planas,[143] W. Plastino,[243,244] C. Pluchar,[139] R. Poggiani,[73,18] E. Polini,[29] D. Y. T. Pong,[108] S. Ponrathnam,[11] P. Popolizio,[41] E. K. Porter,[35] R. Poulton,[41] J. Powell,[141] M. Pracchia,[29] T. Pradier,[161] A. K. Prajapati,[79] K. Prasai,[72] R. Prasanna,[206] G. Pratten,[14] M. Principe,[81,264,96] G. A. Prodi,[266,91] L. Prokhorov,[14] P. Prosposito,[118,119] L. Prudenzi,[104] A. Puecher,[52,113] M. Punturo,[74] F. Puosi,[18,73] P. Puppo,[50] M. Pürrer,[104] H. Qi,[17] V. Quetschke,[149] R. Quitzow-James,[88] N. Qutob,[42] F. J. Raab,[66] G. Raaijmakers,[87,52] H. Radkins,[66] N. Radulesco,[94] P. Raffai,[152] S. X. Rail,[233] S. Raja,[86] C. Rajan,[86] K. E. Ramirez,[6] T. D. Ramirez,[39] A. Ramos-Buades,[104] J. Rana,[147] P. Rapagnani,[97,50] U. D. Rapol,[267] A. Ray,[7] V. Raymond,[17] N. Raza,[179] M. Razzano,[73,18] J. Read,[39] L. A. Rees,[189] T. Regimbau,[29] L. Rei,[84] S. Reid,[31] S. W. Reid,[56] D. H. Reitze,[1,71] P. Relton,[17] A. Renzini,[1] P. Rettegno,[268,23] A. Reza,[52] M. Rezac,[39] F. Ricci,[97,50] D. Richards,[140] J. W. Richardson,[1] L. Richardson,[184] G. Riemenschneider,[268,23] K. Riles,[183] S. Rinaldi,[18,73] K. Rink,[179] M. Rizzo,[15] N. A. Robertson,[1,68] R. Robie,[1] F. Robinet,[40] A. Rocchi,[119] S. Rodriguez,[39] L. Rolland,[29] J. G. Rollins,[1] M. Romanelli,[98] R. Romano,[3,4] C. L. Romel,[66] A. Romero-Rodríguez,[215] I. M. Romero-Shaw,[5] J. H. Romie,[6] S. Ronchini,[30,100] L. Rosa,[4,24] C. A. Rose,[7] D. Rosińska,[102] M. P. Ross,[242] S. Rowan,[68] S. J. Rowlinson,[14] S. Roy,[113] Santosh Roy,[11] Soumen Roy,[269] D. Rozza,[116,117] P. Ruggi,[41] K. Ruiz-Rocha,[175] K. Ryan,[66] S. Sachdev,[147] T. Sadecki,[66] J. Sadiq,[107] N. Sago,[270] S. Saito,[22] Y. Saito,[191] K. Sakai,[271] Y. Sakai,[196] M. Sakellariadou,[53] Y. Sakuno,[126] O. S. Salafia,[65,64,63] L. Salconi,[41] M. Saleem,[62] F. Salemi,[90,91] A. Samajdar,[52,113] E. J. Sanchez,[1] J. H. Sanchez,[39] L. E. Sanchez,[1] N. Sanchis-Gual,[272] J. R. Sanders,[273] A. Sanuy,[28] T. R. Saravanan,[11] N. Sarin,[5] B. Sassolas,[156] H. Satari,[85] B. S. Sathyaprakash,[147,17] S. Sato,[274] T. Sato,[174] O. Sauter,[71] R. L. Savage,[66] T. Sawada,[203] D. Sawant,[99] H. L. Sawant,[11]

S. Sayah,[156] D. Schaetzl,[1] M. Scheel,[131] J. Scheuer,[15] M. Schiworski,[82] P. Schmidt,[14] S. Schmidt,[113] R. Schnabel,[123] M. Schneewind,[9,10] R. M. S. Schofield,[59] A. Schönbeck,[123] B. W. Schulte,[9,10] B. F. Schutz,[17,9,10] E. Schwartz,[17] J. Scott,[68] S. M. Scott,[8] M. Seglar-Arroyo,[29] T. Sekiguchi,[27] Y. Sekiguchi,[275] D. Sellers,[6] A. S. Sengupta,[269] D. Sentenac,[41] E. G. Seo,[108] V. Sequino,[24,4] A. Sergeev,[218] Y. Setyawati,[113] T. Shaffer,[66] M. S. Shahriar,[15] B. Shams,[170] L. Shao,[200] A. Sharma,[30,100] P. Sharma,[86] P. Shawhan,[103] N. S. Shcheblanov,[237] S. Shibagaki,[126] M. Shikauchi,[27] R. Shimizu,[22] T. Shimoda,[26] K. Shimode,[191] H. Shinkai,[276] T. Shishido,[47] A. Shoda,[21] D. H. Shoemaker,[69] D. M. Shoemaker,[166] S. ShyamSundar,[86] M. Sieniawska,[102] D. Sigg,[66] L. P. Singer,[111] D. Singh,[147] N. Singh,[102] A. Singha,[154,52] A. M. Sintes,[143] V. Sipala,[116,117] V. Skliris,[17] B. J. J. Slagmolen,[8] T. J. Slaven-Blair,[85] J. Smetana,[14] J. R. Smith,[39] R. J. E. Smith,[5] J. Soldateschi,[277,278,49] S. N. Somala,[279] K. Somiya,[216] E. J. Son,[223] K. Soni,[11] S. Soni,[2] V. Sordini,[135] F. Sorrentino,[84] N. Sorrentino,[73,18] H. Sotani,[280] R. Soulard,[94] T. Souradeep,[267,11] E. Sowell,[146] V. Spagnuolo,[154,52] A. P. Spencer,[68] M. Spera,[76,77] R. Srinivasan,[94] A. K. Srivastava,[79] V. Srivastava,[60] K. Staats,[15] C. Stachie,[94] D. A. Steer,[35] J. Steinhoff,[104] J. Steinlechner,[154,52] S. Steinlechner,[154,52] S. P. Stevenson,[141] D. J. Stops,[14] M. Stover,[171] K. A. Strain,[68] L. C. Strang,[115] G. Stratta,[281,49] A. Strunk,[66] R. Sturani,[263] A. L. Stuver,[121] S. Sudhagar,[11] V. Sudhir,[69] R. Sugimoto,[282,205] H. G. Suh,[7] A. G. Sullivan,[45] J. M. Sullivan,[42] T. Z. Summerscales,[283] H. Sun,[85] L. Sun,[8] S. Sunil,[79] A. Sur,[80] J. Suresh,[27,36] P. J. Sutton,[17] Takamasa Suzuki,[174] Toshikazu Suzuki,[36] B. L. Swinkels,[52] M. J. Szczepańczyk,[71] P. Szewczyk,[102] M. Tacca,[52] H. Tagoshi,[36] S. C. Tait,[68] H. Takahashi,[284] R. Takahashi,[21] A. Takamori,[38] S. Takano,[26] H. Takeda,[26] M. Takeda,[203] C. J. Talbot,[31] C. Talbot,[1] H. Tanaka,[285] Kazuyuki Tanaka,[203] Kenta Tanaka,[285] Taiki Tanaka,[36] Takahiro Tanaka,[270] A. J. Tanasijczuk,[51] S. Tanioka,[21,47] D. B. Tanner,[71] D. Tao,[1] L. Tao,[71] E. N. Tapia San Martín,[52,21] C. Taranto,[118] J. D. Tasson,[192] S. Telada,[286] R. Tenorio,[143] J. E. Terhune,[121] L. Terkowski,[123] M. P. Thirugnanasambandam,[11] L. Thomas,[14] M. Thomas,[6] P. Thomas,[66] J. E. Thompson,[17] S. R. Thondapu,[86] K. A. Thorne,[6] E. Thrane,[5] Shubhanshu Tiwari,[159] Srishti Tiwari,[11] V. Tiwari,[17] A. M. Toivonen,[62] K. Toland,[68] A. E. Tolley,[106] T. Tomaru,[21] Y. Tomigami,[203] T. Tomura,[191] M. Tonelli,[73,18] A. Torres-Forné,[122] C. I. Torrie,[1] I. Tosta e Melo,[116,117] D. Töyrä,[8] A. Trapananti,[247,74] F. Travasso,[74,247] G. Traylor,[6] M. Trevor,[103] M. C. Tringali,[41] A. Tripathee,[183] L. Troiano,[287,96] A. Trovato,[35] L. Trozzo,[4,191] R. J. Trudeau,[1] D. S. Tsai,[125] D. Tsai,[125] K. W. Tsang,[52,288,113] T. Tsang,[289] J-S. Tsao,[197] M. Tse,[69] R. Tso,[131] K. Tsubono,[26] S. Tsuchida,[203] L. Tsukada,[27] D. Tsuna,[27] T. Tsutsui,[27] T. Tsuzuki,[22] K. Turbang,[290,207] M. Turconi,[94] D. Tuyenbayev,[203] A. S. Ubhi,[14] N. Uchikata,[36] T. Uchiyama,[191] R. P. Udall,[1] A. Ueda,[186] T. Uehara,[291,292] K. Ueno,[27] G. Ueshima,[293] C. S. Unnikrishnan,[180] F. Uraguchi,[22] A. L. Urban,[2] T. Ushiba,[191] A. Utina,[154,52] H. Vahlbruch,[9,10] G. Vajente,[1] A. Vajpeyi,[5] G. Valdes,[184] M. Valentini,[90,91] V. Valsan,[7] N. van Bakel,[52] M. van Beuzekom,[52] J. F. J. van den Brand,[154,294,52] C. Van Den Broeck,[113,52] D. C. Vander-Hyde,[60] L. van der Schaaf,[52] J. V. van Heijningen,[51] J. Vanosky,[1] M. H. P. M. van Putten,[295] N. van Remortel,[207] M. Vardaro,[240,52] A. F. Vargas,[115] V. Varma,[178] M. Vasúth,[70] A. Vecchio,[14] G. Vedovato,[77] J. Veitch,[68] P. J. Veitch,[82] J. Venneberg,[9,10] G. Venugopalan,[1] D. Verkindt,[29] P. Verma,[230] Y. Verma,[86] D. Veske,[45] F. Vetrano,[48] A. Viceré,[48,49] S. Vidyant,[60] A. D. Viets,[246] A. Vijaykumar,[19] V. Villa-Ortega,[107] J.-Y. Vinet,[94] A. Virtuoso,[187,33] S. Vitale,[69] T. Vo,[60] H. Vocca,[75,74] E. R. G. von Reis,[66] J. S. A. von Wrangel,[9,10] C. Vorvick,[66] S. P. Vyatchanin,[89] L. E. Wade,[171] M. Wade,[171] K. J. Wagner,[124] R. C. Walet,[52] M. Walker,[56] G. S. Wallace,[31] L. Wallace,[1] S. Walsh,[7] J. Wang,[176] J. Z. Wang,[183] W. H. Wang,[149] R. L. Ward,[8] J. Warner,[66] M. Was,[29] T. Washimi,[21] N. Y. Washington,[1] J. Watchi,[144] B. Weaver,[66] S. A. Webster,[68] M. Weinert,[9,10] A. J. Weinstein,[1] R. Weiss,[69] C. M. Weller,[242] R. A. Weller,[175] F. Wellmann,[9,10] L. Wen,[85] P. Weßels,[9,10] K. Wette,[8] J. T. Whelan,[124] D. D. White,[39] B. F. Whiting,[71] C. Whittle,[69] D. Wilken,[9,10] D. Williams,[68] M. J. Williams,[68] N. Williams,[14] A. R. Williamson,[106] J. L. Willis,[1] B. Willke,[9,10] D. J. Wilson,[139] W. Winkler,[9,10] C. C. Wipf,[1] T. Wlodarczyk,[104] G. Woan,[68] J. Woehler,[9,10] J. K. Wofford,[124] I. C. F. Wong,[108] C. Wu,[132] D. S. Wu,[9,10] H. Wu,[132] S. Wu,[132] D. M. Wysocki,[7] L. Xiao,[1] W-R. Xu,[197] T. Yamada,[285] H. Yamamoto,[1] Kazuhiro Yamamoto,[190] Kohei Yamamoto,[285] T. Yamamoto,[191] K. Yamashita,[202] R. Yamazaki,[199] F. W. Yang,[170] L. Yang,[164] Y. Yang,[296] Yang Yang,[71] Z. Yang,[62] M. J. Yap,[8] D. W. Yeeles,[17] A. B. Yelikar,[124] M. Ying,[125] K. Yokogawa,[202] J. Yokoyama,[27,26] T. Yokozawa,[191] J. Yoo,[178] T. Yoshioka,[202] Hang Yu,[131] Haocun Yu,[69] H. Yuzurihara,[36] A Zadrożny,[230] M. Zanolin,[34] S. Zeidler,[297] T. Zelenova,[41] J.-P. Zendri,[77] M. Zevin,[160] M. Zhan,[176] H. Zhang,[197] J. Zhang,[85] L. Zhang,[1] T. Zhang,[14] Y. Zhang,[184] C. Zhao,[85] G. Zhao,[144] Y. Zhao,[21] Yue Zhao,[170] Y. Zheng,[88] R. Zhou,[193] Z. Zhou,[15] X. J. Zhu,[5] Z.-H. Zhu,[114] A. B. Zimmerman,[166] Y. Zlochower,[124] M. E. Zucker,[1,69] and J. Zweizig[1]

(LIGO Scientific Collaboration, Virgo Collaboration, and KAGRA Collaboration)

[1]LIGO Laboratory, California Institute of Technology, Pasadena, California 91125, USA
[2]Louisiana State University, Baton Rouge, Louisiana 70803, USA
[3]Dipartimento di Farmacia, Università di Salerno, I-84084 Fisciano, Salerno, Italy
[4]INFN, Sezione di Napoli, Complesso Universitario di Monte S. Angelo, I-80126 Napoli, Italy
[5]OzGrav, School of Physics & Astronomy, Monash University, Clayton 3800, Victoria, Australia
[6]LIGO Livingston Observatory, Livingston, Louisiana 70754, USA
[7]University of Wisconsin-Milwaukee, Milwaukee, Wisconsin 53201, USA
[8]OzGrav, Australian National University, Canberra, Australian Capital Territory 0200, Australia
[9]Max Planck Institute for Gravitational Physics (Albert Einstein Institute), D-30167 Hannover, Germany
[10]Leibniz Universität Hannover, D-30167 Hannover, Germany
[11]Inter-University Centre for Astronomy and Astrophysics, Pune 411007, India
[12]University of Cambridge, Cambridge CB2 1TN, United Kingdom
[13]Theoretisch-Physikalisches Institut, Friedrich-Schiller-Universität Jena, D-07743 Jena, Germany
[14]University of Birmingham, Birmingham B15 2TT, United Kingdom
[15]Center for Interdisciplinary Exploration and Research in Astrophysics (CIERA), Northwestern University, Evanston, Illinois 60208, USA
[16]Instituto Nacional de Pesquisas Espaciais, 12227-010 São José dos Campos, São Paulo, Brazil
[17]Gravity Exploration Institute, Cardiff University, Cardiff CF24 3AA, United Kingdom
[18]INFN, Sezione di Pisa, I-56127 Pisa, Italy
[19]International Centre for Theoretical Sciences, Tata Institute of Fundamental Research, Bengaluru 560089, India
[20]University College Dublin, Dublin 4, Ireland
[21]Gravitational Wave Science Project, National Astronomical Observatory of Japan (NAOJ), Mitaka City, Tokyo 181-8588, Japan
[22]Advanced Technology Center, National Astronomical Observatory of Japan (NAOJ), Mitaka City, Tokyo 181-8588, Japan
[23]INFN Sezione di Torino, I-10125 Torino, Italy
[24]Università di Napoli "Federico II", Complesso Universitario di Monte S. Angelo, I-80126 Napoli, Italy
[25]Université de Lyon, Université Claude Bernard Lyon 1, CNRS, Institut Lumière Matière, F-69622 Villeurbanne, France
[26]Department of Physics, The University of Tokyo, Bunkyo-ku, Tokyo 113-0033, Japan
[27]Research Center for the Early Universe (RESCEU), The University of Tokyo, Bunkyo-ku, Tokyo 113-0033, Japan
[28]Institut de Ciències del Cosmos (ICCUB), Universitat de Barcelona, C/ Martí i Franquès 1, Barcelona, 08028, Spain
[29]Laboratoire d'Annecy de Physique des Particules (LAPP), Univ. Grenoble Alpes, Université Savoie Mont Blanc, CNRS/IN2P3, F-74941 Annecy, France
[30]Gran Sasso Science Institute (GSSI), I-67100 L'Aquila, Italy
[31]SUPA, University of Strathclyde, Glasgow G1 1XQ, United Kingdom
[32]Dipartimento di Scienze Matematiche, Informatiche e Fisiche, Università di Udine, I-33100 Udine, Italy
[33]INFN, Sezione di Trieste, I-34127 Trieste, Italy
[34]Embry-Riddle Aeronautical University, Prescott, Arizona 86301, USA
[35]Université de Paris, CNRS, Astroparticule et Cosmologie, F-75006 Paris, France
[36]Institute for Cosmic Ray Research (ICRR), KAGRA Observatory, The University of Tokyo, Kashiwa City, Chiba 277-8582, Japan
[37]Accelerator Laboratory, High Energy Accelerator Research Organization (KEK), Tsukuba City, Ibaraki 305-0801, Japan
[38]Earthquake Research Institute, The University of Tokyo, Bunkyo-ku, Tokyo 113-0032, Japan
[39]California State University Fullerton, Fullerton, California 92831, USA
[40]Université Paris-Saclay, CNRS/IN2P3, IJCLab, 91405 Orsay, France
[41]European Gravitational Observatory (EGO), I-56021 Cascina, Pisa, Italy
[42]School of Physics, Georgia Institute of Technology, Atlanta, Georgia 30332, USA
[43]Chennai Mathematical Institute, Chennai 603103, India
[44]Department of Mathematics and Physics, Gravitational Wave Science Project, Hirosaki University, Hirosaki City, Aomori 036-8561, Japan
[45]Columbia University, New York, New York 10027, USA
[46]Kamioka Branch, National Astronomical Observatory of Japan (NAOJ), Kamioka-cho, Hida City, Gifu 506-1205, Japan
[47]The Graduate University for Advanced Studies (SOKENDAI), Mitaka City, Tokyo 181-8588, Japan
[48]Università degli Studi di Urbino "Carlo Bo", I-61029 Urbino, Italy

[49]*INFN, Sezione di Firenze, I-50019 Sesto Fiorentino, Firenze, Italy*
[50]*INFN, Sezione di Roma, I-00185 Roma, Italy*
[51]*Université catholique de Louvain, B-1348 Louvain-la-Neuve, Belgium*
[52]*Nikhef, Science Park 105, 1098 XG Amsterdam, Netherlands*
[53]*King's College London, University of London, London WC2R 2LS, United Kingdom*
[54]*Korea Institute of Science and Technology Information (KISTI), Yuseong-gu, Daejeon 34141, Republic of Korea*
[55]*National Institute for Mathematical Sciences, Yuseong-gu, Daejeon 34047, Republic of Korea*
[56]*Christopher Newport University, Newport News, Virginia 23606, USA*
[57]*International College, Osaka University, Toyonaka City, Osaka 560-0043, Japan*
[58]*School of High Energy Accelerator Science, The Graduate University for Advanced Studies (SOKENDAI), Tsukuba City, Ibaraki 305-0801, Japan*
[59]*University of Oregon, Eugene, Oregon 97403, USA*
[60]*Syracuse University, Syracuse, New York 13244, USA*
[61]*Université de Liège, B-4000 Liège, Belgium*
[62]*University of Minnesota, Minneapolis, Minnesota 55455, USA*
[63]*Università degli Studi di Milano-Bicocca, I-20126 Milano, Italy*
[64]*INFN, Sezione di Milano-Bicocca, I-20126 Milano, Italy*
[65]*INAF, Osservatorio Astronomico di Brera sede di Merate, I-23807 Merate, Lecco, Italy*
[66]*LIGO Hanford Observatory, Richland, Washington 99352, USA*
[67]*Dipartimento di Medicina, Chirurgia e Odontoiatria "Scuola Medica Salernitana", Università di Salerno, I-84081 Baronissi, Salerno, Italy*
[68]*SUPA, University of Glasgow, Glasgow G12 8QQ, United Kingdom*
[69]*LIGO Laboratory, Massachusetts Institute of Technology, Cambridge, Massachusetts 02139, USA*
[70]*Wigner RCP, RMKI, H-1121 Budapest, Konkoly Thege Miklós út 29-33, Hungary*
[71]*University of Florida, Gainesville, Florida 32611, USA*
[72]*Stanford University, Stanford, California 94305, USA*
[73]*Università di Pisa, I-56127 Pisa, Italy*
[74]*INFN, Sezione di Perugia, I-06123 Perugia, Italy*
[75]*Università di Perugia, I-06123 Perugia, Italy*
[76]*Università di Padova, Dipartimento di Fisica e Astronomia, I-35131 Padova, Italy*
[77]*INFN, Sezione di Padova, I-35131 Padova, Italy*
[78]*Montana State University, Bozeman, Montana 59717, USA*
[79]*Institute for Plasma Research, Bhat, Gandhinagar 382428, India*
[80]*Nicolaus Copernicus Astronomical Center, Polish Academy of Sciences, 00-716, Warsaw, Poland*
[81]*Dipartimento di Ingegneria, Università del Sannio, I-82100 Benevento, Italy*
[82]*OzGrav, University of Adelaide, Adelaide, South Australia 5005, Australia*
[83]*California State University, Los Angeles, 5151 State University Drive, Los Angeles, California 90032, USA*
[84]*INFN, Sezione di Genova, I-16146 Genova, Italy*
[85]*OzGrav, University of Western Australia, Crawley, Western Australia 6009, Australia*
[86]*RRCAT, Indore, Madhya Pradesh 452013, India*
[87]*GRAPPA, Anton Pannekoek Institute for Astronomy and Institute for High-Energy Physics, University of Amsterdam, Science Park 904, 1098 XH Amsterdam, Netherlands*
[88]*Missouri University of Science and Technology, Rolla, Missouri 65409, USA*
[89]*Faculty of Physics, Lomonosov Moscow State University, Moscow 119991, Russia*
[90]*Università di Trento, Dipartimento di Fisica, I-38123 Povo, Trento, Italy*
[91]*INFN, Trento Institute for Fundamental Physics and Applications, I-38123 Povo, Trento, Italy*
[92]*SUPA, University of the West of Scotland, Paisley PA1 2BE, United Kingdom*
[93]*Bar-Ilan University, Ramat Gan, 5290002, Israel*
[94]*Artemis, Université Côte d'Azur, Observatoire de la Côte d'Azur, CNRS, F-06304 Nice, France*
[95]*Dipartimento di Fisica "E.R. Caianiello", Università di Salerno, I-84084 Fisciano, Salerno, Italy*
[96]*INFN, Sezione di Napoli, Gruppo Collegato di Salerno, Complesso Universitario di Monte S. Angelo, I-80126 Napoli, Italy*
[97]*Università di Roma "La Sapienza", I-00185 Roma, Italy*
[98]*Univ Rennes, CNRS, Institut FOTON-UMR6082, F-3500 Rennes, France*
[99]*Indian Institute of Technology Bombay, Powai, Mumbai 400 076, India*
[100]*INFN, Laboratori Nazionali del Gran Sasso, I-67100 Assergi, Italy*
[101]*Laboratoire Kastler Brossel, Sorbonne Université, CNRS, ENS-Université PSL, Collège de France, F-75005 Paris, France*

[102]*Astronomical Observatory Warsaw University, 00-478 Warsaw, Poland*
[103]*University of Maryland, College Park, Maryland 20742, USA*
[104]*Max Planck Institute for Gravitational Physics (Albert Einstein Institute), D-14476 Potsdam, Germany*
[105]*L2IT, Laboratoire des 2 Infinis-Toulouse, Université de Toulouse, CNRS/IN2P3, UPS, F-31062 Toulouse Cedex 9, France*
[106]*University of Portsmouth, Portsmouth, PO1 3FX, United Kingdom*
[107]*IGFAE, Campus Sur, Universidade de Santiago de Compostela, 15782 Spain*
[108]*The Chinese University of Hong Kong, Shatin, New Territories, Hong Kong*
[109]*Stony Brook University, Stony Brook, New York 11794, USA*
[110]*Center for Computational Astrophysics, Flatiron Institute, New York, New York 10010, USA*
[111]*NASA Goddard Space Flight Center, Greenbelt, Maryland 20771, USA*
[112]*Dipartimento di Fisica, Università degli Studi di Genova, I-16146 Genova, Italy*
[113]*Institute for Gravitational and Subatomic Physics (GRASP), Utrecht University, Princetonplein 1, 3584 CC Utrecht, Netherlands*
[114]*Department of Astronomy, Beijing Normal University, Beijing 100875, China*
[115]*OzGrav, University of Melbourne, Parkville, Victoria 3010, Australia*
[116]*Università degli Studi di Sassari, I-07100 Sassari, Italy*
[117]*INFN, Laboratori Nazionali del Sud, I-95125 Catania, Italy*
[118]*Università di Roma Tor Vergata, I-00133 Roma, Italy*
[119]*INFN, Sezione di Roma Tor Vergata, I-00133 Roma, Italy*
[120]*University of Sannio at Benevento, I-82100 Benevento, Italy and INFN, Sezione di Napoli, I-80100 Napoli, Italy*
[121]*Villanova University, 800 Lancaster Avenue, Villanova, Pennsylvania 19085, USA*
[122]*Departamento de Astronomía y Astrofísica, Universitat de València, E-46100 Burjassot, València, Spain*
[123]*Universität Hamburg, D-22761 Hamburg, Germany*
[124]*Rochester Institute of Technology, Rochester, New York 14623, USA*
[125]*National Tsing Hua University, Hsinchu City, 30013 Taiwan, Republic of China*
[126]*Department of Applied Physics, Fukuoka University, Jonan, Fukuoka City, Fukuoka 814-0180, Japan*
[127]*OzGrav, Charles Sturt University, Wagga Wagga, New South Wales 2678, Australia*
[128]*Department of Physics, Tamkang University, Danshui District, New Taipei City 25137, Taiwan*
[129]*Department of Physics and Institute of Astronomy, National Tsing Hua University, Hsinchu 30013, Taiwan*
[130]*Department of Physics, Center for High Energy and High Field Physics, National Central University, Zhongli District, Taoyuan City 32001, Taiwan*
[131]*CaRT, California Institute of Technology, Pasadena, California 91125, USA*
[132]*Department of Physics, National Tsing Hua University, Hsinchu 30013, Taiwan*
[133]*Dipartimento di Ingegneria Industriale (DIIN), Università di Salerno, I-84084 Fisciano, Salerno, Italy*
[134]*Institute of Physics, Academia Sinica, Nankang, Taipei 11529, Taiwan*
[135]*Université Lyon, Université Claude Bernard Lyon 1, CNRS, IP2I Lyon/IN2P3, UMR 5822, F-69622 Villeurbanne, France*
[136]*Seoul National University, Seoul 08826, Republic of Korea*
[137]*Pusan National University, Busan 46241, Republic of Korea*
[138]*INAF, Osservatorio Astronomico di Padova, I-35122 Padova, Italy*
[139]*University of Arizona, Tucson, Arizona 85721, USA*
[140]*Rutherford Appleton Laboratory, Didcot OX11 0DE, United Kingdom*
[141]*OzGrav, Swinburne University of Technology, Hawthorn, Victoria 3122, Australia*
[142]*Université libre de Bruxelles, Avenue Franklin Roosevelt 50–1050 Bruxelles, Belgium*
[143]*Universitat de les Illes Balears, IAC3—IEEC, E-07122 Palma de Mallorca, Spain*
[144]*Université Libre de Bruxelles, Brussels 1050, Belgium*
[145]*Departamento de Matemáticas, Universitat de València, E-46100 Burjassot, València, Spain*
[146]*Texas Tech University, Lubbock, Texas 79409, USA*
[147]*The Pennsylvania State University, University Park, Pennsylvania 16802, USA*
[148]*University of Rhode Island, Kingston, Rhode Island 02881, USA*
[149]*The University of Texas Rio Grande Valley, Brownsville, Texas 78520, USA*
[150]*Bellevue College, Bellevue, Washington 98007, USA*
[151]*Scuola Normale Superiore, Piazza dei Cavalieri, 7–56126 Pisa, Italy*
[152]*MTA-ELTE Astrophysics Research Group, Institute of Physics, Eötvös University, Budapest 1117, Hungary*
[153]*University of Szeged, Dóm tér 9, Szeged 6720, Hungary*

[154]*Maastricht University, P.O. Box 616, 6200 MD Maastricht, Netherlands*
[155]*The University of Sheffield, Sheffield S10 2TN, United Kingdom*
[156]*Université Lyon, Université Claude Bernard Lyon 1, CNRS, Laboratoire des Matériaux Avancés (LMA), IP2I Lyon/IN2P3, UMR 5822, F-69622 Villeurbanne, France*
[157]*Dipartimento di Scienze Matematiche, Fisiche e Informatiche, Università di Parma, I-43124 Parma, Italy*
[158]*INFN, Sezione di Milano Bicocca, Gruppo Collegato di Parma, I-43124 Parma, Italy*
[159]*Physik-Institut, University of Zurich, Winterthurerstrasse 190, 8057 Zurich, Switzerland*
[160]*University of Chicago, Chicago, Illinois 60637, USA*
[161]*Université de Strasbourg, CNRS, IPHC UMR 7178, F-67000 Strasbourg, France*
[162]*West Virginia University, Morgantown, West Virginia 26506, USA*
[163]*Montclair State University, Montclair, New Jersey 07043, USA*
[164]*Colorado State University, Fort Collins, Colorado 80523, USA*
[165]*Institute for Nuclear Research, Hungarian Academy of Sciences, Bem t'er 18/c, H-4026 Debrecen, Hungary*
[166]*Department of Physics, University of Texas, Austin, Texas 78712, USA*
[167]*CNR-SPIN, c/o Università di Salerno, I-84084 Fisciano, Salerno, Italy*
[168]*Scuola di Ingegneria, Università della Basilicata, I-85100 Potenza, Italy*
[169]*Observatori Astronòmic, Universitat de València, E-46980 Paterna, València, Spain*
[170]*The University of Utah, Salt Lake City, Utah 84112, USA*
[171]*Kenyon College, Gambier, Ohio 43022, USA*
[172]*Vrije Universiteit Amsterdam, 1081 HV, Amsterdam, Netherlands*
[173]*Department of Astronomy, The University of Tokyo, Mitaka City, Tokyo 181-8588, Japan*
[174]*Faculty of Engineering, Niigata University, Nishi-ku, Niigata City, Niigata 950-2181, Japan*
[175]*Vanderbilt University, Nashville, Tennessee 37235, USA*
[176]*State Key Laboratory of Magnetic Resonance and Atomic and Molecular Physics, Innovation Academy for Precision Measurement Science and Technology (APM), Chinese Academy of Sciences, Xiao Hong Shan, Wuhan 430071, China*
[177]*Universiteit Gent, B-9000 Gent, Belgium*
[178]*Cornell University, Ithaca, New York 14850, USA*
[179]*University of British Columbia, Vancouver, British Columbia V6T 1Z4, Canada*
[180]*Tata Institute of Fundamental Research, Mumbai 400005, India*
[181]*INAF, Osservatorio Astronomico di Capodimonte, I-80131 Napoli, Italy*
[182]*The University of Mississippi, University, Mississippi 38677, USA*
[183]*University of Michigan, Ann Arbor, Michigan 48109, USA*
[184]*Texas A&M University, College Station, Texas 77843, USA*
[185]*Department of Physics, Ulsan National Institute of Science and Technology (UNIST), Ulju-gun, Ulsan 44919, Republic of Korea*
[186]*Applied Research Laboratory, High Energy Accelerator Research Organization (KEK), Tsukuba City, Ibaraki 305-0801, Japan*
[187]*Dipartimento di Fisica, Università di Trieste, I-34127 Trieste, Italy*
[188]*Shanghai Astronomical Observatory, Chinese Academy of Sciences, Shanghai 200030, China*
[189]*American University, Washington, D.C. 20016, USA*
[190]*Faculty of Science, University of Toyama, Toyama City, Toyama 930-8555, Japan*
[191]*Institute for Cosmic Ray Research (ICRR), KAGRA Observatory, The University of Tokyo, Kamioka-cho, Hida City, Gifu 506-1205, Japan*
[192]*Carleton College, Northfield, Minnesota 55057, USA*
[193]*University of California, Berkeley, California 94720, USA*
[194]*Maastricht University, 6200 MD, Maastricht, Netherlands*
[195]*College of Industrial Technology, Nihon University, Narashino City, Chiba 275-8575, Japan*
[196]*Graduate School of Science and Technology, Niigata University, Nishi-ku, Niigata City, Niigata 950-2181, Japan*
[197]*Department of Physics, National Taiwan Normal University, sec. 4, Taipei 116, Taiwan*
[198]*Astronomy & Space Science, Chungnam National University, Yuseong-gu, Daejeon 34134, Republic of Korea, Republic of Korea*
[199]*Department of Physics and Mathematics, Aoyama Gakuin University, Sagamihara City, Kanagawa 252-5258, Japan*
[200]*Kavli Institute for Astronomy and Astrophysics, Peking University, Haidian District, Beijing 100871, China*

[201]Yukawa Institute for Theoretical Physics (YITP), Kyoto University, Sakyou-ku, Kyoto City, Kyoto 606-8502, Japan
[202]Graduate School of Science and Engineering, University of Toyama, Toyama City, Toyama 930-8555, Japan
[203]Department of Physics, Graduate School of Science, Osaka City University, Sumiyoshi-ku, Osaka City, Osaka 558-8585, Japan
[204]Nambu Yoichiro Institute of Theoretical and Experimental Physics (NITEP), Osaka City University, Sumiyoshi-ku, Osaka City, Osaka 558-8585, Japan
[205]Institute of Space and Astronautical Science (JAXA), Chuo-ku, Sagamihara City, Kanagawa 252-0222, Japan
[206]Directorate of Construction, Services & Estate Management, Mumbai 400094, India
[207]Universiteit Antwerpen, Prinsstraat 13, 2000 Antwerpen, Belgium
[208]University of Białystok, 15-424 Białystok, Poland
[209]Department of Physics, Ewha Womans University, Seodaemun-gu, Seoul 03760, Republic of Korea
[210]National Astronomical Observatories, Chinese Academic of Sciences, Chaoyang District, Beijing, China
[211]School of Astronomy and Space Science, University of Chinese Academy of Sciences, Chaoyang District, Beijing, China
[212]University of Southampton, Southampton SO17 1BJ, United Kingdom
[213]Institute for Cosmic Ray Research (ICRR), The University of Tokyo, Kashiwa City, Chiba 277-8582, Japan
[214]Chung-Ang University, Seoul 06974, Republic of Korea
[215]Institut de Física d'Altes Energies (IFAE), Barcelona Institute of Science and Technology, and ICREA, E-08193 Barcelona, Spain
[216]Graduate School of Science, Tokyo Institute of Technology, Meguro-ku, Tokyo 152-8551, Japan
[217]University of Washington Bothell, Bothell, Washington 98011, USA
[218]Institute of Applied Physics, Nizhny Novgorod, 603950, Russia
[219]Ewha Womans University, Seoul 03760, Republic of Korea
[220]Inje University Gimhae, South Gyeongsang 50834, Republic of Korea
[221]Department of Physics, Myongji University, Yongin 17058, Republic of Korea
[222]Korea Astronomy and Space Science Institute, Daejeon 34055, Republic of Korea
[223]National Institute for Mathematical Sciences, Daejeon 34047, Republic of Korea
[224]Ulsan National Institute of Science and Technology, Ulsan 44919, Republic of Korea
[225]Department of Physical Science, Hiroshima University, Higashihiroshima City, Hiroshima 903-0213, Japan
[226]School of Physics and Astronomy, Cardiff University, Cardiff, CF24 3AA, UK
[227]Institute of Astronomy, National Tsing Hua University, Hsinchu 30013, Taiwan
[228]Bard College, 30 Campus Road, Annandale-On-Hudson, New York 12504, USA
[229]Institute of Mathematics, Polish Academy of Sciences, 00656 Warsaw, Poland
[230]National Center for Nuclear Research, 05-400 Świerk-Otwock, Poland
[231]Instituto de Fisica Teorica UAM-CSIC, Universidad Autónoma de Madrid, 28049 Madrid, Spain
[232]Department of Physics, Nagoya University, Chikusa-ku, Nagoya, Aichi 464-8602, Japan
[233]Université de Montréal/Polytechnique, Montreal, Quebec H3T 1J4, Canada
[234]Laboratoire Lagrange, Université Côte d'Azur, Observatoire Côte d'Azur, CNRS, F-06304 Nice, France
[235]Department of Physics, Hanyang University, Seoul 04763, Republic of Korea
[236]Sungkyunkwan University, Seoul 03063, Republic of Korea
[237]NAVIER, École des Ponts, Univ Gustave Eiffel, CNRS, Marne-la-Vallée, France
[238]Department of Physics, National Cheng Kung University, Tainan City 701, Taiwan
[239]National Center for High-performance computing, National Applied Research Laboratories, Hsinchu Science Park, Hsinchu City 30076, Taiwan
[240]Institute for High-Energy Physics, University of Amsterdam, Science Park 904, 1098 XH Amsterdam, Netherlands
[241]NASA Marshall Space Flight Center, Huntsville, Alabama 35811, USA
[242]University of Washington, Seattle, Washington 98195, USA
[243]Dipartimento di Matematica e Fisica, Università degli Studi Roma Tre, I-00146 Roma, Italy
[244]INFN, Sezione di Roma Tre, I-00146 Roma, Italy
[245]ESPCI, CNRS, F-75005 Paris, France
[246]Concordia University Wisconsin, Mequon, Wisconsin 53097, USA
[247]Università di Camerino, Dipartimento di Fisica, I-62032 Camerino, Italy

[248]*School of Physics Science and Engineering, Tongji University, Shanghai 200092, China*
[249]*Southern University and A&M College, Baton Rouge, Louisiana 70813, USA*
[250]*Centre Scientifique de Monaco, 8 quai Antoine Ier, MC-98000, Monaco*
[251]*Institute for Photon Science and Technology, The University of Tokyo, Bunkyo-ku, Tokyo 113-8656, Japan*
[252]*Indian Institute of Technology Madras, Chennai 600036, India*
[253]*Saha Institute of Nuclear Physics, Bidhannagar, West Bengal 700064, India*
[254]*The Applied Electromagnetic Research Institute, National Institute of Information and Communications Technology (NICT), Koganei City, Tokyo 184-8795, Japan*
[255]*Institut des Hautes Etudes Scientifiques, F-91440 Bures-sur-Yvette, France*
[256]*Faculty of Law, Ryukoku University, Fushimi-ku, Kyoto City, Kyoto 612-8577, Japan*
[257]*Indian Institute of Science Education and Research, Kolkata, Mohanpur, West Bengal 741252, India*
[258]*Department of Astrophysics/IMAPP, Radboud University Nijmegen, P.O. Box 9010, 6500 GL Nijmegen, Netherlands*
[259]*Department of Physics, University of Notre Dame, Notre Dame, Indiana 46556, USA*
[260]*Consiglio Nazionale delle Ricerche-Istituto dei Sistemi Complessi, Piazzale Aldo Moro 5, I-00185 Roma, Italy*
[261]*Korea Astronomy and Space Science Institute (KASI), Yuseong-gu, Daejeon 34055, Republic of Korea*
[262]*Hobart and William Smith Colleges, Geneva, New York 14456, USA*
[263]*International Institute of Physics, Universidade Federal do Rio Grande do Norte, Natal RN 59078-970, Brazil*
[264]*Museo Storico della Fisica e Centro Studi e Ricerche "Enrico Fermi", I-00184 Roma, Italy*
[265]*Lancaster University, Lancaster LA1 4YW, United Kingdom*
[266]*Università di Trento, Dipartimento di Matematica, I-38123 Povo, Trento, Italy*
[267]*Indian Institute of Science Education and Research, Pune, Maharashtra 411008, India*
[268]*Dipartimento di Fisica, Università degli Studi di Torino, I-10125 Torino, Italy*
[269]*Indian Institute of Technology, Palaj, Gandhinagar, Gujarat 382355, India*
[270]*Department of Physics, Kyoto University, Sakyou-ku, Kyoto City, Kyoto 606-8502, Japan*
[271]*Department of Electronic Control Engineering, National Institute of Technology, Nagaoka College, Nagaoka City, Niigata 940-8532, Japan*
[272]*Departamento de Matemática da Universidade de Aveiro and Centre for Research and Development in Mathematics and Applications, Campus de Santiago, 3810-183 Aveiro, Portugal*
[273]*Marquette University, 11420 West Clybourn Street, Milwaukee, Wisconsin 53233, USA*
[274]*Graduate School of Science and Engineering, Hosei University, Koganei City, Tokyo 184-8584, Japan*
[275]*Faculty of Science, Toho University, Funabashi City, Chiba 274-8510, Japan*
[276]*Faculty of Information Science and Technology, Osaka Institute of Technology, Hirakata City, Osaka 573-0196, Japan*
[277]*Università di Firenze, Sesto Fiorentino I-50019, Italy*
[278]*INAF, Osservatorio Astrofisico di Arcetri, Largo E. Fermi 5, I-50125 Firenze, Italy*
[279]*Indian Institute of Technology Hyderabad, Sangareddy, Khandi, Telangana 502285, India*
[280]*iTHEMS (Interdisciplinary Theoretical and Mathematical Sciences Program), The Institute of Physical and Chemical Research (RIKEN), Wako, Saitama 351-0198, Japan*
[281]*INAF, Osservatorio di Astrofisica e Scienza dello Spazio, I-40129 Bologna, Italy*
[282]*Department of Space and Astronautical Science, The Graduate University for Advanced Studies (SOKENDAI), Sagamihara City, Kanagawa 252-5210, Japan*
[283]*Andrews University, Berrien Springs, Michigan 49104, USA*
[284]*Research Center for Space Science, Advanced Research Laboratories, Tokyo City University, Setagaya, Tokyo 158-0082, Japan*
[285]*Institute for Cosmic Ray Research (ICRR), Research Center for Cosmic Neutrinos (RCCN), The University of Tokyo, Kashiwa City, Chiba 277-8582, Japan*
[286]*National Metrology Institute of Japan, National Institute of Advanced Industrial Science and Technology, Tsukuba City, Ibaraki 305-8568, Japan*
[287]*Dipartimento di Scienze Aziendali-Management and Innovation Systems (DISA-MIS), Università di Salerno, I-84084 Fisciano, Salerno, Italy*
[288]*Van Swinderen Institute for Particle Physics and Gravity, University of Groningen, Nijenborgh 4, 9747 AG Groningen, Netherlands*
[289]*Faculty of Science, Department of Physics, The Chinese University of Hong Kong, Shatin, New Territories, Hong Kong*
[290]*Vrije Universiteit Brussel, Boulevard de la Plaine 2, 1050 Ixelles, Belgium*

[291]*Department of Communications Engineering, National Defense Academy of Japan, Yokosuka City, Kanagawa 239-8686, Japan*
[292]*Department of Physics, University of Florida, Gainesville, Florida 32611, USA*
[293]*Department of Information and Management Systems Engineering, Nagaoka University of Technology, Nagaoka City, Niigata 940-2188, Japan*
[294]*Vrije Universiteit Amsterdam, 1081 HV Amsterdam, Netherlands*
[295]*Department of Physics and Astronomy, Sejong University, Gwangjin-gu, Seoul 143-747, Republic of Korea*
[296]*Department of Electrophysics, National Chiao Tung University, Hsinchu, Taiwan*
[297]*Department of Physics, Rikkyo University, Toshima-ku, Tokyo 171-8501, Japan*

[†]Deceased.